Channel Investigation of Outdoor Millimeter-Wave Access Links

vorgelegt von
Dipl.-Ing. Dipl.-Wirt.Ing.
Richard Jürgen Weiler
geb. in Bergisch Gladbach

von der Fakultät IV – Elektrotechnik und Informatik
der Technischen Universität Berlin
zur Erlangung des akademischen Grades

Doktor der Ingenieurwissenschaften
– Dr.-Ing. –

genehmigte Dissertation

Promotionsausschuss:

Vorsitzender:	Prof. Giuseppe Caire, Ph.D.
Gutachter:	Prof. Dr.-Ing. Slawomir Stanczak
Gutachter:	Prof. Alexander Maltsev
Gutachter:	Prof. Makoto Ando

Tag der wissenschaftlichen Aussprache: 26. September 2016

Berlin 2016

Abstract

This thesis presents measurements, characterizations and modeling approaches of the outdoor millimeter-wave access channel. More specifically, in this thesis I address an overlay concept for millimeter-wave 5G networks and corresponding channel measurement campaigns. These campaigns were planned and executed with an approach that focuses on fine spatial and temporal sampling of the channel. This differs from other reported measurements, which mostly rely on mechanically steerable high gain antennas.

The approach chosen in this work greatly reduces the measurement time needed to obtain a channel snapshot from minutes to the order of microseconds, thereby enabling the acquisition of a large number of spatial samples. These samples are an important basis to derive statistically valid information, e.g. on the path loss and dynamic shadow fading caused by the environment. This comes at the price of no inherently available angular information.

In this work, a general concept for millimeter-wave based 5G mobile radio access networks is introduced. The channel measurements and modeling approaches presented here focus on urban outdoor access scenarios, which are seen as the most challenging outdoor environments due to the dense nature of the surroundings and high number of users. Two measurements in urban street canyons and open square scenarios are reported, one at 60 GHz and the other at 10 and 60 GHz carrier frequency simultaneously. Another measurement campaigns focused on ground reflection properties for distances up to 1 km at 60 GHz. A fourth campaign was performed using an electronically steerable 64-element antenna array, focusing on human body shadowing mitigation. The last measurement campaign in this work investigates the impact of dynamic shadow fading, caused by cars, buses and pedestrians in a 28 GHz access scenario.

Two types of channel models are derived based on the measurements. A path loss model and parameters are introduced that generate instantaneous path loss values. A more sophisticated model, the quasi-deterministic model, is also introduced. This model uses a description of the environment to generate

spatially consistent impulse responses with angular resolution. The most dominant components of the impulse response are explicitly expressed, while others, such as random reflections and shadow fading from moving objects are modeled as stochastic processes. The properties of these processes, e.g. the strength of human body blockage or the duration of shadowing events, are derived from the measurement results.

In this work I also present a hardware concept for the implementation of electronic beam switching. This concept allows the parallelization of multiple transmit amplifiers to mitigate the low achievable output power of today's devices. The direction of the switchable beams can be configured arbitrarily to cover an area of interest, as might be needed on the base station side of small cell deployments.

Zusammenfassung

Die vorliegende Arbeit befasst sich mit der Messung, Charakterisierung und Modellierung des Millimeterwellen-Funkkanals zwischen mobilen Kommunikationsendgeräten und der Mobilfunkinfrastruktur. Dabei wird ein Konzept für Mobilfunknetze der fünften Generation (5G) zugrunde gelegt, bei dem das Millimeterwellen-Spektrum als zusätzliche Schicht über bestehenden Netzen der vierten Generation genutzt wird, um die Datenübertragungskapazität dort zu erhöhen, wo der Bedarf tatsächlich besteht. Die in dieser Arbeit beschriebenen Messkampagnen wurden dahingehend entwickelt, diese Funkkanäle mit einer feinen räumlichen und zeitlichen Auflösung abzutasten und unterscheiden sich darin von anderen veröffentlichten Arbeiten, in denen vorwiegend mechanisch rotierte Richtantennen mit hohem Antennengewinn und entsprechend kleinen Öffnungswinkeln zum Einsatz kamen.

Der Ansatz in der vorliegenden Arbeit führt zu einer Reduzierung des Zeitaufwandes für die Messung einer Kanalimpulsantwort in den Bereich von Mikrosekunden. Damit wird die Messung einer großen Zahl von räumlich verteilten Impulsantworten möglich. Dies ist eine wichtige Voraussetzung für die Ableitung verlässlicher statistischer Werte, wie zum Beispiel des Pfadverlusts. Erkauft wird dieser Vorteil mit dem Fehlen von inhärent verfügbaren Richtungsinformationen.

In dieser Arbeit liegt der Fokus auf dem Zugangsnetz außerhalb geschlossener Räume in innerstädtischen Ballungsgebieten, da diese Umgebung zum einen als schwierig aus funktechnischer Sicht gilt, zum anderen jedoch durchaus als eine der ersten Umgebungen mit der neuen Technologie versorgt werden könnte. Zwei Messkampagnen wurden in einer typischen urbanen Häuserschlucht, sowie auf einem innerstädtischen Platz durchgeführt, eine bei 60 GHz Trägerfrequenz und die andere gleichzeitig bei 10 GHz und 60 GHz. Eine weitere Messkampagne hatte die Untersuchung von Bodenreflexionseigenschaften bei Entfernungen bis zu 1000 Metern bei 60 GHz zum Ziel. In einer vierten Messkampagne wurde ein elektronisch steuerbares 60-GHz-Antennenarray mit 64 Antennenelementen genutzt, um Ausweichmöglichkeiten bei Abschattung der Funkverbindung

durch Menschen zu untersuchen. Die letzte Messkampagne in dieser Arbeit untersucht den Einfluss einer urbanen Umgebung, darunter die Abschattung durch Fahrzeuge und Fußgänger bei 28 GHz.

Zwei Kanalmodelle werden basierend auf den Messergebnissen abgeleitet. Ein Pfadverlustmodell wird vorgestellt, das die augenblickliche Dämpfung des Kanals berechnet. Das quasi-deterministische Kanalmodell wird als komplexeres Modell eingeführt, mit dem räumlich konsistente Kanalimpulsantworten mit Richtungsauflösung berechnet werden können. Dabei werden die dominanten Anteile der Wellenausbreitung explizit formuliert und die weiteren Komponenten, wie zum Beispiel Reflexionen an bewegten Objekten als stochastische Prozesse hinterlegt. Die Eigenschaften dieser Prozesse, wie zum Beispiel die Stärke der Dämpfung durch den menschlichen Körper können aus den Messkampagnen abgeleitet werden.

Den Abschluss der Arbeit bildet ein Konzept für eine elektronisch steuerbare Strahlumschaltung. Dieses Konzept erlaubt die Parallelisierung mehrerer Sendeleistungsverstärker, um die begrenzte Ausgangsleistung heutiger integrierter Leistungsverstärker zu umgehen. Die einzelnen Richtungen der Ausgänge der Strahlumschaltung kann dabei frei gestaltet werden, um beispielsweise dem Installationsort einer kleinen Basisstation (sog. Small Cell) optimiert angepasst zu werden.

Danksagung

Diese Seite möchte ich all jene Menschen widmen, die diese Arbeit möglich gemacht haben, denn ich glaube dass es nicht nur die Schultern der Riesen sind, die uns emporheben, um Neues zu entdecken, sondern dass auch die Menschen um uns herum einen wesentlichen Anteil daran haben![1]

Mein besonderer Dank gilt Dr. Wilhelm Keusgen für seine Anleitung, seinen Rat und seine Unterstützung um tief das Thema der Millimeterwellenkommunikation vorzudringen. Ebenso möchte ich herzlich meinen Kollegen, allen voran Michael Peter, für Tat und Rat, sowie Motivation und auch gelegentliche Ablenkung danken.

Gleichermaßen möchte ich mich bei Prof. Slawomir Stanczak für die Betreuung meiner Arbeit bedanken. Natürlich gilt dieser Dank auch Prof. Giuseppe Caire, Prof. Alexander Maltsev und Prof. Makoto Ando für ihre Bereitschaft als Vorsitzender bzw. Gutachter zur Verfügung zu stehen.

Den wichtigsten Menschen in meinem Leben, meiner zauberhaften Frau Han, sowie meinen Kindern Friedrich und Luise, meinen Eltern, Schwiegereltern und meinem Bruder kann ich auf diesem Weg nur ansatzweise für die Zeit, ihr Verständnis und ihre großartige Unterstützung, aber auch kritische Nachfragen danken. 谢谢你们!

[1] *Bernhard von Chartres sagte, wir seien gleichsam Zwerge, die auf den Schultern von Riesen sitzen, um mehr und Entfernteres als diese sehen zu können – freilich nicht dank eigener scharfer Sehkraft oder Körpergröße, sondern weil die Größe der Riesen uns emporhebt.* — Johannes von Salisbury: Metalogicon 3,4,46-50

List of Publications

This work is a thesis by publication. It is based on and contains all of these publications, which I wrote as first author. Detailed references are given below and in the bibliography.

1 Richard J. Weiler, Michael Peter, Wilhelm Keusgen, Emilio Calvanese-Strinati, Antonio De Domenico, Ilario Filippini, Antonio Capone, Isabelle Siaud, Anne-Marie Ulmer-Moll, Alexander Maltsev, and Thomas Haustein and Kei Sakaguchi. Enabling 5G backhaul and access with millimeter-waves. In *Conference on Networks and Communications (EuCNC), 2014 European*, Bologna, Italy, 2014.

2 Richard J. Weiler, Wilhelm Keusgen, Hung-Anh Nguyen, and Michael Peter. On the choice of carrier frequency and bandwidth for 5G small cell deployments. In *Personal Indoor and Mobile Radio Communications*

(PIMRC), 2014 IEEE 25rd International Symposium on, Washington D.C., USA, 2014.

3 Richard J. Weiler, Wilhelm Keusgen, Ilario Filippini, and Antonio Capone. Split control plane functionality in millimeter-wave overlay access. In *1st International Conference on 5G for Ubiquitous Connectivity*, Levi, Finland, 2014.

4 Richard J. Weiler, Michael Peter, Wilhelm Keusgen, Andreas Kortke, and Mike Wisotzki. Millimeter-wave channel sounding of outdoor ground reflections. In *Radio and Wireless Symposium (RWS), 2015 IEEE*, San Diego, USA, Jan 2015.

5 Richard J. Weiler, Michael Peter, Wilhelm Keusgen, and Mike Wisotzki. Measuring the busy urban 60 GHz outdoor access radio channel. In *Ultra-Wideband (ICUWB), 2014 IEEE International Conference on*, Paris, France, 2014.

6 Richard J. Weiler, Michael Peter, Thomas Kühne, Mike Wisotzki, and Wilhelm Keusgen. Simultaneous millimeter-wave multi-band channel sounding in an urban access scenario. In *Antennas and Propagation (EUCAP), 2015 9th European Conference on*, Lisbon, Portugal, April 2015.

7 Richard J. Weiler, Michael Peter, Wilhelm Keusgen, Hidekazu Shimodaira, Khanh Tran Gia, and Kei Sakaguchi. Outdoor millimeter-wave access for heterogeneous networks – path loss and system performance. In *Personal, Indoor and Mobile Radio Communications (PIMRC Workshops), 2014 IEEE 25th International Symposium on*, Washington D.C., USA, 2014.

8 Richard J. Weiler, Michael Peter, Wilhelm Keusgen, Alexander Maltsev, Ingolf Karls, Andrey Pudeyev, Ilya Bolotin, Isabelle Siaud, and Anne-Marie Ulmer-Moll. Quasi-deterministic millimeter-wave channel models in MiWEBA. *EURASIP Journal on Wireless Communications and Networking*, 2016(1):1–16, 2016.

9 Richard J. Weiler, Michael Peter, Wilhelm Keusgen, and Kei Sakaguchi. Environment induced shadowing of urban micro millimeter-wave access links. *IEEE Wireless Communications Letters*, vol. 5, no. 4, pp. 440-443, Aug. 2016.

10 Richard J. Weiler, Wilhelm Keusgen, Alexander Maltsev, Thomas Kühne, Andrey Pudeyev, Liang Xian, Joongheon Kim, and Michael Peter. Millimeter-Wave outdoor access shadowing mitigation using beamforming arrays. In *Antennas and Propagation (EuCAP), 2016 10th European Conference on*, pages 1900–1904, Davos, Switzerland, April 2016.

11 Richard Weiler and Wilhelm Keusgen. Combined power transmission. European Patent 2 624 475, 2015. filed January 31, 2012, and issued January 28, 2015.

Contents

Abbreviations

2G	Second Generation Mobile Radio Network (e.g. GSM)
3G	Third Generation Mobile Radio Network (e.g. UMTS)
4G	Fourth Generation Mobile Radio Network (e.g. LTE)
5G	Fifth Generation Mobile Radio Network
ADC	Analog-to-Digital Converter
AGC	Automatic Gain Control
BPF	Band-Pass Filter
CIR	Channel Impulse Response
DAC	Digital To Analog Converter
DFT	Discrete Fourier Transform
FPGA	Field-Programmable Gate Array
GSM	Global System for Mobile Communications 2nd Generation Mobile Radio Network
IF	Intermediate Frequency
LNA	Low Noise Amplifier
LO	Local Oscillator
LOS	Line-Of-Sight
LTE	Long Term Evolution 4th Generation Mobile Radio Network
LTI	Linear Time-Invariant
LTV	Linear Time-Variant

mm-wave	Millimeter-Wave
MPC	Multipath Component
NLOS	Non-Line-Of-Sight
OLOS	Obstructed Line-Of-Sight
PA	Power Amplifier
PAPR	Peak-to-Average Power Ratio
QD	Quasi-Determinstic
RAM	Random Access Memory
RAN	Radio Access Network
RF	Radio Frequency
UE	User Equipment (e.g. mobile phones)
UMTS	Universal Mobile Telecommunications System 3rd Generation Mobile Radio Network
VGA	Variable Gain Amplifier
VNA	Vector Network Analyzer

1 Introduction

1.1 Why millimeter-wave access links?

The invention of the smartphone has undoubtedly changed the usage of mobile wireless data connections. It has become a permanent companion for billions of users worldwide and drives the ongoing increase in mobile data usage. A thousand fold increase of mobile data throughput and the rise of new services is expected to take place in this decade[OBB+14].

Looking further ahead, completely new ways of interacting with information are expected to take their place in our lives. Being it large information screens everywhere around us or displays embedded in contact lenses, connectivity to the internet will be part of this new technology and there will be many more connected devices than today [Kak11].

Mobile radio networks today have a history of rapid development of over 50 years. With the evolution from systems for limited subscriber groups to 2G, 3G and today 4G the number of users and transported amount of data have steadily increased. At the moment the mobile radio industry and scientific community is working on 5G to lay the groundwork for the coming decade and to prepare for the use cases and applications to come.

Utilizing the frequency spectrum above 6 GHz is one of the key technological elements predicted for 5G [BHL+14]. Available bandwidth in the order of multiple gigahertz and reduced interference due to more directional transmission will drive this trend as well as the shortage of available spectrum in the legacy bands.

To my knowledge, these bands above 6 GHz were so far not used for wide deployments of outdoor & indoor mobile radio access links. The knowledge and experience on wireless propagation and channel models is therefore still limited.

In this dissertation I present my work on the investigation of outdoor millimeter-wave access links. Different channel measurement campaigns have been performed to study the wireless propagation of these links. Typical small

cell deployment scenarios in dense urban environments are the key focus of my work, as they are one candidate for first deployments of such a 5G system. The channel investigations and derived models are being submitted to the scientific community and standardization processes. I believe that they are a substantial contribution to the development of 5G standards and system implementations.

1.2 The millimeter-wave wireless outdoor channel

A radio transmitting a wireless signal to a receiver sends energy in the form of electro-magnetic waves into the space around it. The direction in which the energy is transmitted depends on the properties of the antenna, its radiation pattern. The electro-magnetic waves interact with the environment and eventually a fraction of the transmitted energy excites the receiving antenna. The interaction with the environment and the relationship between the transmitted signal and the received signal in time and frequency domain is called the wireless channel. While the fundamental effects of interaction are well known and understood, real-world environments are too complex to express the wireless channel in closed analytical form. Channel measurements in real scenarios are therefore used to investigate the channel and to develop channel models, as has been done extensively for existing wireless communication standards in the sub 6 GHz bands. These models need to be a good representation of the wireless channel as it affects the signal transmission between transmitter and receiver. Different types of models or different levels of detail may be needed for link level and system level development and assessment, while keeping the complexity at a manageable level.

The following gives an overview over the fundamental effects of outdoor propagation with a special focus on the millimeter-wave frequency band.

The free-space path loss, which is a part of Friis transmission equation, scales with the link distance and the carrier frequency [Fri46]. Hence a signal in the millimeter-wave bands undergoes a much higher attenuation on the same distance compared to a signal below 6 GHz under the assumption of constant antenna gain. Atmospheric effects and their impact on free-space propagation were extensively investigated and integrated into an atmospheric millimeter-wave propagation model ranging up to 1000 GHz by Liebe in 1989 [Lie89]. The logarithmic attenuation caused by water vapor, suspended water droplets and rain grows linear with the distance and the amount of fog and rain rate respectively. The well-known absorption effects due to oxygen absorption

(at 60 GHz) and water vapor absorption (at 183 GHz) are also modeled. While this attenuation might be negligible for small link distances (around 100 m), it becomes a crucial limit for longer link distances at these frequencies. The impact of rain has similar influence for the higher frequency bands. While it might impact long distance links, shorter links, such as found in small cell base stations, will only see a minimal effect [QL06].

Penetration losses and shadowing through human bodies drastically increase with the carrier frequency. It was reported, that human body shadowing can cause attenuations of more than 20 or even 30 dB on indoor 60 GHz links [CZZ04, PWRM+12]. Common building materials like concrete walls were reported to cause severe penetration loss, see e.g. [ASC08] for losses at 40 GHz. A coverage of indoor users by outdoor millimeter-wave base stations, as is the case in today's mobile radio networks might therefore be unlikely.

Specular reflections of electro-magnetic waves are independent of the carrier frequency under the condition that the reflecting surface is smooth and large compared to the wavelength. Roughness of the surface however can lead to more diffuse reflections, spreading the energy in all directions and attenuating the specular component. The Rayleigh criterion can be used to determine whether a reflection is specular or diffuse [Par00]. Diffraction effects at millimeter-wave frequencies are negligible compared to the lower bands, imposing a significant difference when comparing links with unobstructed line-of-sight (LOS) to obstructed LOS (OLOS) or non-line-of-sight (NLOS) ones [PK11]. In outdoor measurements, only a limited number of reflecting clusters have been found in an urban environment [ALS+14].

Outdoor measurements showed that the path loss exponent in unobstructed line-of-sight environments was close to 2 and therefore close to free space propagation [RSM+13a, RGBD+13, RASM12]. The path loss under NLOS conditions however tends to show a stronger dependency on the scattering environment. Reported path loss values for different urban environments vary between 3.9 and 5.8. These values were obtained fitting a log distance model with additional shadowing margin to measured values [RGBD+13, RSM+13b].

Due to the limited number of reflecting clusters and the reflection properties, time dispersion under LOS conditions is typically small (RMS delay spreads[1] below 20 ns were reported) but highly dependent on the environment as well as on the antennas [SC97, CR96]. Under NLOS conditions the spread increases due to the absence of the strong LOS component. The values obtained under

[1] For the definition of the RMS delay spread see [Gol05], p. 86.

these conditions vary greatly with average values in the order of 7-24 ns, while maximum values exceeding 100 ns were observed [SC97]. Using antennas with a high gain of 25 dBi, very low delay spreads of up to 1.4 ns only were reported in peer-to-peer and cellular scenarios [RBDMQ12].

While some fundamental properties of millimeter-wave propagation are understood and reported, other aspects still need further investigation, as laid out in the next section.

1.3 State of the art and research gaps

The interest in channel measurements at millimeter-wave frequencies has seen a steady growth in the last years. However, fundamental investigations of radio propagation and atmospheric effects, such as the oxygen absorption peak at 60 GHz and the effect on rainfall have already been performed decades ago, e.g. by H.J. Liebe [Lie89]. Advances in semiconductor technology and favorable regulatory decisions, such as the allocation of the license free spectrum at 60 GHz have led to a rising interest in indoor millimeter-wave channel measurements. Three different standards have been defined for very high throughput indoor wireless communication, ECMA-387, IEEE 802.15.3c and IEEE 802.11ad, while only the latter has to date been used in prototypes and products [ECM10, IEE09, IEE12]. Measurements have been performed by a large variety of researchers worldwide. The focus varies greatly from path loss and delay spread (e.g. [SC97]) to fully directionally resolved measurements (e.g. [MMS+09, MMS+10]), virtual array measurements (e.g. [RKH+09]) and polarimetric MIMO measurements (e.g. [THR+01, AMS+12, MHD+14, MDS+14]).

Measurement of wireless outdoor access channels has been and is a key element of the development and deployment of mobile radio networks, such as GSM, UMTS, LTE and others [Par00]. Based on these measurements and trials, a large number of channel models have been proposed and used for sub 6 GHz wireless communication and different kinds of applications and use cases. A well-known model for mobile radio networks is e.g. the WINNER II channel model [KMH+07]. It relies on a geometry-based stochastic approach and was designed for frequencies from 2 to 6 GHz with up to 100 MHz bandwidth. Its parameters are determined stochastically, based on statistical distributions extracted from channel measurement data. The model was developed for a wide range of propagation scenarios ranging from indoor office, urban micro-

cell to urban and rural macro-cell. Different scenarios are modeled by the same approach but with different parameters. When going to higher carrier frequencies in the millimeter-wave band and wider bandwidths, the WINNER II model and similar geometry-based stochastic models might not be valid any more.

The group of professor Rappaport at the University of Texas at Austin and NYU Wireless has performed a number of outdoor measurements, ranging from 38 GHz to 72 GHz. They used a sliding correlator based channel sounder with a bandwidth of 400 MHz and mechanically steered directional antennas [RBDMQ12, RQT+12, RSM+13b, MZNR13, RGBD+13, RMSS15]. Recent results were reported on channel modeling approaches and system evaluation [MSR15, SR15], as well as effects of human body interaction [WRC15]. Due to the mechanical steering, the measurement duration for one transmitter-receiver position is quite high, therefore limiting the number of total positions available for the derivation of path loss information. Additionally, the directional measurements have to be combined to generate an artificial omnidirectional antenna pattern. Non-stationary effects of the channel can not be resolved, as the measurement duration is much longer than the channel coherence time.

A group from Samsung Electronics has provided results for indoor and outdoor measurements at 28 GHz [HCL+14a, HCL+14b]. They used mechanically steered high gain antennas on both ends to obtain spatially resolved channel impulse responses. To obtain more statistical data for channel modeling, they also performed ray tracing simulations on outdoor deployment scenarios [CBH+14, HBK+15]. Other reported outdoor measurements used a spectrum analyzer to measure the received power versus the angle of arrival [RASM12].

The above mentioned works on millimeter-wave outdoor channel measurements relied on directional antennas. This inherently limits the number of spatial measurement locations due to the time consumption of a measurement run with mechanically steered antennas. Other measurement campaigns used a frequency domain approach (VNA based) which also requires a rather long time to acquire a single snapshot and which can usually not be acquired and stored in a continuous way. Both these approaches are not fit to measure urban access channels with moving objects, such as pedestrians, cars and busses that lead to channel coherence times in the order of milliseconds or even below. The limited number of different spatial positions is problematic when this data is used to parameterize statistical models. A larger number of samples would greatly improve the stability of the regression.

The spatial selectivity of the used high gain antennas in azimuth direction has to be well known and needs to be considered when calculating omnidirectional channel impulse responses from this kind of measurements. It is also necessary to rotate the antenna exactly around its phase center to coherently combine the CIRs.

Some of the cited references compared the millimeter-wave channel at several frequencies, but the underlaying channel data was not acquired at the same time or the exact same location.

The measurements provided in this thesis were designed to improve these aspects. This approach and its benefits and shortcomings to the existing work are explained in the following introductory chapter. I also present a measurement campaign using an electronically steered 60 GHz antenna array.

1.4 Contributions and structure of this thesis

This work is a thesis by publication and is based on a number of peer-reviewed publications that I have authored [WK15, WPK+14a, WPK+14b, WKNP14, WPKW14, WKFC14, WPK+15a, WPK+15b, WKM+16, WPK+16b]. These publications are reprinted within this document, along with a detailed introduction and summary. I also co-authored additional relevant publications that will also be referenced in the course of the document [PKW15, KKK+11, KKPW13, KWP+14, MPK+14, GPWK15, PWK+16].

An overview over the structure and contents of this thesis is given below.

Chapter 2: Channel sounder design and implementation

In this chapter I introduce general aspects of channel sounding and the system model. I then introduce the channel sounder hardware as an overview to my publications. The details of the technical setup and measurement procedures are explained in greater detail than in the individual publications.

Chapter 3: Millimeter-waves for mobile data communication

This chapter comprises three publications covering fundamental aspects of millimeter-wave communication for mobile data communication. The first introduces the overlay concept. In this concept, existing 4G networks, such as LTE, are enriched with an overlay of millimeter-wave capable small cells to increase the capacity of the wireless network. This concept provides benefits,

such as seamless coverage, and forms an implicit basis for the remainder of the publications.

The second publication is a more general investigation of the channel capacity with respect to the carrier frequency, link distance and energy consumption. A small cell model is introduced to show that utilizing the mm-wave band is beneficial in view of today's spectrum shortage and beyond.

The third publication investigates the localization of fundamental functionality in the overlay concept. This is an important aspect, as the design space increases, when the overlay network is introduced and with respect to the specific properties of the millimeter-wave channel.

Chapter 4: Measurement campaigns and modeling approaches

In this chapter, my contributions on channel measurement and modeling are presented. It comprises seven publications. Five different measurement campaigns are presented. Two of them focus on the path loss, delay spread and multipath components of urban street canyon small cell access channels, measured at 10 GHz and 60 GHz. Two different modeling approaches are derived based on the measurements. One model provides instantaneous path loss values, matching the measurement. The other is a more sophisticated model, based on a geometrical description of the environment in combination with a quasi-deterministic approach.

Another measurement campaign focuses on the ground reflection properties of asphalt at 60 GHz with link distances up to 1000 meter. A two-ray propagation model is introduced that accurately matches the distance dependent fading effects observed in the measurements. This work also supports the derivation of the quasi-deterministic model and has some implications on the use of millimeter-wave frequencies for street-level backhaul deployments that are also introduced with the overlay concept in Section 3.1.

The last two measurements introduced in this chapter focus on system level evaluation of millimeter-wave links. The work presented in Section 4.6 investigates the impact of a busy environment, such as cars and pedestrians on a millimeter-wave link. This measurement was set up at 28 GHz with the transmitter (small cell) and the receiver on opposing sides of a busy street. Long term observation of the link reveals typical events through shadowing, as well as multipath propagation from the surrounding open square.

The last work of this chapter, introduced in Section 4.7, uses a 60 GHz 128

element beamforming array at the transmitter to evaluate possibilities of human body shadowing mitigation. The receiver was placed on 58 different positions and the transmitter performed a sweep over 133 predefined transmitter beam settings, while recording the channel impulse response for each setting. Each measurement was repeated with a human obstructing the line-of-sight right next to the receiver.

Chapter 5: Hardware aspects

In this chapter I introduce a hardware concept for electronic beam steering and parallelization of transmit power amplifiers. The results from the measurement campaigns prove that fast beam switching is necessary to adapt the link to changes in the user position and the environment. The parallelization of power amplifiers and the ability to connect high gain directional antennas to the switchable outputs will help to achieve sufficient coverage in typical small cell distances. This hardware concept is well suited for the base station side of small cells as the directional antennas can be arbitrarily positioned to provide site specific coverage.

1.5 Notation

Square brackets [ ] are used to signify the index of the discrete-variable for a dependent quantity. A discrete quantity $y(x_i)$, sampled at $x_i \in \mathbb{R}$, $i \in [1, \ldots, N_y] \subset \mathbb{N}$ of a continuous quantity dependent on $x \in \mathbb{R}$ is described as $y(x_i)\,|_{x_i \in [x_1, \ldots, x_{N_y}]} \coloneqq y[i]\,|_{i \in [1, \ldots, N_y]}$.

In the included publications the terms path loss and path gain are used to describe the same quantity. The path loss is the attenuation of the electromagnetic wave, propagating from one point in space to another. It is therefore larger than one. Expressed in decibel, the path loss in channel measurements is usually positive and the path gain has the same magnitude but with negative sign.

The term millimeter-wave is used throughout this work. Technically this term refers to the range of frequencies with a wave length between 1 mm and 10 mm, which is the approximate equivalent of 30 GHz to 300 GHz. In the discussion on the fifth generation mobile radio networks (5G), the term mm-wave is also largely used for any frequency band beyond today's used bands, i.e. anything above 6 GHz. In this work I also follow this pragmatic

approach to easily denominate the frequency bands, so far mostly unused for mobile wireless communication.

In the course of this work the names of the stations in the channel sounding setups vary gradually. However, the transmitter was always placed on a tripod on elevated fixed positions. It is therefore also referred to as base station or small cell base station. The receiver on the other hand was mounted on a mobile platform and is therefore also referred to as mobile station or user equipment (UE).

2 Channel sounder design and implementation

This chapter presents the channel sounder method and hardware setups used for the various millimeter-wave measurement campaigns introduced in Chapter 4. In the following Section 2.1 I introduce the measurement principle and the system model. Section 2.2 explains how the calibration of the sounder is performed. In section 2.3 I introduce the hardware related implementation and the last section 2.4 describes the measurement protocols.

2.1 Measurement principle and system model

The wireless radio channel can be measured in a variety of ways. A review on different methods and their advantages and shortcomings was given by Parsons [PDT91]. A correlation based method, termed swept time-delay crosscorelation method, was shown to be the best candidate for wideband radio channel characterization and is adopted here.

In a linear time-invariant (LTI) wireless channel, the channel impulse response (CIR) $h(t)$ characterizes the channel. In the equivalent baseband model, the received signal $y(t)$ can be expressed in dependence of the transmit signal $s(t)$ according to

$$y(t) = s(t) * h(t) = \int_{-\infty}^{\infty} s(\tau)\, h(t-\tau)\, d\tau \tag{2.1}$$

The millimeter-wave mobile access channel however is varying in time and frequency domain due to the mobility of the user and surrounding objects, such as cars. The wireless channel is therefore a linear time-variant (LTV) system, where the channel impulse is not constant over time. The channel sounding method has to estimate the instantaneous channel impulse response $h(t)$ over a wide bandwidth within the coherence time of the channel.

In 1969 Bello proposed [Bel69], based on Kailath's work [Kai62], that a time

varying channel is measurable if the area, where its scattering function[1] is (significantly) different from zero, is smaller than 1. Kozek [KP05] and Pfander [PW06] recently proved this assumption.

A similar criterion was introduced by Kozek [Koz97] to define an underspread channel as one where $2\tau_{max}\nu_{max} \ll 1$ or equivalently the area $A = \{\tau \in [0, \tau_{max}], \nu \in [-\nu_{max}, \nu_{max}]\} \ll 1$ holds, where τ_{max} is the maximum path delay and ν_{max} is the maximum Doppler shift of the channel. This is the rectangular area of the scattering function, defined by the minimum and maximum values of the support in both the memory (in delay-time) and filter bandwidth (in Doppler shift frequency) dimension.

In the case of the urban access channel, we assume $\tau_{max} = 4\,\mu$s which corresponds to a free space propagation distance of 1,200 m, which is much larger than the dimensions of the urban locations under investigation. The maximum filter bandwidth is assumed to be $\nu_{max} = 2.8\,$kHz, which corresponds to the extreme case of a car driving at a relative speed of $50\,{}^{km}/_{\mathrm{h}}$ at 60 GHz. We thus obtain $2\tau_{max}\nu_{max} = 2 \times 4\,\mu\mathrm{s} \times 2.8\,\mathrm{kHz} = 0.0224 \ll 1$, proving the measurability of the outdoor channel under the given assumptions.

The systematic errors that occur when sounding a time variant channel with a correlation based method were derived by Matz et. al [MMS+99, MMH+02]. Four errors were identified: the *commutation*, the *pulse compression*, the *aliasing* and the *misinterpretation error*. The bounds on these errors are derived based on their relation to the spread of the channel in terms of delay and Doppler. It was shown that the errors for the measurement of the highly mobile vehicular channel at 6 GHz with a very similar sounder setup have an error bound of $\sim 20\,$dB [Pas14]. In the present work, the transmitter location was always static and the receiver was moved with a maximum speed of $0.5\,{}^{m}/_{\mathrm{s}}$. As stated previously, the highest Doppler spreads are caused by reflections on moving cars, which only account for a small fraction of the channel impulse response. The spread of the wireless channels under investigation in the present work is therefore smaller than the one in the referenced work. The cited error bound can therefore also be applied as an upper bound to this work.

Verification measurements have been performed on the channel sounder hardware setup by Peter et. al [PWK+16]. The achievable dynamic range, maximum measurable path loss (MMPL), amplitude error and phase stability were analyzed for the back-to-back calibrated channel sounder. The dynamic

[1] The scattering function $S(\lambda, f)$ can be interpreted as the power that is received at a certain delay λ and with a certain frequency offset f, see [Kai62].

range and MMPL are in line with the observations in this work. The very low amplitude error that was determined during verification supports the measurement results.

The estimation of the channel impulse response used in this work relies on the correlation based approach. The sounding signal is derived from a complex valued sequence $s[n]$ with length $N_s \in \mathbb{N}$. This sequence has perfect auto-correlation properties and is optimized for a low peak-to-average power ratio (PAPR), see Section 2.3.1. The periodic baseband transmitter signal $s(t)$ is generated by pulse shaping the sequence $s[n]$ according to

$$s(t) = \sum_{n=-\infty}^{\infty} s[n \mod N_s]\, p(t - nT_s) \tag{2.2}$$

with $T_s = 1/f_c$ being the sampling time of sampling rate f_c. The modulus operator is written as mod . The pulse shape function $p(t)$ results from digital low pass filtering in the digital to analog converter (DAC) and analog low-pass filtering in the transmitter system. As the signal is transmitted periodically, the sequence length N_s has to be chosen appropriately to be longer than the maximum resolvable delay of the measured channel to allow unambiguous estimation of the CIR. At the same time the sequence period $T_p = N_s T_s$ is chosen much shorter than the channel coherence time to assure that the received signals are approximately periodic. This allows the application of the circular convolution theorem and the Discrete Fourier Transform (DFT). Periodic band limited signals are completely described by the DFT transform of one signal period [Por97].

With these assumptions, the received signal from Equation (2.1) can be expressed as the DFT transform of one receiver signal period

$$Y[q] = S[q]\, H_{Rx}[q]\, H[q]\, H_{Tx}[q] + N[q] \tag{2.3}$$

where H_{Rx} and H_{Tx} are the transfer functions of the receiver and transmitter frontends. H is the frequency domain channel transfer function. Note that it depends on the calibration method (see Section 2.2) whether the antennas are included in the frontend or channel transfer function. N is the additive noise contribution to the received signal.

During calibration, a known channel is placed between transmitter and receiver. This allows recording the calibration signal

$$Y_{cal}[q] = S[q]\, H_{Rx}[q]\, H_{cal}[q]\, H_{Tx}[q] + N_{cal}[q] \tag{2.4}$$

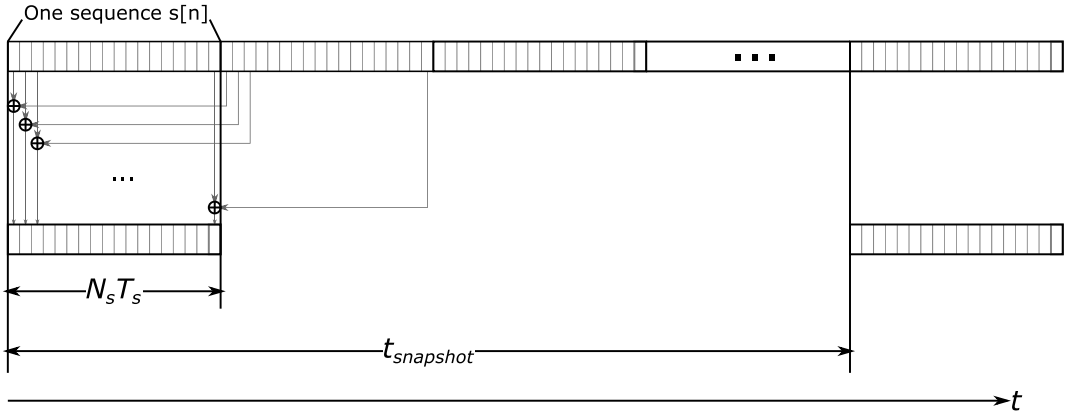

Figure 2.1: Timing of channel measurements

Equation (2.4) can be used to determine $H_{Rx}H_{Tx}$. Using Equation (2.3) the channel transfer function can then be estimated in frequency domain as

$$H[q] = \frac{Y[q]}{S[q]\,H_{Rx}[q]\,H_{Tx}[q]} + \tilde{N}[q] = \frac{Y[q]}{Y_{cal}[q]} H_{cal}[q] + \tilde{N}_t[q] \tag{2.5}$$

where $\tilde{N}_t$ contains both noise processes from the measurement and the calibration. When using the calibration signal to estimate the channel transfer function, no explicit knowledge of the pulse shaped transmit sequence is needed at the receiver side. The recorded receive signal Y is also referred to as one channel snapshot.

The contribution of the noise process N is usually dominated by zero-mean thermal noise. Its contribution to the measured signal vector Y can therefore be reduced by applying averaging over M sequence periods as

$$\begin{aligned} Y_{av}[q] &= \sum_{m=0}^{M-1} \frac{1}{M} S[q+mN_s]\,H_{Rx}[q+mN_s]\,H[q+mN_s]\,H_{Tx}[q+mN_s] \\ &\quad + N[q+mN_s] \\ &= S[q]\,H_{Rx}[q]\,H[q]\,H_{Tx}[q] + N'[q] \end{aligned} \tag{2.6}$$

where N' denotes the samples of the averaged noise process[2]. The transmit signal and the transfer functions of the transmitter, the receiver and the channel need to be constant within the averaging duration. The contribution of the noise process then reduces with increasing M. Figure 2.1 shows the timing of

[2]The logarithmic power of zero-mean Gaussian noise drops linearly with the logarithmic number of averages.

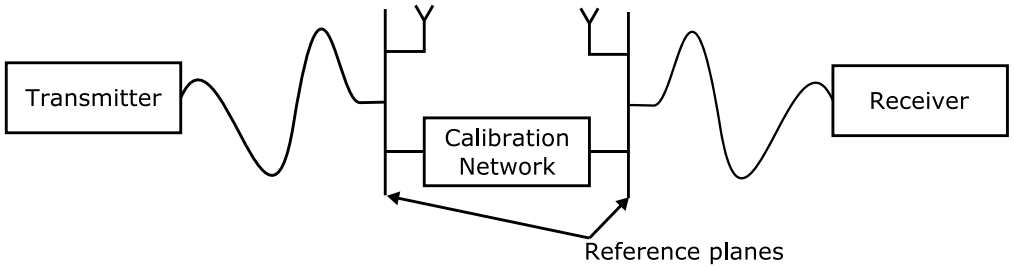

Figure 2.2: Calibration setup

channel measurements with an averaging factor of $M = 2$. The periodically repeating transmit signal is shown on top with a duration of $N_s T_s$ for each of its periods. The received signal Y is shown below, where each element consists of the average (division by 2 not shown) of two consecutive transmit signals. A new snapshot is recorded after a configurable delay time of $t_{snapshot}$ which needs to be a multiple of the transmit sequence duration.

A campaigns was performed with simultaneous sounding of two non-overlapping frequency bands. In this case, the channel impulse responses (CIR) for each carrier frequency can be seen as independent from each other, because the transmit signals and receive signals are separated in frequency domain.

2.2 Calibration

The calibration is an essential step of channel measurements and is the prerequisite to obtain correct and reproducible results. As described in Section 2.1, the output of this step is the determination of the transmitter and receiver frequency responses. Figure 2.2 shows how the calibration is performed. A reference network with two ports is connected between the transmitter and the receiver. The antennas are therefore disconnected from the system during this step. The calibration provides results related to the reference planes, as indicated in the figure. The transfer function of the calibration network is characterized in an extra step using a standard vector network analyzer (VNA). Over the air calibration in an anechoic environment is also possible, but not practically feasible in an outdoor measurement campaign.

The requirement on the calibration networks are:

1. Tunable insertion loss in the order of magnitude of channel under investigation

2. Repeatability (of the tuning)

3. Stability over time
4. Flatness of frequency response
5. Linearity (i.e. no non-linear behavior)

The receiver of a channel sounder usually contains an Automatic Gain Control (AGC) to guarantee full resolution of the analog-to-digital converters (ADC). As described in Section 2.3.4, the AGC is based on variable gain amplifiers, whose frequency response can change with the gain setting. The calibration therefore needs to be performed individually for all gain settings that are also used during the actual channel measurements. To obtain best dynamic range during this step, the calibration network should be tunable to the order of magnitude of the path loss of the channel under investigation. This is also necessary to avoid any clipping in the receiver chain as the transmit chain needs to be operating with the output power also used during the measurement. In practice, the AGC is deactivated during the calibration step and its gain is synchronized to the setting of the calibration network by the channel sounder setup. The repeatability and stability of the calibration network is necessary to guarantee a valid determination of the transmitter and receiver transfer functions.

The flatness of its frequency response is not strictly necessary as it is implicitly removed in the process. A non-flat response however unnecessarily reduces the usable dynamic range during the calibration measurement.

Linearity is important, because the estimation of the channel transfer function, as described in the previous section does not allow identification of non-linear behavior, leading to unwanted distortions.

The measurements in this thesis have been performed with an electronically switchable attenuator for all frequencies up to 30 GHz and with waveguide based tunable attenuators for all frequencies above 30 GHz.

The calibration signal in eq. (2.4) is also subject to noise N_{cal} in the same order of magnitude as the channel measurement itself. Under the assumption that this noise is dominated by zero-mean thermal noise and phase noise, its effect can be reduced by averaging multiple calibration measurements. Care has to be taken that the reference clocks of the transmitter and receiver are tightly synchronized within the averaging duration. A frequency offset would lead to a phase shift, effectively reducing the amplitude of the calibration signal for long averaging durations.

Figure 2.3: HIRATE platform

The antenna transfer function and antenna gain are not part of the calibration procedure as stated above. They are measured in a separate step, as described in Section 2.3.5 and are then applied on the measured channel during post-processing, assuming perfectly matching impedances of the calibration network and the antennas.

2.3 Channel sounder implementation

The hardware platform used for the measurement campaigns presented in this thesis is the HIRATE (High Performance Digital Radio Testbed) platform shown in Figure 2.3 [KKPW13]. It is based on a custom build FPGA platform and has two parallel transmitter and receiver chains, each with 250 MHz bandwidth. It also features frequency synthesizers and IQ-modulators and demodulators for the lower GHz range.

The platform contains a firmware that takes care of timing and triggering, AGC, averaging and storage of received signals. The recorded signals are stored to on-board memory and offloaded to a connected PC after the measurement run is completed. The calculation of the channel impulse response is done in a post-processing step on the recorded data.

In the rest of this section I describe the hardware implementation.

2.3.1 Sounding sequences

The signal $s(t)$, derived from the sequence $s[n]$, should adhere to certain requirements to perform the best channel measurement possible. It should be maximally flat in the frequency domain over the entire bandwidth under investigation. The estimation of the channel impulse response relies on the

autocorrelation of the sequence. It should therefore ideally have an impulse-like periodic autocorrelation function. Such sequences exist and are called perfect [Lük88] and their autocorrelation function ϕ_n is equal to the signal energy at $n = 0$ and zero everywhere else [JP99].

Frank et al. provided a method to generate polyphase codes that adhere to these properties [FZH62]. A generalization to sequences of any length $N_{ZC} \in \mathbb{N}$ was given by Chu [Chu72]. These sequences, called Zadoff-Chu or Frank-Zadoff-Chu sequence, can be seen as multitone sequences with constant amplitude and perfect autocorrelation properties. One period of the sequence can be constructed as

$$s_u[n] = e^{-j\pi un(n+1)/N_{\mathrm{ZC}}} \tag{2.7}$$

with $0 \leq n < N_{ZC}$, $0 < u < N_{ZC} \wedge \gcd(N_{ZC}, u) = 1$, $n, u \in \mathbb{Z}$, where $\gcd(a, b)$ is the greatest common divisor of a and b. The constant amplitude of the complex sequence is a desirable property, as it allows a linear operating point of the transmit power amplifier with very low power backoff. In this work, sequences of length $N_{ZC} = 256$ and $N_{ZC} = 1024$ were used. The sampling rate was fixed at $f_s = 1/T_s = 250\,\mathrm{MHz}$, resulting in sequence period of $T_p = 1.024\,\mu\mathrm{s}$ and $4.096\,\mu\mathrm{s}$.

2.3.2 Timing reference and synchronization

The correlation based method for channel sounding relies on time synchronization between the transmitter and the receiver side. Ideally, all clocks on each side should be phase locked to a single reference. This comprises the following clocks:

- DAC clock (transmit sequence)
- Transmitter intermediate frequency (IF) & radio frequency (RF) local oscillators (see Section 2.3.3)
- Receiver IF & RF local oscillators (LO)
- ADC clock (receiver sampling)

A frequency offset between the DAC clock and the ADC clock directly translates to a timing and phase offset of the estimated channel impulse response that grows linear over time. An offset between the IF & RF local oscillators only affects the phase of the received signal.

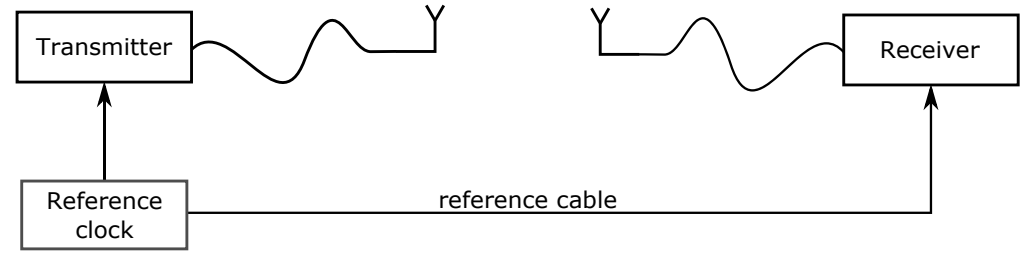

(a) Cable reference

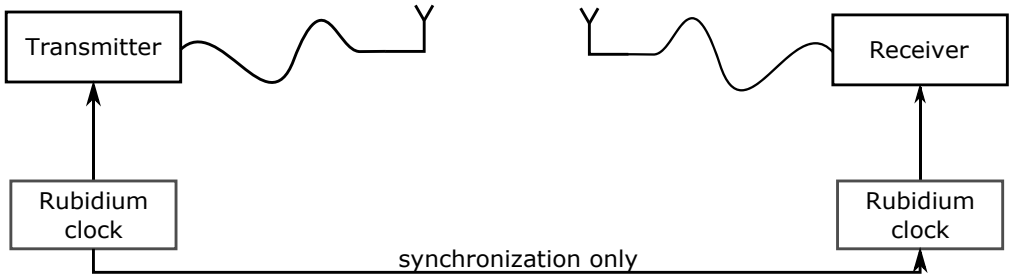

(b) Rubidum clock

Figure 2.4: Clocking options

Figure 2.4 shows the two options that were used for the measurements in this work. The cable reference shown in Figure 2.4a uses only one reference clock (100 MHz in that case) that is distributed to the receiver side via a cable. All other clocks are derived from this reference signal using phase locked loops (PLL). Having a cable between transmitter and receiver is cumbersome, especially when the receiver is moved along busy sidewalks. It also limits the scenarios, as the cable cannot easily span across busy streets.

Time synchronization between transmitter and receiver can also be achieved with short term stable frequency standards. This clocking option is shown in Figure 2.4b. An independent rubidium clock is used as reference signal on both sides. At the beginning of a measurement, before performing the calibration, the two clocks need to be synchronized. This is performed by defining one clock as the master and the other as a slave, adjusting its frequency to be phase locked to the master via a cable. The cable is then removed and transmitter and receiver can be moved around independently from each other. The rubidium clocks used are described in [Wis07].

The channel snapshot measurement is triggered at fixed intervals which are multiples of the sequence length (see Section 2.1). This is implemented using a counter in the FPGA that is also clocked from the reference clock.

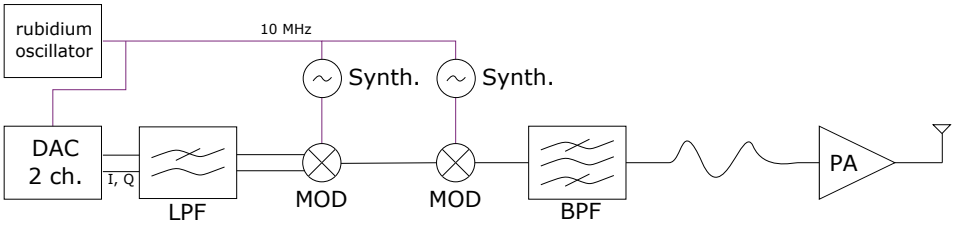

Figure 2.5: Transmit signal generation

2.3.3 Transmit signal generation

The transmitter side of the channel sounder follows a straightforward approach. The block diagram is shown in Figure 2.5. A two channel digital to analog converter (DAC) generates the inphase (I, real) and quadrature (Q, imaginary) parts of the transmit sequence. This signal is fed into a first modulator that is driven by a local oscillator (Synth.) with the intermediate frequency (IF) signal. This signal is then fed into a second modulator. A band-pass filter (BPF) or high-pass filter is used to eliminate the unwanted side band. This signal is fed into a power amplifier (PA), connected to the transmit antenna. A common reference clock is used to derive the sampling clock of the DAC as well as the local oscillator (Synth.).

The baseband source used in this work was either the HIRATE platform or a Rohde & Schwarz AFQ100B. In both cases the transmit sequence previously described is continuously played from memory with a fixed sample rate of 250 MHz. The first modulator is part of the HIRATE platform and based on a MMIC design. The second modulator must be chosen according to the desired frequency band. The filter also depends on the frequency band and was either an integrated coaxial module (below 30 GHz) or a waveguide filter. The local oscillator clock signals are generated using low phase noise frequency generators.

An alternative approach was used for the signal generation of the measurements described in Section 4.6. A Rohde & Schwarz SMW200A signal generator was used. It was fed with the baseband signals and the reference clock and performed the upconversion, filtering and power amplification of the 28.5 GHz signal.

2.3.4 Received signal sampling

The receiver chain is set-up as a superheterodyne receiver, as shown in Figure 2.6. A low noise amplifier (LNA) and an optional band-pass filter amplify the

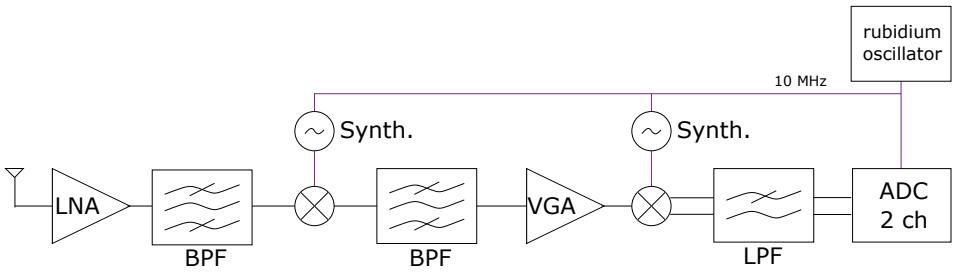

Figure 2.6: Receiver chain

received signal from the antenna and remove unwanted out-of-band interference. A first demodulator stage is used to convert the received signal to a lower intermediate frequency, where it is filtered and amplified again. A second stage with an I/Q demodulator is then used to generate the baseband signal that is fed into the analog-to-digital converter.

The first LNA, filter and demodulator stage is set-up from discrete commercially available components for each frequency band. The second stage, including the variable gain amplifier (VGA) is integrated in the HIRATE platform with a tunable IF frequency in the order of 2 GHz. The low-pass filter in front of the ADC is used to remove any remaining out-of-band signals and to avoid aliasing effects.

The FPGA that processes and stored the received samples is not shown in this figure. It is however also connected to the VGA and an automatic gain control (AGC) is implemented in the digital domain. The power levels at the ADC inputs are monitored and the VGA is controlled to guarantee a high input level without clipping. The snapshot timing and the averaging is also performed in digital domain and controlled by the FPGA. The recorded snapshots are stored in on-board RAM and are downloaded to a connected PC after completing the measurement run.

2.3.5 Antennas

The antennas are the interface between the transmitter, receiver and the wireless channel itself. Their radiation pattern and polarization have a direct influence on the measured and estimated channel.

Ideally, the antenna would have an isotropic pattern, radiating with equal gain in all directions. Then, the channel measurement would include the propagation effects in all spatial directions around the transmitter and receiver. Isotropic radiators are however only a theoretical concept and cannot be fully realized in real hardware. As the environments under investigation in this

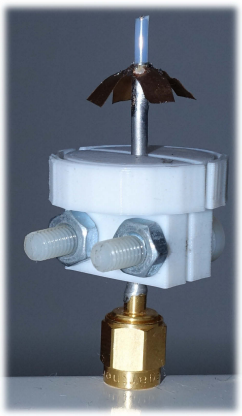

(a) 10 GHz Antenna

(b) 28 GHz Antenna

Figure 2.7: Antenna designs

work are of an urban outdoor nature, omnidirectional antenna patterns with the main lobe in the horizontal plane and a large enough opening angle in elevation direction can be assumed to be a good approximation to measure their channels. Thus, the requirement for the antenna pattern reduces to uniform gain in azimuth direction as well as uniform gain in the relevant part of the elevation region above and below the horizon.

A half-lambda dipole antenna is a good approximation to these requirements for vertical polarization. For horizontal polarization however, more complex designs are needed, for example the Alford loop [AK40].

For the measurements in this work, vertical polarization was chosen and antennas for 10 GHz and 28 GHz were built. They are shown in Figure 2.7a and 2.7b respectively. They are constructed based on semi-rigid coaxial cable as quarter-lambda monopoles. The inner conductor serves as the monopole and a copper sheet is soldered to the outer conductor to serve as a reflecting plane that matches the antenna impedance to the coaxial cable impedance of $50\,\Omega$. Opposed to a full dipole, the pattern of these antennas is asymmetric in elevation direction.

Figures 2.8 and 2.9 show the patterns of both antennas in azimuth and elevation direction. I measured these patterns using a vector network analyzer and an automated rotation positioner. Both antennas exhibit a relatively uniform gain in azimuth direction, which is in line with the requirement. The visible residual variation can be attributed to imperfections of the inner

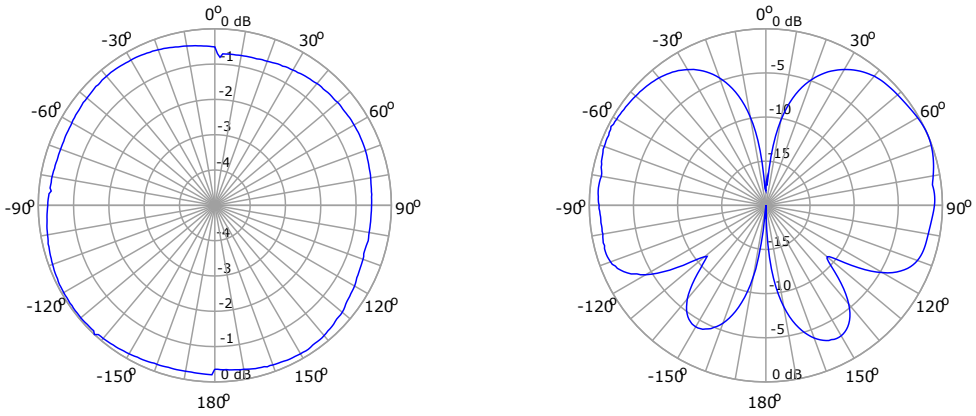

(a) Azimuth pattern ($\theta = \pi/2$)

(b) Elevation pattern

Figure 2.8: Antenna pattern of 10 GHz antenna

conductor and the shield. Note that the figures show the pattern at $\theta = \pi/2$, i.e. perpendicular to the axis of symmetry.

The elevation pattern shows a high dependence on θ. In both cases the maximum gain can be observed at $\theta = \pm 60°$ with a degradation of 1 dB and 2.5 dB towards broadside direction ($\theta = \pm 90°$) for the 10 GHz and 28 GHz antenna respectively. In both cases the 3 dB width is larger than 60°, which is desirable.

When using the antennas on an elevated position, such as the base station side, it is advisable that they are mounted upside down. This avoids a significant influence of the gain taper when the user terminal is located close to the transmit antenna. This consideration was taken into account in the measurement campaigns.

2.4 Measurement protocols

Two different types of measurements were used throughout all measurement campaigns: static measurements and dynamic measurements. In both cases the transmitter was installed at a fixed position.

In the case of static measurements, the receiver is also located at a fixed position during the acquisition of all snapshots. As the measurement environment is usually non-static (moving cars, pedestrians, etc.) this type of measurement allows the observation of the effect of the environment on the wireless channel.

In the case of dynamic measurements, the receiver is moving with constant

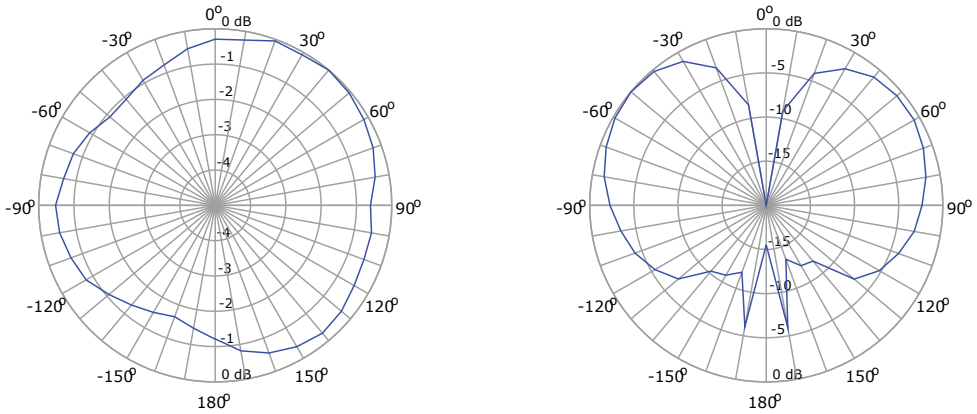

(a) Azimuth pattern ($\theta = \pi/2$)

(b) Elevation pattern

Figure 2.9: Antenna pattern of 28 GHz antenna

speed along a predefined trajectory. This allows sampling the wireless channel along the trajectory, which is for example useful for the derivation of path loss data.

In both cases, the measurement timing is determined by the temporal separation of the snapshots $t_{snapshot}$ as introduces in Section 2.1 and the total number of snapshots N_{total}. The temporal separation can also be expressed as a snapshot rate $f_{snapshot} = 1/t_{snapshot}$.

The speed of the receiver movement v_{Rx} and the snapshot separation directly determine the granularity of the spatial sampling. The spatial distance of two snapshots can be expressed as $d = v_{Rx} t_{snapshot}$. The full length of a single dynamic measurement trajectory can be expressed as $d_{total} = d \times N_{total}$. Measurement tracks longer than this limit were acquired in multiple adjacent measurement runs.

The total number of snapshots that can be recorded at the constant rate is limited by the available memory. Most measurements were performed with a memory limit of ca. 62.000 snapshots. An extension of the memory, implemented during the course of this work, made measurement runs with up to ca. 250.000 snapshots possible.

Table 2.1 reports typical measurement parameters that were used in the measurement campaigns described in this work.

The high receiver speed of 7.5 m/s was only used for the ground reflection measurement, presented in Section 4.1, leading to the length of the trajectory of 300 m. All other mobile measurements in urban scenarios used the lower

Variable	Description	Typical values
f_c	Carrier Frequency	10 GHz, 28.5 GHz, 60 GHz
T_P	Sequence length	1.024 μs, 4.096 μs
$t_{snapshot}$	Snapshot separation (temporal)	800 μs, 667.65 μs
v_{Rx}	Receiver speed	0.5 $^{\mathrm{m}}/_{\mathrm{s}}$, 7.5 $^{\mathrm{m}}/_{\mathrm{s}}$
d	Snapshot distance (dynamic measurement)	0.4 mm, 5 mm
N_{total}	Number of snapshots	62.000, 250.000
d_{total}	Length of single measurement trajectory	25 m, 300 m

Table 2.1: Typical measurement parameters

speed of 0.5 $^{\mathrm{m}}/_{\mathrm{s}}$ and length d_{total} of 25 m.

3 Millimeter-waves for mobile data communication

In this section I provide a deeper look into some fundamental aspects of mm-wave radio communication. It consists of three papers, investigating how a millimeter-wave overlay could be introduced into 4G networks, fundamental investigations of the capacity of mm-wave channels and the localization of functionality in the overlay architecture.

3.1 Overlay concept

The propagation properties at the high frequencies of the millimeter-wave band make it much more difficult to provide full coverage of an outdoor area compared to the lower frequencies employed by today's 3G and 4G networks (see Chapters 1.2 and 4). It is unlikely that a mm-wave based 5G network will be deployed as sole radio access network (RAN). Instead it is more likely that the operators will step-by-step enhance their networks by rolling out additional mm-wave equipment, where needed. User equipment (UE) that supports dual-connectivity on a 4G technology (such as LTE) in the legacy bands and 5G mm-wave technology could simultaneously use both networks to have seamless connectivity everywhere and maximum network capacity, where available. The following publication shows the concept how this could be implemented as overlay networks and discusses the challenges that arise with it [WPK+14a].

Contribution

This paper was a joint work on the overall concept of the MiWEBA project. All partners of the project contributed to this, but the overall coordination was done by me. I authored the introduction and the system overview. I edited the section on the mm-wave propagation and wrote the challenges on the channel characterization and PHY & MAC layer.

Enabling 5G Backhaul and Access with millimeter-waves

Richard J. Weiler*, Michael Peter*, Wilhelm Keusgen*, Emilio Calvanese-Strinati†, Antonio De Domenico†, Ilario Filippini‡, Antonio Capone‡, Isabelle Siaud§, Anne-Marie Ulmer-Moll§, Alexander Maltsev¶, Thomas Haustein* and Kei Sakaguchi‖

*Fraunhofer Heinrich Hertz Institute, Berlin, Germany
†CEA/LETI Labs - MINATEC, 38000, Grenoble, France
‡Advanced Networking Technologies Lab, Politecnico di Milano, Milano, Italy
§Orange Labs, Rennes, France
¶Intel Corporation, Nizhny Novgorod, Russia
‖Graduate School of Engineering, Osaka University, Japan

***Abstract*—This paper presents the approach of extending cellular networks with millimeter-wave backhaul and access links. Introducing a logical split between control and user plane will permit full coverage while seamlessly achieving very high data rates in the vicinity of mm-wave small cells.**

***Index Terms*—5G, Millimeter-wave, 60 GHz, Centralized-RAN, HetNet, Backhaul, Fronthaul, Millimeter-wave radio channel, Overlay, Small Cell, C/U plane split**

I. Introduction

Within the evolution of the fifth generation mobile networks (5G) several radio technologies are targeted for improvement and millimeter-wave communication is seen as one of the key technologies [1]. In this paper we present the joint European-Japanese research project MiWEBA [2] that is part of the European initiative for the development of 5G, e.g. METIS and 5GNOW. Especially the license free 60 GHz band is under focus in MiWEBA as it delivers up to 9 GHz of continuous spectrum available almost everywhere in the world. Furthermore the high propagation loss in free space due to oxygen absorption helps in reducing interference between neighboring connections. Additionally, monolithic microwave integrated circuits are expected to be available on a large scale basis soon with the advent of the 60 GHz extension of Wi-Fi in IEEE 802.11ad.

MiWEBA proposes research and proof of concept of a millimeter-wave overlay in densely populated heterogeneous networks (HetNet) where millimeter-wave small cell base stations are integrated into conventional cellular networks. The project aims to extend the network capacity massively at reasonable cost and without loss of convenience to users. The envisioned HetNet consists of the mm-wave backhaul/fronthaul integrating small cells in the cellular network. The small cell can have an access link compromising both conventional cellular access such as LTE and a novel millimeter-wave link utilizing a centralized radio access network (C-RAN). The architecture and technical solution proposed by MiWEBA introduces for the first time a holistic approach for enabling data and control plane splitting to overcome the restricted coverage problem of mm-wave links. Multi-Technology HetNet and network densification composed of independent technologies for small and macro-cells respectively will be optimized along green criteria owing to novel link adaptation metrics implemented in the centralized architecture.

The paper is organized as follows: First the detailed concepts and the defined scenarios are presented. In section III a summary of the conditions of mm-wave propagation is given. Section IV details the technical challenges and the approaches to solving them.

II. Concepts and Scenarios

A. System overview

The different elements and connections that we address are shown in figure 1. Traditional macro base stations are placed on rooftops and give full network coverage in the traditional frequency bands. Smaller base stations (small cells) are placed within their footprint to give increased data rates or coverage where needed. In this concept there is no further differentiation between different sizes of the small cells.

The base stations are connected to the core network through backhaul links that transport the payload data. These links can be either wired (fibre) or wireless and can also be routed through other base stations in a multi-hop scheme. For the wireless links millimeter-wave technology might be needed to support the high data rates of future systems. Some of the functionality of the base stations can be moved to a more central position in the network. This enables advanced optimizations of the network such as interference control, topology reconfiguration, power saving, etc. This is referred to as centralized radio access network (C-RAN) and is explained later in this section. The requirements for the connection of these C-RAN base stations to the core network are different and to reflect the different logical split they are called fronthaul.

The user terminals (UE) are directly connected to one or multiple base stations via the access link. This link can be on 3G/4G technology or on millimeter-wave as is explained in the next section.

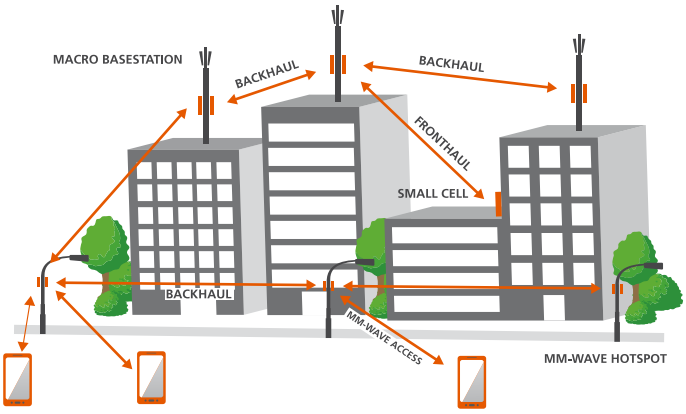

Figure 1. MiWEBA system physical topology

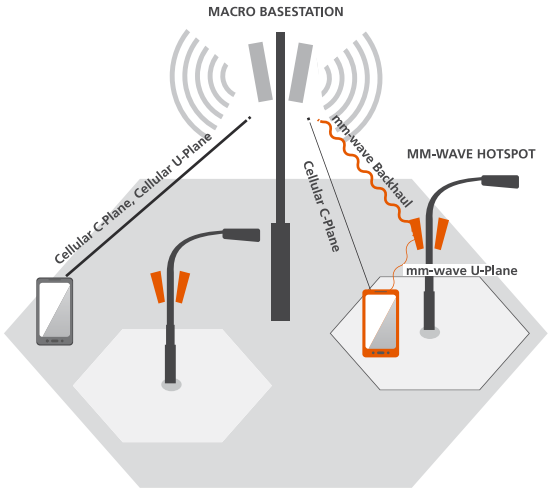

Figure 2. Control/user plane physical links

B. Control/user plane splitting

The basic idea of control/user plane (C/U plane) splitting is to enable mobile terminals to receive system information, issue access requests to a base station and getting assigned radio resources for high-rate data transmission at a different base station, see fig. 2. Signaling and data services can be provided by specialized base stations or implemented as separated and independent services into the same physical equipment. In the case of HetNets a possible approach is to have the macro base station providing the signaling service for the whole area and the small cells specialized in data resources for high-rate transmission with a light control overhead and appropriate air interface.

The main advantage of separation is the removal of the constraint for which radio resources for data transmission are assigned by the same base station used for accessing the service, which is autonomously selected by user terminals. In terms of energy efficiency, this is a big advantage since it allows to activate small cells only when needed, with "on demand" data coverage, while providing everywhere and anytime service accessibility through the full coverage signaling function. More in general, the additional flexibility in resource assignment allows to shift the control of access selection from mobile terminals to a logical Network Access Entity (NAE) and to optimize the resource assignment with a larger view on several parameters, at both user and network side. The NAE can be implemented as a network virtual function that can be migrated throughout the network. On a longer-term perspective, the separation enables new approaches for sharing infrastructures owned by different operators that can be managed by the control plane according to the specific commercial policies they agreed upon, as well as on the network status and the user characteristics and preferences.

C. Centralized-RAN

Recently, the "C-RAN" approach has been proposed by different vendors and operators [3], [4]. The main idea of C-RAN is to shift the baseband processing from the cell to a central location where coordinated processing and resource management is performed while the remaining functions are executed at the antenna location, see fig. 3. This paradigm enables to increase the spectral resource usage as well as the overall energy and computational costs by exploiting multi-user, traffic, and computational diversity. Nevertheless, these gains come at the price of high-capacity links, which usually implies the deployment of optical fiber links. Small cells will likely be deployed at about 3-6m above street level (on street furniture and building facades) to improve the system coverage [5]. However, at these locations, installing fixed broadband access (such as fiber links) for backhaul or Line-Of-Sight (LOS) based microwave links may be too expensive. Hence, in a given area, different small cells will be characterized by heterogeneous backhaul connections, with regard to physical design (wired/wireless), capacity, latency, and topology.

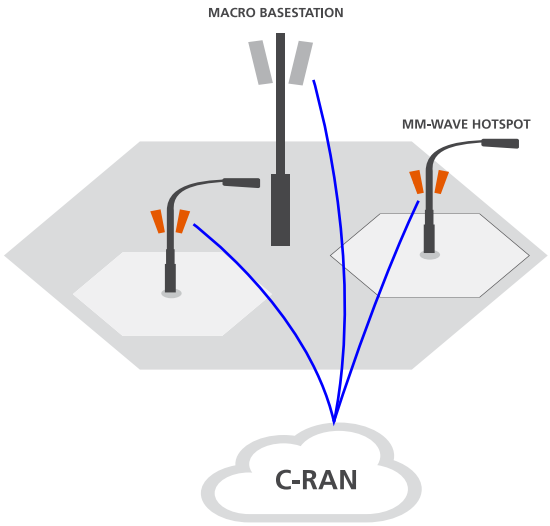

Figure 3. C-RAN logical architecture

To cope with this challenge, depending on the momentary backhaul characteristics (in terms of capacity and latency), service requirements, and network conditions (i.e., load, interference) only a part of the RAN functionalities can be actually implemented at the central coordinator. In particular, we can envisage three principal functional split options: at the PHY

layer, at the MAC layer, and at the Radio Resource Control (RRC).

Functional split on PHY layer enables to fully exploit spatial and computational diversity and by implementing advanced signal processing mechanisms, inter-cell interference can be mitigated or even exploited to enhance the overall spectral efficiency. Functional split can also be implemented at the MAC layer, which enables coordinated radio resource management (RRM) and centralized scheduler. This solution increases the network throughput by mitigating inter-cell interference and exploiting multiplexing gains. A full centralized RRM approach still requires high-capacity backhaul links, since sharing channel state information (CSI) is necessary to correctly implement i.e., multi-cell scheduler. Furthermore, performance relies also on the backhaul latency, since outdated CSI strongly affects the achievable gains.

Third, coordinated RRC enables to optimize the mobility management process, to implement global load balancing mechanisms, and to realize mid-term cell activation/deactivation schemes for energy saving purposes. Although the PHY/MAC adapting mechanisms are implemented in short-time scale to reply to fast changes due to i.e., the channel conditions, coordinated RRC operates in a second basis, which results on less stringent constraints in terms of latency and bandwidth.

D. Multi-Technology HetNet deployment

The Multi-Technology HetNet (MT-HetNets) concept resorts from two fundamental technical challenges: offering high QoS seamless connectivity everywhere with interference limitations and efficient radio resource management and designing Energy Efficient networks by considering MT HetNet architectures able to dynamically select the most green oriented technology to be deployed in a local zone. For that purpose, three research topics are addressed in the MiWEBA project: Multi-Technology (MT) link adaptation techniques are investigated using novel channel quality indicator (CQI) metrics able to limit transmit power whilst ensuring QoS and desired radio coverage of mobile access and backhaul scenarios. The second research topic points at the implementation of such metrics upon cross layer mechanisms that overcome latency, ensure backward compatibility with PHY and MAC in MT base stations, signaling protocols of implemented systems in MT base stations and terminals. Depending on radio link profiles, several solutions are envisioned as the Fast Session Transfer to switch between Wi-Fi label standards (typically IEEE802.11ac and IEE802.11ad), the integration of a new L2.5 layer for Multiple Interface Management as developed in the ICT-FP7 OMEGA project ([6], Deliverable 5.5) and evolved green oriented access network discovery and selection function (ANDSF) discovery protocols currently considered in the 3GPP/Wi-Fi convergence work items. The third research topic deals with the network densification and inter-cell distance (ICD) optimization in MT-HetNets in extending radio engineering functionalities that integrate link adaptation metrics. The CQI metrics previously designed for energy efficient (EE) air interface selection will be mapped into radio planification tools in order to optimize MT-HetNet infrastructure deployments encountering Line-Of-Sight / Non-Line-Of-Sight (LOS/NLOS) critera, base station position and environment topologies under green radio criteria. This new functionality will support active and sleep modes of transmitters, thus ensuring radio coverage with a transmit power minimization.

E. Scenarios

A set of scenarios is defined that serves as a common baseline for all research aspects. The scenarios can be differentiated in indoor and outdoor with the focus being on outdoor environments. The first outdoor scenario are large public areas that are covered with traditional cellular technology and a large number of mm-wave small cells that also provide full coverage of the space. This also includes a mixture of open spaces and adjacent rooms. Typical situations described by this could be e.g. shopping malls. The second outdoor scenario are ultra high-rate hot-spots. In this case, the area is also fully covered by traditional cellular technology and supplemented by mm-wave small cells only on non overlapping spots. The third outdoor scenario are high-rate areas. This is an extension of the second case with a denser distribution of small-cells that can also overlap.

III. Millimeter-wave propagation

Radio wave propagation is affected by diverse physical mechanisms. To what extend each mechanism contributes to the overall signal attenuation and distortion highly depends on the scenario and radio frequency. Millimeter-wave mobile communication will take place at frequencies far above the classical bands – a fact which necessitates a closer look at the principles of propagation.

The free-space path loss scales with the square of link distance and carrier frequency. Hence a signal at 60 GHz undergoes an almost 36 dB higher attenuation on the same way to the receiver compared to a signal at 1 GHz. Atmospheric effects mainly involve oxygen absorption (peak at 60 GHz) and water vapor absorption (peak at 183 GHz) as well as fog and precipitation. They scale exponentially with the link distance. They become relevant for millimeter-wave links exceeding 100 m and crucial for longer distances like 1 km. Furthermore, penetration losses drastically increase with frequency. Whereas up to several GHz, it is possible to achieve good coverage inside buildings from a base station outside, solid walls are practically impenetrable for millimeter-waves.

The frequency dependence of reflections, which are the main reason for multipath propagation, is mainly related to surface roughness. The roughness of typical exterior building materials only moderately affects propagation in the lower GHz range. However, in the millimeter-wave band it may decide between receiving a beneficial near-specular reflection path and none at all. Diffraction effects decrease rapidly as frequency increases. In the millimeter-wave band they are typically only relevant if the size of the obstacle is quite small like in the order of tens of cm. As a result even human body shadowing can cause severe losses exceeding 30 dB [7].

Recently, characterization of millimeter-wave outdoor channels has been emerging as important research topic [8], [9]. The most important finding of previous studies is that multipath

propagation is an issue for outdoor scenarios as it is for indoor propagation. Buildings, the ground, cars and also small objects like trash cans or signs act as reflectors. Measurements consistently confirm that the path loss exponent is close to two for LOS propagation.

Though mainly LOS scenarios are focused for millimeter-wave mobile communication, the presence of specular reflections with significant power in relation with highly directional steerable antennas also motivates the investigation of millimeter-wave usage under obstructed LOS (OLOS) or NLOS conditions. NLOS path loss behavior was found to be similar to that at lower frequencies, but keeping in mind that the results are related to much smaller cell sizes [8], [9].

Time dispersion under LOS conditions is typically small (RMS delay spreads below 20 ns) but highly dependent on the environment as well as on the antennas [10], [11]. Very low delay spreads (only up to 1.4 ns) were observed for the peer-to-peer and cellular scenario with 25 dBi antennas in [8]. Under NLOS conditions the spread increases. Though average values are still moderate (7–24 ns), maximum values exceeding 100 ns are reported in [8]. The results indicate that the RMS delay spread of millimeter-wave outdoor channels are of the same order as for indoor and in-cabin propagation, where values between 10–100 ns have been found [10], [12]. It stays one order below the spread occurring at classical cellular frequencies.

IV. Challenges and envisioned solutions

A. Channel characterization & modeling

The requirements for an outdoor millimeter-wave channel model are expected to be very similar to the indoor case which is well-described in IEEE 802.11ad documents [13]. The channel model should provide accurate space-time characteristics of the propagation channel (basic requirement) for main usage models of interest, support beamforming with steerable directional antennas on both TX and RX sides with no limitation on the antenna technology, take into account polarization characteristics of antennas and signals and support non-stationary characteristics of the propagation channel. This can be achieved by using a dynamic space-time clustered channel model approach.

The investigated channel model adopts the clustering approach with each cluster consisting of several rays closely spaced in time and angular domains. In a real environment, time and angular parameters of different clusters and rays are time varying functions due to a non-stationary setup. However, the rate of these variations is expected to be relatively slow. Within MiWEBA measurements as well as ray tracing simulations based on the defined scenarios will be done and combined into the channel model.

B. PHY and MAC layer

The design space for the physical layer and the wave forms of a new system in the millimetre-wave region is very large. Unlike in lower frequencies the bandwidth available is not dictated by available spectrum. As part of MiWEBA this design space will be evaluated under technical constraints such as phase noise, channel length, fading characteristics etc. Existing approaches such as the recently standardized IEEE 802.11ad will serve as a starting point. Time reversal processing, foreseen as a green PHY/MAC technique [14], will be investigated for millimeter-wave hotspot transmissions benefiting from multi-path diversity and small scale multi-antennas. The MiWEBA project will focus on Link level performance as well as efficient channel sounding techniques for access and backhaul scenarios.

For the MAC layer the focus will lie on seamless integration with the legacy cellular systems in the context of the splitting between control and user plane.

C. Antenna technology and Beamforming

Insertion losses at millimeter-wave frequencies are much higher than in the sub 6 GHz band. To enable connections with sufficient SNR, antennas with high directionality are a necessity. While backhaul and fronthaul connections are generally static, the channel and direction of access links is constantly changing due to movement of the UE and changing environments. High gain beamforming antennas are therefore needed at the small cell base station as well as the user terminal. The most straightforward solution that qualifies for all requirements is the millimeter-wave phased array antenna, that is successfully used for prototypes [15]. However, creation of such large-aperture antenna arrays may pose a problem due to production cost, heat dissipation and feed circuitry complexity.

A solution that helps to overcome mentioned difficulties is the concept of large aperture modular antenna arrays (MAA) recently proposed. The large antenna array is constructed from a number of smaller array modules, each with its own on-chip RF part and common baseband. Another option that may be used in low-cost devices is chip-lens antennas [16] that have great directionality but limited beamsteering ability and will not be able to create several beams simultaneously.

Robust beamforming algorithms that enable fast tracking the beams are also necessary to maximize the link performance. A thorough analysis of the available link budgets under the channel conditions in the defined scenarios will serve as a basis for this research.

D. Small cell discovery

The discovery of millimeter-wave small cells is tightly connected to the above mentioned problem of high gain directional access links and the concept of split planes. The end user terminal must be enabled to detect whether it is under coverage of a small cell quickly in order to profit of the higher data rated of that cell. The design space for such detection mechanisms is dictated by the beamforming antennas and algorithms but also includes side channel information such as the geographical position of the device and small cells in its vicinity.

E. Control/User plane splitting

The most crucial aspects brought in by the C/U splitting is that of providing the information necessary for performing the radio resource assignment and management in an optimized way to the logical network entity. This constitutes the context characterizing service requests and its management represents one of the main differences between the new architecture and the traditional ones. The control plane separation facilitates the

coexistence of different radio access technologies within the same network, that are piloted by a common control infrastructure to serve "on-demand" user requests. The heterogeneity can be extended to legacy technologies, like 4G, as well.

We envision a common control channel architecture where the signaling function can be jointly provided by legacy 4G BSs and new generation ones. Service requests issued through the signaling function can be served according to a resource allocation algorithm that can assign the service to the same 4G BS or alternative BSs according to device capabilities. The architecture can be centralized, where a macro BS controls the data service of small base stations under its coverage umbrella, or distributed, where control entities of peer BSs cooperate to provide a logical network entity to the users. A further architectural choice is between the implementation of the control entity as a different and independent type of BS or as a separated function within a device that hosts both user and control plane interfaces. The selection of the best paradigm will be driven by the deployment scenario.

The investigations related to this challenge will design the best solution according to several key performance indicators, like data channel acquisition delay, data session retainability during mobility, network load increase due to a larger amount of exchanged information, and network capacity and energy consumption trade-offs.

F. Centralized-RAN

The joint implementation of the C/U splitting with the dual connectivity enables reliable radio resource control at a central location. This allows for coordinating the mobility management, the network discovery, the small cell activation/deactivation, the load balancing and inter-cell interference coordination. Finally, coverage areas become dynamic, and virtual cells can be created through the cooperation of multiple neighboring millimeter-wave small cells. Coordinated Multi Point clusters and distributed Massive MIMO can further enhance the performance perceived at the end user.

The C/U splitting will reduce signaling overhead to the small cells. Nevertheless, while being active, small cells will have to transmit to their serving UEs other signals to i.e., indicate the resource allocation, to acquire channel state information, and local synchronization. This approach can be easily integrated in our architecture; however, the transmission of these signals has to be coordinated with the management of the antenna steering. Neighboring small cell cooperation can be required to manage the UE tracking and prevent outage events, i.e., by proactive handover.

Another approach consists in optimizing the beam angle of a dynamic set of neighboring small cells to perform joint transmission towards the nearby user and avoid connection loss due to radio environments. In this way, the average spectral efficiency can be notably improved and coverage holes avoided [17].

V. Conclusion

A concept that uses millimeter-wave links for backhaul, fronthaul and access with a novel control/user plane split is presented as a candidate for 5G system evolution. This concept will enable high data rate densities and other innovative approaches such as centralized RAN (C-RAN) architectures. Technical challenges associated with this concept, such as the need for coordinated centralized resource management and adaptive beamforming and beam tracking were outlined.

Acknowledgment

The research leading to these results has received funding from the European Union's Seventh Framework Programme (FP7-ICT-2013-EU-Japan) under grant agreement n° 608637 and was also supported by MIC in Japan.

References

[1] F. Boccardi, J. Heath, R.W., A. Lozano, T. Marzetta, and P. Popovski, "Five disruptive technology directions for 5G," *Communications Magazine, IEEE*, vol. 52, no. 2, pp. 74–80, February 2014.

[2] MiWEBA Website. [Online]. Available: http://www.miweba.eu/

[3] China Mobile Research Institute, "C-RAN - Road Towards Green Radio Access Network," in *Wireless World Research Forum, Meeting 27 (WWRF 27), Düsseldorf*, 2011, pp. pp. 73–80.

[4] NGMN. (2013, Jan.) Suggestions on Potential Solutions to C-RAN by NGMN Alliance.

[5] Next Generation Mobile Networks (NGMN) Alliance, "Small cell backhaul requirements," *Backhaul Evolution*, June 2012.

[6] Omega Website. [Online]. Available: http://www.ict-omega.eu/

[7] M. Peter, M. Wisotzki, M. Raceala-Motoc, W. Keusgen, R. Felbecker, M. Jacob, S. Priebe, and T. Kurner, "Analyzing human body shadowing at 60 GHz: Systematic wideband MIMO measurements and modeling approaches," in *Antennas and Propagation (EUCAP), 2012 6th European Conference on*. IEEE, 2012, pp. 468–472.

[8] T. S. Rappaport, E. Ben-Dor, J. N. Murdock, and Y. Qiao, "38 GHz and 60 GHz angle-dependent propagation for cellular & peer-to-peer wireless communications," in *Communications (ICC), 2012 IEEE International Conference on*. IEEE, 2012, pp. 4568–4573.

[9] S. Rajagopal, S. Abu-Surra, and M. Malmirchegini, "Channel Feasibility for Outdoor Non-Line-of-Sight mmWave Mobile Communication," in *Vehicular Technology Conference (VTC Fall), 2012 IEEE*. IEEE, 2012, pp. 1–6.

[10] P. Smulders and L. Correia, "Characterisation of propagation in 60 GHz radio channels," *Electronics & communication engineering journal*, vol. 9, no. 2, pp. 73–80, 1997.

[11] L. M. Correia and J. R. Reis, "Wideband characterisation of the propagation channel for outdoors at 60 GHz," in *Personal, Indoor and Mobile Radio Communications, 1996. PIMRC'96., Seventh IEEE International Symposium on*, vol. 2. IEEE, 1996, pp. 752–755.

[12] M. Peter, W. Keusgen, A. Kortke, and M. Schirrmacher, "Measurement and analysis of the 60 GHz in-vehicular broadband radio channel," in *Vehicular Technology Conference, 2007. VTC-2007 Fall. 2007 IEEE 66th*. IEEE, 2007, pp. 834–838.

[13] IEEE doc. 802.11-09/0334r8, "Channel Models for 60 GHz WLAN Systems," Tech. Rep., 2010.

[14] M.-A. Bouzigues, I. Siaud, A.-M. Ulmer-Moll, and M. Hélard, "On the use of time-reversal for packet switching in green communications," in *Wireless and Mobile Computing, Networking and Communications (WiMob), 2013 IEEE 9th International Conference on*. IEEE, 2013, pp. 22–27.

[15] W. Roh, J.-Y. Seol, J. Park, B. Lee, J. Lee, Y. Kim, J. Cho, K. Cheun, and F. Aryanfar, "Millimeter-wave beamforming as an enabling technology for 5G cellular communications: theoretical feasibility and prototype results," *Communications Magazine, IEEE*, vol. 52, no. 2, pp. 106–113, February 2014.

[16] A. Artemenko, A. Maltsev, A. Mozharovskiy, A. Sevastyanov, V. Ssorin, and R. Maslennikov, "Millimeter-wave electronically steerable integrated lens antennas for WLAN/WPAN applications," *Antennas and Propagation, IEEE Transactions on*, vol. 61, no. 4, pp. 1665–1671, 2013.

[17] K. Sakaguchi, S. Sampei, H. Shimodaira, R. Rezagah, G. K. Tran, and K. Araki, "Cloud cooperated heterogeneous cellular networks," in *Intelligent Signal Processing and Communications Systems (ISPACS), 2013 International Symposium on*. IEEE, 2013, pp. 787–791.

3.2 Choice of carrier frequency in small cell context

In the introduction I explained that an increase of the carrier frequency also leads to an increase in the free space path loss. This is only true under the assumption of constant antenna gain, which might not necessarily hold looking at real hardware systems. In the following publication I therefore investigate, how the channel capacity behaves under different assumptions of the antenna gain and carrier frequency [WKNP14]. It is remarkable to note that under the assumption of a constant antenna aperture (i.e. effective size), the channel capacity even grows with an increase in frequency. I also show a small cell model with realistic assumptions on the antenna properties to illustrate that utilizing the millimeter-wave bands as an access technology is a good choice from a capacity and energy consumption point of view.

Contribution

This paper was inspired by the derivation of the "optimum grid" by my colleagues for the case of the constant antenna gain. I derived the other cases and calculated the capacity in each case. The small cell context was evaluated by myself and I set up and parameterized the small cell system model and performed the simulations. I also wrote the introduction, outlook and conclusions of this publication.

On the choice of carrier frequency and bandwidth for 5G small cell deployments

Richard J. Weiler, Wilhelm Keusgen, Hung-Anh Nguyen and Michael Peter
Fraunhofer Heinrich Hertz Institute
Berlin, Germany
Email: richard.weiler@hhi.fraunhofer.de

***Abstract*—The use of previously unused spectrum in the millimeter-wave band is discussed for future fifth generation (5G) mobile communications systems. The legacy frequency bands are very densely used and free spaces are rare, but the question remains, whether increasing the carrier frequency is a good idea. In this paper we derive frequency dependent link capacities and energy efficiency measures for a small cell heterogeneous network scenario.**

***Index Terms*—5G, millimeter-wave, 60 GHz, millimeter-wave communication, millimeter-wave access, HetNet, small cell, energy efficiency**

I. Introduction

The evolution of mobile communications systems towards the fifth generation (5G) is a current and very active research topic. The increase of capacity is one of the main targets of this development. Supplementing the existing cell infrastructure with additional cells that serve smaller areas is a step that is already taken in current 4G LTE deployments [1].

For 5G the use of new spectrum in the millimeter-wave band was proposed to circumvent issues of increased inter-cell interference and due to the almost unused wide bandwidth available [2], [3]. Due to the scarcity of available free spectrum in the sub 6 GHz bands this is a logical choice, being supported by favorable free, light or block license models, endorsed by the regulatory bodies worldwide.

The question remains whether this is a good choice from a channel capacity and energy efficiency point of view. Is it better to transmit signals in a small bandwidth with high spectral efficiency or transmit in a wide bandwidth with lower SNR and less spectral efficiency? In the following we approach this question from a capacity point of view with theoretical and practical assumptions. To our best knowledge, no such fundamental evaluation has been done, but the interest in the millimeter-wave band was driven by the amount of available spectrum.

The rest of the paper is organized as follows. In section II the channel capacity is derived for different definitions of transmit and receive antennas. These results are applied to a small cell system model and evaluated in section III. Section IV gives an overview of aspects that can be included in the system model to enhance its applicability to specific scenarios.

II. Channel capacity

The channel capacity describes the amount of information, that can be transferred through that channel in a certain amount of time. The capacity C of a band limited AWGN wireless transmission channel of frequency bandwidth W, received signal power P_{RX} and receiver noise power spectral density N_0 was given by Shannon [4]:

$$C = W \log_2\left(1 + \frac{P_{RX}}{W N_0}\right) \tag{1}$$

here, the noise power density is assumed to be purely caused by thermal noise and amounts at normal temperature to $N_0 = kT \approx -173\,^{dBm}/_{\mathrm{Hz}}$. Other sources of noise, such as interference, are neglected. For systems operating in the millimeter-wave band directional antennas are mandatory in order to achieve communication ranges of more than a few meters, effectively reducing interference, as the transmitted energy is spatially focused towards the remote station. Furthermore, depending on the channelization of the large bandwidths available, a separation of neighboring transmitters via frequency might be viable.

The received signal power can then be related to the transmit power using the Friis transmission equation for free space propagation [5]:

$$\begin{aligned} P_{RX} &= P_{TX} G_{TX} G_{RX} \left(\frac{\lambda}{4\pi d}\right)^2 \\ &= P_{TX} G_{TX} G_{RX} \left(\frac{c_0}{4\pi d f}\right)^2 \end{aligned} \tag{2}$$

with the transmit power P_{TX}, the transmit and receive antenna gains G_{TX} and G_{RX} respectively, the wavelength λ, distance d, carrier frequency f and the speed of light c_0.

The energy efficiency of a radio transmission can be expressed as the energy E_b that is needed to transmit a single bit of information. Assuming an ideal system, reaching the full channel capacity, it can be expressed as the transmit energy divided by the channel capacity:

$$E_b = \frac{P_{TX}}{C}. \tag{3}$$

In the following sections the Shannon capacity is combined with the Friis equation. Different assumptions can be made on the transmit and receive antenna that are discussed in the following. In II-A constant antenna gain, independent of the frequency, at both sides is assumed. As a more practical assumption a constant size of the effective antenna aperture is used in II-B. For high frequencies or large apertures this

approach lead to unrealistic and impractical antenna gains. Therefore a third method based on a constant equivalent isotropically radiated power (EIRP) is made in section II-C.

A. Constant antenna gain

The Shannon's noisy channel capacity states that for a power limited input signal, the channel capacity increases with increasing bandwidth. When the bandwidth W is small, i.e. signal-to-noise ratio $SNR \gg 0\,\mathrm{dB}$, the capacity $C \approx W \log_2 \left[P_{RX}/N_0 W\right]$ is logarithmic in power and approximately linear in bandwidth. When the bandwidth W is large, i.e. $SNR \ll 0\,\mathrm{dB}$, the capacity $C \approx P_{RX}{}^{\log_2(e)}/_{N_0}$ is linear in power and insensitive to bandwidth. The first case is called the bandwidth limited regime, and the second case the power limited regime. We will show that the Shannon's statement for the bandwidth needs to be modified for the transmit frequency in consideration of path loss. At this point we may define the so called relative bandwidth α according to the formula

$$\alpha = \frac{W}{f} \tag{4}$$

This value is unitless and theoretically bound by 2. In practice, due to technical and regulatory reasons, we may assume $\alpha \leq 0.1$. Existing standards such as IEEE 802.11 define physical layer parameters with 4-8% bandwidth at 2.4 GHz and 3% at 60 GHz. Thus a frequency independent fixed relative bandwidth is a realistic assumption.

We now focus on the line of sight (LOS) Gaussian noise channel. The receive signal power is given in terms of the transmit power by the fundamental relationship (2). The path loss increases tremendously with the frequency. Putting the equation into the Shannon's capacity in (1) we have

$$C = \alpha f \log_2 \left(1 + \frac{P_{TX} G_{TX} G_{RX}}{N_0} \left(\frac{c_0}{4\pi d}\right)^2 \frac{1}{\alpha f^3}\right). \tag{5}$$

The channel capacity depends on six arguments P_{TX}, G_{TX}, G_{RX}, d, f and α. We now assume that the arguments P_{TX}, G_{TX}, G_{RX}, d and α are constant. Thus systems with the same effective antenna gain, operating at different frequencies are compared.

Then there exists an optimum frequency f_0, at which the maximum channel capacity C_0 is achieved. Since

$$\frac{dC(f)}{df} = \frac{\alpha}{\ln 2}\left[\ln\left(1 + \frac{\chi}{\alpha f^3}\right) - \frac{3}{1 + {\alpha f^3}/{\chi}}\right] \tag{6}$$

where

$$\chi = \frac{P_{TX}}{N_0}\left(\frac{c_0}{4\pi d}\right)^2 \tag{7}$$

the maximum capacity according to the formula

$$\begin{aligned} C_0 &\approx 4.07 \alpha f_0 \\ &\approx 1.62 \sqrt[3]{\frac{P_{TX}}{N_0}\left(\frac{\alpha c}{4\pi d}\right)^2} \end{aligned} \tag{8}$$

is obtained at the optimum transmit frequency

$$f_0 \approx 0.40 \sqrt[3]{\frac{P_{TX}}{\alpha N_0}\left(\frac{c}{4\pi d}\right)^2}. \tag{9}$$

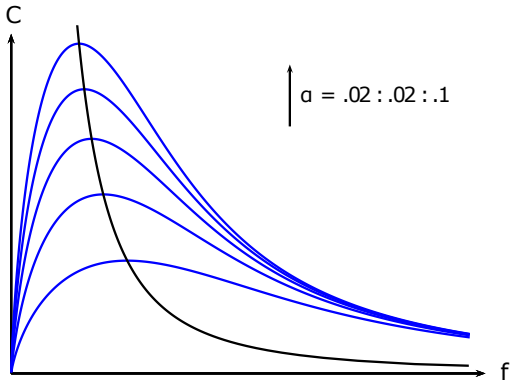

Figure 1. Channel capacity for constant antenna gain

The function $C(f)$ is depicted in Figure 1. On the first hand this obtains the constant spectral efficiency, which is given as

$$\frac{C_0}{W_0} \approx 4.07 \tag{10}$$

For an arbitrary AWGN channel, information transmission with $4.07\,{}^{\mathrm{bps}}/_{\mathrm{Hz}}$ is optimal. For example, a simple nearly optimal system design is uncoded 16QAM using Nyquist rate, which gives the spectral efficiency of $4\,{}^{bps}/_{\mathrm{Hz}}$. On the other hand the value ${}^{E_b}/_{N_0}$, which states how much power per information bit is received, is even constant and given as

$$\begin{aligned} \frac{E_b}{N_0} &= \frac{P_{RX}}{N_0 C_0} \\ &= \frac{P_{TX}}{N_0}\left(\frac{c}{4\pi d}\right)^2 \frac{1}{f_0^2 C_0} \\ &= 5.8\,\mathrm{dB}. \end{aligned} \tag{11}$$

This knowledge is of practical importance to choose an acceptable combination of modulation and coding techniques to come close to the optimum operating point.

A further important graphic visualization is called the optimum grid, in which the optimum capacities are depicted for a fixed distance d. We can take from the grid the required transmit power P_{TX} and relative bandwidth α in relation to the desired optimum frequency f_0 and maximum available capacity C_0. The grid is useful to choose suitable system parameters for a given connection distance d.

Figure 2 shows the optimum grid for several distances. The frequency scale is shown in red and the capacity is depicted in blue color. At $d = 30\,\mathrm{m}$ the Gigahertz region may be applied, and a capacity up to Gigabit/s is reached. For example, the system designed with $\alpha = 5\%$ and $P_{TX} = 25\,\mathrm{dBm}$ for $f_0 = 40\,\mathrm{GHz}$ has the maximum capacity $C_0 = 8\,{}^{Gbit}/_{\mathrm{s}}$. For decreasing the distance to $d = 3\mathrm{m}$ the grid is shifted to the left, so that the Terahertz region occurs and the line $f_0 = 60\,\mathrm{GHz}$ has almost disappeared from the given region of parameters P_{TX} and α.

B. Constant antenna aperture

The antenna equivalent aperture or area is defined as the ratio of the available power at the terminals of a receiving

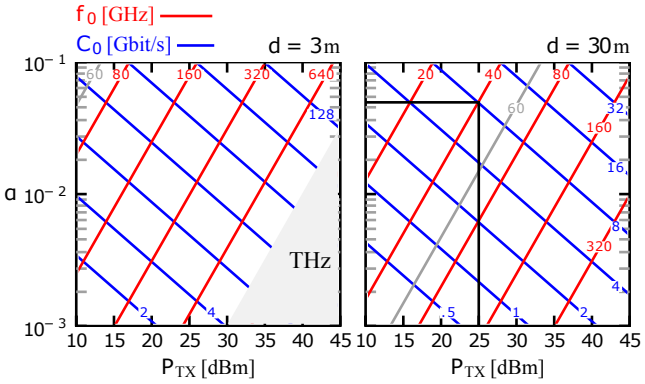

Figure 2. Optimum grid for constant antenna gain

antenna to the power flux density of a plane wave incident on the antenna from that direction [6]. It is independent of the practical antenna type. It is used to derive an antennas maximum directivity D_0 from its effective aperture A at a certain frequency:

$$D_0 = 4\pi \left(\frac{A}{\lambda^2}\right) = 4\pi \frac{f^2}{c_0^2} A. \tag{12}$$

A constant size of the effective aperture ($A = const.$), independent of the frequency, is assumed in this section. Additionally antenna efficiency is neglected, thus the antenna gain is defined as $G = D_0$. Inserting (12) in (1) and (2) leads to the channel capacity with a constant effective antenna aperture:

$$C = \alpha f \log_2 \left(1 + \frac{P_{TX}}{N_0} \left(\frac{A}{d}\right)^2 \frac{f}{\alpha c_0^2}\right). \tag{13}$$

Given a constant transmit power P_{TX} and distance d this capacity grows unlimited with the carrier frequency. For a given distance and capacity a higher frequency on the other hand would lead to a decrease in the necessary transmit power.

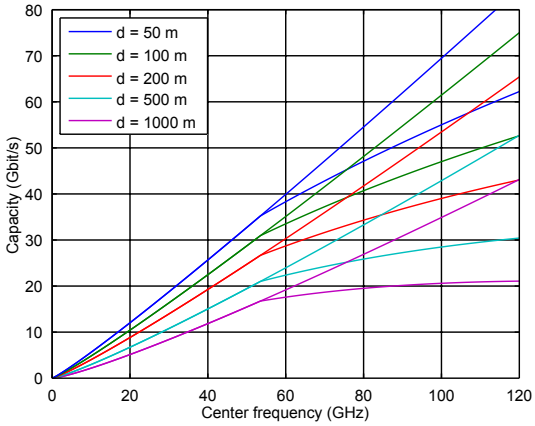

Figure 3. Frequency dependent capacity for constant antenna aperture

This theoretical benefit of higher frequencies can not be achieved without limits in real systems. The antenna gain derived above has to be realized in a real antenna. For high frequency bands this can become challenging, as for example the substrate losses in an antenna patch array grow exponentially with the size while the gain only grows quadratic.

The beam width of an antenna with a large aperture and therefore high gain will become very narrow and has to point towards the remote station. This will become very challenging with mobile applications and very narrow beams.

Another aspect to be considered is the far field assumption that is implicitly part of (2). The gain of an antenna is generally only valid in the far field region, that is usually defined based on the Fraunhofer distance [6]

$$d_{farfield} \geq \frac{2D^2}{\lambda} \tag{14}$$

where D is the largest dimension of the aperture. When considering large antenna apertures and high frequencies e.g. in the millimeter-wave band this distance can be in the order of tens of meters, well within the radius of typical small cell deployments.

Figure 3 shows the frequency dependent link capacity for different distances. The dotted lines deviating from the solid and dashed ones were calculated for a maximum realizable gain of 30 dBi. These capacities behave similar to the ones with constant gain from (II-A), having a maximum at a certain frequency. The transmit power was chosen as 10 dBm and the aperture was set to $0.025\,\mathrm{m}^2$.

C. Constant EIRP

The assumptions of constant gain and constant aperture are problematic for realistic systems. Therefore a third approach is made with focus on a small cell downlink scenario.

Regulatory bodies usually limit the equivalent isotropically radiated power (EIRP) of wireless transmitters (e.g. [7]). This is especially true for wireless systems at higher frequencies, usually relying on directional antennas, in order to prevent excessive exposure to electro-magnetic radiation. The EIRP can be calculated (neglecting losses) by multiplying the antenna gain with the transmit power and is assumed to be constant, independent of the frequency:

$$G_{TX} P_{TX} = const. \tag{15}$$

As the antenna gain is ambiguous, this EIRP assumption can not be adopted for the receiver side at the mobile terminal. As the physical space at the receiver is limited, a small but constant aperture can be selected, thus mitigating the problems mentioned in the previous section. Combining these assumptions with the Shannon capacity leads to

$$C = \alpha f \log_2 \left(1 + \frac{P_{TX} G_{TX}}{N_0} \frac{A}{4\pi d^2} \frac{1}{\alpha f}\right). \tag{16}$$

This capacity is growing but bound with an upper capacity limit, with increasing frequency:

$$\lim_{f \to \infty} C = \frac{A}{\pi d^2} \frac{1}{\log(16)} \frac{G_{TX} P_{TX}}{N_0}. \tag{17}$$

Figure 4 shows the frequency dependent capacity (solid, dashed) and the limits (dotted) for an arbitrary choice of EIRP ($20\,\mathrm{dBm}$), RX aperture ($0.01^2\,\mathrm{m}^2$), relative bandwidth (4%) and several distances d. Depending on the transmission distance there is a great potential to increase the channel capacity when increasing the carrier frequency (and thus absolute bandwidth). For larger distances this effect is negligible as a great percentage of the capacity limit is reached at lower frequencies already. This example already demonstrates the great potential of the millimeter-wave band for relatively short distance transmission.

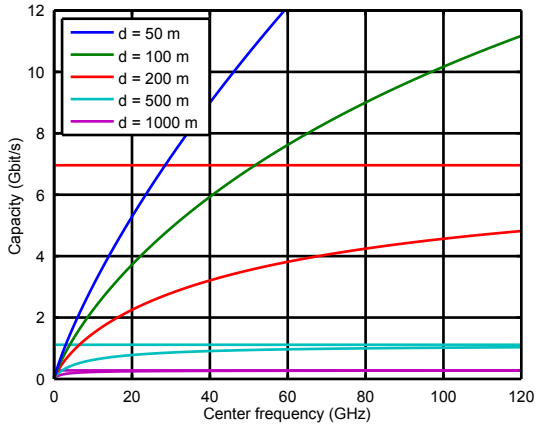

Figure 4. Frequency dependent capacity for constant EIRP

D. Comparison

Three different approaches have been considered for the frequency dependence of the transmit and receive antenna gains. The constant gain approach leads to an optimum operation point (frequency) where the channel capacity for a given transmit power and distance becomes maximal. The implication of the constant gain is that the equivalent antenna aperture size shrinks with increasing frequency, which might not be the desired behavior when considering systems with a certain fixed build size.

The second approach with a constant effective antenna aperture leads to a channel capacity that increases with frequency. Though this might be appealing, the feasibility, especially for large apertures or high frequencies becomes questionable. Technical and practical problems, such as antenna losses and narrow beam sizes might impose an upper limit on the realizable gain.

The third approach is based on a constant EIRP on transmitter side and a sensible choice of a constant aperture at the receiver side to mitigate the aforementioned problems. The transmitter behavior respects that usually in real world systems the EIRP is regulated, independent of the relation between gain and transmit power.

The last approach was selected as being most realistic for the evaluation in a small cell application scenario in the next section.

III. Evaluation in Small Cell Context

The small cell system model is shown in Figure 5. It focuses on a single small cell base station that covers a certain part of a circular area with a minimum distance d_{min} and a maximum distance d_{max}. This small cell usually lies within a macro cell that covers a much larger area. Interference from the macro cell level or neighboring small cells is neglected, but could later be included in a more complex system model. Mobile devices are distributed randomly inside the coverage area. The traffic is assumed to be fully buffered, as the growing amount of data in mobile networks is one of the major drivers for their further development. Other aspects such as very low latency requirements that are also discussed for 5G systems target physical and MAC layer aspects and are not examined here. The channel access is shared equally in time domain among all mobile devices without any overhead. The model focuses on downlink traffic only.

The physical build size of a mobile handheld device is limited. Therefore an effective aperture of $2\,\mathrm{cm}$ by $2\,\mathrm{cm}$ ($0.004\,\mathrm{m}^2$) is assumed. At a operating frequency of 60 GHz for example this would lead to an ideal gain of $23\,\mathrm{dBi}$ which should practically be achievable. The build size of the small cell base station itself will also be generally limited but the derivation of an antenna aperture is not necessary as a constant EIRP will be used.

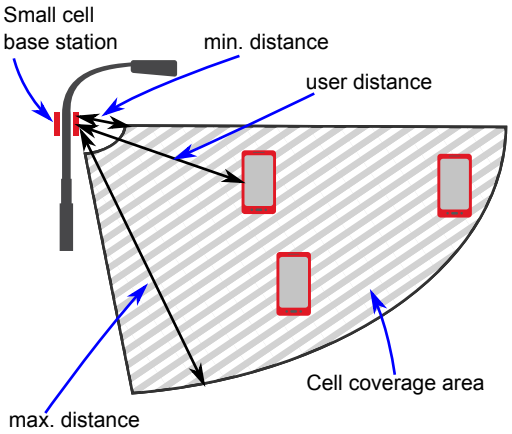

Figure 5. Small cell system model

The per user capacity of a small cell with a maximum distance of 500 meter is shown in Figure 6. A minimum distance of 3 meters was chosen. The green and red lines represent the rates achievable at the cell edge and close to the base station respectively, when only a single link is active. The transmit EIRP was assumed to be 30 dBm and the relative bandwidth was set to 4%. The blue line shows the average cell throughput for uniform mobile device per area distribution. A large gap can be observed between users at the cell center and users at the cell edge. This strong discrepancy will not be observed in real systems due to other noise source, such as phase noise, that effectively limit the achievable throughput in the high SNR case. A reduction of transmit power might be considered in this case to optimize the energy consumption.

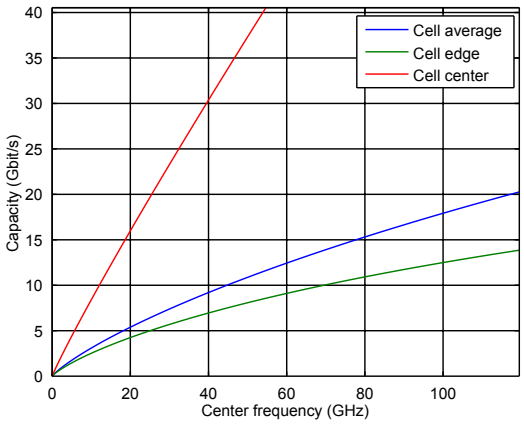

Figure 6. Small cell capacity

The simulated small cell capacity can be used to compare a system working at a legacy frequency of 2.5 GHz with a system operating at 60 GHz. The average cell capacity at 2.5 GHz is around 1 Gbit/s, while the achievable capacity at 60 GHz is more than twelve fold with 12.4 Gbit/s. At the cell edge the capacity increase is tenfold from 0.83 Gbit/s to 9.1 Gbit/s.

Figure 7 shows the average energy per bit E_b for different cell radii d_{max} and carrier frequencies f. For a given frequency E_b grows with the cell radius, caused by the longer link distances and the lower achievable rate at the same transmit power. When comparing the energy per bit for a fixed cell radius the benefit of using higher carrier frequencies becomes apparent. For example, at a radius of 500 meter a link operating at 60 GHz consumes 6.7% of the energy per bit of a link operating at 2 GHz. Looking at the fast growing amount of data being transported in mobile networks this is a very important aspect to keep the total energy consumption constant or even help reduce it.

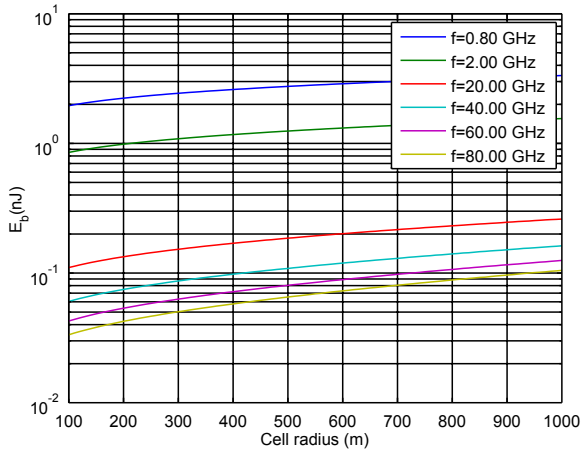

Figure 7. Energy per bit in small cell scenario

IV. Outlook

The examination of the channel capacity in this work was subject to some abstraction and simplification from real world systems. A more detailed system model could take more effects into account and lead to results that are more applicable to specific scenarios.

Aspects for future consideration include interference caused by neighboring cells, signaling and protocol overhead and realistic channel models. Such channel models would reflect the different propagation behavior (shadowing margins, etc.) between the legacy sub-6 GHz bands and the millimeter-wave bands but, to our knowledge, unfortunately no comprehensive channel model covering such a wide frequency range for the outdoor access scenario is available. Another aspect that could be taken into account are implementation constraints, such as overall component power consumption, other sources of noise, such as phase noise, and generally the availability and performance of semiconductors for the millimeter-wave band. Additionally, concerning the energy efficiency, a holistic view on the entire network architecture, including energy consumption for data processing and backhauling becomes necessary to derive optimum sizes for small cells.

V. Conclusions

Departing from the fundamental channel capacity the capacity of small cell access links, depending on the carrier frequency, has been derived. Realistic assumptions, such as a constant transmit EIRP and a small but constant antenna aperture at the receiver were introduced. It was shown that short range links up to a few hundred meters can greatly be improved in capacity when going to millimeter-wave bands. At the same time the energy efficiency of the wireless link can significantly be reduced when going to smaller cell radii and higher frequencies.

Acknowledgment

The research leading to these results has received funding from the European Union's Seventh Framework Program (FP7-ICT-2013-EU-Japan) under grant agreement number 608637.

References

[1] A. Khandekar, N. Bhushan, J. Tingfang, and V. Vanghi, "LTE-Advanced: Heterogeneous networks," in *Wireless Conference (EW), 2010 European*, April 2010, pp. 978–982.

[2] T. Rappaport, S. Sun, R. Mayzus, H. Zhao, Y. Azar, K. Wang, G. Wong, J. Schulz, M. Samimi, and F. Gutierrez, "Millimeter wave mobile communications for 5G cellular: It will work!" *Access, IEEE*, vol. 1, pp. 335–349, 2013.

[3] F. Boccardi, J. Heath, R.W., A. Lozano, T. Marzetta, and P. Popovski, "Five disruptive technology directions for 5G," *Communications Magazine, IEEE*, vol. 52, no. 2, pp. 74–80, February 2014.

[4] C. E. Shannon, "A mathematical theory of communication," *Bell System Technical Journal*, vol. 27, pp. 379–423, 623–656, July-October.

[5] H. T. Friis, "A note on a simple transmission formula," *proc. IRE*, vol. 34, no. 5, pp. 254–256, 1946.

[6] C. A. Balanis, *Antenna Theory: Analysis and Design*, third edition ed. Wiley-Interscience, 2005.

[7] European Commission, "Commission implementing decision of 8 december 2011 amending decision 2006/771/ec on harmonisation of the radio spectrum for use by short-range devices," December 2011.

3.3 Mobility support and functional localization

In the frame of the previously introduced overlay concept, the logical localization of functionalities on the two available wireless links (3G/4G and mm-wave) is not inherently obvious. Instead, the concept opens up a new design space. This design space is explored in the following publication that also highlights how mobility support as part of higher layer functionality relates to the requirements of an mm-wave physical layer link [WKFC14]. Existing millimeter-wave indoor communication standards are reviewed as a starting point for this exploration. While some of the functionality can clearly be assigned to the macro cellular control plane or the small cell control plane, other functionality, such as the cell discovery for example, will need to be located and implemented on a mixture of both planes.

Contribution

This publication was motivated by my research on the mm-wave channel and the questions that arise with the overlay concept. I wrote the first draft of the document entirely by myself. This was used to discuss and refine my findings with the other authors, who contributed some additional thoughts (mainly concerning the split plane concept) and corrections.

Split Control Plane Functionality in Millimeter-Wave Overlay Access

Richard J. Weiler and Wilhelm Keusgen
Fraunhofer Heinrich Hertz Institute
Berlin, Germany
{richard.weiler, wilhelm.keusgen}@hhi.fraunhofer.de

Ilario Filippini and Antonio Capone
Dipartimento di Elettronica, Informazione e Bioingegneria
Politecnico di Milano
Milano, Italy
{ilario.filippini, antonio.capone}@polimi.it

***Abstract*—The millimeter-wave band is a candidate to overcome the spectrum shortage in future mobile radio networks. As the coverage area of base stations operating at these frequencies is expected to be more limited than at the sub 6 GHz bands, they will supplement existing base stations instead of replacing them. With these additional small cells a split plane architecture becomes an interesting architectural candidate, where capacity is provided by the small cells while continuous connectivity is guaranteed as it is available today. The introduction of such a split between the control and the data plane introduces new options and degrees of freedom of system and protocol design that are investigated in this paper.**

***Index Terms*—heterogeneous networks, millimeter-wave communication, 60 GHz, 5G, HetNet, small cell**

I. Introduction

Network densification and spectrum extension are two trends in the development of mobile radio networks [1], [2]. Adding small cell base stations in areas of existing macro cellular coverage promises to increase the network capacity as well as scalability and is a form of densification. This is commonly known as heterogeneous networks (HetNet). In current deployments the small cells often use the same frequency band as the macro cell, causing increasing levels of interference. Leveraging previously unused frequency resources in the millimeter-wave bands is a form of spectrum extension and promises decreased interference as well as increased capacity.

As we will discuss in section III the radio channel at millimeter-wave frequencies is much more challenging than the legacy ones in the sub 6 GHz range. In order to maintain seamless connectivity in these bands recently a split plane approach was proposed where the control plane remains on the legacy frequency bands and the data (or user) plane can be moved to the millimeter-wave bands [3].

The millimeter-wave frequency band, ranging from 30 GHz to 300 GHz, offers much wider bandwidths of contiguous spectrum than the legacy bands. During the last years a number of communication standards, using the widely license free available 60 GHz band, have been defined. These standards however target indoor WPAN applications and are not designed for outdoor environments.

Adding an overlay of millimeter-wave capable small cells to the HetNet leads to additional control and user planes. This gives new options for the logical localization of network functionality on the planes.

In this paper we investigate the special requirements for the control plane with respect to millimeter-wave specific characteristics and we discuss the resulting options for the additional planes. We analyze which control functionality must be on the millimeter-wave link, which can be chosen arbitrarily and which is bound to the macro cellular control plane. For that purpose the existing 60 GHz indoor communication standards are used as a starting point.

Section II introduces the small cell overlay system architecture in more detail. The existing indoor communication standards are studied in section IV. Section V investigates the options for the split plane concept.

II. System architecture

The millimeter-wave overlay system architecture with split user and control planes is shown in Figure 1. A macro base station (BS) provides coverage to all mobile terminals (UE) within its coverage area. Millimeter-wave small cell base stations are placed within the area of the macro base station and provide a smaller area of coverage with a millimeter-wave access link. The small cell base stations are connected to the macro base station via a high capacity backhaul. They can be in an active or inactive state, depending on the presence of users within their coverage area.

The user terminal possesses two wireless interfaces, one for the legacy connection to the macro cell (e.g. LTE) and one for the connection to a millimeter-wave link. In general the UE is connected to the small cell via the millimeter-wave link when necessary. At the same time the UE is attached to the macro BS via the legacy communication link.

On each physical connection control and/or user data can be transported. Thus, when the UE is connected on both the legacy and the millimeter-wave interface, two control and two data connections exist. One of each to the macro cell and one to the small cell. In the rest of this paper the first one will be referred to as macro cell or legacy connection and the second one as small cell or millimeter-wave connection.

III. Millimeter-wave specifics

The millimeter-wave band between 30 and 300 GHz recently received increasing interest for new communication

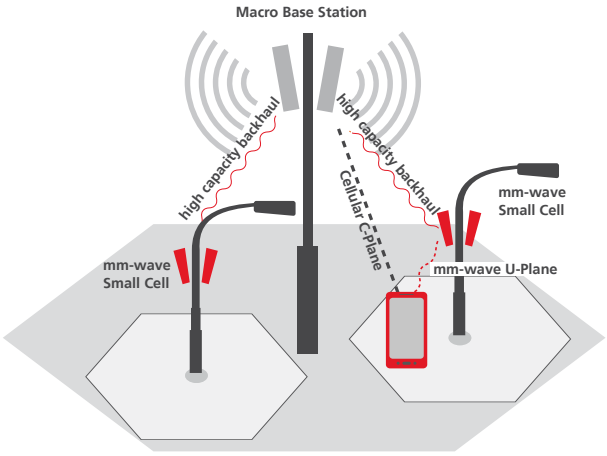

Figure 1. System architecture

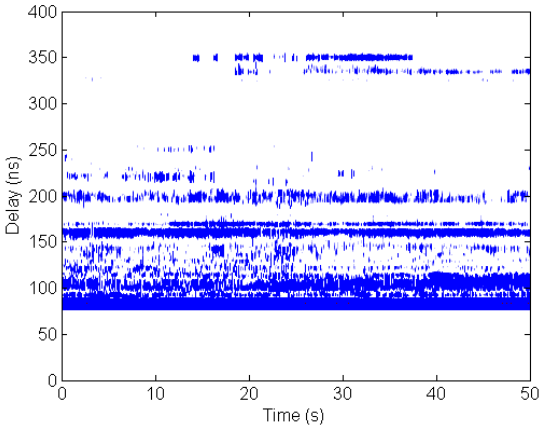

Figure 2. Time evolution of 60 GHz outdoor channel impulse response

standards to overcome the shortage of spectrum [1]. The increase in carrier frequency however leads to a higher pathloss. In free-space conditions the Friis equation shows that the received signal power is inversely proportional to the carrier frequency.

Several measurement campaigns of outdoor millimeter-wave channels were reported recently [4]–[7]. The time dynamic behavior of the link and especially of the spatial multipath components is important for the design and parametrization of the beam forming algorithms in the millimeter-wave band. An analysis of channel measurements performed at 60 GHz in a busy urban outdoor access scenario shows that the different multipath components arriving at the receiver can be grouped into different classes, according to their availability over time [8]. Figure 2 shows the behavior of the omnidirectional channel impulse response for static transmitter and receiver locations on a busy urban street over a time of 50 seconds (see [6]–[8] for more details). Multipath components with a path loss of less than 120 dB are shown in blue. This threshold represents the maximum allowable path loss for communication and depends on the system implementation (e.g. antenna gain, noise figure, transmit power, modulation). It was chosen arbitrarily here. The distance between transmitter and receiver was 25 meters, which can be clearly seen by the constant path of the unblocked line of sight component at around 80 ns delay. Other multipath components at higher delays are caused by reflecting objects, such as the ground, surrounding buildings, street furniture, cars, etc. It can be seen that some exist throughout the measurement and are only interrupted while others only appear for a short period of time. In order to counter the higher path loss compared to sub 6 GHz communication systems, millimeter-wave communication systems have to use directional antennas with high gain. To support mobile devices in outdoor environments the direction of the beam will need to adapt to the changing radio channel very fast, thus making electronic beam forming or beam steering, such as beam forming arrays necessary.

A thorough statistical analysis of this multipath component behavior over time is still open work. When assuming a blocked line of sight however, there are still a number of candidate multipath components that could be used to establish a directional link between the transmitter and the receiver, assuming that different multipath components stem from different spatial directions. The frequent interruption of some multipath components however indicates that a frequent switching between spatial directions might be necessary for a stable connection.

In cases when all multipath components between the transmitter and the receiver are too weak to support a communication link, the connection would have to fall back to the legacy connection.

IV. Existing 60 GHz indoor communication standards

A number of standards were defined during the last few years for very high data rate indoor communication at 60 GHz. The standards ECMA-387 and IEEE 802.15.3c were published in 2009 but no products were released so far based on them. The standard IEEE 802.11ad was published in December 2012, based on a standard that was previously developed by the WiGig Alliance [9]. This part of the IEEE 802.11 standard also recently got part of the Wi-Fi Alliance.

In the rest of this section we focus on IEEE 802.11ad as it is the most recent standard and due to it being part of a family of sub 6 GHz transmission protocols. Nevertheless all three standards share some basic concepts, such as channel bandwidth, channelization and directional transmission with beamforming antennas.

A. Overall topology

The standard IEEE 802.11ad builds on top of the other IEEE 802.11 WPAN standards and introduces the extension to 60 GHz. In this extension one of the participating stations of a network or an access point (AP) takes the role of the PCP (personal basic service set control point) and provides basic timing information to all stations nearby.

The radio transmissions are organized in so called beacon intervals, shown in Figure 3. Within a beacon interval there is a beacon header interval (BHI) and a data transfer interval (DTI). In the BHI one or multiple beacon signals (BTI) are transmitted by the PCP, some basic beamforming training (A-BFT) can be performed and announcements can be transmitted (ATI). The DTI consists of a contention-based access period (CBAP) and a contention free service period (SP).

While the stations can compete for access during the CBAP, the PCP schedules the transmissions according to the demand during the SP. Special care is taken to reduce interference that might occur through neighboring PBSS.

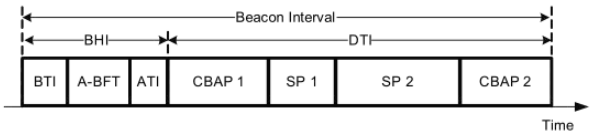

Figure 3. An IEEE 802.11ad beacon interval (BI) structure

B. Beacon and discovery

The beacon signal is transmitted by the PCP during the beacon transmission interval, as previously shown. During this interval the PCP can transmit multiple beacon signals in different spatial directions. As information on the spatial transmission is included in the beacon this is also the first step for the beamforming training.

C. Beamforming support

For any pair of communicating stations there is a total of 4 beamforming vectors that needs to be trained: transmit and receive vectors for each station. When the hardware supports reciprocity by using the same antenna array for transmission and reception and calibrated phase shifters, only one vector has to be trained per station.

The beamforming training is performed at the setup of a communication link and consists of the two phases sector-level sweep (SLS) and beam refinement protocol (BRP). A beam tracking protocol is used to update the beamforming vectors in an established link.

All protocols are based on the selection of the best performing beamforming vector out of a selection of candidates, for example from a code book. Multiple transmit beamforming vectors are applied sequentially and receiver feedback highlights the best one. This beamforming technique was developed for indoor environments and its applicability to outdoor environments with much larger distances and possibly higher time variance remains an open issue.

D. Fast session transfer

Fast session transfer (FST) allows to transfer a session from one physical channel to another channel (i.e. frequency band). A session is the state information that is kept in a pair of stations that have an established direct physical link. The FST allows the stations e.g. to switch to the 2.4 GHz band when reaching the limits of coverage at 60 GHz. Each station can initialize or request the fast session transfer and it completes when both stations have established a connection in the new band.

From its design this approach is independent of the concrete implementation of the physical channels and does not rely on dedicated stable control channel. Such a channel however, as it is available in the split plane concept, could be used to improve the seamless transfer between the different channels or bands.

E. Frame format

The frame format is shown in Figure 4. A frame consists of a preamble, a header, the data payload and optional beamforming tracking (TRN) fields. The preamble is composed of a short training field (STF) and the channel estimation (CE) sequence. Both of these fields use special concatenations of Golay sequences. The short training field is used for AGC training, frequency offset estimation, synchronization and determines the type of frame (e.g. control frame, OFDM frame, single carrier frame). The channel estimation sequence is designed in a way that allows efficient calculation of the channel impulse response.

The header contains various fields, depending on the type of the frame. Fields can be the definition of the modulation and coding scheme (MCS) of the payload symbols, the number of payload bits, beamforming tracking requests, etc.

The optional beamforming tracking fields are inserted upon request and can be transmitted for receiver (R) or transmitter (T) tracking.

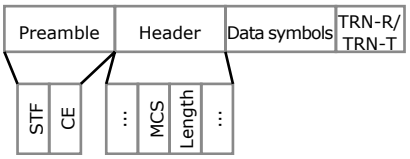

Figure 4. IEEE 802.11ad frame format

F. Applicability to outdoor access

The general topology of IEEE 802.11ad is similar to what would be needed for an evolution of wireless radio networks with millimeter-wave overlay cells. These small cells might advertise their existence with beacon signals and will coordinate the communication. They will also have to take care of beamforming training and tracking, which might become even more challenging in dynamic outdoor environments, compared to the indoor environments targeted by IEEE 802.11ad.

The fast session transfer is a building block that is also needed for outdoor access. Though its implementation in IEEE 802.11ad relies on a stable link in the old band. This might be problematic when this link gets suddenly lost. By relying on a separate, more stable control plane the reliability of the fast session transfer could be increased.

The frame format and the physical layer (PHY) (not described here in detail) could form a basis for an millimeter-wave outdoor access system. The challenges of initial synchronization, channel estimation, etc. are well addressed for wide bandwidth channels. Regular beam tracking is also included, though this might need to be extended.

V. Split plane concept

As introduced in section II the concept envisioned for the overlay of millimeter-wave small cells foresees a split of the control and data connection of the UE to the access network. Through this the UE can keep a main control-plane connection active, typically within a long-range macro cell, and activate user-plane connections to different base stations which provide the best data traffic bearers according to both user and network status. Different connection configurations can be possible in order to adapt to different network and traffic layouts [10]. User-plane connections can be established with both macro cells and small cells leaving room for the development of optimized resource allocation algorithms. In this scenario we can identify two types of mobility, a so-called small-scale mobility, where the UE moves within the coverage of a single control-plane macro cell and performs user-plane handovers through small cells, while traditional mobility occurs when the UE crosses macro cell boundaries.

A. Time dynamic behavior

Two aspects of time dynamic behavior that might have a great impact on the design of the split plane concept are worth mentioning. One is the behavior of a UE with respect to the coverage area of a small cell and the other are the implications of the kind of traffic that is requested by the UE.

1) UE behavior: Several possible behaviors of the UE with respect to its position within the macro cell can be identified: entering a small cell, staying or moving within a small cell, exiting a small cell. Even the type of mobility is important: very fast users with irregular trajectory can be difficult to serve with millimeter- wave small cells, while users with predictable trajectory can be served by properly allocating resources in advance.

2) Traffic model: The traffic model or type of traffic has a great impact on the way the control functionality should behave. While a traffic with fully buffered maximum demand simply requires a continuous high speed data connection two other cases are more challenging. One would be sporadic or regular high data traffic demand with gaps between transmissions (Fig. 5a) and the other would be low or medium rate continuous traffic (Fig. 5b).

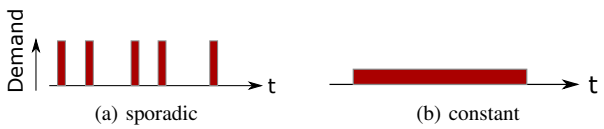

(a) sporadic (b) constant

Figure 5. Traffic models

In the case of intermitted traffic the decision has to be made whether the connection between the UE and the millimeter-wave small cell should remain active. When it is kept active the beamforming vectors have to be updated, even though the link is unused. In the case of low or medium rate traffic the decision has to be made whether the millimeter-wave or the legacy wireless connection should be used. For these decisions a number of factors, such as total traffic demand, link quality, power consumption of components or links have to be taken into account. Also the delay tolerance of the requested service is an important factor, it may or may not allow buffering techniques to help network reconfigurations.

B. Logical localization of control functionality

Despite UE double connectivity and control-/user-plane split, control functionalities should not be entirely relegated to one wireless interface. There are some control functions, like channel estimation and beamforming tracking, that must be carried out on the millimeter-wave link. Other functions, instead, can be partially or totally moved to the legacy 4G connection. Generally speaking, 4G connection is more avaialable, has higher reliability and requires fewer handovers than the millimeter connection, therefore, it can be used for exchanging information not directly related to the use of millimer-wave resources, but rather, to critical network management functions, like session setup, location update and context acquisition. In addition, control functionalities, having no strict bandwidth requirements, can waste millimeter-wave resources, which are better suited for high-rates and would be less efficiently utilized.

We can divide the control plane in two subplanes: macro cell control plane (on legacy 4G connection) and small cell control plane (on millimeter-wave link). We discuss about control function allocation on each subplane in the following paragraphs.

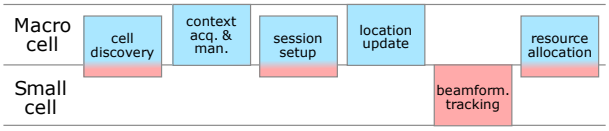

Figure 6. Control functionality and possible localization on control plane

1) Cell discovery: The UEs discovery and attachment to a macro cell base station is made as usual. The discovery of millimeter-wave small cell base stations does not necessarily have to be performed continuously but only when needed or requested. Discovering available small cells becomes more complicated with the increased path loss in the millimeter-wave bands. This requires either omnidirectional modes with low data rates and signal processing gain (e.g. spreading sequences) or directional antenna patterns with a certain gain. The support of a separated control-plane connection established with a macro cell becomes crucial to provide information for a fast discovery. The information can go from a minimal list of millimeter-wave small cell positions to a

smart antenna configuration suggestion to connect to the best small cell.

2) Context acquisition and management: In order to make smart choices for cell discovery the system must rely on a rich context about UE and network status. The network collects information on UE position, antenna configurations, related channel quality and builds a context database that is used to predict the performance experienced by future UE requests at the same position. This information, together with UE type, capabilities, and traffic requirements, is conveyed to the resource allocation engine through the macro cell connection, which is more reliable.

3) Session setup: The session setup discussed here is the process of starting a communication between the UE and the access network on request by either entity. When the UE is in idle state it is connected to the legacy macro base station. It is assumed that the UE is not connected to a millimeter-wave link when idle, in order to reduce the energy consumption. This reduce both UE power consumption and network power consumption. Indeed, due to control-/user-plane separation, millimeter-wave base stations, which are typically deployed in large number and are mainly used to provide high-rate traffic bearers, can be switched off when no data session is active.

When the session is initiated by a request from the macro base station, the macro cellular control plane has to be used to alert the UE. Then the UE and the appropriate small cell have to initiate the directional millimeter-wave connection. This could be performed solely on the millimeter-wave control plane or with support on the macro cellular control plane. Such support context information could be for example position information of the UE, physical locations of small cells within the macro cell area, timing information, etc.

Once a millimeter-wave link is established, further control information can be transferred on either of both control planes.

4) Location update: As described above, the expected directionality of the millimeter-wave links requires a new kind of mobility support on the link or beam level. This is discussed as beamforming tracking. The traditional understanding of mobility, i.e. a UEs attachment to a certain macro base station or area, will undoubted remain on the legacy control plane, due to the much higher robustness of the link.

5) Beamforming tracking: The beamforming tracking is a crucial part of the millimeter-wave connectivity. As discussed in section III the directional millimeter-wave link continuously changes and updates of beamforming vectors have to be performed frequently. Such information is needed on both ends of the millimeter-wave link. This functionality will therefore undoubtedly be located at the small cell control plane.

6) Resource allocation: The resource allocation describes how and when the UE and the small cell should access the millimeter-wave channel. Depending on the granularity of the channel access and due to the increased complexity with directional communication this can generate a noteworthy amount of traffic. Taking IEEE 802.11ad as an example the small cell polls the UEs for their demand to communicate and allocates time slots. However, the use of macro cell control plane allows to orchestrate the operation of surrounding millimeter-wave small cells. This, on one hand, facilitates the wireless medium access of millimeter-wave devices, on the other hand, allows to fine tuning available resources enable scenarios where UEs receive multiple streams from different millimeter-wave base stations and, vice versa, a millimeter-wave base station simultaneously communicates with multiple UEs. In addition, interference coordination techniques can further improve the wireless resource exploitation. The following scenario can be envisioned: medium access and high-level connection management are carried out through macro cell control plane, while small cell control plane is involved in local millimeter-wave resource allocation and adaptation.

VI. Conclusions

The introduction of the millimeter-wave frequency bands into future generations of mobile radio networks requires new architectural approaches and opens a new design space. In this paper we investigated the specific requirements of these high frequencies in the context of outdoor access systems. Based on a review of existing recent 60 GHz indoor standards we investigated the design options for a split plane concept where data and control traffic can be transported on different physical interfaces (i.e. frequency bands).

While the localization of some functionality (e.g. location update, beamforming tracking) in such an architecture is very clear, the other functionality still offers a large design space. The exploration of the design space and the choice of a solution within this space relies on the knowledge of the whole system, from the physical propagation channel to the network architecture and type of traffic model. Further detailed investigations are necessary to fully leverage the potentials of the millimeter-wave spectrum in future mobile radio networks.

Acknowledgment

The research leading to these results has received funding from the European Union's Seventh Framework Program (FP7-ICT-2013-EU-Japan) under grant agreement number 608637.

References

[1] F. Boccardi, J. Heath, R.W., A. Lozano, T. Marzetta, and P. Popovski, "Five disruptive technology directions for 5G," *Communications Magazine, IEEE*, vol. 52, no. 2, pp. 74–80, February 2014.

[2] W. Roh, J.-Y. Seol, J. Park, B. Lee, J. Lee, Y. Kim, J. Cho, K. Cheun, and F. Aryanfar, "Millimeter-wave beamforming as an enabling technology for 5G cellular communications: theoretical feasibility and prototype results," *Communications Magazine, IEEE*, vol. 52, no. 2, pp. 106–113, February 2014.

[3] R. J. Weiler, M. Peter, W. Keusgen, E. Calvanese-Strinati, Antonio De Domenico, Ilario Filippini, Antonio Capone, Isabelle Siaud, Anne-Marie Ulmer-Moll, Alexander Maltsev, Thomas Haustein, and and Kei Sakaguchi, "Enabling 5G backhaul and access with millimeter-waves," in *Conference on Networks and Communications (EuCNC), 2014 European*, 2014.

[4] E. Ben-Dor, T. S. Rappaport, Y. Qiao, and S. J. Lauffenburger, "Millimeter-wave 60 GHz outdoor and vehicle AOA propagation measurements using a broadband channel sounder," in *Global Telecommunications Conference (GLOBECOM 2011), 2011 IEEE*. IEEE, 2011, pp. 1–6.

[5] T. S. Rappaport, E. Ben-Dor, J. N. Murdock, and Y. Qiao, "38 GHz and 60 GHz angle-dependent propagation for cellular & peer-to-peer wireless communications," in *Communications (ICC), 2012 IEEE International Conference on*. IEEE, 2012, pp. 4568–4573.

[6] W. Keusgen, R. J. Weiler, M. Peter, and M. Wisotzki, "Propagation measurements and simulations for millimeter-wave mobile access in a busy urban environment," in *39th International Conference on Infrared, Millimeter, and Terahertz Waves*, 2014.

[7] R. J. Weiler, M. Peter, W. Keusgen, and M. Wisotzki, "Measuring the busy urban 60 ghz outdoor access radio channel," in *Ultra-Wideband (ICUWB), 2014 IEEE International Conference on*, 2014.

[8] A. Maltsev, A. Pudeyev, I. Bolotin, G. Morozov, I. Karls, M. Faerber, I. Siaud, A.-M. Ulmer-Moll, J.-M. Conrat, R. Weiler, and M. Peter, "MiWEBA Deliverable D5.1: Channel modeling and characterization," 2014. [Online]. Available: http://www.miweba.eu

[9] *IEEE Standard for Information technology - Part 11: Wireless LAN Medium Access Control (MAC) and Physical Layer (PHY) Specifications - Amendment 3: Enhancements for Very High Throughput in the 60 GHz Band*, IEEE Std., December 2012.

[10] T. Sakurai, S. Okasaka, T. Sotoyama, I. Siaud, A.-M. Ulmer-Moll, A. Capone, I. Filippini, A. D. Domenico, R. Weiler, and K. Sakaguchi, "MiWEBA Deliverable D1.2: Specification of architecture," 2014. [Online]. Available: http://www.miweba.eu

4 Measurement campaigns and modeling approaches

This section builds on the previously explained channel measurement system. Here I present measurement campaigns, modeling approaches and parameters that were obtained from the measurements. The first publication investigates the ground reflection at 60 GHz and its fading effect on wireless point-to-point links. The subsequent publications present measurement results on mm-wave access links in urban small cell scenarios. These results are then applied to two different types of channel models, a path loss model and a quasi-deterministic channel model. Two publications with investigations of the impact of dynamic shadowing on access links at 28 GHz and 60 GHz complete this section.

4.1 Ground reflection measurement

The measurement campaign described in the following publication was planned and executed to investigate the impact of the ground reflection on the band limited channel [WPK+15a]. An old airport was chosen as the measurement location, due to the absence of other reflectors than the tarmac. With typical heights and distances of street level small cell deployments, the angle of incidence is typically close to 90°, leading to a strong specular reflection on the ground. In combination with the excess delay of this ground reflection, flat fading occurs and can be well described with a two-ray propagation model. Furthermore, the reflection properties of asphalt at 60 GHz, as well as the oxygen absorption were verified against values in the literature.

The following publications investigate the path loss in an urban street canyon. As can be seen from the results (see Section 4.2 and 4.3; also refer to Section 4.4), significant fading effects are visible within the measurement bandwidth, as investigated here in the context of ground reflection.

The results are also significant for the deployment of street level backhaul links, as is also part of the overlay concept described in Section 3.1. Depending

on the geometry of the environment and the position of the antennas on both ends, severe flat fading can affect the link budget, even for very large signal bandwidths of 2 GHz or more.

Contribution

This measurement campaign was planned and executed by my colleagues and co-authors. I did post-processing of the raw measurement data and the path loss analysis. I also set up the two-ray simulation model and performed the numerical simulations and comparative analysis. I authored the publication text and created the figures by myself. Some parts of the channel sounder description are based on internal documentation by my co-authors. They also provided proof-reading and smaller corrections of the text.

Millimeter-Wave Channel Sounding of Outdoor Ground Reflections

Richard J. Weiler*, Michael Peter*, Wilhelm Keusgen*, Andreas Kortke‡ and Mike Wisotzki*
*Fraunhofer Heinrich Hertz Institute, 10587 Berlin, Germany
‡Communications and Information Theory Chair, TU Berlin, 10587 Berlin, Germany

***Abstract*—A channel sounder for time variant channels is presented. A 60 GHz outdoor measurement campaign was conducted with focus on the properties of ground reflections over large distances up to 1000 m. A two-ray propagation model is introduced and compared to the measurement results in order to derive the ground reflection properties.**

***Index Terms*—millimeter-wave, 5G, millimeter-wave propagation, electromagnetic reflection, multipath channels, fading channels**

I. Introduction

Millimeter-wave transmission is seen as one of the new technologies that will impact the next mobile radio network standards, commonly termed as 5G [1]. Network densification through the addition of new base stations, so called small cells, is another predicted trend [2]. Wireless backhaul links are seen as a key enabler for these cells and the millimeter-wave band promises to provide enough bandwidth, even for very high capacity links in dense environments. As these links will be deployed in urban environments, e.g. on street level height, the ground reflection can produce a strong propagation path that superimposes with the direct path and induces severe fading effects. In order to investigate the properties of these effects we have performed a measurement campaign focusing on the line-of-sight (LOS) channel in an open area. It was investigated with a channel sounder that is described in Section II. The channel was measured for different common ground materials, variable heights and at distances from 40 to 1000 m, giving a full characterization of the ground reflection effect.

The measurement campaign is presented in Section III and Section IV shows some measurement results and their comparison to a two-ray propagation model.

II. Channel sounder

The channel sounder used for the measurements is based on a self developed FPGA platform [3]. The basic principle of the channel sounder is shown in Figure 1. A special channel sounding signal is generated and transmitted through the wireless channel. At the receiver the channel characteristics are estimated based on the received signal. Generally time variant wireless channels are considered with limited time variations (channel coherence time $T_{coh,ch}$, measurement bandwidth B): $T_{coh,ch} \ggg {}^1\!/_B$.

For short observation time intervals the input (x) to output (y) relation can be described as the (aperiodic) convolution $y = h * x$, where h is the impulse response of the wireless channel.

Figure 1 shows the equivalent baseband model of the sounding in more detail. The baseband signal is modulated to an intermediate frequency (IF) with an IQ modulator and then converted to the RF domain.

The effects of the modulators, the amplifiers (power amplifier PA, low noise amplifier LNA) and the antennas are assumed to be of linear behavior, as is the case for the wireless channel. The equivalent baseband model can therefore be employed. The influence of the Tx and Rx front-ends on the measurement results are removed by system calibration. The antennas are considered as part of the wireless channel.

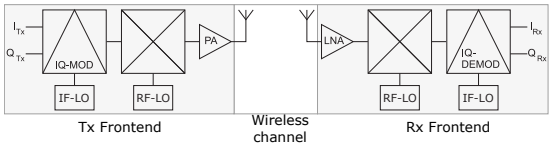

Figure 1: Equivalent baseband model

Broadband periodic correlation sequences are used as measurement baseband signals. A Frank sequence of length $N = 256$ is used in the presented implementation (vectorized 16×16 Fourier matrix). The period time is $T_P = N/B \ll T_{coh,ch}$. The whole measurement bandwidth is excited and measured within one period, which enables fast broadband measurements.

The channel impulse response vector can be calculated as $\mathbf{h} = \mathrm{idft}\left(\frac{\mathrm{dft(y)}}{\mathrm{dft(x)}}\right)$.

The sampling rate and measurement bandwidth of the system is $B = 250\,\mathrm{MHz}$. The period length of the transmit signal sequence is $T_p = {}^{256\,\mathrm{Samples}}\!/_{250\,\mathrm{Msps}} = 1.024\,\mu\mathrm{s}$. An averaging is performed over 64 periods of the sequence, leading to a snapshot measurement duration of $65.536\,\mu\mathrm{s}$. A snapshot is taken every $667.65\,\mu\mathrm{s}$ ($1.50\,\mathrm{kHz}$ snapshot rate).

III. Measurement campaign

The measurement campaign was performed at the site of the former airport Berlin-Gatow in Berlin, Germany. Figure 2 shows the map of the measurement site. The

runway (top) and the apron (bottom) each have a length of ca. 800 m and are paved with asphalt. The surrounding field (light green) is covered with grass. The area to the right (darker green) is forest and the area to the left is also covered with grass and weeds. At the dashed line a metal fence made of thin wire with a height of 2 m cuts through the area.

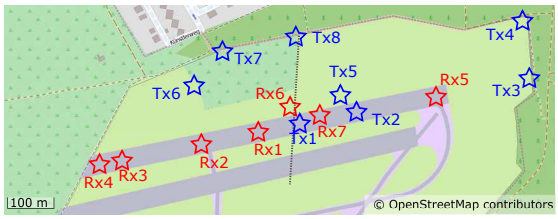

Figure 2: Map of measurement location

The channel sounder equipment was mounted onto cars as shown in Figure 3. The front-ends were mounted onto tripods that allow easy adjustment of the height. The measurements were operated from a computer connected to the channel sounder. Table I lists the parameters and properties of the measurements performed.

Table I: Measurement and environmental parameters

Type	Value
Center frequency	60 GHz
Rx height	4 m
Tx height const.	4 m
Tx height var.	3 - 5 m
Distance	40 - 1000 m
Rx & Tx antenna	20 dBi horn
Half-power beamwidth	19.5 ° E-plane, horizontal
	18.1 ° H-plane, vertical
Rx & Tx antenna polarization	vertical, horizontal
Atmospheric pressure	1015 hPa
Relative humidity	50 - 60 %
Air temperature	28° C

Figure 3: Channel sounder mounted on car

A measurement plan was prepared before the measurement campaign. Every measurement carries a unique number and is defined according to the positions on the map in Figure 2. Further parameters are the height of Tx and Rx and the polarization. While the position of the transmitter was static during each measurement, the receiver was moved at constant speed in some measurements. Each measurement consists of a configurable number of measurement snapshots (here set to 60,000). As the length of the sounding sequence only allows for a unique range of ca. 300 m, a reference range was measured at known positions and saved as calibration data.

A total of 144 measurements have been performed on the airfield. Between the measurements the distance between Tx and Rx and the height of the Tx antenna was varied with constant speed to measure fading behavior. Static measurements were also conducted. All measurements were repeated on different ground materials and with vertical and horizontal polarization. A total of 8.64 million channel snapshots was taken during the measurement campaign.

IV. Ground Reflection

A. Measurement results

The measurement channel snapshots are taken at equidistant positions of 1 mm as described in Section III. For each snapshot (channel impulse response) the instantaneous path loss is calculated. Figure 4 shows the measured path loss over a range from 40 to 1000 m on the tarmac (transmitter at Tx1, Tx2, Tx3; receiver moved between Rx1 and Rx4, horizontal polarization). A moving average filter with a width of 20 samples has been applied to reduce noise effects. A distance of 60 m is covered in one measurement run. The figure therefore shows the combination of 16 subsequent measurement runs. Some artifacts can be observed at the seams between the individual measurement runs. This can be caused by slight variations in antenna height above ground and positioning errors when the transmitter was relocated from Tx1 to Tx2 and Tx3. The measurement results for vertical polarization are not shown here but exhibit the same behavior as the ones in Fig. 4.

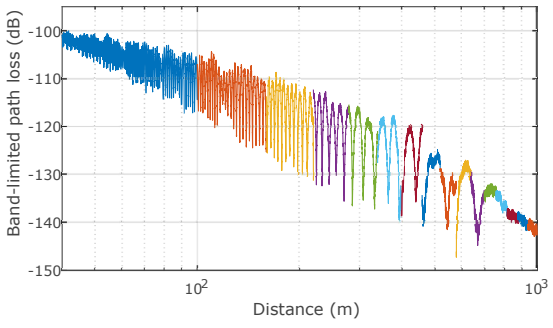

Figure 4: Measured path loss ($H_{Tx} = H_{Rx} = 4\,\mathrm{m}$, horizontal polarization, asphalt runway)

B. Simulation model

The simulation model is shown in Figure 5. Transmit and receive antennas are mounted at a height H_{Tx} and

H_{Rx} respectively and a distance D. The line of sight path (LOS) and a single ground reflection path are calculated in a polarimetric way. The ground reflection properties are modeled according to Fresnels reflection laws and the Oxygen absorption is taken into account. The discrete channel impulse response can be expressed as:

$$h(t) = \sum_{i=1}^{2} G_i \, e^{\frac{-2\pi j l_i}{\lambda}} \, \delta\left(t - \frac{l_i}{c_0}\right)$$

Where i selects the path (1: LOS, 2: ground reflection) and l_i is the total length of the path. $G_i = \frac{\lambda}{4\pi l_i} 10^{-\frac{l_i l_{Ox}}{1000 \cdot 20}} R_i$ is the path gain with the Oxygen attenuation l_{Ox} in $^{\mathrm{dB}}/_{\mathrm{km}}$ and the reflection coefficient R_i. The attenuation of the ground reflection due to the antenna beamwidth is neglected here, as it only has an influence at short distances.

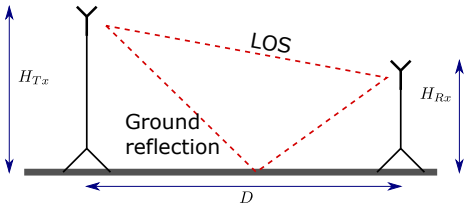

Figure 5: Two-ray simulation model

The discrete impulse response is then binned and computed into a band limited channel impulse response and the path loss is calculated. Figure 6 shows the path loss over a range from 40 to 1000 m with a bandwidth of 250 MHz for Oxygen absorption rates of $0\,^{\mathrm{dB}}/_{\mathrm{km}}$ and $14\,^{\mathrm{dB}}/_{\mathrm{km}}$. The latter value gives a good match between measurement and simulation. It is well in line with the MPM model [4], that gives an attenuation of $13.9\,^{\mathrm{dB}}/_{\mathrm{km}}$ for the environmental parameters at the day of the measurement (Table I).

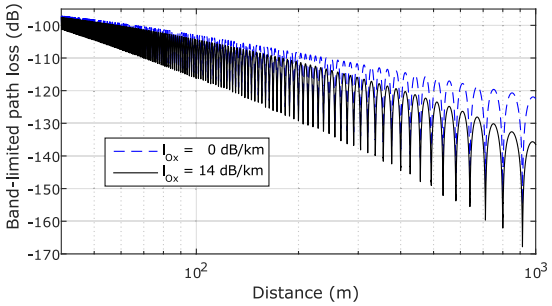

Figure 6: Simulated path loss ($H_{Tx} = H_{Rx} = 4\,\mathrm{m}$, horizontal polarization, $\epsilon_r = 2$, $B = 250\,\mathrm{MHz}$)

Comparing the measured and the simulated path loss shows that the number and distance of the fading holes are generally well aligned. In the measurement however, some additional disturbing effects exist. A major observation is the absence of fading effects at a distance greater than 700 m, which needs further investigation.

Increasing the bandwidth can help to reduce the fading effect, as the two propagation paths can be better resolved in the receiver. At large distances however, flat fading cannot be prevented and leads to a significant increase in path loss. This can be seen in Figure 7, that shows the same simulation setup with an increased bandwidth of 2 GHz.

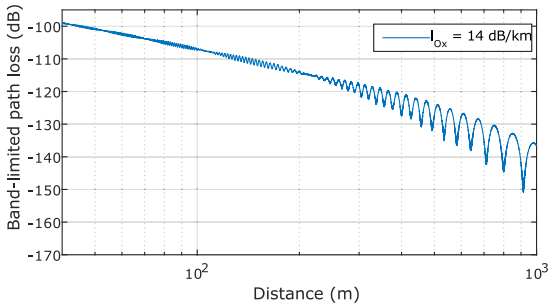

Figure 7: Simulated path loss ($H_{Tx} = H_{Rx} = 4\,\mathrm{m}$, horizontal polarization, $\epsilon_r = 2$, $B = 2\,\mathrm{GHz}$)

V. Conclusions

A channel sounder with a measurement bandwidth of 250 MHz is presented. This channel sounder enables Doppler resolved measurements of time variant channels.

Extensive outdoor measurements on asphalt and grass have been performed at distances of 40 to 1000 m. The measurement results were then analyzed and compared to a two-ray model. The fading can cause a significant increase in path loss at certain positions, as can be clearly seen from the measurements and simulation. Increasing the signal bandwidth can only mitigate this effect at shorter distances. The fading effect caused by the ground reflection should therefore be taken into account for street level backhaul links.

Acknowlegment

Part of the research leading to these results has received funding from the EU's FP7 Program (FP7-ICT-2013-EU-Japan) under grant agreement number 608637 (MiWEBA).

References

[1] F. Boccardi, J. Heath, R.W., A. Lozano, T. Marzetta, and P. Popovski, "Five disruptive technology directions for 5G," *Communications Magazine, IEEE*, vol. 52, no. 2, pp. 74–80, February 2014.

[2] N. Bhushan, J. Li, D. Malladi, R. Gilmore, D. Brenner, A. Damnjanovic, R. Sukhavasi, C. Patel, and S. Geirhofer, "Network densification: the dominant theme for wireless evolution into 5G," *Communications Magazine, IEEE*, vol. 52, no. 2, pp. 82–89, February 2014.

[3] W. Keusgen, A. Kortke, M. Peter, and R. Weiler, "A highly flexible digital radio testbed and 60 GHz application examples," in *Microwave Conference (EuMC), 2013 European*. IEEE, 2013, pp. 740–743.

[4] H. J. Liebe, "MPM-An atmospheric millimeter-wave propagation model," *International Journal of Infrared and Millimeter Waves*, vol. 10, no. 6, pp. 631–650, 1989.

4.2 Street canyon path loss measurement

The following publication presents path loss measurements at 60 GHz in a street canyon scenario [WPKW14]. The transmitter was positioned between the sidewalk and the road, as a possible way of small cell deployment on existing street lights. The receiver was moved along the sidewalk up to link distances of 50 m. This scenario matches the small cell access described in Section 3.1.

The path loss analysis is based on the strongest multipath components (MPCs), selected based on delay domain windowing. As fading effects were clearly visible on the MPCs, the path loss was investigated based on average power delay profiles. This approach was shown to provide exact path loss results even in the presence of a limited measurement bandwidth [PKW15].

Static measurements focusing on the time variant effects of the surrounding on the channel are also described in this publication.

Contribution

The measurement campaign that this paper is based on was planned and executed by my colleagues and myself. I authored most of the publication myself. The description of the mobile measurements was based on an analysis of the measurement data, performed by a co-author. The analysis of the time variant behavior (static measurements) was performed by me. The co-authors also provided proof-reading and smaller additions to the text.

Measuring the Busy Urban 60 GHz Outdoor Access Radio Channel

Invited Paper

Richard J. Weiler, Michael Peter, Wilhelm Keusgen, Mike Wisotzki
Fraunhofer Heinrich Hertz Institute
Berlin, Germany
Email: richard.weiler@hhi.fraunhofer.de

***Abstract*—The millimeter-wave frequency band is a promising candidate for future mobile communication in dense environments. The knowledge on the radio channel in outdoor environments is still very limited. In this paper we present measurements that have been performed in a busy urban outdoor environment at 60 GHz together with initial results. A typical small cell deployment scenario was used with static and mobile terminal positions. Human body shadowing events that affect the line-of-sight propagation have also been investigated.**

***Index Terms*—5G, millimeter-wave, 60 GHz, millimeter-wave radio channel, millimeter-wave access, channel sounding, HetNet, small cell**

I. Introduction

The massive increase of the data amounts and data rates in mobile radio networks is expected to continue over the next years. The deployment of fourth generation (4G) technology with LTE-Advanced is currently in progress worldwide. The next evolution of the access technologies is currently being discussed as 5G. The millimeter-wave frequency band is seen as a good candidate to increase the data rates in dense environments. Though this frequency band has been standardized for the physical layer of indoor applications, its use in outdoor environments is still very limited. Outdoor applications to date are fixed high gain point-to-point links for backhauling applications. A profound knowledge of the radio channel properties for cellular access scenarios is essential for the design of future systems. Comparing to the legacy frequency bands, the knowledge at millimeter-wave frequencies is still very limited [1], especially when taking the time variance of the environment into account.

In this paper we present the measurement method employed, the scenario and selected initial results.

II. Channel characteristics

The millimeter-wave frequency range is a relatively new candidate for mobile radio networks. In comparison to the crowded and scarce legacy frequencies in the sub 6 GHz range, almost unlimited contiguous spectrum of multiple GHz is available almost all over the world. Some part of this spectrum, e.g. the 60 GHz band, can be used license free while other bands are operated under a so called light license or block license.

The downside to these opportunities are the high propagation losses compared to the legacy frequencies. Establishing a broadband communication link over more than a few meters becomes very difficult with omnidirectional antennas due to technological and regulatory limitation of transmit power. To overcome these drawbacks it becomes necessary to use antennas with narrow beamwidth and medium or high gain at both ends of the communication link. Mechanical or electronic beam switching or beam steering becomes necessary to support applications with mobile handheld user devices and changing environments, such as pedestrians temporarily blocking propagation paths, etc. Designing such beam steering or beam forming solutions requires a profound knowledge on the spatial and temporal properties of the propagation channel.

While the radio channels in the legacy frequency bands have been studied in depth, the knowledge on outdoor millimeter-wave channels is still very limited. With respect to 60 GHz channel characterization, considerable work has been carried out since the 1990s [2]–[4]. Stochastic and deterministic models [5]–[8] are a valuable basis for the evaluation of 60 GHz indoor communication standards, like the recently developed IEEE 802.11ad. Concerning the outdoor channel some measurement campaigns have been reported. Most of these measurements used directional high-gain antennas and mechanical steering to identify individual propagation paths [9]–[11]. While this gives a very comprehensive understanding of the behavior of static reflecting objects in the environment, time variant channel behavior can not be observed. Furthermore the number of channel observations is limited due to the time consuming exhaustive path search, thus making derivation of valid statistical parameters for model generation very difficult.

Measuring with spatial and temporal resolution becomes a great challenge at millimeter-wave frequencies. Unlike the lower legacy frequencies, a fully three dimensional spatial resolution becomes necessary, as the cell radius of millimeter-wave cells will be much smaller and elevation information will play a crucial role. Receive antenna arrays with adequate post processing for directional estimation become necessary. Antenna switching solutions might not come into question due to the highly non-stationary environment. Additional to the high cost of the necessary parallel receiver chains exists the problem of proper calibration of these chains which might

render them as not feasible with the current state of the art. To our best knowledge no such comprehensive measurements have been conducted for outdoor environments.

III. Measurement Setup

The urban access small cell scenario was selected for the measurements presented in this paper. The Potsdamer Straße in Berlin, Germany, was chosen as measurement environment. It is a street canyon of 51.5 meters width as can be seen in Figure 1. The buildings on both sides are of modern type with mixed glass and stone facades. There are three car lanes per direction that are separated by a pedestrian walkway. Medium sized trees (around 4 to 5 meters) and street furniture such as bus stops, bicycle stands and seats are placed on the sidewalks.

The transmitter was placed on several locations at the edge of the sidewalk, aligned to existing lamp posts as indicated in the figure. The transmit antenna was mounted on a tripod at a height of 3.5 meter to represent a typical position of small cells being added to existing street furniture. The receiver was mounted on a mobile cart with an antenna height of 1.5 meter to represent a mobile handheld user device. Multiple measurements were performed at static receiver positions 25 meters separated to the transmitter as indicated. Mobile measurements were conducted as well, where the receiver was moved at a constant speed on a straight line on the sidewalk, passing the transmitter up to 50 meter to each side.

The measurement system itself is based on a self-developed FPGA platform [12]. The key parameters are listed in Table I. One measurement run contains 62,500 snapshots and took 50 seconds. During the measurement campaign a total of 3.75 million snapshots have been recorded with the mobile receiver, and 2 million snapshots have been recorded at static positions. The usage of omnidirectional antennas at both the transmitter and receiver side is very important to gather comprehensive results in the chosen time variant environment.

The measurement environment is also available as a detailed three-dimensional computer model. This model can be used to repeat the measurements with a ray tracing tool. Spatial information on the propagation environment can then be found by matching the simulated paths to the measurement results on the propagation delay axis. The limited measurement bandwidth can then also be neglected as the ray tracing results are generally frequency-independent. This procedure will permit a complete view of the time variant 3D millimeter-wave propagation environment that can serve as a basis for the generation of valid channel models.

IV. Measurement Results

The primary output of the channel sounder is a channel impulse response (CIR) for each measurement snapshot taken every 800 µs. This CIR shows the delay and magnitude of each multipath component (MPC) reaching the receive antenna. As the transmit and receive antenna have almost omnidirectional radiation patterns, no spatial filtering of the MPCs occurs. An exemplary plot of 100 snapshots of the CIR with static transmitter and receiver is shown in Figure 2. The

Table I
Channel Sounder Parameters

Type	Value
Frequency	60 GHz
Bandwidth	250 MHz
Output power	15 dBm
Snapshot measurement duration	64 µs
Temporal separation of snapshots	800 µs
Antenna gain	2 dBi
Antenna pattern	Omnidirectional
Antenna polarization	Linear, vertical
Maximum instantaneous dynamic range	45 dB

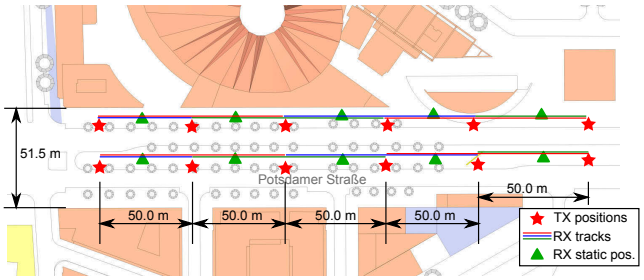

Figure 1. Measurement environment

delay of the first MPC is approximately 83 ns, being caused by the 25 meter line-of-sight distance between transmitter and receiver. The following MPCs then form a limited but distinctive number of peaks. The channel length observed in all measurements is in the order of multiple hundreds of nanoseconds.

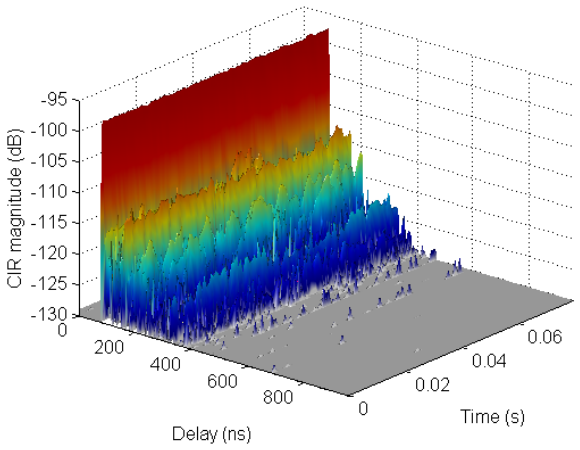

Figure 2. Example of channel impulse response for static setup

The following interpretation of the measurement results concentrates on these multipath components. It is important to note that the observed MPC at a certain delay can be caused by one or more waves arriving at the receiver from different angles of arrival, e.g. coming from different reflecting surfaces with the same total path length between transmitter and receiver. Due to the limited bandwidth of the measurement the CIR is susceptible to large and small scale channel effects.

A. Mobile measurements

For the mobile measurements, the transmitter was placed at fixed locations and the receiver was moved along the sidewalk along a distance of 50 meter to each side of the transmitter. A number of 40 measurements with 62.500 CIR snapshots each, giving a total of 2,500,000 snapshots was used for the following analysis.

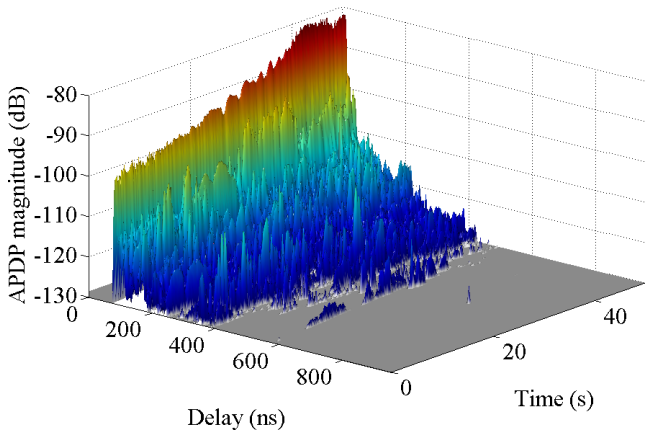

Figure 3. APDP of mobile measurement

The limited bandwidth of the measurement can cause fading effects on multipath components due to interference of multiple propagation paths with the same length. These fading effects can indeed be observed within the measured data. To circumvent problems arising from this effect the average power delay profile (APDP) was used instead of the CIR. The i-th APDP can be calculated from the CIR by $APDP_i = \frac{1}{N}\sum_{k=1}^{N}\left[CIR_{(iN+k)}(\tau)\right]^2$. The APDPs shown in this paper were generated with an averaging factor N set to 250.

Figure 4 shows the individual path loss for the five strongest multipath components of each APDP snapshot and linear regressions plotted against the line-of-sight (LOS) distance between transmitter and receiver. The different MPCs exhibit different path loss exponents, with the exponent of the strongest MPC being the largest. From the measurement setup it can be assumed that the strongest MPC in most cases was the LOS path. The increased variance towards larger distances can be attributed to higher chances of objects blocking this LOS path during the measurement. A derivation of path loss exponents of the individual MPCs would be possible but a more profound analysis of the propagation conditions (LOS vs. NLOS case) would be necessary. This will be regarded as next steps in the future.

These path loss results were generated with omnidirectional antennas, as stated before. When directive antennas are taken into account, some of these MPC will amplified and others will be attenuated, depending on the antenna pointing and its radiation pattern. Assuming medium gain antennas at the transmitter and receiver (in the order of 20-25 dBi) the observed individual path loss, even for the MPCs besides the first one, would give a link budget allowing high data rate communication with standard OFDM schemes for example.

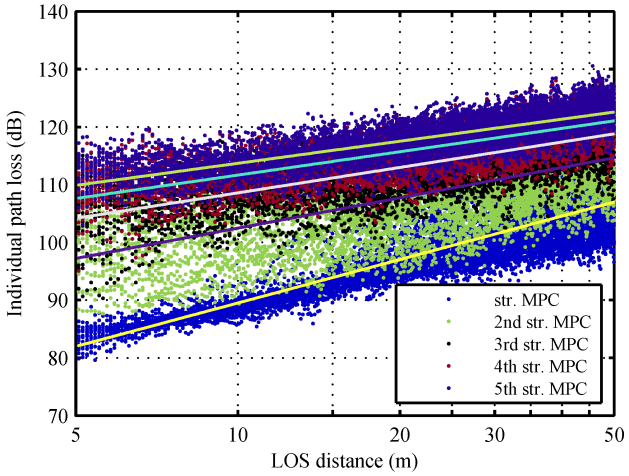

Figure 4. Individual path loss of multipath components

The statistical distribution of the individual path loss (PL) is shown in Figure 5. For every measurement snapshot the free space path loss is calculated from the known distance and subtracted from the individual PL. The cumulative distribution function then allows to derive the typical behavior of the path loss in the propagation environment. The magnitude of the second strongest MPC for example is less than 13 dB weaker than the free space path loss in 50 % of the measured snapshots.

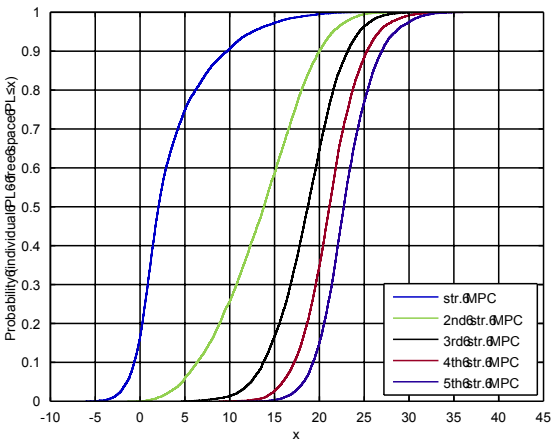

Figure 5. Empirical cumulative distribution function of MPC individual path loss

B. Static measurements

The static measurements have been performed with stationary transmitter and receiver at a distance of 25 meter. Figure 2 shows 100 snapshots of the channel impulse response of such a measurement. As noted before, the first peak occurs at 83 ns delay, representing the delay caused by the 25 meter separation

distance. The following peaks on the delay axis exhibit a strong time varying behavior even in the small observation window shown.

A further analysis of the behavior of the multipath components over the time axis becomes necessary. In each of the 62,500 snapshots of a measurement the two strongest peaks have been identified. Based on a histogram analysis of the position of these peaks, the four most frequent delays have been selected. The first of these delays belongs to the LOS path that was unblocked, at least most of the time, in all measurements.

The time evolution for one measurement of these four selected MPCs is shown in Figure 6. To suppress small scale effects and focus on large scale behavior, the average power delay profile was used as evaluation basis. The delays selected were: $\tau = \{83, 92, 105, 161\}$ ns. As can be seen, the magnitude of the first MPC is very stable while the magnitudes of the other three MPCs vary significantly over time.

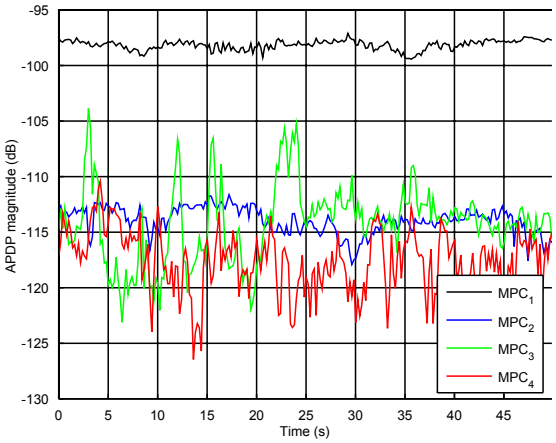

Figure 6. Time evolution of static measurement

Figure 7 shows the cumulative distribution function (CDF) of the four selected multipath components. The first MPC can be attributed to the line-of-sight path that was constantly present throughout the measurement, causing the steep transition of the CDF around its mean value. The same observation can be made for multipath component 2, indicating that it is caused by one or multiple static reflectors. The other two MPCs exhibit a more smooth transition indicating a stronger variation of their magnitude throughout the measurement.

C. Human body shadowing

In the investigated millimeter-wave urban access scenario the effects of pedestrians are very relevant. They can temporarily block the line-of-sight connection between the terminal and the base station, thus severly affecting the received signal. Measurements have been performed where the transmitter and receiver were 50 meters apart. The transmit antenna was mounted at 3.5 meter height and the receive antenna was mounted at 1.25 meter height. A single or multiple persons

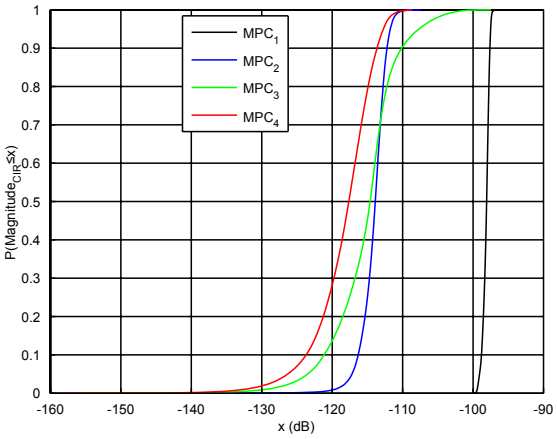

Figure 7. Empirical cumulative distribution function of MPC strength in static measurement

then moved adjacent to the LOS path in the vicinity of the receiver, thus temporarily fully blocking the line-of-sight path. The line-of-sight multipath component based on the channel impulse response for such a measurement is shown in Figure 8. The plot exhibits the typical behavior of the LOS path that was previously described and modeled with the double knife edge model [13]. The observed line-of-sight MPC attenuation during shadowing events is in the order of 10 to 15 dB on average but can increase up to 40 dB or more.

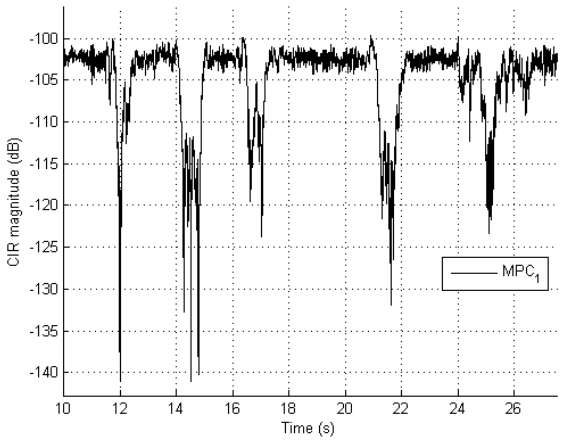

Figure 8. LOS multipath component under temporary human body shadowing

A more detailed plot of a single shadowing event is shown in Figure 9. Additionally to the line-of-sight MPC (delay of 164 ns), two other multipath components with delays of 244 ns and 172 ns are shown. It can be seen that these MPCs are not affected when the shadowing event occurs. This indicates that the propagation paths associated to these MPCs arrive from different directions than the LOS MPC.

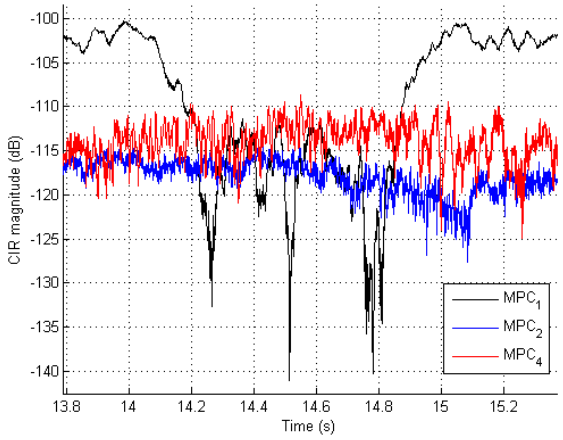

Figure 9. Human body shadowing event

V. Conclusions

The 60 GHz channel for an outdoor urban small cell access scenario has been measured with millions of wideband channel snapshots. The results indicate that the channel is highly time variant. Derivation of individual path loss parameters prove the general feasibility of millimeter-wave communication, even when the line-of-sight multipath component is blocked. The observed channel length in this environment with the used omnidirectional antennas at transmitter and receiver lies in the order of multiple hundred nanoseconds. The influence of human body shadowing on the line-of-sight multipath component has been confirmed against earlier findings for indoor environments. Spatial information on the propagation environment cannot directly be extracted from these measurements but a future fit with ray tracing results from the same environment is planned as next steps.

Acknowledgment

The research leading to these results has received funding from the European Union's Seventh Framework Programme (FP7-ICT-2013-EU-Japan) under grant agreement number 608637.

References

[1] T. Rappaport, F. Gutierrez, E. Ben-Dor, J. Murdock, Y. Qiao, and J. Tamir, "Broadband millimeter-wave propagation measurements and models using adaptive-beam antennas for outdoor urban cellular communications," *Antennas and Propagation, IEEE Transactions on*, vol. 61, no. 4, pp. 1850–1859, April 2013.

[2] P. Smulders and L. Correia, "Characterisation of propagation in 60 GHz radio channels," *Electronics & communication engineering journal*, vol. 9, no. 2, pp. 73–80, 1997.

[3] H. Xu, V. Kukshya, and T. Rappaport, "Spatial and temporal characteristics of 60-GHz indoor channels," *Selected Areas in Communications, IEEE Journal on*, vol. 20, no. 3, pp. 620–630, 2002.

[4] P. F. M. Smulders, "Statistical characterization of 60-GHz indoor radio channels," *Antennas and Propagation, IEEE Transactions on*, vol. 57, no. 10, pp. 2820–2829, 2009.

[5] A. Maltsev, R. Maslennikov, A. Sevastyanov, A. Lomayev, and A. Khoryaev, "Statistical channel model for 60 GHz WLAN systems in conference room environment," in *Antennas and Propagation (EuCAP), 2010 Proceedings of the Fourth European Conference on*, 2010, pp. 1–5.

[6] M. Jacob, S. Priebe, A. Maltsev, A. Lomayev, V. Erceg, and T. Kurner, "A ray tracing based stochastic human blockage model for the IEEE 802.11ad 60 GHz channel model," in *Antennas and Propagation (EUCAP), Proceedings of the 5th European Conference on*, 2011, pp. 3084–3088.

[7] M. Kyro, K. Haneda, J. Simola, K.-i. Takizawa, H. Hagiwara, and P. Vainikainen, "Statistical channel models for 60 GHz radio propagation in hospital environments," *Antennas and Propagation, IEEE Transactions on*, vol. 60, no. 3, pp. 1569–1577, 2012.

[8] D. Cassioli, "60 GHz UWB channel measurement and model," in *Ultra-Wideband (ICUWB), 2012 IEEE International Conference on*, 2012, pp. 145–149.

[9] E. Ben-Dor, T. S. Rappaport, Y. Qiao, and S. J. Lauffenburger, "Millimeter-wave 60 GHz outdoor and vehicle AOA propagation measurements using a broadband channel sounder," in *Global Telecommunications Conference (GLOBECOM 2011), 2011 IEEE*. IEEE, 2011, pp. 1–6.

[10] T. S. Rappaport, E. Ben-Dor, J. N. Murdock, and Y. Qiao, "38 GHz and 60 GHz angle-dependent propagation for cellular & peer-to-peer wireless communications," in *Communications (ICC), 2012 IEEE International Conference on*. IEEE, 2012, pp. 4568–4573.

[11] S. Rajagopal, S. Abu-Surra, and M. Malmirchegini, "Channel feasibility for outdoor non-line-of-sight mmWave mobile communication," in *Vehicular Technology Conference (VTC Fall), 2012 IEEE*. IEEE, 2012, pp. 1–6.

[12] W. Keusgen, A. Kortke, M. Peter, and R. Weiler, "A highly flexible digital radio testbed and 60 GHz application examples," in *Microwave Conference (EuMC), 2013 European*. IEEE, 2013, pp. 740–743.

[13] M. Peter, M. Wisotzki, M. Raceala-Motoc, W. Keusgen, R. Felbecker, M. Jacob, S. Priebe, and T. Kurner, "Analyzing human body shadowing at 60 GHz: Systematic wideband MIMO measurements and modeling approaches," in *Antennas and Propagation (EUCAP), 2012 6th European Conference on*. IEEE, 2012, pp. 468–472.

4.3 Dual-frequency path loss measurement

The millimeter-wave band ranges from lower gigahertz frequencies up to 300 GHz. The previous two publications investigated the wireless channel at 60 GHz, where a large block of up to 9 GHz contiguous spectrum is available as license-free spectrum in wide parts of the world. Due to this fact, possible interference and operator preferences it might not be the first candidate for fixed mobile radio networks. The following publication introduces a channel measurement campaign, similar to the previous one, but sounding the channel at 10 and 60 GHz simultaneously [WPK+15b]. The channel sounder setup was extended to two parallel transmit and receive chains and the respective antennas were placed next to each other. The additional band of 10 GHz was chosen as a value close to the lower end of the mm-wave spectrum.

The measurement setup was extended to distances up to 200 m and positions with non-line-of-sight conditions (NLOS), induced by buildings were added to investigate how the link deteriorates, when moving around a street corner. The residential street canyon is similar to the previous street canyon, but with a narrower street and without any trees along the sidewalks.

The path loss found in line-of-sight (LOS) conditions is similar to the previous campaign and there is no significant frequency dependence of the path loss coefficient. In NLOS conditions, a small difference can be observed, but these measurements suffer from limited achievable dynamic range due to the high loss. The delay spread at 60 GHz is lower than the one found at 10 GHz, which is in line with the knowledge on the propagation mechanisms (see Section 1.2).

Contribution

This measurement campaign was planned and executed by my co-authors and myself. I took care of the hardware setup, including the design and production of the 10 GHz antennas. The paper was authored by me. I also performed the analysis of the raw measurement data, partly based on pre-existing data processing scripts. The co-authors also provided proof-reading and smaller corrections of the text.

Simultaneous Millimeter-Wave Multi-Band Channel Sounding in an Urban Access Scenario

Richard J. Weiler*, Michael Peter*, Thomas Kühne†, Mike Wisotzki* and Wilhelm Keusgen*
*Fraunhofer Heinrich Hertz Institute, 10587 Berlin, Germany
†Communications and Information Theory Chair, TU Berlin, 10587 Berlin, Germany

***Abstract*—The frequency bands above 6 GHz up to millimeter-waves are a promising candidate to mitigate the scarcity of available spectrum in future mobile radio network deployments. The knowledge of the radio channel in these bands and a comprehensive channel model is vital for the design of such future systems. In this paper we present channel measurements that have been simultaneously performed at 10 GHz and 60.4 GHz in an urban access scenario. These measurement results are intended to contribute to the ongoing discussion on 5G channel models for the frequency bands above 6 GHz.**

***Index Terms*—millimeter-wave, 5G, millimeter-wave propagation, multipath propagation**

I. Introduction

The ever growing mobile traffic demand is one of the major drivers of the current discussion on the next (fifth) generation of mobile radio networks, often called 5G. Spectrum extension in the form of utilizing previously unused frequency bands is one of the proposed solutions for this [1]. During the recent years there has been increasing interest and research on the bands above 6 GHz for wireless communication. While some considerable work on channel measurements at millimeter-wave frequencies has recently been done, a comprehensive, unified channel model covering a wide frequency range is still missing. This would be helpful as the currently discussed candidate bands for 5G vary greatly between geographic regions [2].

In this paper we present channel measurements that have been performed in a dense, outdoor access scenario. The propagation channel was measured at 10 GHz and 60.4 GHz simultaneously at the exact same transmit and receiver positions. More than 6 million channel impulse responses were collected at continuous distances ranging from a few meters up to around 200 meters. Measurements were performed with clear line-of-sight along a street canyon, as well as non-line-of-sight around house corners at intersections. We provide an analysis of path loss and delay spread data both at 10 GHz and 60 GHz. The results of this campaign can serve as a starting point to develop a model that is able to describe the channel behavior over a large frequency range.

Other reported measurement campaigns at similar bands and frequencies are for example reported in [3], though they feature only a small number of samples and are based on synthetic omnidirectional values from directional measurements. These measurements were taken at similar locations but at different times, further complicating comparability.

In section II the channel sounder hardware and measurement parameters are introduced. Section III describes the measurement environment and section IV describes the results obtained from the measurement campaign.

II. Channel sounder

The channel sounder used for the measurements presented in this paper is based on a self developed FPGA platform [4] and described in [5]. The channel sounder uses broadband periodic correlation sequences with a bandwidth of 250 MHz as measurement signals. Figure 1 gives a simplified overview over the hardware elements. The transmitter side consists of a baseband chain that generates the correlation sequence. This signal is then converted up to 10 GHz and 60.4 GHz center frequency on two independent RF chains and fed through power amplifiers on two transmit antennas. After being transmitted through the wireless channel, two fully parallel RF and baseband chains receive the signals on the two bands.

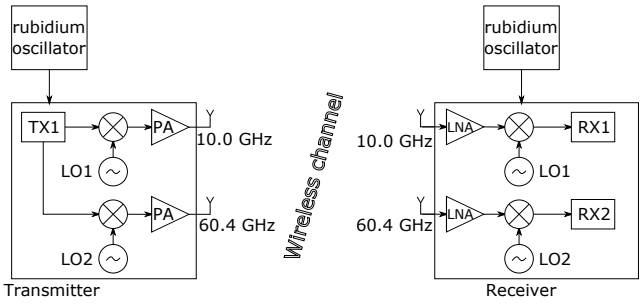

Figure 1. Channel sounder overview

At both bands vertical polarized, omnidirectional antennas with a half power beamwidth (elevation) of more than 60° (10 GHz) and 80° (60.4 GHz) are used on both the transmitter and the receiver. The 10 GHz antenna is a $\lambda/4$-Dipole design. Figure 2 shows its measured radiation pattern in the $\theta = 0°$ and $\theta = 90°$ plane. Its diagram in azimuth direction is flat to 1 dB. In elevation the diagram exhibits slightly larger variations. At 60 GHz a commercial antenna with similar patterns is used. Its pattern is shown in Figure 3. The radiation pattern is less uniform, especially in elevation direction, but assumed to be flat enough for the measurement data analysis.

Table I lists the important channel sounder parameters.

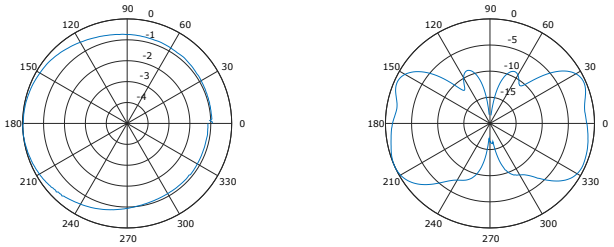

(a) $\theta = 0°$ (b) $\theta = 90°$

Figure 2. 10 GHz antenna patterns (dB normalized)

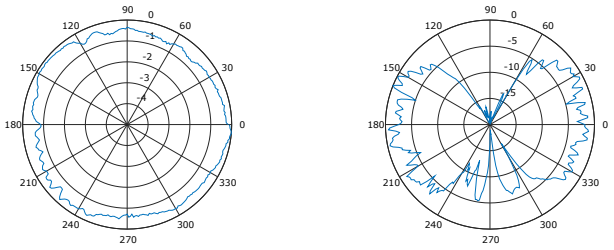

(a) $\theta = 0°$ (b) $\theta = 90°$

Figure 3. 60 GHz antenna patterns (dB normalized)

III. Measurement Campaign

The measurement campaign was conducted in Kreuzberg, Berlin, Germany. This is a typical residential and commercial area. The streets are limited by 5 to 6 story buildings to both sides, thus forming a street canyon. The transmitter was placed on the sidewalk at a height of 5 meter above ground, representing a street level small cell base station. The receiver was mounted on a mobile cart at a height of 1.5 meter, representing a mobile terminal. Figure 4 shows a map of the scenario. The positions, where the transmitter was placed during the campaign are indicated with a red and green circle. The tracks where the receiver was moved are indicated using lines of corresponding color to the transmitter position.

Table I
Channel Sounder Parameter

Type		Value
Tx output power	10 GHz	20 dBm
	60.4 GHz	15 dBm
Antenna gain	10 GHz	0 dBi
	60.4 GHz	-0.7 dBi
Antenna pattern		Omnidirectional
Sounding bandwidth		250 MHz
Temporal snapshot separation		800 µs
Number of CIR snapshots per set		62,500
Number of sets used in this paper		60
Receiver speed		0.5 $^{\mathrm{m}}/_{\mathrm{s}}$

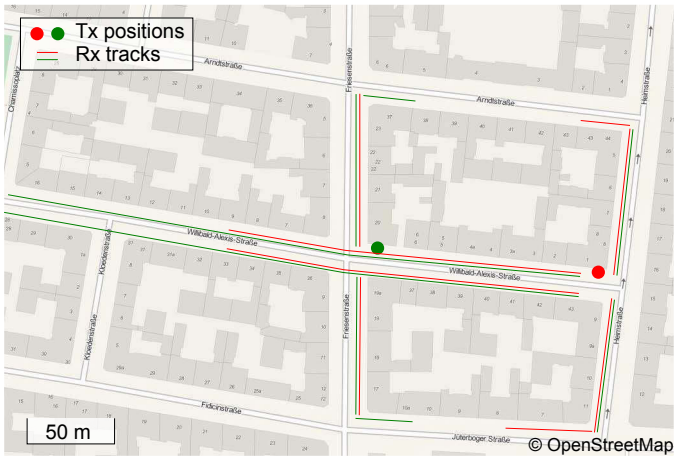

Figure 4. Location map of measurements

As can be seen, measurements were performed with free line-of-sight (LOS) between the transmitter and the receiver as well as with non-line-of-sight (NLOS) around house corners at intersections. The minimum Tx-Rx distance was around 4 m and the maximum distance at around 200 m.

Figure 5. Receiver cart and residential street

IV. Measurement Results

A. Data preprocessing

The channel sounder outputs a complete channel impulse (CIR) response every 800 µs as indicated in Table I. At the speed of receiver movement this is a channel snapshot distance of 0.4 mm. The geometry of the environment and

the bandwidth of the sounding system can lead to severe small-scale fading effects, caused e.g. by the ground reflection. To mitigate this effect, spatial averaging is performed on the CIRs by calculating average power delay profiles (APDP) over 3,125 samples, equaling to $1.25\,\mathrm{m}$ [6]. These APDPs are used throughout the rest of this paper.

B. Path loss

The path loss was evaluated based on the spatially averaged power delay profiles. Figure 6 shows a scatter plot of all path loss values that were taken in line-of-sight condition. This LOS condition was identified through the geometric of the environment, i.e. buildings. Short temporary blockage through street lights etc. might occur in LOS classified areas. The influence of such short blockage effects however should be very minor, due to the spatial averaging.

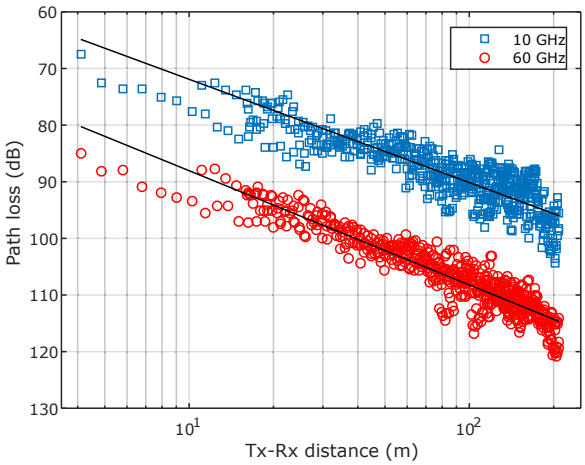

Figure 6. Line-of-sight path loss and linear regression

The solid lines in Figure 6 show the linear least squares fit to the data samples. The path loss exponent model is used and takes the form:

$$L_{PL}\left(d\right)_{|dB} = \bar{L}_{PL}\left(d_0\right)_{|dB} + 10n\log_{10}\left(\frac{d}{d_0}\right),$$

where d_0 is the reference distance, here set to 5 m, and $\bar{L}_{PL}\left(d_0\right)_{|dB}$ is the path loss at that distance. For the full set of path loss samples taken at distances from 4 m to 200 m the path loss coefficients in Table II are obtained. The value of $\bar{L}_{PL}\left(d_0\right)_{|dB}$ was set to be equal to the free space path loss ($\bar{L}_{PL}\left(d_0\right)_{|dB} = 20\log_{10}\left(4\pi d_0/\lambda\right)$) and n was obtained through the fit.

The same evaluation has been performed for the measurements without free line-of-sight (NLOS). All of these measurement samples were taken around a corner of a house at a street intersection. The distance however is not the geometric distance between transmitter and receiver, but the full path length around the corner. This modified measure was used, because we observed a quick signal degradation when moving around a faraway corner without proper representation in the geometric distance. As can be observed, some signal values at distances larger than 100 m go against a limit. This is caused by the noise floor of the system.

Table II
LINEAR LEAST SQUARES FIT LOS PATH LOSS PARAMETERS

Type		Value
n	10 GHz	1.82
	60.4 GHz	2.02
d_0		5 m
$\bar{L}_{PL}\left(d_0\right)_{\|dB}$	10 GHz	66.42 dB
	60.4 GHz	82.04 dB

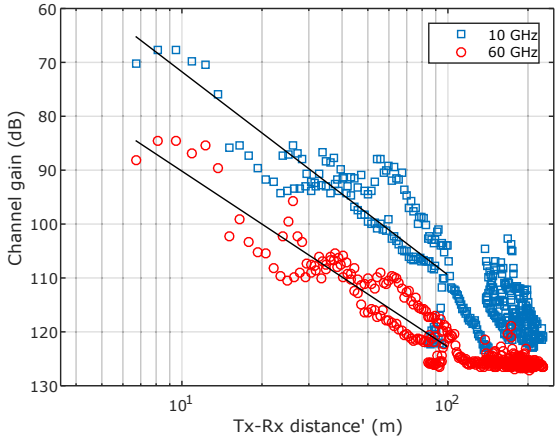

Figure 7. NLOS path loss and linear regression

Due to the influence of the noise floor, the linear least squares fit was performed on the measurements up to a distance of 100 m. The fit is based on a limited number of samples only, compared to the LOS case. The values in Table III were obtained by fitting both n and $\bar{L}_{PL}\left(d_0\right)_{|dB}$, in contrast to the LOS case where $\bar{L}_{PL}\left(d_0\right)_{|dB}$ was given as a fixed value.

Table III
LINEAR LEAST SQUARES FIT NLOS PATH LOSS PARAMETERS

Type		Value
n	10 GHz	3.77
	60.4 GHz	3.26
d_0		5 m
$\bar{L}_{PL}\left(d_0\right)_{\|dB}$	10 GHz	60.4 dB
	60.4 GHz	80.4 dB

C. Delay spread

The delay spread is a measure to describe the channel concerning multipath propagation. Here we calculate the root mean square (rms) delay spread as the second moment of the APDPs. Figures 8 and 9 show normalized APDPs at 10 and 60.4 GHz respectively. They were taken at the same location at 68 m Tx-Rx distance. The figures are normalized, so that the first multipath component, caused by the line-of-sight path,

are positioned at zero delay and amplitude. Here, an evaluation threshold of 25 dB is applied, meaning that all parts of the signal below the normalized power of -25 dB are not taken into account. Only the parts highlighted in red are used to calculate the excess delays.

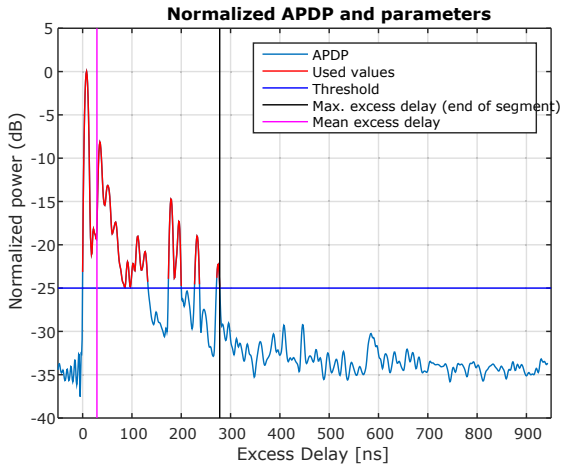

Figure 8. Normalized APDP and excess delay, 10 GHz, 25 dB threshold

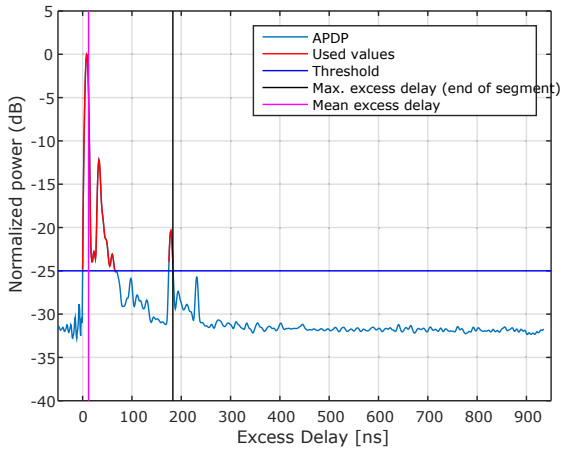

Figure 9. Normalized APDP and excess delay, 60 GHz, 25 dB threshold

The choice of the threshold has a strong influence on the value of the delay spread [7]. If it is chosen too small, then very few multipath components are taken into account, thus reducing the delay spread unnaturally. If it is chosen too large, then the noise floor will also be considered, thus falsifying the result towards larger values. The practical choice of the threshold therefore highly depends on the available dynamic range and the noise floor of the measurements, as well as how the delay spread information will be used. In our measurements, we found values in the range of 20 to 30 dB to be a good compromise. Values in this region should also be in line with the dynamic range of practical communication systems.

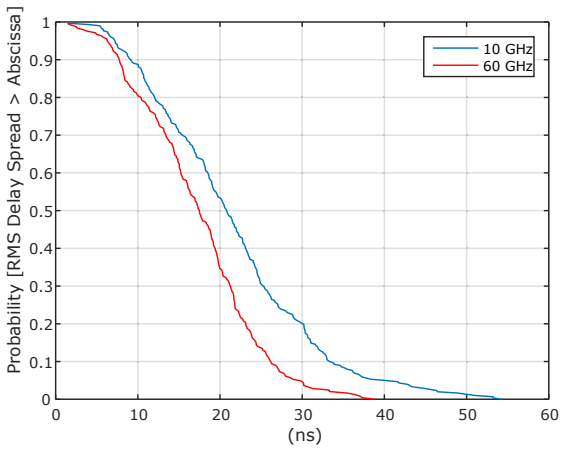

Figure 10. CCDF of RMS delay spread, LOS scenario, 25 dB threshold

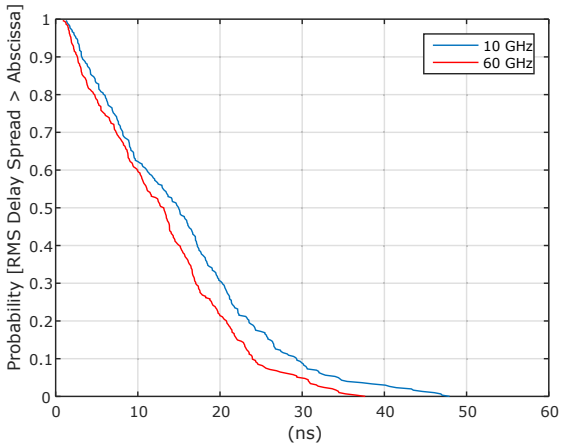

Figure 11. CCDF of RMS delay spread, LOS scenario, 20 dB threshold

Figures 10 and 11 show complementary cumulative density functions (CCDF) of the values observed for the rms delay spread with 25 and 20 dB threshold, respectively. As expected, the observed delay spreads decrease with a decrease of the threshold.

It is interesting to notice that at 60 GHz the radio channel has lower rms delay spread than at 10 GHz. As the transmit and receive antennas were at the same positions, multiple effects can be the source this observation. Reflections that occur at buildings, cars and other objects present in the street can differ due to the different wavelength and relative roughness of the surfaces. Additionally, the Oxygen absorption that has a peak in the 60 GHz band of up to $20\,^{\mathrm{dB}}/_{\mathrm{km}}$ can additionally attenuate longer paths, thus reducing the delay spread compared to 10 GHz.

The same evaluation has also been performed for the NLOS measurements. The CCDF with a threshold of 25 dB can be seen in Figure 12. Though number of available samples is limited by the higher path loss, a major increase of the rms delay spread can be observed against the LOS case.

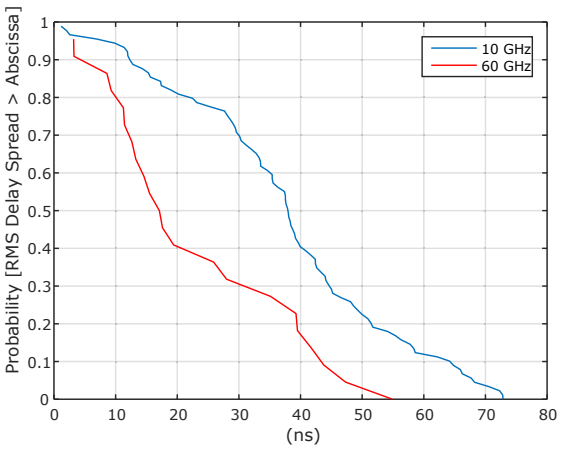

Figure 12. CCDF of RMS delay spread, NLOS scenario, 25 dB threshold

This observation can be attributed to the fact, that the LOS multipath component is blocked and the power distribution between the other multipath components is more uniform.

In Figure 13 the LOS rms delay spread is plotted over the distance. Only a slight effect of increase with the distance can be observed. Besides the difference already observed in the CCDF plots, no further observation can be made comparing the different frequencies.

It has to be noted that the delay spread was only evaluated when the normalized APDP had a dynamic range larger than the chosen threshold. In order to derive a statistical model from these measurements, these values should not be omitted, but taken into account accordingly [8].

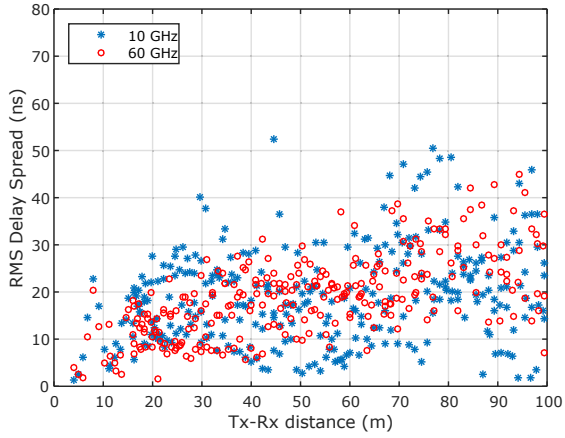

Figure 13. Distance dependent RMS delay spread, LOS scenario, 25 dB threshold

V. Conclusions

In this paper we presented a channel sounder that simultaneously supports two channels at different frequencies. We also presented a measurement campaign that was performed in an outdoor urban access scenario with omnidirectional antennas at 10 GHz and 60.4 GHz.

We presented a collection of measurement results. The main difference of the path loss under line-of-sight conditions is caused by the difference in reference path loss (antenna aperture). In non-line-of-sight conditions the path loss was observed to be much higher, but the system dynamic range imposes a limit on the usable distance of the system.

A comparison of the delay spread reveals different behavior between the frequency bands in form of a reduction of the rms delay spread when going from 10 to 60.4 GHz.

Acknowlegment

Part of this work has been performed in the framework of the FP7 project ICT-317669 METIS, which is partly funded by the European Union.

References

[1] F. Boccardi, J. Heath, R.W., A. Lozano, T. Marzetta, and P. Popovski, "Five disruptive technology directions for 5G," *Communications Magazine, IEEE*, vol. 52, no. 2, pp. 74–80, February 2014.

[2] T. Rosowski, J. Kronander, T. Irnich, O. Queseth, M. Tercero, K. Chatzikokolakis, R. Arapoglou, K. Koufos, A. A. Widaa, J. I. Markendahl, H. Schotten, M. A. Uusitalo, L. M. Campoy, and C. Markwart, "Deliverable D5.3 - Description of the spectrum needs and usage principles," in *Mobile and wireless communications Enablers for the Twenty-twenty Information Society (METIS)*, 2014. [Online]. Available: https://www.metis2020.com/

[3] G. MacCartney Jr, M. Samimi, and T. Rappaport, "Omnidirectional path loss models in New York City at 28 GHz and 73 GHz," in *IEEE Int. Symp. PIMRC*, 2014, pp. 303–307.

[4] W. Keusgen, A. Kortke, M. Peter, and R. Weiler, "A highly flexible digital radio testbed and 60 GHz application examples," in *Microwave Conference (EuMC), 2013 European*. IEEE, 2013, pp. 740–743.

[5] R. J. Weiler, M. Peter, W. Keusgen, A. Kortke, and M. Wisotzki, "Millimeter-wave channel sounding of outdoor ground reflections," in *IEEE Radio and Wireless Symposium*, 2015.

[6] M. Peter, W. Keusgen, and R. J. Weiler, "On path loss measurement and modeling for millimeter-wave 5G," in *Antennas and Propagation, 2015. EuCAP 2015. 9th European Conference on*, 2015.

[7] T. Zwick, T. Beukema, and H. Nam, "Wideband channel sounder with measurements and model for the 60 GHz indoor radio channel," *Vehicular Technology, IEEE Transactions on*, vol. 54, no. 4, pp. 1266–1277, July 2005.

[8] T. Abbas, C. Gustafson, and F. Tufvesson, "Pathloss estimation techniques for incomplete channel measurement data," in *COST IC1004 10th Management Committee and Scientific Meeting*, 2014, p. 5. [Online]. Available: https://lup.lub.lu.se/search/publication/4442929

4.4 Instantaneous path loss model

Street canyon path loss measurements were presented in the previous sections. Based on the raw path loss data from the measurement in Section 4.2, the following publication [WPK+14b] introduces a model that was parameterized to match the measurement observation. The model provides instantaneous path loss values depending on the distance between transmitter and receiver. This model was used as an input to system level simulations. These simulations are set up to evaluate the system rate of an overlay heterogeneous network, matching the scheme introduced in Chapter 3.1.

The model presented in this publication has a high level of abstraction and outputs instantaneous path loss values. It does not include spatial and temporal resolution and consistency. Therefore it cannot be applied to link level investigations. The publication then introduces a system level simulation, based on a heterogeneous network deployment as introduced in Section 3.1 and the path loss model is compared to a pure free-space path loss model. The comparison yields no significant impact of the model on the overall system rate gain.

Contribution

This publication is a cooperative work in the frame of the MiWEBA project. It consists of the two major parts, the wireless channel and its modeling and the system performance evaluation. I authored the introduction, Section III (Path loss model) based on post-processing of the measurement data done by myself and major parts of Sections II (Path loss measurement). Section IV (System level simulation) was provided by my co-authors.

Outdoor Millimeter-Wave Access for Heterogeneous Networks – Path Loss and System Performance

Richard J. Weiler, Michael Peter, and Wilhelm Keusgen
Fraunhofer Heinrich Hertz Institute, Berlin, Germany
Email: richard.weiler@hhi.fraunhofer.de

Hidekazu Shimodaira, and Khanh Tran Gia
Tokyo Institute of Technology, Japan
Email: {shimodaira, khanhtg}@mobile.ee.titech.ac.jp

Kei Sakaguchi
Osaka University, Osaka, Japan
Email: sakaguchi@comm.eng.osaka-u.ac.jp

***Abstract*—The millimeter-wave frequency bands, especially the license free band at 60 GHz, is a candidate for future broadband access links. Path loss measurements have been performed in a typical small cell access scenario. Path loss model parameters were derived for these results, including large and small scale effects. Using this model a system level analysis was performed to evaluate the performance of a heterogeneous network using millimeter-wave access links.**

***Index Terms*—5G, Millimeter-wave, 60 GHz, Millimeter-wave propagation, Propagation losses, Centralized-RAN, HetNet, Millimeter-wave radio channel, Overlay, Small Cell**

I. Introduction

Network densification and the usage of new spectrum are very important technical aspects that are currently considered for future fifth generation mobile radio networks (5G) [1], [2]. The millimeter-wave frequency band, e.g. the license free 60 GHz band, is a very promising candidate for the spectral extension with multiple Gigahertz of previously unused bandwidth. Due to the propagation properties in the millimeter-wave bands, the coverage provided by such cells is expected to be much smaller than with the legacy sub 6 GHz frequencies. Therefore small cell deployment scenarios in form of a heterogeneous network (HetNet) in combination with legacy macro cell base stations is a more suitable architecture [2].

The discussion on millimeter-wave frequencies for cellular access is relatively new and the knowledge on the channel properties in these environments is still very limited. However, evaluating the baseline performance of such heterogeneous networks and comparing the performance to other approaches discussed for 5G, requires system level models incorporating suitable path loss models. In this paper we present an outdoor 60 GHz measurement campaign and the derivation of path loss parameters. We then used these parameters to compare a heterogeneous network with millimeter-wave overlay small cells with these channel parameters to free space propagation.

The rest of this paper is organized as follows. Section II presents an overview on the state of the art and the measurement campaign that was performed. Section III explains the derivation of the path loss. In section IV the model is applied to system level simulations.

II. Path loss measurement

A. State of the art

The indoor millimeter-wave channel, especially at 60 GHz has recently received much attention. There even exists a number of standards for high data rate indoor communication, such as IEEE 802.11ad and 802.15.3c. For outdoor environments however the knowledge on the channel properties is still very limited. Comprehensive path loss models and spatial channel models for millimeter-wave small cell deployments in outdoor environments do not yet exist. A fundamental understanding of the characteristic propagation effects is essential to elaborate appropriate models.

Recently some measurements have been reported and some initial models have been derived [3]–[6]. These measurements were performed using steerable directional antennas at a number of fixed transmitter and receiver locations. As the number of positions is very limited due to the high complexity and time consuming measurement procedure, it is difficult to derive reliable statistical models and parameters.

Generally the propagation at millimeter-wave frequencies heavily depends on the specific scenario and whether the line-of-sight (LOS) path between the transmitter and the receiver is free or obstructed. To what extent reflections originating from objects in the environment can be used to establish communications links is still under investigation. Especially the temporal channel behavior in dynamic outdoor environments still needs to be investigated thoroughly.

The frequency dependence of reflections, which are the main reason for multipath propagation, is mainly related to surface roughness [7]. The roughness of typical exterior building materials only moderately affects propagation in the lower GHz range. However, in the millimeter-wave band it may decide between receiving a beneficial near-specular reflection path and none at all. Diffraction effects decrease rapidly as frequency increases. In the millimeter-wave band they are typically only relevant if the size of the obstacle is quite small like in the order of tens of cm. As a result even human body shadowing can cause severe losses exceeding 30 dB [8].

B. Measurement campaign

A measurement campaign in an outdoor small cell access environment has been performed. The Potsdamer Straße in downtown Berlin, Germany was selected as a typical densely built and busy environment. Such places with a large number of pedestrians are expected to be among the first places that will be equipped with millimeter-wave small cell base stations.

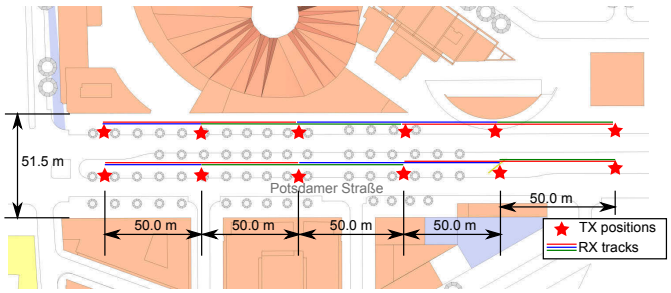

Figure 1. Measurement scenario

Figure 1 shows the scenario. It is a street canyon of 51.5 meter width with high modern buildings to each side. There are pedestrian sidewalks on each side of the road and in the middle between the lanes. A transmitter was placed at several static positions marked with red stars in the figure. The transmitter was mounted on a pole at a height of 3.5 meter to simulate a typical small cell deployment on street furniture, such as street lights. The receiver was mounted on a mobile cart at a height of 1.5 meter and moved along the sidewalk at constant speed. This should reflect a typical mobile user terminal. The receiver was moved from 50 meter to one side of the transmitter to 50 meter to the other side for each TX position, as indicated by the colored lines in the figure. On the sidewalks there are typical objects such as trees, bus stops, trash cans and bicycle stands. Aside of some small objects such as tree branches without leaves, at almost all receiver positions there was an unobstructed line of sight to the transmit antenna.

The channel sounder is based on a self-developed, flexible FPGA-based hardware platform [9]. The center frequency of the signal was 60 GHz and the measurement bandwidth was 250 MHz. The output power was 15 dBm with omnidirectional antennas at both the transmitter and receiver location. The receiver was calibrated by directly connecting it to the transmitter. A measurement snapshot was taken every 800 µs. Every snapshot contains a channel impulse response. A total of 2.5 million snapshots was taken using this configuration.

III. Path loss model

Based on the results of the measurement campaign a specific path loss model was derived. This model does not separate large-scale and small scale behavior, but considers both effects to be part of the instantaneous path loss. This model can be useful as input for system simulations to generate path loss values without taking into account the detailed temporal structure of the channel and differentiating between large-scale and small-scale effects. It is therefore called “conjoint instantaneous path loss model”.

A. Conjoint instantaneous path loss model

As described in Section II, the measurement snapshots were taken using omnidirectional antennas. When calculating the path loss on this basis all possible propagation paths between transmitter and receiver are taken into account. This is reasonable if the targeted communication system makes use of omnidirectional antennas, too. However, it is somewhat unrealistic as real millimeter-wave communication systems will most probably employ directional antennas to improve their link budget. Directional antennas imply that a spatial filtering of signals propagating towards the antenna is performed, depending on its orientation and antenna pattern. In order to replicate this behavior, a window in the delay domain around the LOS delay was applied to each CIR from the measurement, before it was used to calculate the path loss. In this way only the line-of-sight component, the ground reflection and reflections from other objects very close to the line-of-sight path are taken into account. It is assumed that this windowing approach is a good approximation of a spatial filtering around the line-of-sight between transmitter and receiver. There are cases conceivable where this approximation is not true, e.g. objects between transmitter and receiver that would reflect the waves back and forth before arriving at the receiver. However, verification measurements that were performed using directional antennas support our approximation.

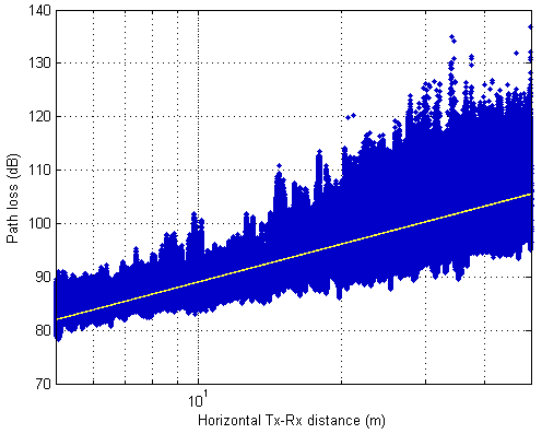

Figure 2. Measured path loss and mean path loss least squares fit.

In Figure 2 the path loss for all distances from 5 to 50 meter distance is shown as a scatter plot (blue). The yellow line represents the linear least squares (LS) fit corresponding to the mean path loss. The parameters identified for this path loss model can be found in Table I.

Table I
PATH LOSS PARAMETERS

Type	Value
d_0	5 m
$L_{PL}(d_0)$	82.02 dB
n	2.36

The deviations of the path loss from the mean, as can be

seen in Figure 2, are considerably larger than for spatially averaged values, which are to be used to derive path loss parameters for the classical large-scale model. Investigations revealed that small-scale fading due to a strong ground reflection is the main reason for that behavior. It superimposes with shadow fading caused by temporary obstructions of the line-of-sight path by small objects or pedestrians.

To further investigate the path loss in a statistical manner, the data in Figure 2 was normalized with the fitted mean path loss. Then the relative amplitude of each snapshot was calculated and empirical probability distributions for bins of 5 meter distance were generated. For each of these distributions a Rician distribution was fit onto the data, which has been identified to be well suited for this purpose. Figure 3 exemplarily shows the distribution and the Rician fit for the bins from 5 to 10 meter (Fig. 3a) and from 45 to 50 meter (Fig. 3b). As can be seen the quality of the approximation through the Rician distribution varies between samples but is seen as good, given the limited number of experimental samples.

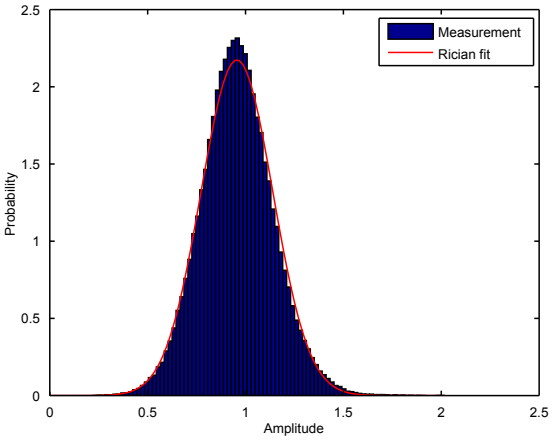

(a) 5 to 10 meter

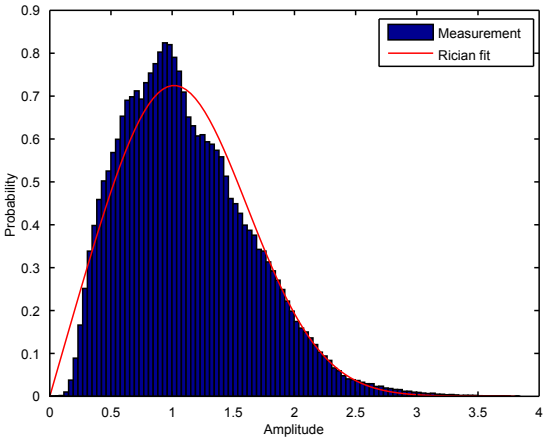

(b) 45 to 50 meter

Figure 3. Empirical probability density function of relative amplitude.

The fitted parameters K and Ω of the Rician distribution are shown in Figure 4. To simplify the model, a linear fit has been performed on both parameters. The parameters are:

$$K = -0.62 \cdot d + 25\,\mathrm{dB}$$

and

$$\Omega = 0.013 \cdot d + 1,$$

where d is the TX-RX distance.

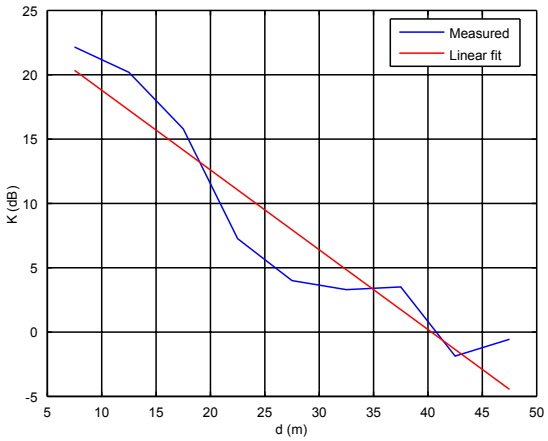

(a) Parameter K

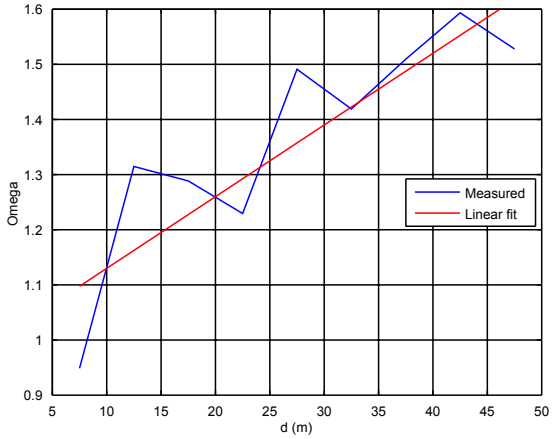

(b) Parameter Ω

Figure 4. Distance dependent model parameters.

Based on these evaluations, the conjoint instantaneous path loss model takes the following form:

$$L_{\mathrm{PL}}(d)_{|\mathrm{dB}} = \bar{L}_{\mathrm{PL}}(d_0)_{|\mathrm{dB}} + 10n \log_{10}\left(\frac{d}{d_0}\right) - 20 \cdot \log_{10} R_{K,\Omega},$$

where $R_{K,\Omega}$is a distance-dependent Rician random variable.

Using the derived model Figure 5 shows a simulated scatter plot of the path loss. Compared to the measured path loss in Figure 2 the model yields a very good accordance.

It has to emphasized that the derived model delivers independent instantaneous values of the path loss. This means that two consecutively drawn path loss values for the same or a similar distance are uncorrelated and do not reflect the evolution of the path loss when the receiver is moving. In

practice, there are strong correlations between consecutive channel observations and the fading caused by the ground reflection. Furthermore this path loss model is derived from band limited measurements with a bandwidth of 250 MHz that is also included in the overall effects.

If the correlations are important, a more advanced path loss model has to be used, based for example on a two ray propagation model and additional statistical properties. However, the model is well suited for link- and system-level simulations that assume block fading.

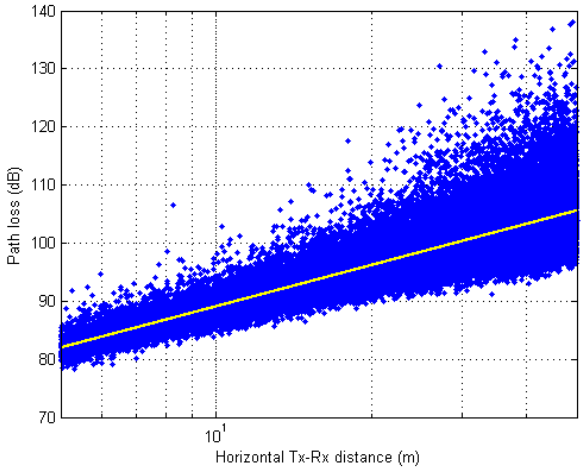

Figure 5. Simulated instantaneous path loss.

B. Comparison to other models

Figure 6 shows a comparison of different path loss models. The blue dots and the yellow line are instantaneous path loss values as described in this paper, extrapolated up to 200 meter. The free space model is based on Friis transmission equation [10]. The "Empirical NYC" models for line-of-sight (LOS) and non-line-of-sight conditions are based on measurements at 73 GHz, reported in [3]. The 3GPP urban micro model (UMi) is based on [11] and was calculated for a frequency of 60 GHz.

The path loss values for "Empirical NYC LOS" and the one derived in Section III-A are very close to that of free space propagation for up to a few hundred meters. The 3GPP standard UMi model overestimates the path loss when it is applied to millimeter-wave frequencies, a band it was primarily not designed for. The "Empirical NYC NLOS" is mentioned for completeness and gives path loss values that are 20 dB greater than the ones observed under line-of-sight conditions.

IV. System Level Simulation

We conducted system level simulations based on previous work [12] to evaluate the performance of millimeter-wave overlay heterogeneous networks. In this study, the system rate

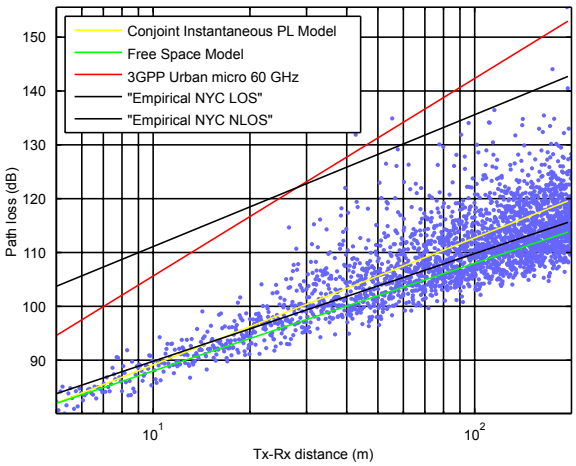

Figure 6. Comparison of path loss models

of the heterogeneous network is defined as follows:

$$R = \sum_{u\in\mathcal{M}} \min\left(\frac{W_{\mathrm{M}} C_{u,\mathrm{M}}}{|\mathcal{M}|}, L_u\right) + \sum_{s=1}^{N_{\mathrm{S}}} \sum_{u\in\mathcal{S}_s} \min\left(\frac{W_s C_{u,s}}{|\mathcal{S}_s|}, L_u\right) \quad (1)$$

where W_{M} and W_s are the available bandwidth for macro and small cell respectively. $C_{u,\mathrm{M}}$ and $C_{u,s}$ are link capacity from macro and s-th small cell [13]. $|\mathcal{M}|$ and $|\mathcal{S}_s|$ represent the number of users belonging to the macro base station (BS) and number of users attached to the s-th small cell BS. N_{S} is a total number of small cell BSs deployed within one macro cell area. L_u is a traffic demand of user u. In this paper, we compare the value of system rate of a free space path loss scenario with that based on the model derived in Section III-A. The performance metric is the system rate gain defined as follows:

$$G = R/R_{\mathrm{HomoNet}} \quad (2)$$

$$R_{\mathrm{HomoNet}} = \sum_{u=1}^{N_{\mathrm{UE}}} \min\left(\frac{W_{\mathrm{M}} C_{u,\mathrm{M}}}{|\mathcal{M}|}, L_u\right), \quad (3)$$

where R_{HomoNet} is the system rate of the macro only cellular network (homogeneous network), N_{UE} is a total number of users.

A. Simulated scenario

This simulation focuses on two types of multi band HetNet systems, i.e.

1) 2 GHz and 60 GHz HetNet, average traffic is 2.6 Mbps
2) 2 GHz and 60 GHz HetNet, average traffic is 64 Mbps

The simulation parameters are listed in Table II.

In the free space path loss scenario, the path loss model is described as

$$20\log_{10}(d) + 20\log_{10}(f) - 147.55 \quad (4)$$

where d is the distance between the BS and the user equipment (UE). f is the center frequency, here 60 GHz.

Table II
SIMULATION PARAMETERS.

Parameter	Value
Bandwidth (Macro / 60 GHz)	10 MHz / 2 GHz
Number of macro cells	7 (1 evaluate, 6 interference)
Number of small cells (per 1 macro site)	0–200
Number of UEs (per 1 macrocell)	5000
Number of BS antennas M	4
Number of UE antennas N	2
Antenna gain (Macro / 60 GHz)	17 dBi / 25 dBi
Antenna beam pattern (Macro / 60 GHz)	3GPP [14] / WiGig [15]
BS antenna height (Macro / 60 GHz)	25 m / 3 m
UE antenna height	1.5 m
Tx power (Macro / 60 GHz)	46 dBm / 10 dBm

The distribution of traffic demand L_u is assumed as Gamma distribution. In this paper, we assume that the mobile traffic load grows about twice every year and two scenarios are evaluated: 5 years later (40 times higher traffic), and 10 years later (1000 times higher traffic).

B. Simulation Results

Numerical results of the system rate gain are shown in Fig. 7. The red line and the blue line represent the scenario based on the conjoint instantaneous path loss model ("Measured") and the free space scenario respectively. There are no significant differences between the two scenarios. This result indicate that the the measurement based channel parameters does not limit the applicability in the investigated millimeter-wave overlay heterogeneous network in comparison to a 60 GHz free space propagation model.

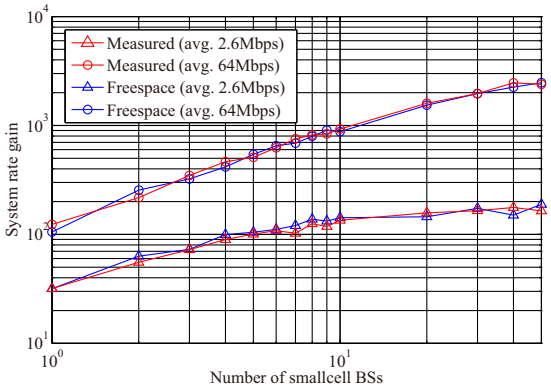

Figure 7. System level simulation result

V. CONCLUSION

In this paper a path loss model for outdoor urban access links was introduced. This conjoint instantaneous path loss model comprises all large and small scale propagation effects and can be used as input to system level simulations. Evaluation of a heterogeneous network architecture with 60 GHz small cell deployments, based on the introduced model shows the feasibility of millimeter-waves as urban outdoor access technology for 5G systems.

ACKNOWLEDGMENT

The research leading to these results has received funding from the European Union's Seventh Framework Programme (FP7-ICT-2013-EU-Japan) under grant agreement number 608637 and was supported by MIC in Japan.

REFERENCES

[1] F. Boccardi, J. Heath, R.W., A. Lozano, T. Marzetta, and P. Popovski, "Five disruptive technology directions for 5G," *Communications Magazine, IEEE*, vol. 52, no. 2, pp. 74–80, February 2014.

[2] N. Bhushan, J. Li, D. Malladi, R. Gilmore, D. Brenner, A. Damnjanovic, R. Sukhavasi, C. Patel, and S. Geirhofer, "Network densification: the dominant theme for wireless evolution into 5g," *Communications Magazine, IEEE*, vol. 52, no. 2, pp. 82–89, February 2014.

[3] M. R. Akdeniz, Y. Liu, S. Sun, S. Rangan, T. S. Rappaport, and E. Erkip, "Millimeter wave channel modeling and cellular capacity evaluation," *CoRR*, vol. arXiv:1312.4921, 2014.

[4] S. Rajagopal, S. Abu-Surra, and M. Malmirchegini, "Channel Feasibility for Outdoor Non-Line-of-Sight mmWave Mobile Communication," in *Vehicular Technology Conference (VTC Fall), 2012 IEEE*. IEEE, 2012, pp. 1–6.

[5] T. S. Rappaport, E. Ben-Dor, J. N. Murdock, and Y. Qiao, "38 GHz and 60 GHz angle-dependent propagation for cellular & peer-to-peer wireless communications," in *Communications (ICC), 2012 IEEE International Conference on*. IEEE, 2012, pp. 4568–4573.

[6] G. R. MacCartney, J. Zhang, S. Nie, and T. S. Rappaport, "Path loss models for 5G millimeter wave propagation channels in urban microcells," in *Global Communications Conference (GLOBECOM), 2013 IEEE*, Dec 2013, pp. 3948–3953.

[7] O. Landron, M. J. Feuerstein, and T. S. Rappaport, "A comparison of theoretical and empirical reflection coefficients for typical exterior wall surfaces in a mobile radio environment," *Antennas and Propagation, IEEE Transactions on*, vol. 44, no. 3, pp. 341–351, 1996.

[8] M. Peter, M. Wisotzki, M. Raceala-Motoc, W. Keusgen, R. Felbecker, M. Jacob, S. Priebe, and T. Kurner, "Analyzing human body shadowing at 60 GHz: Systematic wideband MIMO measurements and modeling approaches," in *Antennas and Propagation (EUCAP), 2012 6th European Conference on*. IEEE, 2012, pp. 468–472.

[9] W. Keusgen, A. Kortke, M. Peter, and R. Weiler, "A highly flexible digital radio testbed and 60 GHz application examples," in *Microwave Conference (EuMC), 2013 European*. IEEE, 2013, pp. 740–743.

[10] H. T. Friis, "A note on a simple transmission formula," *proc. IRE*, vol. 34, no. 5, pp. 254–256, 1946.

[11] 3GPP, "Further advancement for E-UTRA physical layer aspects," *TR 36.814 (release 9)*, 2010.

[12] K. Sakaguchi, S. Sampei, H. Shimodaira, R. Rezagah, G. K. Tran, and K. Araki, "Cloud cooperated heterogeneous cellular networks," in *Intelligent Signal Processing and Communications Systems (ISPACS), 2013 International Symposium on*. IEEE, 2013, pp. 787–791.

[13] H. Shimodaira, G. K. Tran, K. Araki, K. Sakaguchi, S. Nanba, T. Hayashi, and S. Konishi, "Cell association method for multi band heterogeneous networks (submitted)," in *The 7th International WDN Workshop on Cooperative and Heterogeneous Cellular Networks (PIMRC Workshops)*, 2014.

[14] 3GPP TR 36.814, "Further advancements for E-UTRA physical layer aspects."

[15] IEEE 802.11 Wireless LANs, "Channel Models for 60 GHz WLAN Systems."

4.5 Quasi-deterministic channel model

The previously introduced model provides instantaneous path loss values, drawn from a statistical process, matching the measurement results. This is insufficient, when investigating the link level of millimeter-wave communication systems. When designing the physical and MAC layer of a system for example, a number of requirements need to be satisfied. Details on the multipath nature of the channel impulse response and spatial and temporal consistency for moving users are important. Additionally, detailed information on the angles of departure and arrival of the multipath components is necessary when investigating communication links with directional or beamforming antennas. Information on interference from neighboring stations also needs to be provided by the model.

The following publication describes a quasi-deterministic modeling approach and its parameterization that answers these requirements [WPK+16b]. The model was developed and published in the MiWEBA project [MPK+14, MPB+14]. It is based on parts of the IEEE 802.11ad channel model [MMS+10] and was extended and adapted to outdoor scenarios. The model relies on a geometrical description of the environment, an open square scenario in the present case. Major contributors to the receive signal, such as the line-of-sight propagation and the ground reflection are expressed in a deterministic way. Other components, such as random reflections and shadow fading, observed in the measurements, are modeled as stochastic components. Through its deterministic construction, spatial consistency and resolution of angle of departure and arrival is inherently provided. Patterns of beam steering or beam forming antennas can be applied on top. Even interference from neighboring stations can be obtained in a link level simulation.

The detailed output of the channel model relies on the detailed description of the environment and needs to be adapted to each scenario under investigation. However, the general construction of the model does not need to be changed. Future steps towards a next generation, millimeter-wave channel model might define a set of reference scenarios, such as the scenarios and use cases defined by the METIS project [OBB+14]. A set of model parameters can then be derived for each scenario and used for the link level investigations.

The publication also introduces another type of channel model that was developed by some of the co-authors in the MiWEBA project. This model can generate channel impulse responses for heterogeneous network deployments with varying bandwidth but does not provide spatial and temporal consistency

as the quasi-deterministic model does.

Contribution

The quasi-deterministic modeling approach was developed and published in the MiWEBA project by some of the co-authors and myself [MPK+14, MPB+14]. The present publication contains an updated model with parameters adapted to the open square scenario. The writing of the publication was coordinated by myself and I entirely authored Sections 1, 2 and 6. The underlying measurement campaign was planned and executed by some of my co-authors and myself and the data analysis and post-processing was performed by me. Sections 3, 4 and 5 were contributed by my co-authors, with contributions and reviews provided by myself, especially to Section 4.

Weiler et al. EURASIP Journal on Wireless Communications and Networking (2016) 2016:84
DOI 10.1186/s13638-016-0568-6

EURASIP Journal on Wireless Communications and Networking
a SpringerOpen Journal

RESEARCH Open Access

Quasi-deterministic millimeter-wave channel models in MiWEBA

Richard J. Weiler[1*], Michael Peter[1], Wilhelm Keusgen[1], Alexander Maltsev[2,3], Ingolf Karls[2], Andrey Pudeyev[2], Ilya Bolotin[2], Isabelle Siaud[4] and Anne-Marie Ulmer-Moll[4]

Abstract

This article introduces a quasi-deterministic channel model and a link level-focused channel model, developed with a focus on millimeter-wave outdoor access channels. Channel measurements in an open square scenario at 60 GHz are introduced as a basis for the development of the model and its parameterization. The modeling approaches are explained, and their specific area of application is investigated.

Keywords: Millimeter-wave, Channel model, Access, Backhaul

1 Introduction

The increasing mobile traffic demand has led to the proposition of numerous approaches for the future development of mobile radio networks. One popular proposition for the next generation (so-called 5G) is the usage of previously unused spectrum in the millimeter-wave band [1]. Using the spectrum at these high frequencies incurs new challenges, compared to radio systems that operate at frequencies below 6 GHz. The possible applications are in backhaul and fronthaul links on the network side [2] or on the access link. Recent research proves the general feasibility of outdoor access links in the lower millimeter-wave band (30–40 GHz) based on path loss evaluations [3]. At the same time, a high spatial selectivity of the channel is observed in this publication.

The higher free-space path loss motivates a design shift from an omni-directional operation to more spatial focusing, using high-gain beam-forming antennas and multiple input/multiple output (MIMO) approaches. It will also incur a change in system design, towards a more dense deployment of so-called overlay small cell base stations, which will exist in addition to today's macro-cell deployments. These base stations can then provide very high throughput millimeter-wave access links to the user terminals. The small cells themselves will also need backhauling to the core network. This in turn might also be deployed using the millimeter-wave bands for interference and bandwidth considerations. For the successful design and development of such systems, a comprehensive channel model that covers the relevant propagation effects is an essential basis.

The millimeter-wave band has already been used for fixed outdoor applications with success in the recent years [4]. The main concerns for this kind of applications are the impact of weather conditions (rain, snow, fog) and the availability of an unblocked line-of-sight (LOS) on the link quality. As the links are mostly static, simple path loss models are sufficient for these applications.

A large number of channel models have been proposed and used for sub-6 GHz wireless communication and different kinds of applications and use cases. A well-known model for mobile radio networks is, e.g., the WINNER II channel model [5]. It relies on a geometry-based stochastic approach and was designed for frequencies from 2 to 6 GHz with up to 100 MHz bandwidth. Its parameters are determined stochastically, based on statistical distributions extracted from channel measurement data. The model was developed for a wide range of propagation scenarios ranging from indoor office, urban micro-cell to urban and rural macro-cell. Different scenarios are modeled by the same approach but with different parameters. When going to higher carrier frequencies in the millimeter-wave band and wider bandwidths, the WINNER II and similar geometry-based stochastic models might not be valid any more.

* Correspondence: richard.weiler@hhi.fraunhofer.de
[1]Fraunhofer Heinrich-Hertz-Institute, Berlin, Germany
Full list of author information is available at the end of the article

Recently, the widely used IEEE 802.11 standard for wireless local area communication has been extended to the 60-GHz band with the 802.11ad protocol. This standard targets indoor communication. A new channel model was developed for this standard, based on the observation that the wireless channel can be well described with a set of distinct geometry-based propagation paths [6]. Spatial resolved measurements were performed in static indoor environments, showing that ray-tracing-like propagation paths with up to two reflections dominate the received power [7].

Here, we present the quasi-deterministic (Q-D) channel model and the link level-focused Canal Enregistré de Propagation Déterministe (CEPD) model, which have been developed and used within the Millimeter-Wave Evolution for Backhaul and Access (MiWEBA) project. The Q-D model combines a geometry-based approach for a limited number of multipath components and a stochastic approach. In this paper, we show how this channel modeling approach may be applied for specific access use cases (outdoor open square and large indoor area) and further how it can be modified for other environments. This modeling approach was chosen in order to accurately support spatial consistency that would not be possible with a statistical model. New experimental data for an open square scenario measurement are used to improve the modeling methodology described previously in [8, 9]. An extension is given in a form of the CEPD model that can be used to abstract the generic Q-D model to system level requirements, such as limited bandwidth and impact of antennas.

The development of the channel model was driven by a set of reference use cases and scenarios, defined in the MiWEBA project, whose focus is the investigation of new 5G architectures with millimeter-wave technology [10, 11]. These use cases are similar to other 5G-related investigations, with a focus on millimeter-wave frequencies and their limitations. Apart from indoor and backhaul scenarios, emphasis is on outdoor mobile access links of small cell base stations with a typical cell radius of several hundred meters. The work presented in this paper focuses on this kind of links.

Section 2 details the performed outdoor access channel measurements to give an understanding of environment and the observed radio propagation effect. Section 3 then introduces the Q-D modeling approach. The measurement-based parameterization of the model is given in Section 4. Section 5 explains the link layer focus channel model and links it to the Q-D model.

2 Open square scenario experimental measurements

A measurement campaign was performed on "Leipziger Platz" in downtown Berlin, Germany [11]. This is an open square of octagonal shape with modern glass and stone buildings to the sides. A street with three lanes per direction is cutting through the square with a diameter of 150 m. The area itself is covered with grass and some trees and lined with sidewalks, as can be seen in Figs. 1 and 2. The transmitter was placed at a height of 3.5 m at four different positions on the sidewalk and on the grass. This height was assumed as a starting point for small cell deployments being placed on existing street furniture. The receiver was moved along the sidewalk with an antenna height of 1.5 m. The receiver tracks and their associated transmitter positions are colored alike.

The center frequency of the measurement campaign was 60 GHz with a sounding bandwidth of 250 MHz. The antennas used on both sides are commercially available vertical polarized omni-directional antennas with a gain of 2 dBi. Their radiation pattern is flat in the entire azimuth as well as for elevation angles from −30° to 30°. This allows acquiring omni-directional power delay profiles without any mechanical steering. The influence on the antenna pattern in elevation is expected to be minimal, as there are no major sources of reflection outside the 60° half-power opening angle.

The receiver cart is either static or moving at a constant speed of 0.5 m/s, each with a temporal snapshot separation of 800 μs. Due to properties of the measurement system, the maximum number of snapshots per acquisition is ca. 60.000. Tracks requiring longer acquisition are measured in multiple adjacent runs.

Due to the measurement bandwidth and the geometry of LOS and ground-reflected propagation, fading can occur on the measured path power [12]. Averaging allows reducing this effect and simplifies measurements, but for the data analysis in the present paper, no averaging is applied, as the focus lies on the multipath properties of the channel detailed investigation.

A typical channel impulse response vs. time plot on the sidewalk at the middle road (Tx1, receiver at P1) is given in Fig. 3. The LOS path is clearly visible and stable at a delay of 84 ns, which equals exactly the transmitter to receiver distance of 25 m in this measurement. The ground reflection cannot be resolved due to the measurement bandwidth. Other stable propagation paths at higher delays are clearly visible. For example, in Fig. 3 there are strong components at 276, 308, and 324-ns delays, being path lengths of ca. 83, 92, and 97 m respectively. It should be noted that power fluctuation of those stable components in time was less than 1–2 dB. Figure 4 shows an average power delay profile of an entire 50-s measurement run at the same location. Note that this figure shows the full resolvable delay axis up to 1.024 μs, opposed to the previous figure that was restricted to 400 ns.

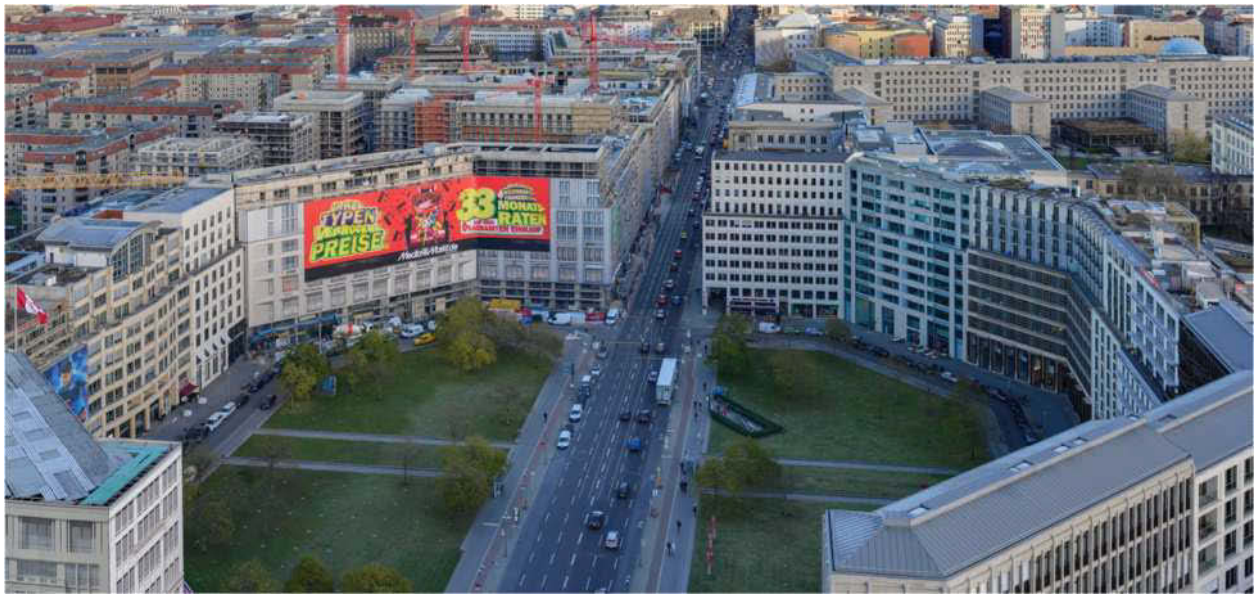

Fig. 1 Leipziger Platz measurement site view (Photo: Arild Vågen, License: CC BY-SA 3.0)

Channel impulse responses for moving receivers are shown in Figs. 5 and 6. In the first case, the transmitter is placed at the position Tx2 and the receiver is moving along track Rx2, starting at the western end. In the second figure, the transmitter is placed on the position Tx4 and the receiver is moving along the dashed part of the Rx4 track, starting at the northern end. Multiple adjacent measurement runs (three and two, respectively) were concatenated for the plots, causing some minor discontinuities. The LOS delay varies in both cases as

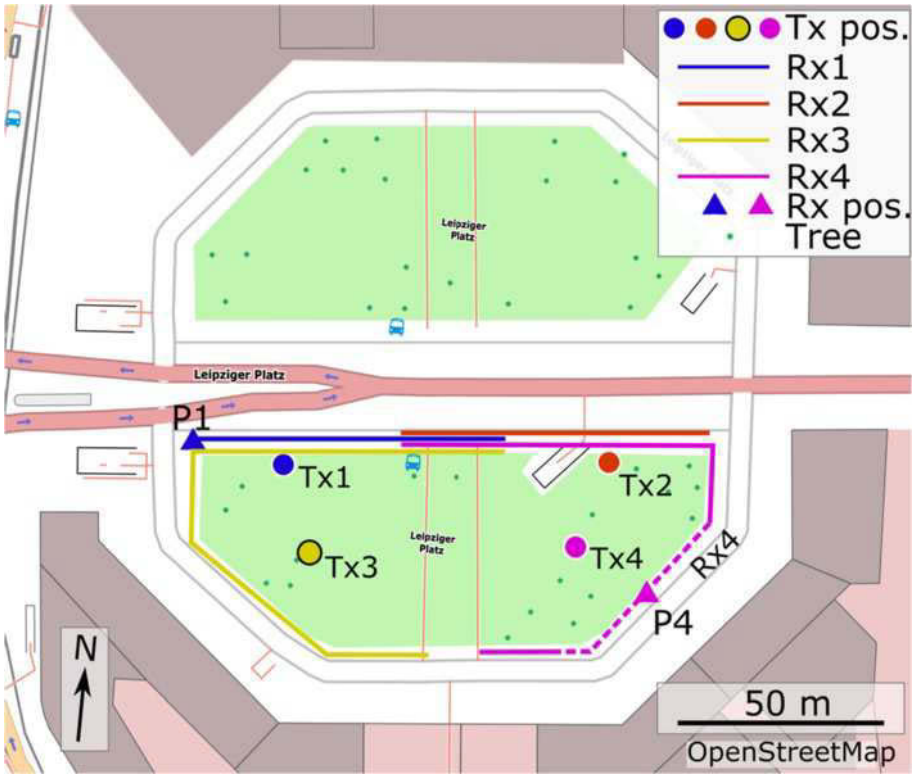

Fig. 2 Map of open square measurements

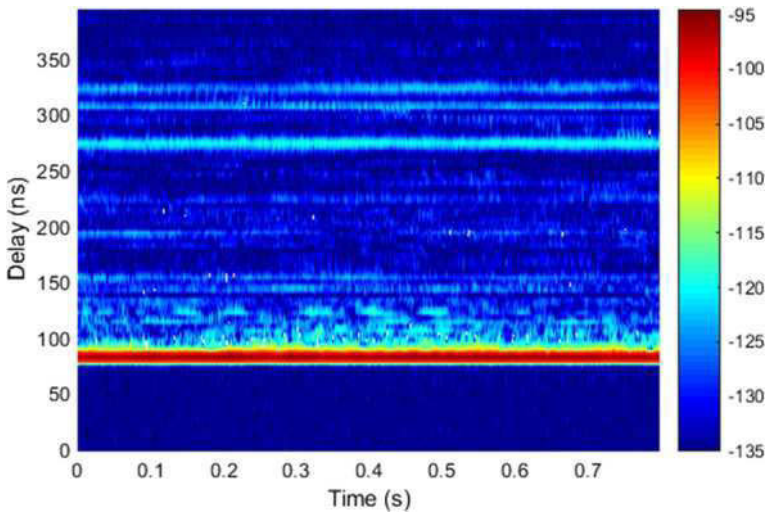

Fig. 3 Channel impulse response with a static receiver, Tx1

the receiver is moving closer and farther from the transmitter location, matching well with the geometrical Tx-Rx distance. In the Tx4 case, a strong multipath component is visible at an excess delay (over LOS) of ca. 25 ns. This path could be identified as a reflection from the closest building. On this reflected component, a strong fading effect is visible, but as described earlier, this can be caused by the reflected ray and its ground reflection, which cannot be resolved with the measurement bandwidth. In the Tx2 measurement, the next building wall is much more distant and therefore much weaker. On the other hand, some multipath components become visible at ca. 80 s when the receiver passes the subway exit with its metallic construction. As with the static measurement, a number of stable multipath components (clearly visible as lines at the time-delay diagram) are caused by surrounding buildings. The "color noise" also present on the diagram is caused by reflections from various objects such as trees and street furniture. The delay of these paths depends on the precise geometrical setup of the environment. Analyzing the channel impulse response at greater delays than shown here reveals that the strength of these components is much weaker and quickly vanishes in the dynamic range of the measurement. The maximum observed relevant delay relative to LOS path is about 150–200 ns.

Another static average power delay profile is given in Fig. 7. The receiver position corresponds to a time of 45 s in Fig. 6. In this position, the multipath component with an excess delay of 50 ns is about 20 dB below the

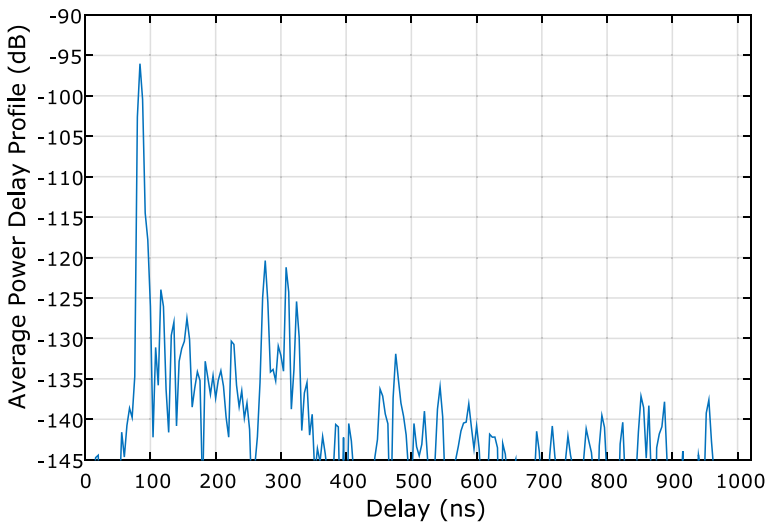

Fig. 4 Average power delay profile of static receiver pos. P1 with Tx1

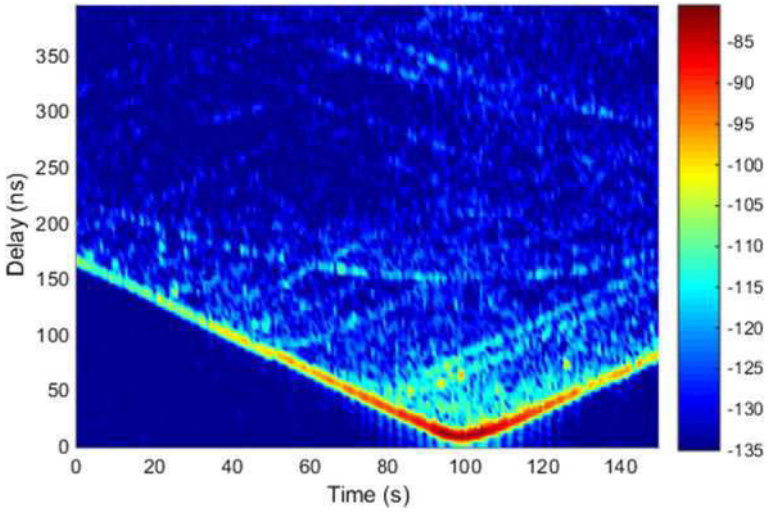

Fig. 5 Channel impulse response with a moving receiver, Tx2

LOS, but another component with an excess delay of ca. 110 ns is visible, which is less than 10 dB below the LOS power. The measurement results for the Tx position Tx3 and the Rx position Rx3 are very similar to the Tx4 and Rx4 results, respectively.

The analysis of other channel parameters from these and similar urban access measurements, such as path loss and delay spread, was presented in earlier work [13, 14].

3 Quasi-deterministic channel model

The experimental measurement results in Section 2, represented in the form of time-delay diagrams (Figs. 3, 4, 5, 6, and 7), illustrate the fact that the channel for static and moving Tx-Rx positions is not completely random, but has some Q-D components, that are represented in the time-delay diagrams by steady, clearly visible lines and traces. Moreover, the strongest traces can be identified as LOS path and reflections from the nearest buildings. The same diagram, plotted by using the ray-tracing reconstruction of the environment, will be very similar to the one seen in the experiments, with difference only in noise-like background and weak short traces that can be caused by small objects. These observations lead to the conclusion that realistic millimeter-wave channel models can consist of deterministic components, defined by the scenario and random components, representing unpredictable factors or objects that are random or insignificant.

Such an approach, called Q-D, was offered for modeling access and backhaul millimeter-wave channels at 60 GHz [9, 15]. The approach builds on the

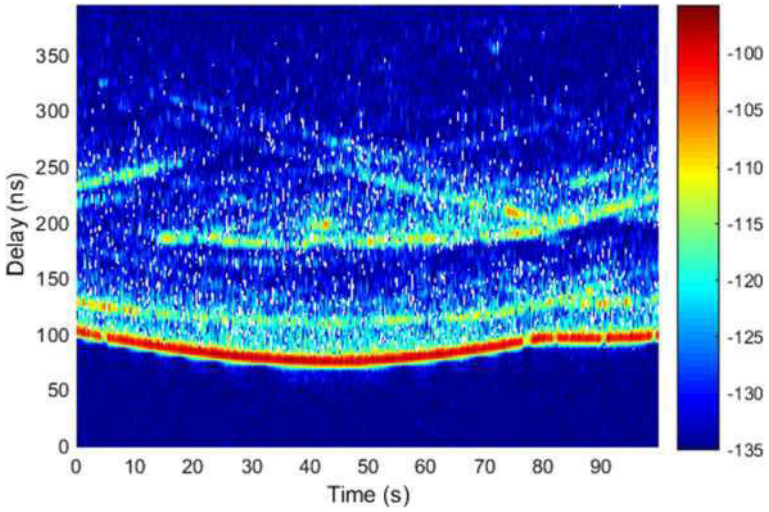

Fig. 6 Channel impulse response with a moving receiver, Tx4

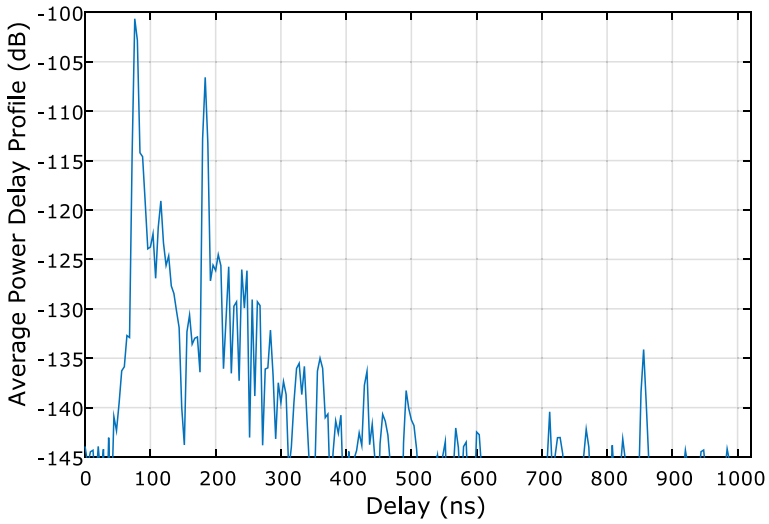

Fig. 7 Average power delay profile of static receiver pos. P4 with Tx4

representation of the millimeter-wave channel impulse response comprised of a few Q-D strong rays (D-rays), a number of relatively weak random rays (R-rays, originating from the static surfaces reflections), and flashing rays (F-rays, originating from moving cars, buses, and other dynamic objects reflections).

The key benefit of this approach compared to pure statistical models is its inherent support for spatial consistency. The deterministic part of the channel impulse response accurately takes the position of the transmitter and receiver into account. Simulating a moving user, for example, the band-limited channel impulse response can accurately reproduce fading effects, observed in real measurements [16]. This is not possible with a purely statistical model.

The first type of rays makes the major contribution into the signal power, is present all the time, and usually can be clearly identified as a reflection from scenario-important macro objects. It is logical to include them into the channel model as deterministic (D-rays), explicitly calculated values. The element of randomness, important for the statistical channel modeling, may be introduced on the intra-cluster level, by adding a random exponentially decaying cluster to the main D-ray.

The second type of rays (R-rays) is the reflections from the random objects or the objects that is not mandatory in the scenario environment. Such type of rays may be included in the model in a classical statistical way, as rays with parameters (power and delays) selected randomly in accordance with the predefined distributions.

The third type of rays (F-rays) may be introduced to the model in the same way as R-rays but with some additional statistic for appearing chance and duration.

All the types of rays are then combined in the single-clustered channel impulse response, shown in Fig. 8. Here, a cluster refers to multipath components with similar delay, angle of departure (AoD), and angle of arrival (AoA) parameters. All of these parameters must be similar in order for the multipath components to form a cluster, and paths belonging to a cluster should have the same physical propagation mechanisms [5].

For each of the channel propagation scenarios, the strongest propagation paths are determined and associated to rays which produce the substantial part of the received useful signal power. Then, the signal propagation over these paths is calculated based on the geometry of the deployment and the locations of the transmitter and receiver, calculating the ray parameters, such as AoA and AoD, power, and polarization characteristics. The signal power conveyed over each of the rays is calculated in accordance to theoretical formulas taking into account free-space losses, reflections, antenna polarization, and receiver mobility effects like Doppler shift. Some of the parameters in these calculations may be considered as random values like reflection coefficients or as random processes like receiver motion. The number of D-rays, which are taken into account, is scenario dependent and is chosen to be in line with the channel measurement results. Additionally to the D-rays, a lot of other reflected waves are received from different directions, coming, for example, from cars, trees, lamp posts, benches, and houses (for outdoor scenarios) or from room furniture and other objects (for indoor scenarios). These rays are modeled as R-rays. These rays are defined as random clusters with specified statistical parameters extracted from available experimental data or ray-tracing modeling.

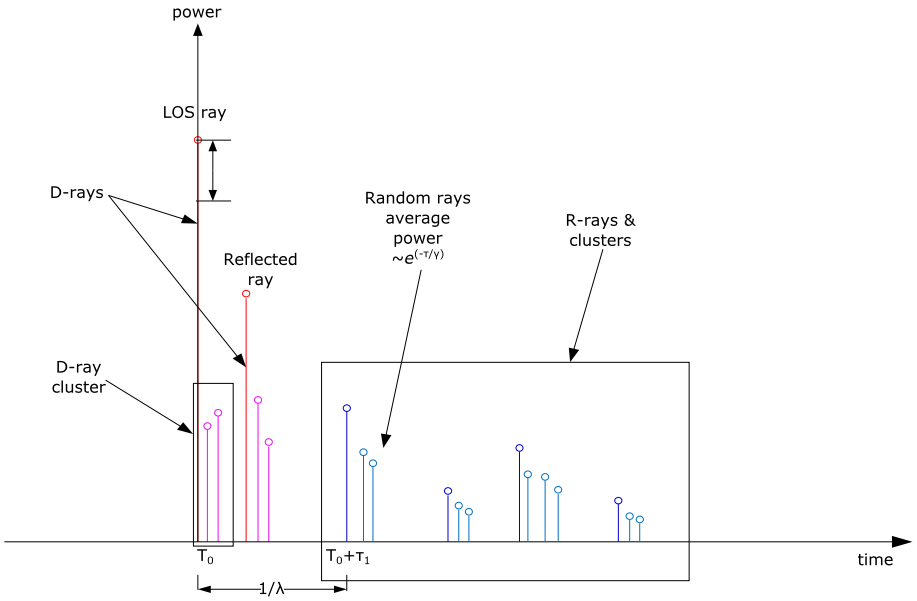

Fig. 8 Q-D channel model channel impulse response structure

For a given environmental scenario, the process of the definition of D-rays and R-rays and their parameters is based both on experimental measurements and ray-tracing reconstruction of the environment. The results presented in Section 2 on experimental measurement may serve as a great example of the process. The experimental measurement processing includes peak detection algorithm [15] with further accumulation of the peak statistics over time, identifying the percentage of the selected ray activity during observation period. The rays with activity percentage above 80–90 % are the D-rays: strong and always present, if not blocked. The blockage percentage for D-rays may be estimated around 2–4 %. The rays with activity percentage about 40–70 % are the R-rays: the reflections from far-away static objects, weaker, and more susceptible to blockage due to longer travel distance. And finally, the rays with activity percentage below 30 % are the F-rays: the flashing reflection from random moving objects. Such rays are not "blocked"; they actually "appear" only for a short time.

Scenarios with obstructed line-of-sight (OLOS) between the transmitter and receiver antennas, caused by moving or fixed objects (e.g., cars, pedestrians, trees), can be integrated in the model with a stochastic process. Scenarios where the LOS is completely blocked by large objects (e.g., buildings) are often referred to as non-line-of-sight (NLOS). These might also be taken into account by the model, by blocking the LOS and ground reflection D-ray permanently and by carefully defining the other D-rays. Measurements have to be performed to derive meaningful parameters for this case. The measurement campaign described in Section 2 focused on LOS and OLOS scenarios and does not provide information on this. Other measurements performed by the authors however show that a millimeter-wave signal can be received in an urban street canyon NLOS scenario, but received signal strength quickly drops with the distance [14].

A clustered structure is added as a final stage for both for Q- and R-rays, introducing the set of exponentially decaying rays after the main ray of the cluster, with the pre-defined K-factor and time of arrival distribution. The resulting channel impulse response can be represented as the sum of clusters corresponding to D-rays (direct ray, ground reflection, etc.), clusters corresponding to R-rays, and clusters corresponding to F-rays: see expression (1). For taking into account the polarization effects, the square channel matrix $\mathbf{H}^i$ is introduced instead of scalar, modeling both polarizations and their dependence.

$$\begin{aligned}\boldsymbol{h}(t,\varphi_{tx},\theta_{tx},\varphi_{rx},\theta_{rx}) &= \sum_i \mathbf{H}^i C^i[t-T^i,\varphi_{tx}-\Phi^i_{tx},\\ &\quad \theta_{tx}-\Theta^i_{tx},\varphi_{rx}-\Phi^i_{rx},\theta_{rx}-\Theta^i_{rx}]\\ C^i(t,\varphi_{tx},\theta_{tx},\varphi_{rx},\theta_{rx}) &= \sum_k \alpha^{i,k}\delta\left(t-\tau^{i,k}\right)\delta\left(\varphi_{tx}-\varphi^{i,k}_{tx}\right)\\ &\quad \times\delta\left(\theta_{tx}-\theta^{i,k}_{tx}\right)\delta\left(\varphi_{rx}-\varphi^{i,k}_{rx}\right)\\ &\quad \times\delta\left(\theta_{rx}-\theta^{i,k}_{rx}\right)\end{aligned} \tag{1}$$

where $\boldsymbol{h}$ is a generated total channel impulse response function and t is current time; φ_{tx}, θ_{tx}, φ_{rx}, θ_{rx} are azimuth and elevation angles at the transmitter and receiver, respectively; $\mathbf{H}^i$ and C^i are the gain matrix and the channel impulse response function for the i-th

cluster, respectively, $\delta()$ is the Dirac delta function; T^i, $\Phi_{tx}{}^i$, $\Theta_{tx}{}^i$, $\Phi_{rx}{}^i$, $\Theta_{rx}{}^i$ are time-angular coordinates of the i-th cluster; $\alpha^{i,k}$ is the amplitude of the k-th ray of the i-th cluster; and $\tau^{i,k}$, $\varphi_{tx}{}^{i,k}$, $\theta_{tx}{}^{i,k}$, $\varphi_{rx}{}^{i,k}$, $\theta_{rx}{}^{i,k}$ are relative time-angular coordinates of the k-th ray of the i-th cluster.

Note that each ray has its own delayτ, angular characteristics, such as AoD (φ_{tx}, θ_{tx}), AoA (φ_{rx}, θ_{rx}), and, finally, the channel matrix **H** that characterizes the polarization, power, and phases of the two polarization components. In this case, the transmission equation for a single-ray channel may be written as:

$$y = G_{tx}(\varphi_{tx}, \theta_{tx}) G_{rx}(\varphi_{rx}, \theta_{rx}) \boldsymbol{e}_{rx}^H \mathbf{H} \boldsymbol{e}_{tx} x \quad (2)$$

where x and y are the transmitted and received signals, $\boldsymbol{e}_{tx}$ and $\boldsymbol{e}_{rx}$ are the polarization (Jones) vectors for the Tx and Rx antennas, respectively, and $G_{tx}(\varphi,\theta)$ and $G_{rx}(\varphi,\theta)$ are antenna gains at given angular coordinates. Generally, the G_{tx} and G_{tx} are different for different polarizations and should be represented as vectors, just like $\boldsymbol{e}_{tx}$ and $\boldsymbol{e}_{rx}$.

4 Q-D channel model development

The analysis of experimental measurements described in Section 2 and the results available from previous experimental campaigns [9, 17] have shown that the Q-D channel model with multiple D-rays may provide appropriate description for the different environments. Based on the Q-D methodology, the millimeter-wave channel model for an open area (open square, university campus, etc.) scenario was developed. Figure 9 illustrates the environment setup with two D-rays (direct ray and ground-reflected ray) with a number of R-rays reflected from random objects in the area. But, as shown in Section 2, the open square scenario may have a few additional strong rays, stemming from different objects, such as metalized bus stop windows and surrounding buildings. To have a more accurate scenario description, these strongest reflections can be taken into account explicitly as additional D-rays, but weaker paths should be included in a statistical manner, as R-rays.

4.1 D-ray modeling

The Q-D rays are explicitly calculated in accordance with scenario parameters, geometry, and propagation conditions. The propagation loss is calculated by the Friis equation, taking additional losses from the oxygen absorption into account (Table 1, second row). An important part of the proposed Q-D approach to the channel modeling is the calculation of the reflected ray parameters. The calculations are based on the Fresnel equations, with additionally taken into account losses due to surface roughness (Table 2, second row)

The feasibility of the proposed approach to the prediction of the signal power is proven in [18] for outdoor micro-cell environments and in [19] and [20] for inter-vehicle communication modeling. In general, problems of the signal power prediction are considered in [21].

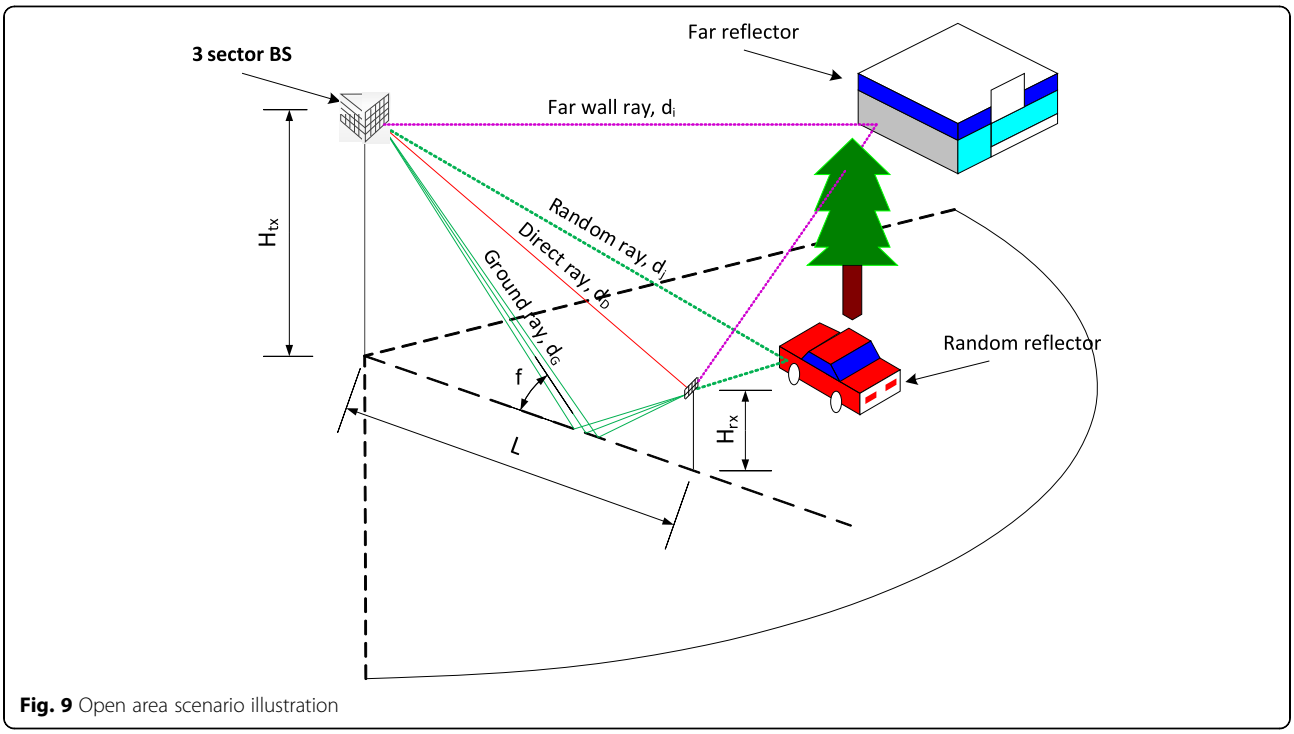

Fig. 9 Open area scenario illustration

Table 1 Direct ray parameters

Parameter	Value
Delay	Direct ray delay is calculated from the model geometry: $\tau_D = d_D/c$ $d_D = \sqrt{L^2 + (H_{tx} - H_{rx})^2}$
Power	Direct ray power calculated as free-space path loss with oxygen absorption: $P_D = 20\log_{10}\left(\frac{\lambda}{4\pi d_D}\right) - A_0 d_D$, in dB
Channel matrix	$\mathbf{H} = \begin{bmatrix} 10^{P_D/20} & 0 \\ 0 & 10^{P_D/20} \end{bmatrix} e^{\frac{j2\pi d_D}{\lambda}}$
AoD	0° azimuth and elevation
AoA	0° azimuth and elevation

AoD angle of departure, *AoA* angle of arrival

The D-rays are strictly scenario dependent, but in all considered scenarios, two basic D-rays are present: the direct LOS ray and the ground-reflected ray. The calculation of those two basic rays' parameters will be the same for all scenarios.

4.1.1 Direct ray

The direct LOS ray is a ray between Tx and Rx.

4.1.2 Ground ray

The ground-reflected ray presents in all considered scenarios. Its parameters are calculated based on the Friis free-space path loss equation and the Fresnel equation to take into account reflection and rough surface scattering factor F. Note that the horizontally and vertically polarized components of the transmitted signal will be differently reflected and, thus, the channel matrix should have different diagonal elements.

Table 2 Ground-reflected ray parameters

Parameter	Value
Delay	Ground-reflected ray delay is calculated from the model geometry: $\tau_G = d_G/c$ $d_G = \sqrt{L^2 + (H_{tx} + H_{rx})^2}$
Power	Ground-reflected power calculated as free-space path loss with oxygen absorption, with additional reflection loss calculated on the base of the Fresnel equations. Reflection loss R is different for vertical and horizontal polarizations $P_\perp = 20\log_{10}\left(\frac{\lambda}{4\pi d_G}\right) - A_0 d_G + R_\perp + F$; $P_\parallel = 20\log_{10}\left(\frac{\lambda}{4\pi d_G}\right) - A_0 d_G + R_\parallel + F$ $F = {}^{80}\Big/ \ln 10(\pi\sigma_h \sin\phi/\lambda)^2$ $R_\perp = 20\log_{10}\left(\frac{\sin\phi - \sqrt{B_\perp}}{\sin\phi + \sqrt{B_\perp}}\right)$; $R_\parallel = 20\log_{10}\left(\frac{\sin\phi - \sqrt{B_\parallel}}{\sin\phi + \sqrt{B_\parallel}}\right)$ $B_\parallel = \varepsilon_r - \cos^2\phi$ for horizontal polarization. $B_\perp = (\varepsilon_r - \cos^2\phi)/\varepsilon_r^2$ for vertical polarization, where $\tan\phi = \frac{H_{tx}+H_{rx}}{L}$ and σ_h is a surface roughness.
Channel matrix	$\mathbf{H} = \begin{bmatrix} 10^{P_\perp/20} & \xi \\ \xi & 10^{P_\parallel/20} \end{bmatrix} e^{\frac{j2\pi d_G}{\lambda}}$
AoD	Azimuth: 0°, elevation: $\theta_{AoD} = \tan^{-1}\left(\frac{L}{H_{tx}-H_{rx}}\right) - \tan^{-1}\left(\frac{L}{H_{tx}+H_{rx}}\right)$
AoA	Azimuth: 0°, elevation: $\theta_{AoA} = \tan^{-1}\left(\frac{H_{tx}+H_{rx}}{L}\right) - \tan^{-1}\left(\frac{H_{tx}-H_{rx}}{L}\right)$

AoD angle of departure, *AoA* angle of arrival

4.1.3 Additional rays

For the open area scenario, with no significant reflection objects other than ground, only two D-rays are considered. However, in more rich scenarios, like the one considered here as the large square, or, for example, street canyon scenario, reflection from one or more walls should be taken into account. The principle of calculation of these additional D-rays is the same; detailed description may be found in [15]. The closest wall can be calculated using the geometry and positions of the transmitter and receiver. The calculation of the path properties is equal to the ground ray reflection in the previous section with adapted material parameters.

4.2 R-ray modeling

For taking into account a number of rays that cannot be easily described deterministically (reflections from objects that are not fully specified in the scenario, objects with random or unknown placement, objects with complex geometry, higher-order reflections, etc.), the statistical approach is used in the Q-D channel modeling methodology. The clusters arrive at moments τ_k according to the Poisson process and have inter-arrival times that are exponentially distributed. The cluster amplitudes $A(\tau_k)$ are independent Rayleigh random variables, and the corresponding phase angles θ_k are independent uniform random variables over $[0,2\pi]$.

The R-ray components of the channel impulse response are given by:

$$h_{cluster}(t) = \sum_{k=1}^{N_{cluster}} A(\tau_k) e^{j\theta_k} \delta(t - \tau_k), \tag{3}$$

where τ_k is the arrival time of the k-th cluster measured from the arrival time of the LOS ray and $A(\tau_k)$, $P(\tau_k)$, and θ_k are the amplitude, power, and phase of the k-th cluster, respectively. The R-rays are random, with Rayleigh-distributed amplitudes and random phases, with exponentially decaying power delay profile. The total power is determined by the K-factor with respect to the direct LOS path.

$$P(\bar{\tau}_k) = P_0 e^{-\tau_k/\gamma} \tag{4}$$

$$\frac{P_{LOS}}{\sum P(\tau_k)} = K \tag{5}$$

Table 3 summarizes the R-ray parameters for the open area/large square models. The power delay profile parameters are derived based on the available experimental data and corresponding ray-tracing simulations. The

Table 3 Open square model R-ray parameters

Parameter	Value
Number of rays, N	3
Poisson arrival rate, λ	0.05 ns^{-1}
Power decay constant, γ	15 ns
K-factor	6 dB
AoA	Elevation: U[−20:20°]
	Azimuth: U[−180:180°]
AoD	Elevation: U[−20:20°]
	Azimuth: U[−180:180°]

AoD angle of departure, *AoA* angle of arrival

AoA and AoD ranges illustrate the fact that random reflectors can be found anywhere around the receiver but are limited in height. Uniform distributions are selected for simplicity and can be further enhanced on the base of more extensive measurements.

In the 802.11ad channel model [6], the set of approximations was proposed for diagonal and off-diagonal elements of the channel matrix **H** for the first- and second-order reflections in typical indoor environments (conference room, cubicle, and living room) as a combination of log-normal and uniform distributions on the base of experimental studies [22]. In the Q-D model, the ray amplitude is approximated by the Rayleigh distribution (which is close to log-normal) so that the simple fixed polarization matrix $\mathbf{H}_{\mathrm{p}}$ may be used for introducing polarization properties to the R-rays (matrix **H** is obtained by multiplication of the scalar amplitudes A to the polarization matrix $\mathbf{H}_{\mathrm{p}}$). The polarization matrix $\mathbf{H}_{\mathrm{p}}$ for R-rays is defined by:

$$\mathbf{H}_{p} = \begin{bmatrix} 1 & \pm 0.1 \\ 0.1 & \pm 1 \end{bmatrix} \tag{6}$$

The values with sign ± are assumed to have a random sign (+1 or −1, for instance), with equal probability, independently from other values. For the cluster rays with the main R-ray, the polarization matrix is the same as the R-ray.

Flashing rays, or F-rays introduced in Section 3, are intended to describe the reflections from fast moving objects like vehicles and are short in duration. Its properties require additional investigations and analyses; thus, the F-rays are not included in the considered Q-D modeling approach application example.

4.3 Intra-cluster structure modeling

The surface roughness and presence of the various irregular objects on the considered reflecting surfaces and inside them (bricks, windows, borders, manholes, advertisement boards on the walls, etc.) lead to separation the specular reflection ray to a number of additional rays with close delays and angles: a cluster. The intra-cluster parameters of the channel model were extracted from the indoor models [6, 7], obtained from the measurement data [23]. The intra-cluster structure is introduced in the Q-D model in the same way as R-rays: as Poisson-distributed in time, exponentially decaying Rayleigh components, dependent on the main ray.

The identification of rays inside of the cluster in the angular domain requires very high angular resolution. The "virtual antenna array" technique where a low directional antenna element is used to perform measurements in multiple positions along the virtual antenna array to form an effective antenna aperture was in the MEDIAN project [24, 25]. These results were processed in [26], deriving the recommendation to model the intra-cluster angle spread for azimuth and elevation angles for both the transmitter and receiver as independent normally distributed random variables with zero mean and root mean square (RMS) equal to 5°, $N(0, 5°)$.

Note that it is reasonable to assume that different types of clusters may have distinctive intra-cluster structure. For example, properties of the clusters reflected from the road surface are different from the properties of the clusters reflected from brick walls because of the different material surface structures. Also, one may assume the properties of the first- and second-order reflected clusters to be different, with the second-order reflected clusters having larger spreads in temporal and angular domains. All these effects are understood to be reasonable. However, since the number of available experimental results was limited, a common intra-cluster model for all types of clusters was developed. Modifications with different intra-cluster models for different types of clusters may be a subject of the future channel model enhancements. The parameters are summarized in Table 4.

5 Link level-focused channel model

The link level-focused propagation channel model presented in this section is a multipath propagation

Table 4 Open square model intra-cluster parameters

Parameter	Value
Intra-cluster ray K-factor	6 dB for LOS ray, 4 dB for NLOS
Power decay time	4.5 ns
Arrival rate	0.31 ns^{-1}
Amplitude distribution	Rayleigh
Number of post-cursor rays	4

LOS line-of-sight, *NLOS* non-line-of-sight

model dedicated to link level simulations. The Q-D model as well as experimental multipath channel impulse response files may be used as inputs of the model for link level assessments generating appropriate channel impulse responses (CIRs) fit with the simulated physical (PHY) layer and the considered propagation scenario. The link level-focused propagation channel model, also denoted CEPD model, is a multipath propagation model which conjunctly exploits multi-rate digital filter processing [27] and experimental multipath measurements to generate propagation CIRs $h(t, \tau)$ with scalable limited bandwidth and clocking rates. When simulating propagation, resampling is required in accordance with the simulated PHY layer. The model generates link level propagation CIRs using multi-rate filter processing to resample and filter the measured propagation channel, adapted to the PHY waveform of the system and simulated use cases [28]. Antenna alignment mismatch test cases allow quantized link level degradation assessments, when the antennas are not aligned. Analytical models are derived from an extension of the multi-slope model [29], describing antenna alignment mismatching effect on multipath channel, using dedicated measurements and CEPD realizations.

Multi-rate filter processing performs a 2×1D conversion rate geared to relative delay τ and time t in order to simulate the multipath propagation channel within the PHY bandwidth of the simulated system at the targeted system sampling rate and appropriate refreshment rate of the CIRs depending on environment topologies and time variations. The complex envelope of the time variant CIR of the propagation channel, $h(t, \tau)$, is described by two independent variables, typically the relative delay τ and the time t as expressed below:

$$\begin{aligned} h(t,\tau) &= \sum_{k=1}^{N_t} a_k(t)\cdot\delta(\tau-\tau_k(t)) \rightarrow h(n,k) \\ &= \sum_{k=1}^{N_t} a_k(n)\cdot\delta(\tau-k/Fsig) \end{aligned} \tag{7}$$

$a_k(t)$ is the time variant amplitude of the relative delay $\tau_k(t)$. Time variant amplitudes $a_k(t)$ are assigned to echoes equally sampled depending on the propagation channel bandwidth size and transmitter and receiver antenna characteristics. In (8), n and k integers refer to relative delay and time sampling processing, respectively, with a sampling rate fixed to F_{sig}. The model dynamically adapts the sampling rate of measurements to the simulated PHY layer system with a 2×1D filtering optimization considering successive conversion rates in relative delay τ and time variation t domains, respectively.

The conversion rate R_c by a non-integer factor, when passing from sampling rate F_1 to F_2, may be achieved by approximating R_c as the ratio of two integers L and M (8) and use expansion and decimation operations combined with filter processing to remove $L-1$ duplicate forms of the interpolated signal and design low-band filter for decimation with a factor M:

$$R_c = \frac{F_1}{F_2} \approx \frac{L}{M} \tag{8}$$

The CEPD model performs an optimization of multi-rate filter design to limit side lobes and preserve delay resolution during the conversion rate (CR) filter

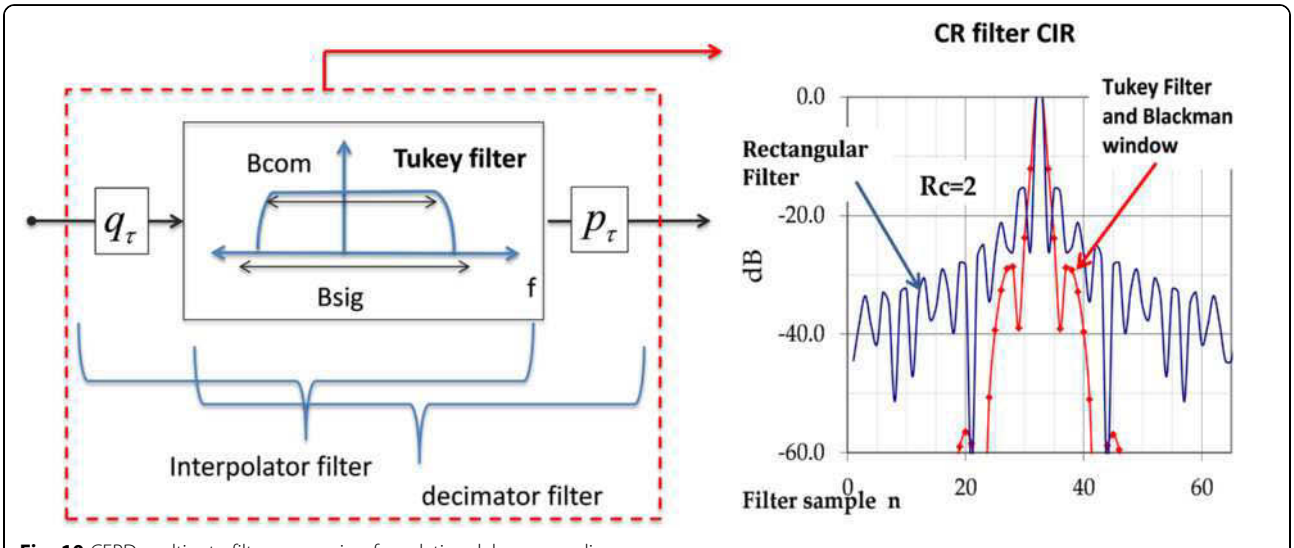

Fig. 10 CEPD multi-rate filter processing for relative delay resampling

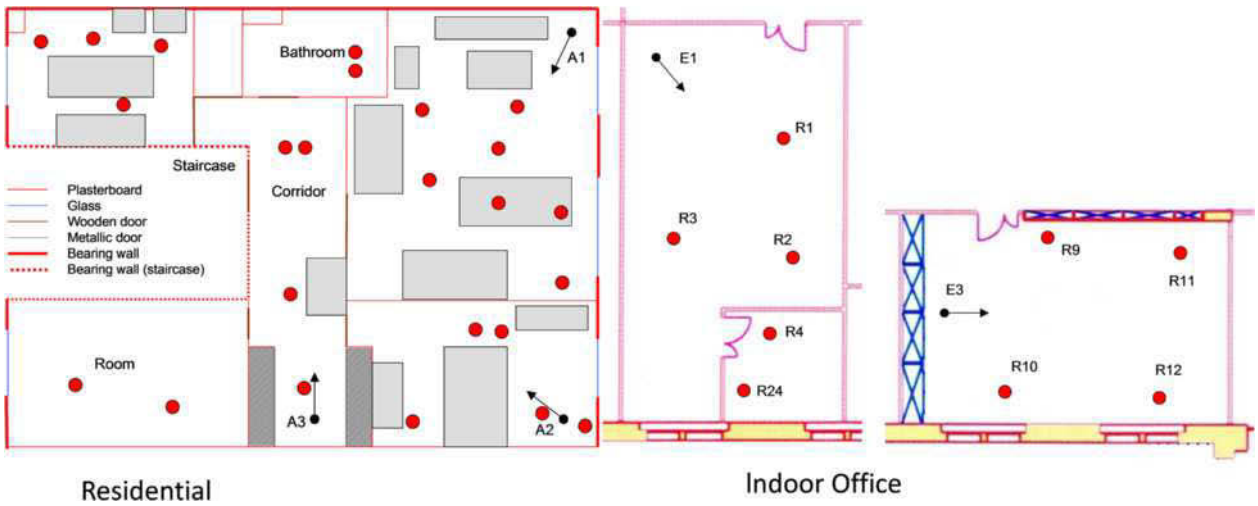

Fig. 11 Indoor measurement environment

processing in the relative delay domain. Simple linear interpolation is done in the time domain t to update the coefficients of the model. Assuming the PHY layer sampling rate is set to F_{sig} and the propagation measurement sampling rate fixed to F_{init}, the relative delay τ conversion rate is then expressed as a ratio of two integers, p and q, combining a q-interpolator filter followed with p-decimator filter to generate the link level-focused propagation channel model. Filter processing is merged in a single filter design resulting from a Tukey filter setup in the frequency domain combined with a time-limited windowing process using a Blackman window. The conversion rate processing and resulting CR impulse response of the interpolator decimator filter are represented in Fig. 10, showing that the combination of filtering and windowing significantly reduces side lobes involved by filtering. Results are compared to a rectangular filter combined with a rectangular delay windowing.

The link level-focused propagation model is fed with dedicated CIR measurements carried out in larger bandwidths than the system bandwidth, involving filtering and lower sampling rate processing to generate the adequate CIR model. This model can be adapted to outdoor millimeter-wave overlay networks as well as to indoor deployments. Input files of the model issued from measurements provide the appropriate coefficients of the model attached to the simulated scenario. The candidate input files of the CEPD model result from a statistical analysis of a large amount of deterministic measurements, performed in each considered scenario. These scenarios are split into *typical* and *atypical* test cases including different levels of multipath dispersion. A typical test case in a deployment scenario results from CIR input files describing the average and median multipath dispersion of multipath selectivity parameters as the delay spread, the coherence bandwidth, the delay window set to 75 %, and the interval delay set to 6 dB, while atypical cases are representative of severe situations corresponding to 90 % of cumulative distribution function (CDF) of those selectivity parameters.

Assuming the first-order statistics of selectivity parameters follow a Gaussian distribution, the typical and atypical input files of the model are deduced from the CDFs of first-order statistic values of those parameters evaluated on N moving experimental points composed each of M

Table 5 CEPD indoor deployment scenario

Scenario	Antenna gain (dBi), Tx-Rx	Link	Deployment scenario	
CM1	8–13	LOS	Antenna alignment	Residential typical home with multiple rooms. The size is comparable to the small office room.
CM2	8–13	NLOS/OLOS	No antenna alignment	
CM'1	8–24.6	LOS	Antenna mismatch alignment	
CM'2	8–24.6	OLOS		
CM3	8–13	LOS	Office antenna alignment	Office with typical office setup furnished with multiple chairs, desks, computers, and workstations
CM4	8–13	NLOS/OLOS	No antenna alignment	

LOS line-of-sight, *NLOS* non-line-of-sight

Table 6 CEPD, selectivity parameters

	CM1	CM2	CM'1	CM'2	CM3	CM4
σ_{DS} (ns)	2.36	6.94	9.41	9.41	6.37	7.11
$Bc_{-0.5}$ (MHz)	114	62.93	88.68	88.68	59.8	59.8

static experimental measurement along a transmitter-receiver path. The CDFs of each selectivity parameter average are established for all measurement points and positions. The selected measurement point is selected if the average value of the concerned selectivity parameter is in the range of interval I given by the Gaussian distribution.

The CDF is expressed as follows:

$$\begin{aligned} &\text{Prob}\left\{\frac{|mi,j-Xj|}{\sigma_j} < \alpha\right\} = \beta,\ \alpha = [10\%-15\%], \\ &I_j = \left\{Xj-\alpha\cdot\sigma_j, Xj+\alpha\cdot\sigma_j\right\} \end{aligned} \tag{9}$$

In eq. (9), $m_{i,j}$ is the average value of the selectivity parameter j (RMS delay spread, coherence bandwidth, etc.) of the measurement point i among N. X_j and s_j are the average and standard deviation, respectively, of the average selectivity parameter j evaluated on N points. The selected measurement point, i.e., the CIRs input file of the model, has the first order of selectivity parameter j, $m_{i,j}$, ranged in the I_j interval. The procedure is iterated for all selectivity parameters indexed by integer j in (9), leading to a selection of a restricted number of measurement points.

This section focuses on indoor multi-cluster modeling using indoor measurements carried out in a house (residential), with a single floor with a maximum transmitter (Tx) to receiver (Rx) distance of 12 m, and in an office environment composed of several furnished desk rooms along a corridor of 20 m.

NLOS corresponds to a transmitter and receiver not located in the same room. Transmissions are then performed by reflections on obstacles without alignment of transmitter and receiver antennas. OLOS refers to the transmitter and receiver located in the same room with partial obstructions. A map of measurements is given in Fig. 11, where several transmitter antenna positions are represented with black dots and measurement points with red dots in both residential and indoor office environments.

The channel sounding technique is based on a frequency sweep mode with a total bandwidth set to 1024 MHz using a VNA "AB millimètre 8-350" [30]. The VNA equipment presents a dynamic range of 40 dB, and the channel is sampled at a rate of 0.1 Hz. The channel transfer functions (CTFs) of the propagation channel have been measured in a frequency sweep mode with a total frequency bandwidth of 1024 MHz and a frequency sweeping step fixed to 4 MHz, leading to an excess relative delay $\tau_{\max}$ of 250 ns. For each Tx-Rx configuration, the measured CTF was calibrated using a reference measurement in which the Tx and Rx ports of the sounder were directly cable connected. The corresponding CIRs have been obtained using an inverse Fourier transform combined with a Hanning window in order to reduce the level of secondary lobes in the relative delay domain due to the limited analyzed bandwidth.

Table 5 summarizes the propagation scenarios associated to measurements and antenna characteristics. At the transmitter side, a vertically polarized horn antenna

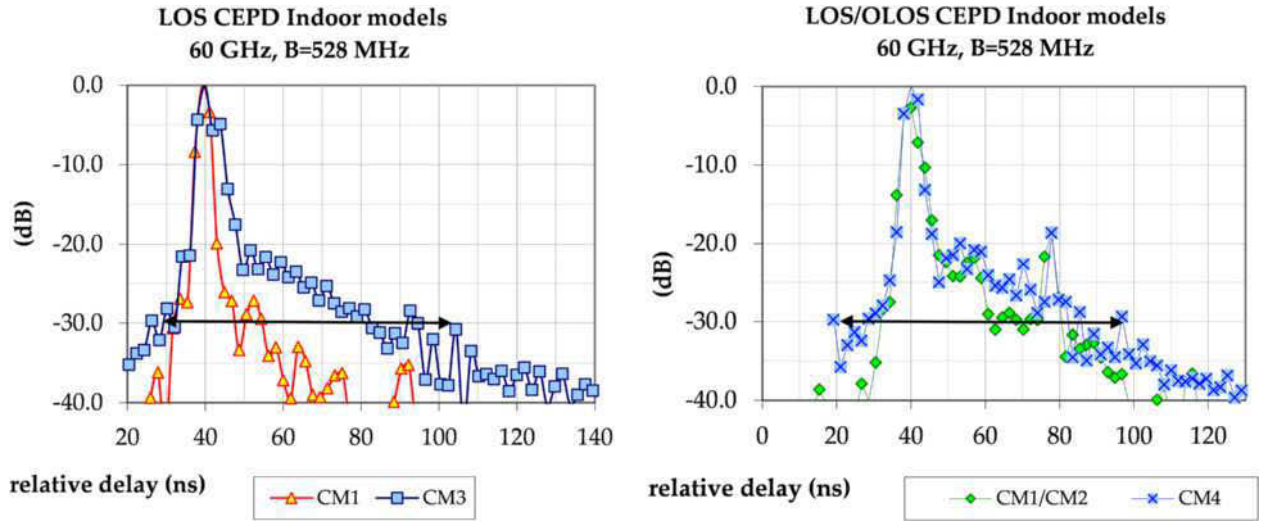

Fig. 12 Average power delay profiles of CEPD indoor models

with a 72° azimuth plane beam width and a gain of 8 dBi was used. At the Rx positions, a vertically polarized narrow beam horn antenna (10° azimuth plane beam width, 24.6-dBi gain) and a vertically polarized sectoral horn antenna (60° azimuth plane pattern beam width, 13-dBi gain) were used in order to analyze antenna radiation pattern effects on multipath propagation characteristics. LOS and NLOS are discriminated. In Table 5, CM1 and CM2 scenarios refer to LOS and NLOS, respectively, in a residential environment with a correct antenna alignment between the transmitter and receiver sides. CM'1 and CM'2 are related to antenna alignment mismatch ranging from 2° to 35° with respect with antennas in alignment (LOS direction, 0°) in the same environment. CM3 and CM4 are complementary scenarios resulting from measurements carried out in an office environment in LOS and NLOS situations, respectively. No antenna alignment mismatch is considered in this scenario.

Selectivity parameters (RMS delay spread σ_{DS} and coherence bandwidth $Bc_{-0.5}$) given in eq. (10) of CEPD model realizations are detailed in Table 6. The RMS delay spread σ_{DS} is the average standard deviation of multipath echoes weighted by the power probability γ_I of each relative delay i. The coherence bandwidth $Bc_{-0.5}$ is the frequency spacing for positive frequency components, providing a 1/2 factor decrease of the normalized average correlation function $|RH(\Delta f)|$ magnitude of the channel with respect to no frequency deviation ($\Delta f = 0$). In other words, the correlation coefficient adjusted to 1/2 and $Bc_{-0.5}$ represents the associated half-bandwidth size as expressed below:

$$
\begin{aligned}
\gamma_i &= E\left\{\frac{|h(t,\tau_i(t)|^2}{P(t)}\right\},\\
P(t) &= \sum_{i=1}^{N}|h(t,\tau_i)|^2, \sigma_{DS}\\
&= E\left\{\sqrt{\frac{\sum_{i=1}^{n}\tau_i^2|h(t,\tau_i(t))|^2}{P(t)} - \left(\frac{\sum_{i=1}^{n}\tau_i|h(t,\tau_i(t))|^2}{P(t)}\right)^2}\right\}\\
RH(\Delta f) &= E\left\{FFT_\tau\left\{\sum_{i=1}^{n}|h(t,\tau_i(t))|\right)^2\right\}(\Delta f)\right\},\\
Bc{-}0.5 &= \Delta f' \Rightarrow RH(\Delta f') = \frac{1}{2}|RH(\Delta f = 0)|, \Delta f > 0
\end{aligned}
\tag{10}
$$

The average power delay profiles of indoor models related to indoor deployment scenarios (Table 5) are illustrated in Fig. 12.

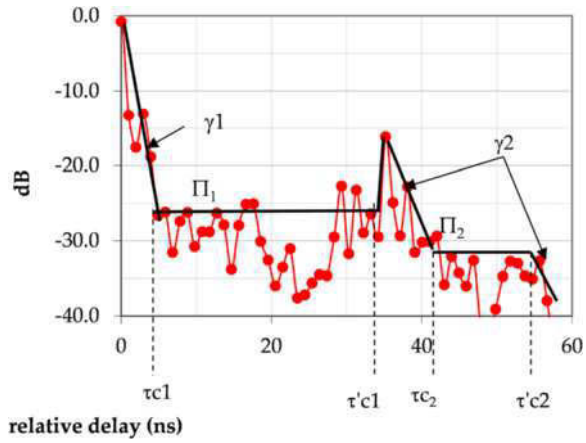

Fig. 13 Average power delay profile of the CEPD model with an antenna alignment mismatch model, typical case, CM'1

CEPD antenna alignment mismatch models are derived from dedicated measurements followed by a CEPD selection procedure and multi-rate filter processing. Additionally, analytical models are designed that are derived from the multi-slope model [29] with an extension to a multi-cluster approach. The proposed model extends the concept to two clusters for each APDP deduced from CEPD realizations, encompassing two slope decays for each intra-cluster (γ_1,γ_2), two intra-cluster arrival time Poisson parameters (λ_1,λ_2), two interval delays ($\Delta\tau I$, $i = \{1,2\}$), and two constant multipath levels ($\Pi i(\Delta\tau i)$, $i = \{1,2\}$) as illustrated in Figs. 13 and 14. The coefficients of the model given in Table 7 are deduced from CEPD realizations with a bandwidth of 528 MHz.

These analytical models derived from the CEPD realizations are an extension of the multi-slope model used to quantify antenna alignment mismatch. These models

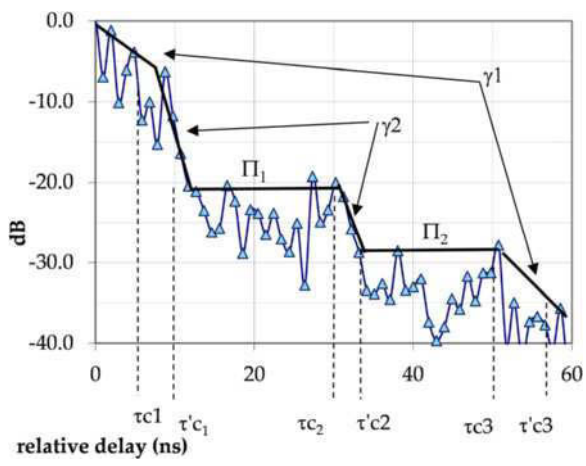

Fig. 14 Average power delay profile of the CEPD antenna alignment mismatch model, atypical case, CM'2

Table 7 CEPD antenna alignment model coefficients

	OLOS Typical	OLOS Atypical	Delay	OLOS Typical	OLOS Atypical
$\Gamma 1$ (dB)	−25	−20.5	$\tau c1$	0.98	8.79
$\Gamma 2$ (dB)	−32.7	−28.8	$\tau' c1$	35.19	11.71
γ_2 (dB/ns)	1.81	4.86	$\tau c2$	43.97	30.27
λ_2 (1/ns)	0.42	1.12	$\tau' c2$	55.69	33.2
γ_1 (dB/ns)	4.45	0.72	$\tau c3$		50.78
$\lambda 1$(1/ns)	1.02	0.17	$\tau' c3$		58.59
d (Tx-Rx)	5.84	7.35			

OLOS obstructed line-of-sight

and associated CEPD realizations may be used to evaluate involved degradations on link level performance and highlight benefits of fast-tracking beam-forming in time variant environments [31].

6 Conclusions

A Q-D channel model and a link level-focused model were introduced. The two models follow different approaches. While the Q-D model gives a full understanding of the spatial channel, it also requires a precise description of the scenario. This spatial resolution, as well as the spatial consistency of the model for moving users, is of key importance for link level design. With the expected shift towards steerable antennas with medium or high gain, the antenna pattern has a much higher influence on the effective channel between the transmitter and receiver. Aspects like initial discovery of millimeter-wave base stations and beacon design also heavily depend on the spatial information.

The flexibility of this Q-D approach allows channel models for access links to be used for scenarios with similar geometries. For example, the "street canyon access mode" can be changed to the "street-level backhaul model" by changing the receiver antenna parameters. These models were validated with different measurements in outdoor scenarios. The Q-D open area channel model was successfully applied to millimeter-wave multi-user MIMO (MU MIMO) small cell access link scenario evaluations [32–34]. Future work remains on some aspects of the model, like the modeling of the flashing rays (F-rays) and NLOS scenarios, where further measurement campaigns are necessary.

The CEPD model results from an optimized multi-rate filtering combined with a statistical analysis of measurements. It allows an extraction of typical (average behavior of the multipath channel related to a measurement campaign) and atypical (severe cases representative of measurement campaign) measurements that are used as inputs of the model to generate model coefficients associated to the targeted scenario. The model is dedicated to link level simulations with multiple underlying technologies and bandwidths. Scenarios covered in the paper consider antenna alignment mismatch where CEPD realizations have been exploited to generate analytical multi-cluster models derived from the multi-slope concept. The CEPD model can also use the Q-D model as an input to the interface with link level simulations. When the link level is not the focus of research, this is a convenient method of abstraction in order to reduce the complexity for larger scale simulations, for example, with multiple users and multiple base stations.

Competing interests

The authors declare that they have no competing interests.

Acknowledgements

The results presented are from the European part of MiWEBA which is a STREP-funded project by the European Union under grant agreement no. 608637 as part of FP7 ICT-2013-EU-Japan [11]. This work was funded with the support from the EU FP7 program, and the results are also publicly available on the project website http://www.miweba.eu.
Furthermore, the authors would like to acknowledge the support of their colleagues, MiWEBA project partners, and the COST IC1004 for their support and fruitful discussions.

Author details

[1]Fraunhofer Heinrich-Hertz-Institute, Berlin, Germany. [2]Platform Engineering Group, Intel Corporation, Santa Clara, USA. [3]University of Nizhny Novgorod, Nizhny Novgorod, Russia. [4]Orange Labs Cesson, Cesson Sevigne, France.

Received: 31 July 2015 Accepted: 24 February 2016
Published online: 15 March 2016

References

1. F Boccardi, RW Heath, A Lozano, TL Marzetta, P Popovski, Five disruptive technology directions for 5G. IEEE Communications Magazine **52**(2), 74–80 (2014)
2. ETSI Group Specification mWT 002, "*Millimetre wave transmission (mWT); applications and use cases of millimetre wave transmission*," V1.1.1 (2015–08), 2015.
3. TS Rappaport, S Sun, R Mayzus, H Zhao, Y Azar, K Wang, GN Wong, JK Schulz, M Samimi, F Gutierrez, Millimeter wave mobile communications for 5G cellular: it will work! IEEE Access **1**, 335–349 (2013)
4. M. Coldrey (ed.) "Maturity and field proven experience of millimetre wave transmission," ETSI White Paper No. 10, First edition—September 2015, ISBN 9791092620078, 2015
5. P. Kyösti, J. Meinilä, L. Hentilä, X. Zhao, T. Jämsä, C. Schneider, M. Narandzić, M. Milojević, A. Hong, J. Ylitalo, V.-M. Holappa, M. Alatossava, R. Bultitude, Y. de Jong, T. Rautiainen, "WINNER II channel models", tech. rep. D1.1.2 V1.2, IST-4-027756 WINNER II, 2007
6. "Channel models for 60 GHz WLAN systems," IEEE document 802.11–09/0334r8
7. A Maltsev, AR Maslennikov, AK Sevastyanov, A Lomayev, Experimental investigation of 60 GHz wireless systems in office environment. IEEE JSAC **27**(8), 1488–1499 (2009)
8. A Maltsev, A Pudeyev, I Karls, I Bolotin, G Morozov, RJ Weiler, M Peter, W Keusgen, *Quasi-deterministic approach to mm-wave channel modeling in a non-stationary environment* (IEEE GLOBECOM, Austin, 2014)
9. A. Maltsev, A. Pudeyev, I. Karls, I. Bolotin, G. Morozov, R.J. Weiler, M. Peter, W. Keusgen, M. Danchenko, A. Kuznetsov, "*Quasi-deterministic approach to Mm-wave channel modeling in the FP7 MiWEBA project," WWRF' 33* (Wireless World Research Forum (WWRF), Guildford, GB, 2014)
10. I. Siaud, A.-M. Ulmer-Moll, A. Capone, A. Filippini, A. De Domenico, E. Calvanese-Strinati, R. Weiler, K. Sakaguchi, "Definition of Scenarios and Use Cases", tech. rep. D1.1, v1.0, FP7-ICT-608637 MiWEBA, 2013
11. "MiWEBA project homepage http://www.miweba.eu (FP7-ICT-2013-EU-Japan, project number: 608637)," 2015
12. M. Peter, W. Keusgen and R.J. Weiler, "*On path loss measurement and modeling for millimeter-wave 5G," in EuCAP* 2015.

13. R. J. Weiler, M. Peter, W. Keusgen and M. Wisotzki, *"Measuring the busy urban 60 GHz outdoor access radio channel," in ICUWB*, 2014
14. R.J. Weiler, M. Peter, T. Kühne, M. Wisotzki, W. Keusgen, "*Simultaneous millimeter-wave multi-band channel sounding in an urban access scenario," in EUCAP*, 2015
15. ICT FP7 MiWEBA project #608637, 'Deliverable D5.1, channel modeling and characterization', Public deliverable, Intel editor, June 2014.
16. RJ Weiler, M Peter, W Keusgen, A Kortke, M Wisotzki, *Millimeter-wave channel sounding of outdoor ground reflections* (IEEE Radio and Wireless Symposium (RWS), San Diego, 2015)
17. R. J. Weiler, M. Peter, W. Keusgen, H. Shimodaira, K. T. Gia and K. Sakaguchi, *"Outdoor millimeter-wave access for heterogeneous networks—path loss and system performance," in PIMRC*, 2014
18. A Hammoudeh, M Sanchez, E Grindrod, Modelling of propagation in outdoor microcells at 62.4GHz. Microwave Conference **1**, 119–123 (1997)
19. K Sarabandi, E Li, A Nashashibi, Modeling and measurements of scattering from road surfaces at millimeter-wave frequencies. IEEE Transactions on Antennas and Propagation **45**(11), 1679–1688 (1997)
20. A Yamamoto, K Ogawa, T Horimatsu, A Kato, M Fujise, Path-loss prediction models for intervehicle communication at 60 GHz. IEEE Transactions on vehicular technology **57**, 1 (2008)
21. ITU Report 1008–1, *Reflection from the surface of the Ear*th
22. A Maltsev, E Perahia, R Maslennikov, A Sevastyanov, A Lomayev, A Khoryaev, Impact of polarization characteristics on 60-GHz indoor radio communication systems. IEEE Antennas And Wireless Propagation Letters **9**, 413 (2010)
23. Sawada H., "Intra-cluster response model and parameter for channel modeling at 60 GHz (Part 3)", IEEE doc. 802.11-10/0112r1, January 2010.
24. IMST 60 GHz indoor radio channel measurement data, ACTS MEDIAN project technical report.
25. K Sato, T Manabe, T Ihara, H Saito, S Ito, T Tanaka, K Sugai, N Ohmi, Y Murakami, M Shibayama, Y Konishi, T Kimura, Measurements of reflection and transmission characteristics of interior structures of office building in the 60-GHz band. Antennas and Propagation, IEEE Transactions on **45**(12), 1783–1792 (1997)
26. Davydov A., Maltsev A., Sadri A., "Saleh-Valenzuela channel model parameters for library environment," IEEE document 802.15-06-0302-02-003c, July 2006
27. R. E. Crochiere, L.R. Rabiner, *Multi-rate digital signal processing*, (Prentice-Hall, New Jersey, 1983), ISBN 0136051626
28. I. Siaud, A.M. Ulmer-Moll, N. Malhouroux-Gaffet, V. Guillet, *Short-range wireless communications, an introduction to 60 GHz communication systems: regulation and services, channel propagation and advanced baseband algorithms, Chapter 18*, ed. Rolf Kraemer and Marcos D. Katz (The Atrium, Southern Gate, Chichester, West Sussex, PO19 8SQ, United Kingdom, John Wiley & Sons Ed. 2009). ISBN: 978-0-470-69995-9
29. H. Yang, F.M. Smulders & Matti H.A.J, Herben, Channel characteristics and transmission performance for various channel configurations at 60 GHz. Eur. J. Wireless Commun. Netw.", **2007**(1), 43-43 (2007), Hindawi Publishing Corp. New York, NY, United States, DOI10.1155/2007/19613.
30. P Goy, S Caroopen, M Gross, *Vector measurements at millimeter and submillimeter wavelengths: feasibility and applications* (ESA Workshop on Millimeter Wave Technology and Applications, Espoo, 1998)
31. I Siaud, AM Ulmer-Moll, N Cassiau, MA Bouzigues, *Adaptive and spatial processing for millimeter wave backhaul architectures* (International Conference ICUWB', Montreal, 2015)
32. A. Maltsev, A. Sadri, A. Pudeyev, R. Nicholls, R. Arefi, A. Davydov, I. Bolotin, G. Morozov, K. Sakaguchi and T. Haustein, "MmWave small cells is a key technology for future 5G wireless communication systems," in European Conference on Networks and Communications, 2014
33. A. Maltsev, A. Sadri, A. Pudeyev, A. Davydov, I. Bolotin, G. Morozov, "Performance evaluation of the MmWave small cells communication system in MU-MIMO mode", EuCNC'2015.
34. ICT FP7 MiWEBA project 608637, 'Deliverable D4.1, system level simulator specification', Public deliverable, http://www.miweba.eu/wp-content/uploads/2014/07/MiWEBA_D4-1_v10.pdf

4.6 Dynamic shadow fading

The components of the quasi-deterministic model can individually be adapted with a stochastic process. This section reports results for dynamic shadow fading (blockage) measurements in an urban environment that can be used to parameterize these processes [WPK+16a]. The shadowing is caused by busses, cars, cyclists and pedestrians on the busy street. Statistical properties are derived for different receiver positions. Individual multipath components, such as the line-of-sight component, can be clearly identified in the delay domain and their properties can be individually identified.

The scenario of the measurement was set up as a small cell access scenario. The transmitter was placed at 3.5 m and 5 m above ground on one side of a 6 lane street, cutting through an open city square. The mobile station (receiver) was positioned on three locations on the opposite side of the street. It was positioned in a way that cars, busses, pedestrians and cyclists cross the line-of-sight between receiver and transmitter. The carrier frequency was chosen as 28.5 GHz, which is one of the candidate bands for 5G.

Accompanying video recordings allow post processing of the measurement data and classification of events according to the source of shadowing.

Contribution

This publication is based on a measurement campaign planned and executed by myself and my co-authors. The data post-processing and analysis were performed by me. The publication was written by me and the co-authors provided a thorough review of the analysis and results, as well as proof reading and corrections to the text.

Environment Induced Shadowing of Urban Millimeter-Wave Access Links

Richard J. Weiler, Michael Peter, Wilhelm Keusgen, Kei Sakaguchi, Fabian Undi
The authors are with Fraunhofer Heinrich Hertz Institute, Einsteinufer 37,
10587 Berlin, Germany (e-mail: richard.weiler@hhi.fraunhofer.de)

***Abstract*—In this paper we investigate how environment induced shadowing influences a 28.5 GHz access link in an urban open square scenario. Shadowing is caused by cars, buses, lorries and pedestrians passing between the small cell base station and the mobile user terminal. We isolate typical single shadowing events and provide a model for their description. We also present statistical evaluations that can be used as input to 5G access channel models.**

***Index Terms*—millimeter-wave, 5G, millimeter-wave propagation, multipath propagation, human body shadowing, channel model, fading, ground reflection**

I. Introduction

The utilization of previously unused spectrum in the millimeter-wave bands is a novelty predicted for the next generation of mobile radio networks (5G). The addition of small cell base stations with a new mm-wave radio access technology will allow the network operators to update their networks where necessary to serve growing user demands. The wireless access channel and its modeling have been the focus of recent research [1], [2]. The impact of dynamic shadow fading through moving objects in outdoor access environments has received initial interest. Investigations on the effects of human body shadowing have been reported [3], [4], but were derived for indoor scenarios only. In the 3GPP channel modelling group for example, a stochastic dynamic blockage model was proposed [5]. Blockage effects are modelled as angular blockage regions around the UE, associated with a normal distributed loss value (in dB). The blockage regions are generated in a way to make them consistent in time and space.

In this paper we investigate, how an outdoor small cell access link in a typical urban scenario at 28 GHz is affected by its environment. Section II explains the setup and Sec. III gives an overview over the observed effects on the wireless channel. Single shadowing events are investigated and modeled in Sec. IV and Sec. V reports statistical evaluations of the results.

II. Measurement Setup

The measurement campaign in this paper was designed to investigate the effect of a non-stationary urban environment on a millimeter-wave small cell access link. This non-stationarity is caused by moving cars, buses, pedestrians and cyclists. The transmitter (Tx) of the channel sounder was therefore placed on one side of a busy street cutting through an orthogonal open city square with a diameter of ca. 150 m (see Fig. 1).

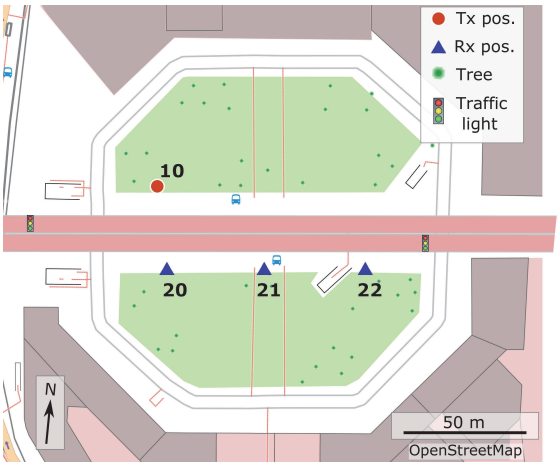

Figure 1. Map of measurement location

The transmitter antenna was mounted on a tripod at 3.5 m and 5 m above ground, representing a small cell base station.

The receiver (Rx) was positioned at three different locations across the street with its antenna 1.3 m above ground to represent a typical handheld user device. Figure 2 shows a schematic view of the setup. Pedestrians and cyclists on the receiver sidewalk, as well as buses and lorries can interrupt the line-of-sight between the transmitter and receiver antenna depending on their location.

A total of 1.5 million channel snapshots were acquired in this measurement setup with 250,000 snapshots per Rx positions 20, 21 and 22, each at a Tx height of 3.5 m and 5 m. The Tx to Rx distances were 32 m, 45 m and 78 m for Rx positions 20, 21 and 22 respectively. The temporal separation of two snapshots was 3.6 ms, leading to a total observation time of 15 minutes per position. Several video cameras were used to document the type, position and speed of the objects causing the shadowing.

The channel sounder hardware is based on a custom FPGA platform, described earlier [6]. It features a signal bandwidth of 250 MHz and uses a correlation based method to estimate the channel impulse response. The antennas used on both sides are based on an identical $\lambda/4$ dipole design and have an omnidirectional pattern in azimuth direction. The half power beamwidth in elevation direction is larger than 60° with its maximum gain at 30° elevation above the horizon (Rx). The

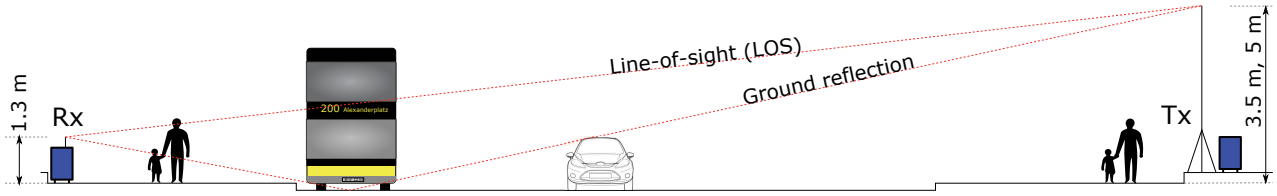

Figure 2. Schematic view of measurement setup (dimensions to scale)

transmitter side antenna was mounted upside down to have its maximum gain at 30° elevation below the horizon, minimizing an impact on the measurements due to gain taper. The impact of the antenna gain taper on the ground reflection is below 1 dB w.r.t. the LOS path. The channel sounder is back-to-back calibrated to the antenna ports and their gain is corrected in a post processing step.

Future millimeter-wave communication systems are expected to rely on electronically steerable high gain antennas. In this work we use omnidirectional antennas to capture the entire multipath propagation environment between transmitter and receiver. Windowing in the delay domain of the obtained channel impulse responses is used as an approximation to reproduce the effect of spatial filtering of directional antennas.

The noise level of the system after calibration corresponds to a path gain of $-136\,\mathrm{dB}$.

III. Observed effects

The measured channel impulse responses (CIR) were processed into two path gain values. One is the omnidirectional path gain, calculated over the entire bandwidth of 250 MHz. The other one is the line-of-sight (LOS) path gain. The latter one was obtained by applying a narrow time domain window on the CIR at the delay tap corresponding to the Tx-Rx distance: $P_{\mathrm{LOS,dB}} = \mathrm{CIR}_{\mathrm{dB}}\left(\tau_{\mathrm{LOS}}\right)$. Due to the limited bandwidth this includes all multipath components with an excess delay with respect to the LOS delay smaller than the window size (4 ns in this case), such as the ground reflected path.

Figure 3 shows the normalized LOS path gain over an observation interval of 15 minutes. The transmitter antenna height was 3.5 m and the receiver was located at position 20. The plot reveals periodic behavior of the path gain between phases with significant shadow fading and phases with almost constant path gain. The length of one pattern is about 90 seconds, which coincides very well with the intervals of the traffic lights that dictate traffic crossing the link (see Fig. 1).

The phases with significant shadow fading were analyzed in detail, allowing the identification of typical events according to the source of shadowing or blockage. The events can be coarsely classified according to the strength of their effect on the LOS and omnidirectional path gain. This is of course only possible if the event can be attributed to a single cause. The following examples have been selected to include only one single source of shadowing. The statistical evaluation in section V is based on the entire data set.

Typical shadowing events that heavily affect the line-of-sight path gain are shown in Figure 4. The path gain was normalized

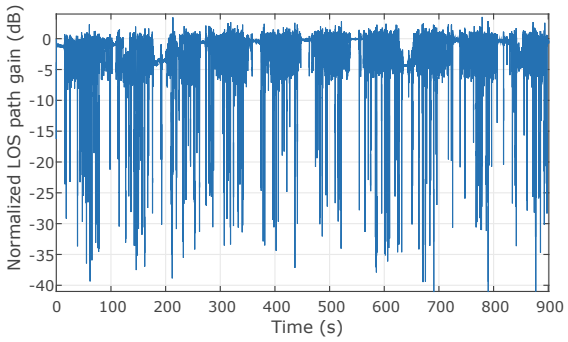

Figure 3. Evolution of line-of-sight path gain at Rx pos. 20

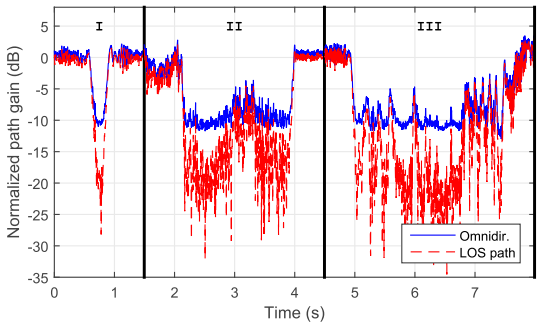

Figure 4. Typical LOS shadowing events at Rx pos. 20 (I: pedestrian, II: bus, III: bus & lorry)

to its average omnidirectional value in unshadowed state. The events shown are a pedestrian passing in the vicinity of the receiver (I), a double-decker bus on the near side of the road (II) and a double-decker bus and a lorry (car transporter) on the far side of the road (III). All events feature 20 to 30 dB fading on the LOS path gain and 10 dB fading on the omnidirectional path gain. The duration of the shadowing events is determined by the size of the objects and their speed of movement. The difference between the LOS path gain and the omnidirectional path gain can be explained by multipath components that are not affected by the shadowing. These components can for example be caused by static reflections from the surrounding high buildings.

Typical events with low effect on the path gain are shown in Figure 5. The events shown are a cyclist passing the receiver (I) and cars passing on the near and far side of the road for receiver position 20 (II) and 21 (III, IV). In all cases the visual line-of-

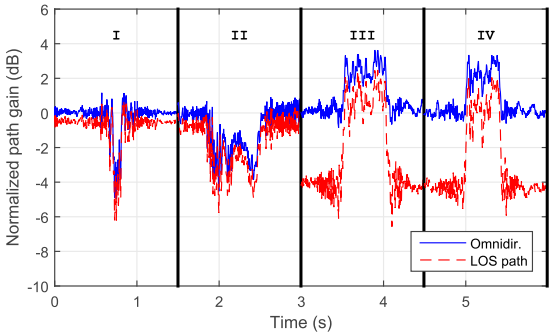

Figure 5. Typical shadowing events (I: bicycle at Rx pos. 20, II: car at Rx pos. 20, III-IV: car at Rx pos. 21)

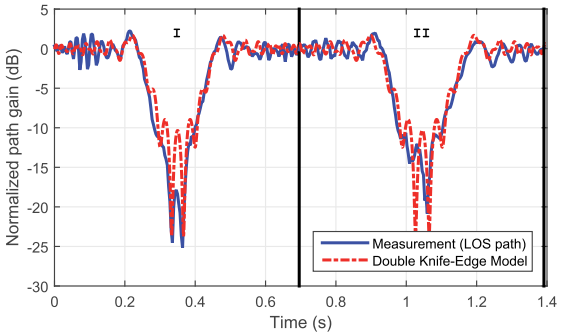

Figure 6. Pedestrian shadowing measurement and DKE model

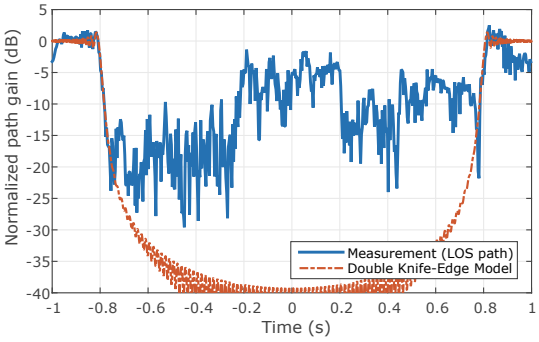

Figure 7. Lorry shadowing measurement and DKE model

sight path between transmitter and receiver is not interrupted by the passing objects. The first two events feature a very similar behavior of LOS and omnidirectional path gain with typical fading depths of only 2 to 4 dB. The other two events, acquired at the receiver position 21, show a counter intuitive behavior, as the path gain increases, when the cars are driving underneath the LOS path. The reason is flat fading, caused by a strong ground reflection as was shown in previous work [7]. With the given distance and antenna heights, a bandwidth much larger than the 250 MHz used here is necessary to resolve the flat fading. The cars passing underneath the LOS path block the ground reflected path and depending on the fading therefore attenuate or amplify the effective band limited path gain. The impact of the flat fading can also be obtained, when the absolute (LOS) path gain value is compared to the free space path loss. The offset between omnidirectional and LOS path gain is caused by strong multipath components that are present at the second receiver position.

The ringing effect before and after the shadowing events is better visible in this figure, but it also appears with the LOS shadowing events in the previous figure.

IV. Single Event Modeling

In this section, we discuss how single shadowing events can be described with adequate models.

Previous investigations were done on the effect of human body shadowing at 60 GHz in an indoor scenario [3]. It was shown that the Double Knife-Edge model (DKE) predicts the typical shadowing event quite well, but tends to underestimate the attenuation. The human body is modeled as an upstanding stripe of width w perpendicular to the link axis and distances d_{Tx} and d_{Rx} to the transmitter and receiver respectively. The total signal at the receiver results from the superposition of the diffracted fields around the stripe edges [8]. Figure 6 shows two pedestrian shadowing events (LOS path) and matching simulations using the DKE model. The path gain was normalized to its average power in the case of no shadowing. The second event (II) shows some asymmetry. The parameter of the model were set according to the geometry of the setup ($d_{\mathsf{Tx}} = 30\,\mathrm{m}$, $d_{\mathsf{Rx}} = 1.4\,\mathrm{m}$) and previous findings ($w = 23\,\mathrm{cm}$). The perpendicular speed of the pedestrian was estimated to $v = 1.6\,{}^{m}\!/_{\mathrm{s}}$ in (I) and $1.4\,{}^{m}\!/_{\mathrm{s}}$ in (II).The overall features of the attenuation (distance and depth of attenuation peaks) behave quite similar. The height of the fading within the shadowing event however does not match too well. This might be caused by the fact that the diffraction is lower than predicted by the sharp edges.

Applying the DKE model on a lorry leads to unsatisfactory results, as can be seen in Fig. 7. An articulated lorry of length $w = 16.5\,\mathrm{m}$ passed the receiver at a distance of $d_{\mathsf{Rx}} = 13\,\mathrm{m}$. Its speed was estimated to $10.4\,{}^{m}\!/_{\mathrm{s}}$. While at the beginning and ending of the shadowing event the model matches the measurement quite well, the attenuation in between differs massively. From other shadowing events however, it can be seen that the vehicles material has a large impact. The lorry in the figure had a canvas cover, explaining the low attenuation, similar to that observed in the double-decker buses. Lorries with a metal construction, such as containers, show a much higher attenuation up to 30 dB or more. The DKE model has no transmission in the stripe between the edges, explaining the difference in the shown example. Furthermore, the model implies an object of infinite height. This neglects the top and bottom edges of a lorry that might also show diffraction effects.

The previous models were derived for single events. Throughout the measurements taken however, they seldom occur as isolated events, but multiple events overlay each other, e.g. multiple pedestrians walk by, while cars cross the link. A

statistical evaluation is therefore performed in the next section as a basis for modeling the overall behavior of multipath components.

V. Statistical evaluation

In this section we compare statistical properties of the different measurements. We use the entire data set of 250,000 snapshots per measurement. Each set contains a mixture of shadowing events and times without shadowing as is apparent from Fig. 3. The statistical observations describe the scenario under investigation with frequent link interruptions, which we estimate to be a typical access scenario. Similar findings have been reported for indoor environments in [5].

Figure 8 shows the combined cumulative distribution function of the omnidirectional and LOS path gains at receiver positions 20, 21 and 22 for both transmit antenna heights of 3.5 m and 5 m. The path gains were normalized to the average omnidirectional path power at each Rx position when no shadowing occurs.

For all positions, the omnidirectional median value is close to 0 dB and small positive path gains up to 3 dB can be observed in almost 50 percent of the snapshots which can be explained with the fading effects described in the previous section. The maximum attenuation observed on the omnidirectional path gain is in the order of 12 dB and around 25 dB for the LOS paths. The plot also shows the distribution of the "Best MPC" value. This value is the multipath component with the maximum path gain in every single channel impulse response. It was selected as an approximation to an idealistic directional receiver that can always select the strongest multipath component through appropriate beam steering (under the assumption that each MPC corresponds to one spatial direction). The best MPC strategy significantly reduces the probability of low path gains below -15 dB. Comparing the individual distributions for the different receiver positions reveals a slight dependence on the link distance. The transition gets steeper for smaller distances and the boundaries extend towards larger path loss. In the omnidir. case for example the minimum of the path gain varies from -5 to -12 dB going from Rx position 20 to 22.

The variation of the transmit antenna height causes a slight variation towards a steeper transition for the higher height. This is also consistent for the LOS and Best MPC statistics.

VI. Conclusions

We have performed a measurement campaign of a 28 GHz small cell access link in presence of random shadow fading, induced by pedestrians, cars and buses. The results show, that environment induced shadowing has a significant impact on the path gain and therefore the link budget. The impact of shadowing events depends on the geometrical position of transmitter, receiver and the object causing it. Consistent to earlier observations, the ground reflection has a major impact on the power received from the line-of-sight direction. The shadowing of the ground reflected path can therefore lead to an increase or attenuation of the power received in this direction, depending on the state of the fading effect.

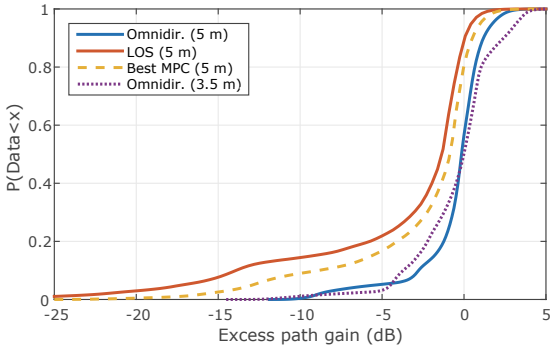

Figure 8. Path gain distribution at Rx positions 20 - 22

The double knife-edge model provides a good approximation to pedestrian single shadowing events, consistent with earlier findings for indoor modeling of human body shadowing. The modeling of vehicles however will need some further investigations, and additional parameters, as their effect highly depends on the type of vehicle (e.g. lorries with canvas covers vs. metal containers).

The statistical observations made can be used as input to the refinement of channel models that go beyond the level of detail mentioned in the Introduction. Exact behavior of the wireless channel on a fine grained time-scale is important for the design and implementation of new physical layer protocols, especially with electronically steerable high gain antennas.

References

[1] T. S. Rappaport, S. Sun, R. Mayzus, H. Zhao, Y. Azar, K. Wang, G. N. Wong, J. K. Schulz, M. Samimi, and F. Gutierrez, "Millimeter wave mobile communications for 5G cellular: It will work!" *IEEE Access*, pp. 335–349, 2013.

[2] R. J. Weiler, M. Peter, W. Keusgen, A. Maltsev, I. Karls, A. Pudeyev, I. Bolotin, I. Siaud, and A.-M. Ulmer-Moll, "Quasi-deterministic millimeter-wave channel models in MiWEBA," *EURASIP Journal on Wireless Communications and Networking*, vol. 2016, no. 1, pp. 1–16, 2016. [Online]. Available: http://dx.doi.org/10.1186/s13638-016-0568-6

[3] M. Peter, M. Wisotzki, M. Raceala-Motoc, W. Keusgen, R. Felbecker, M. Jacob, S. Priebe, and T. Kurner, "Analyzing human body shadowing at 60 GHz: Systematic wideband MIMO measurements and modeling approaches," in *Antennas and Propagation (EUCAP), 2012 6th European Conference on*. IEEE, 2012, pp. 468–472.

[4] M. Yokota, T. Ikegamai, Y. Ohta, and T. Fujii, "Numerical examination of EM wave shadowing by human body," in *Antennas and Propagation (EuCAP), 2010 Proceedings of the Fourth European Conference on*, April 2010, pp. 1–4.

[5] R1-162234, Qualcomm, "TP on dynamic blockage modeling," 3GPP TSG RAN1 #84bis, Busan, South Korea, Apr. 11–15 2016. [Online]. Available: http://www.3gpp.org/ftp/tsg_ran/WG1_RL1/TSGR1_84b/Docs/R1-162234.zip

[6] W. Keusgen, A. Kortke, M. Peter, and R. Weiler, "A highly flexible digital radio testbed and 60 GHz application examples," in *Microwave Conference (EuMC), 2013 European*. IEEE, 2013, pp. 740–743.

[7] R. J. Weiler, M. Peter, W. Keusgen, A. Kortke, and M. Wisotzki, "Millimeter-wave channel sounding of outdoor ground reflections," in *IEEE Radio and Wireless Symposium*, 2015.

[8] J. Kunisch and J. Pamp, "Ultra-wideband double vertical knife-edge model for obstruction of a ray by a person," in *Ultra-Wideband, 2008. ICUWB 2008. IEEE International Conference on*, vol. 2, Sept 2008, pp. 17–20.

4.7 Human body shadowing mitigation

All of the previous measurement campaigns, with the exception of the ground reflection measurement, used omnidirectional antennas for the channel sounding. The measurement approach allows unbiased measurement of the omnidirectional path loss. A millimeter-wave outdoor communication system will however most certainly employ directional antennas to achieve acceptable link budgets (see Section 3.2). The measurement campaign introduced in this section is designed to collect practical experience on the challenges of such a system [WKM+16].

A channel measurement campaign was performed using a 60 GHz beam forming array on the base station (transmitter) side. The receiver was equipped with an omnidirectional antenna at a height of 1.2 m. Measurements at a total of 58 positions with transmitter to receiver distances of 25 to 65 m were performed, each with and without a human standing in the line-of-sight next to the receive antenna. At each position, the channel impulse responses for a total of 133 different beamforming vectors were recorded. Each vector is designed to generate a focused beam to scan the surrounding in 5° steps in azimuth and elevation. The results show that shadowing mitigation by using strong reflections is possible in some locations. In the other locations, the strongest reflected path beam is not necessarily stronger than the attenuated line-of-sight beam.

The results illustrate the challenges when using the millimeter-wave frequency band for small cell access links. Fast beam searching and tracking will become necessary, as well as mechanisms for fast fallback to lower frequencies, where mm-wave links become unavailable.

Contribution

This publication is based on a joint measurement campaign, planned and executed by myself and project partners of the MiWEBA project. I authored the major part of this publication by myself. The antenna array was developed by my co-authors who also provided the characterization and documentation of the array (Section II), as well as ray-tracing results of the environment that was used to interpret the measurements. The publication is based on measurement data post processing and analysis that was done by me. The co-authors provided additional proof-reading and smaller additions to the text.

Millimeter-Wave Outdoor Access Shadowing Mitigation Using Beamforming Arrays

Richard J. Weiler*, Wilhelm Keusgen*, Alexander Maltsev‡§, Thomas Kühne†,
Andrey Pudeyev‡, Liang Xian‡, Joongheon Kim‡, Michael Peter*
*Fraunhofer Heinrich Hertz Institute, Berlin, Germany
†Communications and Information Theory Chair, TU Berlin, Berlin, Germany
‡Intel Corporation
§University of Nizhny Novgorod, Russia

***Abstract*—In this paper we present 60 GHz channel measurements that have been performed in an outdoor access scenario. At the transmitter side (small cell base station) a 128 element beamforming array was used. This array was used to measure the channel impulse response at an omni-directional receiver antenna for 133 different transmit beam settings, each representing a narrow beam in a different spatial direction. A total of 58 different receiver positions was measured and at every location one unobstructed measurement and one measurement with human body blockage was performed. The results show, that at some locations, reflected paths exist with only a minor drop in signal power, relative to the line of sight path.**

***Index Terms*—millimeter-wave, 5G, 60 GHz, millimeter-wave propagation, multipath propagation, beam forming arrays, phased array antenna**

I. Introduction

The ongoing growth of mobile traffic and emergence of new services and applications drives the development of the fifth generation mobile radio networks, 5G. Among other approaches, leveraging the previously unused frequency bands in the bands above 6 GHz is a much discussed candidate technology [1]. A special focus lies on the millimeter-wave band, ranging from 30 to 300 GHz.

For indoor scenarios 60 GHz channels were well studied during the last 20 years [2]–[5]. For the experimental investigations of the indoor channels described in these works, steerable directional horn antennas (with typical gain of 15-18 dBi) were usually exploited. Angular information was obtained in these measurement setups using mechanical rotation of the antennas.

Recently, consumer products (laptops & docking stations) with integrated 60 GHz radio and baseband chipsets, compatible to the IEEE 802.11ad (WiGig) standard, have become available. These solutions and the underlying standard were developed for indoor short range communication and promise multiple gigabit per second throughput, using around 2 GHz of bandwidth.

Outdoor millimeter-wave channels are under intensive investigation nowadays (see e.g. [6]–[8]). Considering these bands for outdoor wireless access with ranges in the order of multiple tens to hundreds of meters poses a number of new challenges. Increasing the coverage range from tens to hundreds of meters requires up to 25-30 dB of additional link budget. This gap may be closed by exploiting both higher transmit power and using antennas with high gains. The antenna design therefore is a crucial part of a millimeter-wave outdoor access system. As the free space path loss is much higher than in the sub 6 GHz bands, directional antennas are necessary at least at the small cell base station side. In access scenarios the user terminal is mobile and the environment is non-stationary (e.g. moving cars), making fast electronic beam steering a must, even for channel investigations. Mechanical steering of directional antennas is not well suited for this task.

In contrast to indoor environments, where a multitude of reflecting objects can help mitigate shadowing of the line of sight path, outdoor environments can have less such objects and building side walls. In this paper we therefore investigate such an outdoor scenario in shadowing conditions in combination with a beamforming array at the transmitter (base station) side.

In section II the electronically steerable antenna prototype is presented. Section III introduces the measurement location, channel sounder and shadowing measurement procedure. The results are presented in sec. IV and conclusions and a way forward are given in sec. V.

II. Steerable Antenna Prototype

Several different approaches exist to implement large-aperture millimeter-wave antennas. The most common ones are phased arrays, lens and reflectarray antennas. Electromagnetic bandgap antennas [9] and micro-electro-mechanical antennas [10] are more recent developments, that are still under investigation.

Phased array antennas in general consist of multiple antenna elements, each with their own phase shifter, allowing to control the antenna pattern. The gain and pattern of phased arrays depends on the number of antenna elements, their individual radiation pattern and the geometrical configuration. Prototypes of such antennas with a medium number of elements (order of tens) have been successfully realized (e.g. see [11] for a 60 GHz 32 element antenna). The drawback of this approach is that they cannot easily be scaled to large number of elements, due to losses in feeding structures.

Steerable lens antennas usually use multiple switchable RF sources and lenses made of materials with special dielectric properties. The gain of this type of antenna is determined by the lens size and design and can be scaled according to

the requirements (e.g. see [12]). Similar approaches exist that build on the lens principle, such as planar transmit arrays. The drawback of the lens antenna approach is the limited steering capability. In [13] a prototype system at 73.5 GHz is presented, that has azimuth steering capabilities in the range of $\pm 18\,\mathrm{deg}$. A full coverage in azimuth would require 10 such systems mounted in a circle.

The antenna we used for the measurements in this paper builds on the principle of the phased arrays but tries to mitigate their drawbacks. The 60 GHz modular antenna array (MAA) is based on small phased antenna array modules with typical number of elements from 4 to 16. Multiple modules are combined to form an array with more elements. As the individual modules are fed using a lower intermediate frequency and on board up conversion and phase shifters, the feeding losses become negligible. A single module is shown in Figure 1. It consists of 16 antenna elements in a 2 by 8 configuration. The digitally programmable phase shifters, up & down conversion as well as amplifiers are all integrated on the module.

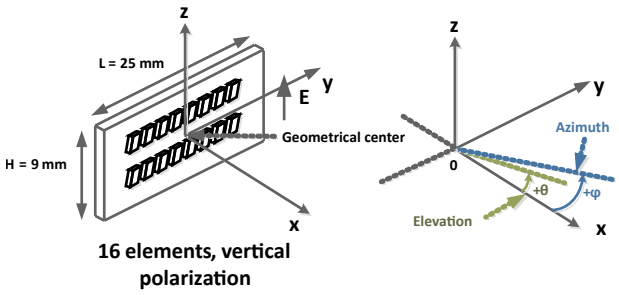

Figure 1: Single 8x2 array module

The measurements in this paper were performed using a MAA configuration of 2 by 4 antenna modules, as shown in Figure 2. Thus it contains 128 antenna elements in total. A single intermediate frequency interface is divided onto the 8 modules. The phase of each individual antenna on each module can be controlled using a digital interface. Due to technical reasons there are larger gaps between the patches, due to the size of the modules. This is a difference to standard phased arrays, where the elements are usually spaced in a grid of $\lambda/2$.

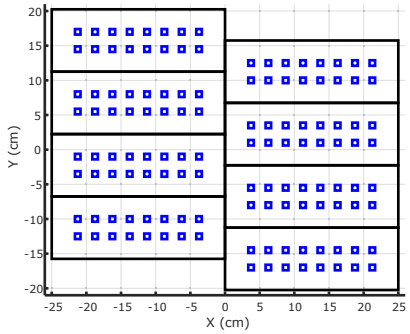

Figure 2: 16x8 element MAA antenna design

Figure 3 shows the azimuth cut of the far field radiation pattern of the 16x8 element modular antenna array. The red line was measured using a far field measurement setup and the blue line was simulated using the same configuration. Due to a phase ambiguity between the individual 8x2 modules, a calibration procedure is performed on power-up. The same procedure was also used in the simulation. The array was steered to broadside direction. As can be seen a secondary side lobe of $-3.4\,\mathrm{dB}$ at $-9.2\,^\circ$ can be observed. This side lobe is caused by the geometrical construction of the array and can not be neglected. Similar side lobe levels and angles are observed, if the beam is steered in the azimuth plane. The pattern has to be taken into account when measurement data is analyzed in angular space.

The elevation pattern shows distinct lobes in the steering direction, as well as sidelobes. The sidelobes however are beyond 10° offset and are therefore not of importance in the observed environment.

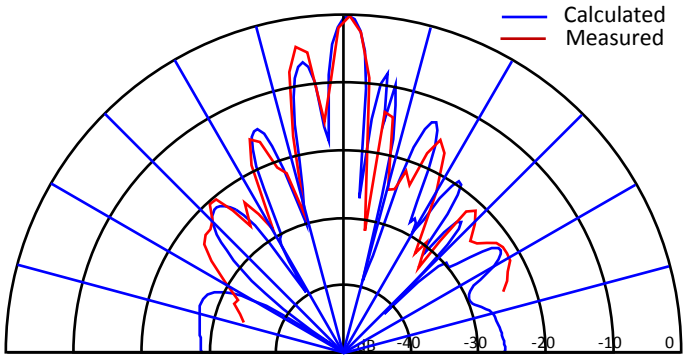

Figure 3: MAA azimuth radiation pattern for broadside setting

III. Measurement Method & Environment

A. Environment

The measurement campaign was performed in Front of the Robert N. Noyce building at Intel headquarters in Santa Clara, California, USA. Figure 4 shows a map of the measurement setup. The transmitter was placed at the right side, 3 m above ground, facing left in the direction of the arrow. The receiver was placed at multiple positions on three linear tracks, as indicated with RX1, RX2 and RX3. The antenna was mounted at 1.2 m above ground. Each dark blue dot indicates a receiver position where the full beam scanning procedure was performed. The individual locations on the tracks are 2 m apart, starting at a distance of roughly 25 m from the transmitter. Having 20 positions each on RX1 and RX2 and 18 on RX3 the maximum projected transmitter to receiver distance was 63 m and 58 positions were measured in total.

There is a large building at the top side of the map with a metal and glass facade. As indicated in the map, several trees stand along the walls and on the parking area. During the measurement some cars were parked on the parking spots as indicated. The weather during the measurement campaign was humid with occasional slight rain showers. Figure 5 shows a picture of the measurement location that was taken on a different day.

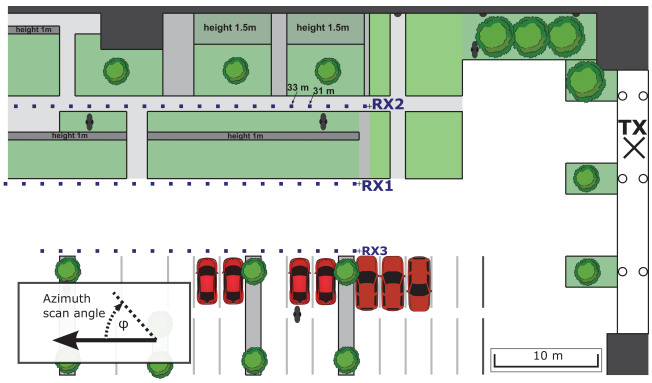

Figure 4: Map of measurement location

Figure 5: The measurement location

B. Channel sounder

The channel sounder used is based on a custom FPGA platform [14]. Its simplified block diagram is shown in Figure 6 and the key parameters are given in Table I. On the transmitter side two up-conversion stages (IQ MOD & MOD) are used to interface the MAA which then transmits the sounding signal at 60.48 GHz. The receiver uses an intermediate frequency of 1.92 GHz before converting to baseband. Note that filters are not shown in the figure. The local oscillators (LO) are fed from a common rubidium reference oscillator on each side. The two rubidium oscillators are synchronized prior to the measurement campaign to guarantee absolute timing between transmitter and receiver.

The MAA on the transmit side is an active device, where the antenna ports are on chip and not accessible. The standard approach for calibration, where the transmit antenna port (or ports) are connected to the receiver antenna port is therefore not possible. Instead the calibration was performed with the MAA and the receiver antenna at a fixed reference distance of 2 m over the air. The transmitter and receiver were placed on a sufficiently large open square, facing each other at a height of 3 m above ground.

C. Measurement procedure

For each of the 58 receiver positions (see sec. III-A) two measurement runs were performed. One with free line of sight (LOS) and one with blocked/obstructed line of sight (OLOS). For the blocking a human was standing in front of the receiver

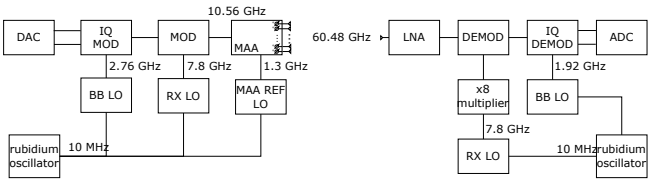

Figure 6: Channel sounder block diagram

Table I: Channel sounder parameter

Type	Value
Bandwidth	250 MHz
TX antenna	16x8 beamforming array, vertical pol.
TX antenna height	3 m
RX antenna	Omnidirectional, vertical polarization
RX gain	0 dBi
RX antenna height	1.2 m
Snapshot separation	800 µs

at a distance of ca. 20 cm, thus obstructing a certain part of the omnidirectional receiver antenna, as indicated in Figure 7.

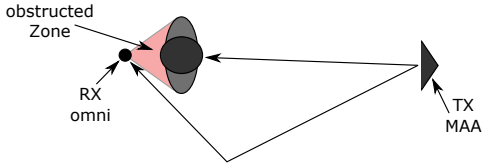

Figure 7: Geometrical setup of human body shadowing

During each measurement a full sector sweep was performed, as described by Algorithm 1. A total of 133 transmitter beam settings was acquired in less than 10 seconds. With the temporal snapshot separation given in Table I, a total of 50 individual channel impulse responses (CIR) was recorded per beam setting.

Algorithm 1 Sector sweep protocol

```
for elevation = -15:5:15
 for azimuth = -45:5:45
  SteerBeam(elevation, azimuth)
  Wait(40ms)
 end
end
```

The function `SteerBeam` calculates and applies the phase shift of each individual array element (i, j). It is calculated according to:

$$Phase_{i,j} = 2\pi[\sin(elevation)\, y_{i,j} + \sin(azimuth)\, x_{i,j}]$$

Where $x_{i,j}$ and $y_{i,j}$ are the positions of the elements relative to the geometric center of the array. The calculated phase is then quantized to the resolution of the phase shifter, described in sec. II.

In a post processing step the individual channel impulse responses per beam setting are separated and stored for further analysis. In order to avoid any effects of drifts in timing and false classification, only 40 of the available 50 CIRs are used.

IV. Results

For every receiver position, 40 channel impulse responses were recorded for each of the 133 transmit beam settings. The following analysis of the results is based on the average received power for each of the beam settings. Figures 8 and 9 show plots for two exemplary receiver locations on the RX2 route, 31 m and 33 m away from the transmitter. The case with free line of sight (unblocked) between the transmitter and receiver is shown in Figures 8a and 9a, while the case with human shadowing of the line of sight (blocked) is shown in Figure 8b and 9b.

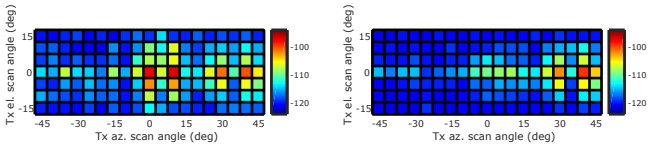

(a) unblocked (b) blocked

Figure 8: RX2 at 31 m distance

Each figure shows the received power for the given transmitter elevation (el.) and azimuth (az.) steering angle. In both unblocked cases (Figs. 8a, 9a) the maximum power is received at 0° elevation and -10° azimuth (LOS path), which is in accordance to the geometrical setup. Both plots also show a strong path at 0° azimuth, which is an effect caused by the secondary sidelobe of the antenna (LOS sidelobe, see sec. II). When the antenna is steered to 0° azimuth, the large sidelobe (at 9° offset) is pointing towards the receiver. Table II gives numerical values for selected az. scan angles.

Table II: Received power of selected beam settings

Fig.	"LOS path" 0°	"Refl. path" 30°	"LOS sidelobe" 10°	"Refl. sidel." 40°
8a	-96.9 dB	-100.3 dB	-97.4 dB	-101.3 dB
8b	-108.3 dB	-99.4 dB	-109.6 dB	-102.2 dB
9a	-99.26 dB	-113.0 dB	-100.0 dB	-115.3 dB
9b	-109.4 dB	-114.4 dB	-114.0 dB	-115.6 dB

A big difference between the two receiver positions can be observed with regard to the second strong path that shows up at 40° azimuth (refl. path). Here again a strong sidelobe is visible at 10° offset (refl. sidelobe). This strong path is most probably caused by a reflection of the building wall, as it is not affected by the human body shadowing (Fig. 8b). At the second position (33 m) however, this reflection is very weak.

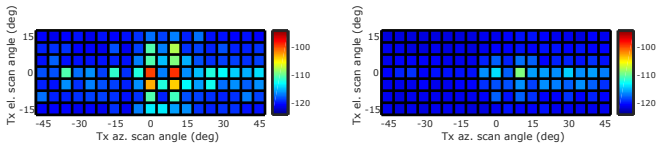

(a) unblocked (b) blocked

Figure 9: RX2 at 33 m distance

Figures 10, 11 and 12 show the path gain (normalized to free space path loss) of the "LOS path" steering and the best "reflected path" steering for all receiver positions. It should be noted, that even the "LOS path steering" can include reflections from the surroundings, according to the effective antenna pattern. The solid line is the free space path loss, calculated using Friis formula. The noise floor of the system was estimated using receiver measurements without transmitted signal and is indicated with the black dashed line.

Due to the limited bandwidth of the channel sounder of 250 MHz, small scale fading of multipath components (e.g. ground reflection) can occur in the measurement data.

The strength of the best reflected path varies greatly from position to position and between the different RX tracks. RX1 and RX3 show larger differences between the LOS and reflected path power. On around half of the positions of RX2 however, the reflected path power is only a few dB weaker than the LOS path.

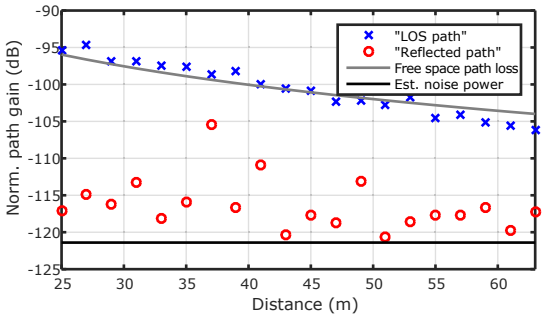

Figure 10: RX1 path power

The different behavior in strength of the reflected path between the receiver tracks is expected to be caused by the different surroundings of the receiver at each position. On RX1 and RX3 there are few objects close to the receiver that could generate a strong reflected path. The building seemingly does not serve as a reflector, due to the limited steering of the transmitter of max. 45°. On RX2 on the other hand the building wall seems to reflect well in some locations. Further studies of the locations and propagation paths could give a clearer picture of the effects that influence the reflection behavior.

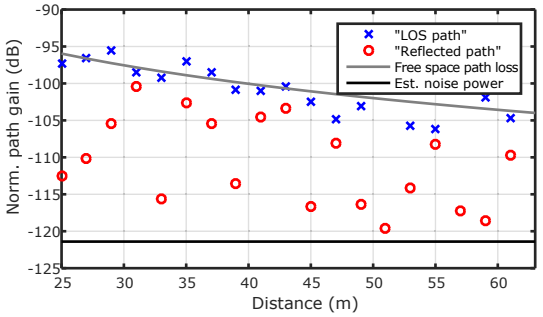

Figure 11: RX2 path power

In Figure 13 an cumulative distribution function (CDF) of P_Δ is given for all three receiver paths, where P_Δ is the difference

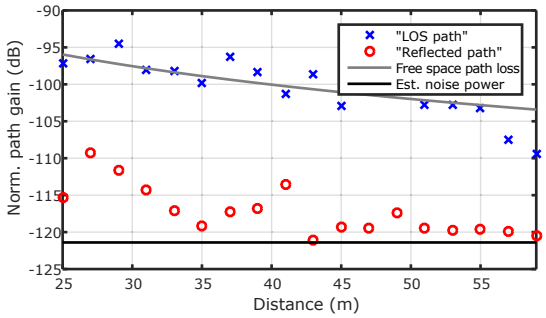

Figure 12: RX3 path power

between the power of the line of sight (LOS) path and the reflected path. Due to the limited number of spatial samples the CDF has some discontinuities. Its median value (probability at 50%) is 16.3 dB. Care has to be taken, as the available signal to noise ration of the measurement also affects the achievable range of P_{Δ}.

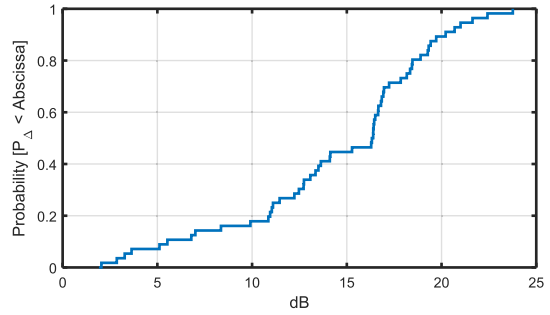

Figure 13: Cumulative distribution function of LOS to reflected path power

V. Conclusions

In this paper we presented a 60 GHz measurement campaign using an 128 element phase array transmit antenna. Though this measurement approach has the big advantage of very fast beam scanning it introduces some challenges. The calibration of the channel sounder becomes difficult, especially as the antenna modules have no antenna ports for the 60 GHz signal. Measured antenna patterns can usually only be provided for some beam settings, as it depends on the phase shifter setting of every single antenna element.

The effect of human body shadowing on steerable paths seemingly highly depends on the environment and the number of objects that can serve as a reflector. In the measured environment, only a fraction of positions provides a reflection with lower path loss than LOS steering. The impact on shadowing mitigation however also depends on the link budget requirements, i.e. the allowable excess path loss.

Future work can take additional results from the measurement campaign into account, that have not yet been employed. As full channel impulse responses are available for each beam setting, number of paths and delay spreads can be analyzed, giving a deeper insight into the physical propagation mechanisms in this environment. Further measurement campaigns can also take different kind of environments and scenarios into account, where more reflecting objects are available. A larger azimuth coverage might be helpful in finding more reflectors.

The phased array design used in this paper suffers from some drawbacks, that could be mitigated in improved versions.

Acknowlegment

The research leading to these results has received funding from the European Union's Seventh Framework Programme (FP7-ICT-2013-EU-Japan) under grant agreement number 608637 (MiWEBA).

References

[1] F. Boccardi, J. Heath, R.W., A. Lozano, T. Marzetta, and P. Popovski, "Five disruptive technology directions for 5G," *Communications Magazine, IEEE*, vol. 52, no. 2, pp. 74–80, February 2014.

[2] H. Droste and G. Kadel, "Measurement and analysis of wide band indoor propagation characteristics at 17 GHz and 60 GHz," in *Antennas and Propagation, 1995., Ninth International Conference on (Conf. Publ. No. 407)*, vol. 2, Apr 1995, pp. 288–291 vol.2.

[3] C. Anderson and T. Rappaport, "In-building wideband partition loss measurements at 2.5 and 60 GHz," *Wireless Communications, IEEE Transactions on*, vol. 3, no. 3, pp. 922–928, May 2004.

[4] A. Maltsev, R. Maslennikov, A. Sevastyanov, A. Khoryaev, and A. Lomayev, "Experimental investigations of 60 GHz WLAN systems in office environment," *Selected Areas in Communications, IEEE Journal on*, vol. 27, no. 8, pp. 1488–1499, October 2009.

[5] A. Maltsev, E. Perahia, R. Maslennikov, A. Sevastyanov, A. Lomayev, and A. Khoryaev, "Impact of polarization characteristics on 60-GHz indoor radio communication systems," *Antennas and Wireless Propagation Letters, IEEE*, vol. 9, pp. 413–416, 2010.

[6] T. S. Rappaport, S. Sun, R. Mayzus, H. Zhao, Y. Azar, K. Wang, G. N. Wong, J. K. Schulz, M. Samimi, and F. Gutierrez, "Millimeter wave mobile communications for 5G cellular: It will work!" *IEEE Access*, pp. 335–349, 2013.

[7] J. Medbo, K. Borner, K. Haneda, V. Hovinen, T. Imai, J. Jarvelainen, T. Jamsa, A. Karttunen, K. Kusume, J. Kyrolainen, P. Kyosti, J. Meinila, V. Nurmela, L. Raschkowski, A. Roivainen, and J. Ylitalo, "Channel modelling for the fifth generation mobile communications," in *Antennas and Propagation (EuCAP), 2014 8th European Conference on*, April 2014, pp. 219–223.

[8] R. J. Weiler, M. Peter, W. Keusgen, and M. Wisotzki, "Measuring the busy urban 60 GHz outdoor access radio channel," in *Ultra-Wideband (ICUWB), 2014 IEEE International Conference on*, 2014.

[9] Y. Rahmat-Samii and H. Mosallaei, "Electromagnetic band-gap structures: classification, characterization, and applications," in *Antennas and Propagation, 2001. Eleventh International Conference on (IEE Conf. Publ. No. 480)*, vol. 2, 2001, pp. 560–564 vol.2.

[10] D. Chauvel, N. Haese, P.-A. Rolland, D. Collard, and H. Fujita, "A micro-machined microwave antenna integrated with its electrostatic spatial scanning," in *Micro Electro Mechanical Systems, 1997. MEMS '97, Proceedings, IEEE., Tenth Annual International Workshop on*, Jan 1997, pp. 84–89.

[11] E. Cohen, C. Jakobson, S. Ravid, and D. Ritter, "A thirty two element phased-array transceiver at 60GHz with RF-IF conversion block in 90nm flip chip CMOS process," in *Radio Frequency Integrated Circuits Symposium (RFIC), 2010 IEEE*, May 2010, pp. 457–460.

[12] A. Artemenko, A. Maltsev, A. Mozharovskiy, A. Sevastyanov, V. Ssorin, and R. Maslennikov, "Millimeter-wave electronically steerable integrated lens antennas for WLAN/WPAN applications," *Antennas and Propagation, IEEE Transactions on*, vol. 61, no. 4, pp. 1665–1671, April 2013.

[13] M. Cudak, T. Kovarik, T. Thomas, A. Ghosh, Y. Kishiyama, and T. Nakamura, "Experimental mm wave 5G cellular system," in *Globecom Workshops (GC Wkshps), 2014*, Dec 2014, pp. 377–381.

[14] W. Keusgen, A. Kortke, M. Peter, and R. Weiler, "A highly flexible digital radio testbed and 60 GHz application examples," in *Microwave Conference (EuMC), 2013 European*. IEEE, 2013, pp. 740–743.

5 Hardware aspects

The millimeter-wave access channel imposes a more sophisticated hardware design than today's sub 6 GHz bands. It is apparent from the properties and results presented in the previous Chapter 4 the the higher free-space path loss makes directional transmission and reception on both the transmitter and the receiver a necessity. The required steerable antennas can only be successfully implemented with electronic beam steering. Shadow fading and movement result in the highly volatile nature of the channel. A technological approach in form of a beamforming array antenna was used to perform the measurements in Section 4.7. Another possible approach to implement steerable high gain beams is given in the following publication [WK15]. It might be especially well suited for applications in small cell base stations.

This patent addresses the problem of limited output power of integrated solid state amplifiers for millimeter-wave RF signals and the spatial steering of the transmitted energy. A number of parallel amplifiers are placed in front of an orthogonal, passive transformer. This leads to a summation of the parallel input power at one of the output ports, when providing the correct signal to each amplifier. The input signal to each amplifier needs to be a phase shifted version of the same transmit signal. By controlling the phase shift on each input, the output port with the combined power can be instantly and arbitrarily chosen. Each output port can be connected to a high gain transmit antenna, covering a certain spatial direction. Opposed to the previously mentioned antenna array, where the beam steering range is limited by the planar construction, the direction and polarization of the individual high gain antennas can be arbitrarily chosen.

The transformer can be implemented as a passive device and does not introduce any limitations on the transmit power. Possible realizations are a Butler matrix or a Rotman lens, which is especially suitable for mm-wave frequencies, due to the small wavelength [RT63]. Realizations of such lens designs as substrate integrated waveguides (SIW) exist and are a possible candidate for integration with the solid state amplifiers [RP92, CHW$^+$08,

RPW97].

Contribution

The concept of this patent, to use a passive transformation unit to combine and steer a signal with a multitude of amplifiers, was invented by me. Together with my co-inventor I then extended the concept to its application in a transmitter and receiver. I then wrote the description of the invention myself. The co-authoring patent attorney translated the description and sketches into the necessary patent form.

(19) Europäisches Patentamt
European Patent Office
Office européen des brevets

(11) EP 2 624 475 B1

(12) **EUROPEAN PATENT SPECIFICATION**

(45) Date of publication and mention of the grant of the patent:
28.01.2015 Bulletin 2015/05

(21) Application number: **12153262.6**

(22) Date of filing: **31.01.2012**

(51) Int Cl.:
H04B 7/06 *(2006.01)* ***H01Q 3/40*** *(2006.01)*

(54) **Combined Power Transmission**

Kombinierte Leistungsübertragung

Transmission de la puissance combinée

(84) Designated Contracting States:
AL AT BE BG CH CY CZ DE DK EE ES FI FR GB GR HR HU IE IS IT LI LT LU LV MC MK MT NL NO PL PT RO RS SE SI SK SM TR

(43) Date of publication of application:
07.08.2013 Bulletin 2013/32

(73) Proprietor: **Fraunhofer-Gesellschaft zur Förderung der angewandten Forschung e.V.**
80686 München (DE)

(72) Inventors:
- **Weiler, Richard**
  10785 Berlin (DE)
- **Keusgen, Wilhelm**
  14089 Berlin (DE)

(74) Representative: **Zimmermann, Tankred Klaus et al**
Schoppe, Zimmermann
Stöckeler & Zinkler & Partner
Patentanwälte
Postfach 246
82043 Pullach bei München (DE)

(56) References cited:
US-A- 5 430 453
US-A1- 2004 027 305
US-A1- 2005 128 022
US-A1- 2011 090 100

EP 2 624 475 B1

Printed by Jouve, 75001 PARIS (FR)

Description

[0001] Embodiments of the present invention relate to a transmitter. Further embodiments of the present invention relate to a transceiver. Some embodiments of the present invention relate to an electrically controllable directional antenna. Some embodiments of the present invention relate to a switched beam power combiner.

[0002] Fig. 1 shows a block diagram of a plurality of radio stations that are communicating by means of high frequency signals. Thereby, in Fig. 1 four radio stations 10_1 to 10_4 are shown by way of example. Each radio link (or radio communication) 12_1 to 12_5 is operated in both directions, i.e. bidirectional. Moreover, each radio station 10_1 to 10_4 comprises a combined transmit receive unit (transceiver) having a downstream signal processing (unit) 14_1 to 14_4 and a common antenna 16_1 to 16_4 for transmitting and receiving (or two separate antennas for transmitting and receiving). Each of the antennas 16_1 to 16_4 can comprise a plurality of interconnected or combined radiating elements. Furthermore, each radio station 10_1 to 10_4 is configured to set-up simultaneous radio links to one or more adjacent radio stations, or even to all radio stations 10_1 to 10_4, e.g. as shown in Fig. 2. Thereby, the radio links 12_1 to 12_5 form a network structure with the individual radio stations 10_1 to 10_4 as nodes. Note that in Fig. 2, a three dimensional Cartesian coordinate system is shown for illustration purposes. The Cartesian coordinate system comprises a x-axis, a y-axis and a z-axis, wherein the x-axis and the y-axis span a horizontal plane perpendicular to an earth gravitational vector, and wherein the z-axis (altitude) is parallel to the earth gravitational vector. Since differences in altitude (z-axis) between the individual radio stations 10_1 to 10_4 are small compared to distances between the radio stations 10_1 to 10_4, the spatial position of the individual radio stations 10_1 to 10_4 is primarily characterized by their horizontal angle or azimuthal angle (angle in the horizontal plane, e.g. relative to the x-axis or y-axis) 20_1 and 20_2.

[0003] Fig. 3 shows a block diagram of the radio stations 10_1 to 10_4 shown in Fig. 1, wherein two of the four radio stations 10_1 to 10_4 are configured as transmitters 10_1 and 10_4 and the other two as receivers 10_2 and 10_3. In order to increase the operating range (coverage) for a given transmit power, or even to implement a secure radio link 12_1, 12_3 or 12_5, the high frequency signals can be bundled by the antennas 16_1 and 16_4 of the transmitters 10_1 and 10_4 and be radiated (or transmitted) mainly in the direction of the receivers 10_2 and 10_3. Bundling of the beams can be performed by appropriate beam patterns 30_1 to 30_3 with distinctive main lobes. Amplification of the radio signals can be effected additionally or alternatively by beam patterns 304 to 30_6 on the receiver side. If the direct line of sight is blocked, e.g. by an obstacle 32, then a directed radio link 12_3 can be set-up by means of an appropriate reflector 34. In Fig. 3 only unidirectional radio links 12_1, 12_3 and 12_5 are shown by way of example, wherein an extension to bidirectional radio links can be performed by means of exchanging transmitters 10_1 and 10_4 and receivers 10_2 and 10_3. Hence, by means of forming (or generating) appropriate beam patterns, each transmitter is capable of radiating the transmit power simultaneously in one or more azimuthal directions and each receiver is capable of receiving signals from one or more azimuthal directions. Generally, the positions of the radio stations 10_1 to 10_4 are not fixed but variable, such that the alignment of the beams or main lobes must be carried out dynamically.

[0004] Moreover, for a secure operation, the radio system requires that the transmit signals have a particular minimal power. The generation of the required transmit power is particularly challenging for micro or millimeter wave radio systems.

[0005] Typical applications for the radio system shown in Fig. 1 are meshed outdoor networks, e.g. for a radio communication between vehicles, buildings or radio masts.

[0006] The simultaneous and adaptive formation of multiple main lobes is so far possible with MIMO signal processing (MIMO = Multiple Input Multiple Output). In these systems each antenna element (or radiating element) is connected via a separate transceiver and a separate digital-to-analog converter or analog-to-digital converter to a common digital signal processing (unit). The signal processing (unit) performs for each desired main lobe a separate complex weighting of the antenna signals, e.g. as described in D. Gesbert, M. Shafi, S. Da-shan, P. Smith and A. Naguib, "From theory to practice: an overview of MIMO space-time coded wireless systems", Selected Areas in Communications, IEEE journal on, vol. 21, no. 3, pp. 281-302, Apr. 2003. The MIMO signal processing allows any manipulation of the transmit and receive signals not only for the entire signal but also for individual signal components in the time or frequency domain. Hence, the MIMO signal processing is very flexible and efficient. Thereby, all antenna elements contribute to the formation of the main lobes, wherein each antenna element usually comprises a low directivity. This solution offers the greatest flexibility at the highest effort because a transceiver including a converter is required for each antenna element (or radiating element). The antenna array is usually planar and hence covers only an azimuthal angle of 120°. In principle, a curved or circular arrangement of the antenna elements (or radiating elements) is also possible in order to achieve a 360° covering. In this case, not all antenna elements can contribute to the formation of a specific main lobe, which results in a poor exploitation of the already complex system.

[0007] Besides, there is the possibility of using antenna arrays having switchable fixed main lobes (switched beam antennas). In this case, the antenna elements are connected via a change-over switch to the transceiver, such that at all times only one specified antenna element having a corresponding main lobe is active. The desired high directivity is realized within each antenna element (or radiating element). With this easy approach a simultaneous formation of main lobes is not possible. A more complex switched beam antenna can be realized by means of a Butler matrix or Rotman

lens, e.g. as described in W. Rotman and R.F. Turner, "Wide-Angle Microwave Lens for Line Source Applications," IEEE Transactions on Antennas and Propagation, November 1963. Thereby, the main lobes are formed by all antenna elements (or radiating elements) together, wherein the Butler matrix or Rotman lens comprises a separate input for each main lobe. Thus, the single antenna element has only a low directivity. If the transceiver is switched to one or more inputs, then one or more simultaneous main lobes can be formed. Switched beam antennas are predominantly assembled with planar antenna arrays with a consequently limited angular range in an azimuthal direction. In principle, a curved or circular arrangement is conceivable, but in this case as well not all antenna elements contribute to the formation of the main lobes resulting in the same disadvantages as in the antenna arrays with MIMO signal processing. Planar switched beam antennas with a Rotman lens are mainly applied in simple radar systems, e.g. for vehicles.

[0008] With mechanically rotating antennas the desired directivity is achieved by a single antenna element (or radiating element) that is rotated or tilted in the desired azimuthal direction. Advantageous is the perfect angular coverage of 360° and the relatively low technical effort, e.g. only one transceiver is required, while the mechanical inertia and the fact that it is not possible to form more than one main lobe at the same time is disadvantageous. Mechanically rotatable antennas are primarily used for ship or plane radars.

[0009] Moreover, when using phased array antennas, the signals of individual antenna elements (or radiating elements) are weighted with complex factors (e.g. amplitude and phase), e.g. as described L.C. Godara, "Application of Antenna Arrays to Mobile Communications, Part II: Beam-Forming and Direction-of-Arrival Considerations," Proceedings of the IEEE, vol. 85, no. 8, August 1997. Hence, each transmit antenna receives an identical, but individually weighted, signal. On the receiver side the individual antenna signals are individually weighted and added. In contrast to antenna arrays with MIMO signal processing, a complete transceiver for each antenna element (or radiating element) is not necessarily required, e.g. a realization with an analog phase shifter for each antenna element may be sufficient. In this case a common transceiver can be used. An upstream or downstream signal processing (unit) on the transmitter or receiveer side thus has no influence on the individual antenna signals. With phased array antennas all antenna elements contribute to the formation of the main lobes. Thus, the single antenna elements only require a small directivity. A planar arrangement of the antennas comprises a restricted angular coverage, wherein curved or circular arrangements have the above mentioned disadvantages. A simultaneous formation of multiple main lobes is limited and has a worse performance than with MIMO signal processing. Therefore, usually no use is made of this possibility. Phased array antennas are primarily used in radar systems and satellite communication, especially for replacing mechanically rotatable antennas.

[0010] There are several technical solutions for estimating the direction that differ in complexity of the transmit receive unit (transceiver) and the usable propagation conditions.

[0011] Systems with MIMO signal processing comprise the highest complexity because each transmit and receive antenna requires a separate transmit receive module. There are numerous known methods for estimating the direction with MIMO signal processing that are applied to mobile communication, e.g. the MUSIC (multiple signal classification) or ESPRIT (estimation of signal parameters via rotational invariance techniques) methods described in R.O. Schmidt, "Multiple Emitter Location and Signal Parameter Estimation," IEEE Transactions on Antennas and Propagation, vols. AP-34, no. 3, March 1986.

[0012] In systems with beamforming signal processing only one transceiver is required per radio station. Numerous methods are known for direction estimation with beamforming signal processing, e.g. as described in P.-J. Chung and J.F. Böhme, "Recursive EM and SAGE-Inspired Algorithms With Application to DOA Estimation," IEEE Transactions on Signal Processing, vol. 53, no. 8, August 2005, D.J. Love and R.W. Heath, "Equal Gain Transmission in Multiple-Input-Multiple-Output Wireless Systems," IEEE Transactions on Communications, Vol. 52, no. 7, July 2003, and S.-H. Wu, L.-K. Lin and S.-J. Chung, "Planar arrays hybrid beamforming for SDMA in millimeter wave applications," Personal, Indoor and Mobile Radio Communications, PIMRC 2008, IEEE 19th International Symposium on, pp. 1-6, 2008. These methods are used, for example, for intercommunication using millimeter waves, e.g. as described in ECMA International, Standard ECMA-387: High Rate 60GHz PHY, MAC and HDMI PAL, Geneva, 2008. These known approaches achieve their greatest performance in multi-path propagation channels. In the communication scenario shown in Fig. 1, an undisturbed line of sight or a single reflection (Fig. 3) of the main propagation path is assumed.

[0013] Besides, there is still the possibility to directly evaluate location information in order to calculate the spatial direction (azimuthal directions) of the transmit and receive antennas when the position of adjacent transceivers is known. Thereby, the location information can be obtained by means of satellite navigation, e.g. GPS (global positioning system). This solution requires that each transceiver is capable of performing a location determination and that each transceiver is capable of communicating this information to the other nodes of the network. Hence, each transceiver must comprise a receiver for the satellite navigation and there must be the possibility for a non-directional wireless data communication, such that the location information can be exchanged before the main lobes are formed. So far this method is used for dynamic alignment of phased array antennas towards airplanes for communicating with satellites.

[0014] In many application cases it is not possible or technically not feasible to generate high transmit powers in an integrated semiconductor. A further parallelization on the semiconductor device would result in large area consumption and high costs and is therefore often not feasible. Furthermore, a high performance cooling concept would be required

in order to dissipate the concentrated dissipation power.

[0015] For the generation of the required power usually multiple power amplifiers are built up discretely and their outputs are combined. Previous solutions to this problem can be separated according to how the output signals of the power amplifiers are combined. When using mechanically oriented directional antennas as well as mechanically oriented directional antennas the power is merged in a power combiner. Power combiners usually comprise cascaded Wilkinson power combiners or 90°-hybrids. These can combine the signals of two inputs to an impedance-controlled output. For example, if 2^n amplifiers should be parallelized, then this can be done by means of a binary tree structure comprising n levels. Depending on the number of amplifiers, these structures can adopt a large structural shape. Furthermore, losses of the power combiner increase with an increasing number of amplifiers, such that from a certain number of amplifiers no significant increase of output power can be achieved. Moreover, inequalities of individual amplifiers may also lead to losses.

[0016] When using MIMO signal processing with separate transceivers per antenna, the signals of the amplifiers are combined in the air as electromagnetic waves, such that the power combiner as a dedicated component can be omitted.

[0017] More complex systems with beamforming signal processing comprise separate transceivers per antenna element (or radiating element) as well. The complex weighting is thereby integrated in the transceivers. Separation or combination of the weighted antenna signals can be performed directly downstream the digital-to-analog conversion or directly before the upstream analog-to-digital conversion. The combination of the transmit signals of the individual transmit amplifiers takes place in the air as electromagnetic waves as well.

[0018] US 2004/0027305 A1 shows a transmit and receiving system including a first array including at least one antenna element disposed to provide a transmit antenna. The system further includes a second array having a second different plurality of antenna elements disposed to provide a receive antenna. The first array is coupled to a switching system, which is operative to selectively form at least one transmit beam. The second array is coupled to a beam combining system, which is operative to selectively form a plurality of receive beams.

[0019] US 2009/0160576 A1 shows a coupling circuit comprising passive analog components for coupling a transceiver to an antenna, such as an antenna array. The coupling circuit transforms an input signal into an appropriate format for each element of the antenna array. The coupling circuit comprises a coupling network having a plurality of inputs and a plurality of outputs. The inputs provide quadriphase versions of at least one input signal. In one embodiment, the coupling circuit performs a Discrete Fourier Transform (DFT) on the input signal. In another embodiment, the coupling circuit performs a Fast Fourier Transform (FFT) on the input signal. In still another embodiment, the FFT performed by the coupling circuit implements a Butler matrix.

[0020] US 2011/090100 A1 refers to the employment of passive signal combiners to transform at least one signal from one domain to another. In some aspects the transformation comprises an NFL an IFFT, a DFT, or an IDFT. The passive signal combiners comprise a set of planar waveguides (e.g., which may be referred to as beamformers or Rotman lenses) that have multiple inputs and outputs and are configured to provide orthogonal output signals. Thereby, an electrical signal (e.g., received via an antenna element) is coupled to passive beamformers that transform the electrical signal from one domain to another domain. A transformation of the electrical signal by a given passive beamformer may have a first resolution, and outputs from the passive beamformers may correspond to orthogonal groups. A combiner circuit may be used to combine the outputs from the passive beamformers and produce a combined output having a second resolution and an associated error.

[0021] It is the object of the present invention to provide a concept for amplifying a transmit signal with an improved power efficiency.

[0022] This object is solved by a transmitter according to claim 1, a transceiver according to claim 6, a method according to claim 10 and a computer program according to claim 11.

[0023] Embodiments of the present invention provide a transmitter comprising a plurality of amplifier circuits, a plurality of antennas adapted to have different main transmit directions and a transformation unit. The transformation unit comprises a plurality of inputs connected to the plurality of amplifier circuits and a plurality of outputs connected to the plurality of antennas. The transformation unit is configured to transform a plurality of amplified transmit signals present at the plurality of inputs into a combined power transmit signal and to provide the combined power transmit signal at one of the plurality of outputs.

[0024] According to the concept of the present invention, a parallel amplification of the transmit signal is achieved by means of the plurality of amplifier circuits, wherein a low loss bundling of the plurality of amplified transmit signals is performed by the transformation unit that is configured to transform the plurality of amplified transmit signals into the combined power transmit signal. Moreover, the transformation unit is configured to provide the combined power transmit signal at one of the plurality of outputs for the antenna connected to the one output. Thus, the combined power transmit signal is radiated by the antenna in the main transmit direction of the antenna.

[0025] In some embodiments of the present invention the transformation unit can be configured to transform the plurality of amplified transmit signals into the combined power transmit signal such that the one output at which the combined power transmit signal is provided is defined by amplitudes and/or phases of the plurality of amplified transmit

signals.

[0026] Moreover, in some embodiments of the present invention the transformation unit can be configured to transform the plurality of amplified transmit power (or signals) into the combined power transmit signal by means of an orthogonal transformation or a discrete Fourier transformation.

[0027] Furthermore, in some embodiments of the present invention the transformation unit can be a high frequency lens, a Rotman lens or a Butler matrix.

[0028] Embodiments of the present invention are described herein making reference to the appended drawings.

Fig. 1 shows a block diagram of a plurality of radio stations that are communicating to each other by means of high frequency signals;

Fig. 2 shows a block diagram of a meshed network formed by the plurality of radio stations shown in Fig. 1;

Fig. 3 shows a block diagram of the radio stations shown in Fig. 1, wherein two of the radio stations are configured as transmitters and the other two as receivers;

Fig. 4 shows a block diagram of a transmitter according to an embodiment of the present invention;

Fig. 5 shows a block diagram of a transmitter according to an embodiment of the present invention;

Fig. 6 shows a block diagram of the transformation unit and the further transformation unit according to an embodiment of the present invention;

Fig. 7 shows a block diagram of a transmitter according to an embodiment of the present invention;

Fig. 8 shows a block diagram of a transmitter according to an embodiment of the present invention;

Fig. 9 shows a block diagram of a transmitter according to an embodiment of the present invention;

Fig. 10 shows a block diagram of a transmitter according to an embodiment of the present invention;

Fig. 11 shows a block diagram of a transmitter according to an embodiment of the present invention;

Fig. 12 shows a block diagram of a transmitter according to an embodiment of the present invention;

Fig. 13 shows a block diagram of a receive path according to an embodiment of the present invention;

Fig. 14 shows a block diagram of a receive path according to an embodiment of the present invention;

Fig. 15 shows a block diagram of a receive path according to an embodiment of the present invention;

Fig. 16 shows a block diagram of a receive path according to an embodiment of the present invention;

Fig. 17 shows a block diagram of a receive path according to an embodiment of the present invention;

Fig. 18 shows a block diagram of a system comprising a first and a second transceiver according to an embodiment of the present invention;

Fig. 19 shows a state diagram of a method for setting-up a connection between a first and a second transceiver according to an embodiment of the present invention.

[0029] Equal or equivalent elements or elements with equal or equivalent functionality are denoted in the following description by equal or equivalent reference numerals.

[0030] In the following description, a plurality of details are set forth to provide a more thorough explanation of embodiments of the present invention. However, it will be apparent to one skilled in the art that embodiments of the preset invention may be practiced without these specific details. In other instances, well-known structures and devices are shown in block diagram form rather than in detail in order to avoid obscuring embodiments of the present invention. In addition, features of the different embodiments described hereinafter may be combined with each other, unless specifically

noted otherwise.

[0031] Fig. 4 shows a block diagram of a transmitter 100 according to an embodiment of the present invention. The transmitter 100 comprises a plurality of amplifier circuits 102, a plurality of antennas 104 adapted to have different main transmit directions and a transformation unit 106. The transformation unit 106 comprises a plurality of inputs 108 connected to the plurality of amplifier circuits 102 and a plurality of outputs 110 connected to the plurality of antennas 104. The transformation unit 106 is configured to transform a plurality of amplified transmit signals present at the plurality of inputs 108 into a combined power transmit signal and to provide the combined power transmit signal at one of the plurality of outputs 110.

[0032] According to the concept of the present invention, a parallel amplification of the transmit signal is achieved by means of the plurality of amplifier circuits 102 (e.g. a plurality of amplifiers), wherein a low loss bundling of the plurality of amplified transmit signals is performed by the transformation unit 106 that is configured to transform the plurality of amplified transmit signals into the combined power transmit signal. Moreover, the transformation unit 106 is configured to provide the combined power transmit signal at one output of the plurality of outputs 110 for the antenna connected to the one output. Thus, the combined power transmit signal is radiated by the antenna in the main transmit direction of the antenna.

[0033] In embodiments, the transformation unit 106 can comprise M inputs 108 and N outputs, wherein M is a natural number greater than or equal to two or three ($M \geq 3$ or $M \geq 2$), and wherein N is a natural number greater than or equal to two or three ($N \geq 3$ or $M \geq 2$). Thereby, in some embodiments, the number of inputs M can be equal to the number of outputs N ($M = N$), wherein in other embodiments the number of inputs M can be unequal to the number of outputs N ($M \neq N$). Since the plurality of amplifier circuits 102 are connected to the plurality of inputs 108 of the transformation unit 106, the number of amplifier circuits can be equal to the number of inputs M of the transformation unit 106.

[0034] In some embodiments, the transformation unit 106 can be configured to transform the plurality of amplified transmit signals into the combined power transmit signal by means of an orthogonal transformation or a discrete Fourier transformation.

[0035] Furthermore, in some embodiments, the transformation unit 106 can be a high frequency lens, a Rotman lens or a Butler matrix.

[0036] Moreover, in some embodiments, the transformation unit 106 can be configured to transform the plurality of amplified transmit signals into the combined power transmit signal such that the one output of the plurality of outputs at which the combined power transmit signal is provided is defined by amplitudes and/or phases of the plurality of amplified transmit signals.

[0037] Hence, by adjusting the amplitudes and/or phases of the plurality of amplified transmit signals that are present at the plurality of inputs 108 of the transformation unit 106, the one output of the plurality of outputs 110 at which the combined power transmit signal is provided can be selected. Thus, the combined power transmit signal can be radiated by the antenna connected to the one output in the main transmit direction of the antenna.

[0038] As already mentioned, the plurality of antennas 104 are adapted to have different main transmit directions. In some embodiments, the plurality of antennas 104 can be directional antennas arranged to have the different main transmit directions. The main transmit directions can be characterized by the main lobes or beams of the plurality of antennas 104. Furthermore, the main transmit directions of the plurality of antennas 104 can be described by azimuthal angles.

[0039] Fig. 5 shows a block diagram of a transmitter 100 according to an embodiment of the present invention. In contrast to Fig. 4, the transmitter 100 comprises a further transformation unit 112 comprising a plurality of inputs 114 and a plurality of outputs 116 connected to the plurality of amplifier circuits 102. The further transformation unit 112 can be configured to transform a transmit signal present at one of the plurality of inputs 114 into a plurality of phase shifted transmit signals such that the input of the plurality of inputs 114 at which the transmit signal is present defines the phases of the plurality of phase shifted transmit signals and to provide the plurality of phase shifted transmit signals at the plurality of outputs 116. The plurality of amplifier circuits 102 can be configured to amplify the plurality of phase shifted transmit signals in order to obtain the plurality of amplified transmit signals.

[0040] In some embodiments, the further transformation unit 112 can be configured to transform the transmit signal into the plurality of phase shifted transmit signals by means of an orthogonal transformation or a discrete Fourier transformation. Moreover, the further transformation unit 112 can be a high frequency lens, a Rotman lens or a Butler matrix. Furthermore, in some embodiments, the transformation unit 106 can be configured to perform a transformation which is inverse to the transformation performed by the further transformation unit 112, such that the one input of the plurality of inputs 114 of the further transformation unit 112 at which the transmit signal is present defines the one output of the plurality of outputs 110 of the transformation unit 106 at which the combined power transmit signal is provided.

[0041] For example, the further transformation unit 112 can be configured to transform the transmit signal present at one of the plurality inputs 114 into the plurality of phase shifted transmit signals present at the plurality of outputs 116 by means of an orthogonal transformation (OT), wherein the transformation unit 106 can be configured to perform an inverse orthogonal transformation (OT^{-1}), which is inverse to the transformation performed by the further transformation

unit 112.

[0042] As shown in Fig. 5, the transmitter 100 can comprise a switching element 118 comprising an input and a plurality of outputs connected to the plurality of inputs 114 of the further transformation unit 112. The switching element 118 (e.g. a switch or a change-over switch) can be configured to provide the transmit signal present at its input at one output of the plurality of its outputs. Hence, the switching element 118 can be used to select the one input of the plurality of inputs 114 of the further transformation unit 112 at which the transmit signal is provided, and thus the one output of the plurality of outputs 110 at which the combined power transmit signal is provided. The combined power transmit signal is radiated by the antenna connected to the one output in the main transmit direction of the antenna.

[0043] In the following, the transformation unit 106 and the further transformation unit 112 are denoted in the drawings with OT (orthogonal transformation unit) and OT^{-1} (inverse orthogonal transformation unit) by way of example. Naturally, the transformation unit 106 and the further transformation unit 112 can be configured to perform any other transformations, including non-orthogonal transformations.

[0044] In some embodiments, the orthogonal transformation units OT and OT^{-1} (106 and 112) are the central components that make the parallel amplification of the transmit signal possible. The transmit direction (or azimuthal angle) can be selected by means of the switching element 118 with which a particular antenna (or radiating element) of the plurality of antennas 104 and thus a particular transmit direction can be determined.

[0045] Fig. 6 shows a block diagram of the transformation unit 106 and the further transformation unit 112 according to an embodiment of the present invention. The further transformation unit 112 can comprise *N* inputs 114 and *M* outputs 116, and be configured to perform an orthogonal transformation (or unitary mapping) of the input signals (present at the *N* inputs 114) to the output signals (present at the *M* outputs 116), wherein *N* and *M* are natural numbers greater than or equal to two or three ($N \geq 3$ or $N \geq 2$; $M \geq 3$ or $M \geq 2$). In Fig. 6, the input signals present at the *N* inputs 114 are denoted with $a_0(t)$ to $a_{N-1}(t)$, wherein the output signals present at the *M* outputs 116 are denoted with $b_0(t)$ to $bM\text{-}1(t)$. The input and output signals can be mathematically described as vectors:

$$a = (a_0, a_1, ..., a_{N-1})$$
$$b = (b_0, b_1, ..., b_{M-1}) \quad (1)$$

[0046] Due to the (orthogonal) transformation performed by the further transformation unit 112, the input signals $a_0(t)$ to $a_{N-1}(t)$ and output signals $b_0(t)$ to $b_{M-1}(t)$ are directly related to each other:

$$b = OT(a) \quad (2)$$

[0047] Thereby, OT describes the mapping function (or representation function) of the further transformation unit 112.

[0048] As already mentioned, the transformation unit 106 can be configured to perform a transformation which is inverse to the transformation performed by the further transformation unit 112. In other words, the transformation unit 106 is an inverse transformation unit.

[0049] The transformation unit 106 can comprise *M* inputs 108 and *N* outputs 110, and be configured to perform an inverse orthogonal transformation (or unitary mapping) of the input signals (present at the *M* inputs 108) to the output signals (present at the *N* outputs 110). The input signals present at the *M* inputs 108 are denoted with $b_0(t)$ to $b_{M-1}(t)$, wherein the output signals present at the *M* outputs 116 are denoted with $c_0(t)$ to $c_{N-1}(1)$. The output signal can be mathematically described as vector:

$$c = (c_0, c_1, ..., c_{N-1}) \quad (3)$$

[0050] Due to the (inverse orthogonal) transformation performed by the transformation unit 106, the input signals $b_0(t)$ to $b_{M-1}(t)$ and output signals $c_0(t)$ to $c_{N-1}(t)$ are directly related to each other:

$$c = OT^{-1}(b) \quad (4)$$

[0051] If the plurality of inputs 108 of the transformation unit 106 are connected to the plurality of outputs 116 of the further transformation 112 unit, then it follows:

$$c = OT^{-1}(OT(a)) = a \tag{5}$$

[0052] This means that the output signals $c_0(t)$ to $c_{N-1}(t)$ of a cascaded (normal) transformation unit (OT) and inverse transformation unit (OT^{-1}) are equivalent to the input signals $a_0(t)$ to $a_{N-1}(t)$.

[0053] The discrete Fourier transformation (DFT) is an orthogonal transformation that fulfills these requirements for a particular class of input signals and that can be implemented in components (or devices) such as in high frequency lenses. The required properties of the input signals are described below.

[0054] In the following, for simplicity it is assumed that the number of inputs are equal to the number of outputs (N = M), nevertheless this is not a necessary requirement. In addition, it is assumed that the discrete Fourier transformation is used as transformation function, nevertheless this is as well not a necessary requirement.

[0055] Fig. 7 shows a transmitter 100 according to an embodiment of the present invention. As shown in Fig. 7, the plurality of (parallel) amplifier circuits 102 are placed (or connected in series) between the plurality of outputs 116 of the further transformation unit 112 (OT) and the plurality of inputs 108 of the transformation unit 106 (OT^{-1}),

[0056] The input signal is applied to the plurality of inputs 114 of the further transformation unit 112. The plurality of outputs 116 of the further transformation unit 112 are connected to the plurality of amplifier circuits 102 which in turn are connected to the plurality of inputs 108 of the transformation unit 106. The transformation unit 106 forms the inverse of the further transformation unit 112 (in the case of the discrete Fourier transformation, both transformation functions (OT and OT^{-1}) may be approximately similar except for an amplitude factor). The plurality of outputs 110 of the transformation unit 106 (form the N output gates and) can be connected to the plurality of transmit antennas 104.

[0057] If the input signal is applied to one (arbitrary) input a_i ($i = 0,1, ...,N$-1) of the plurality of inputs 114 of the further transformation unit 112 and if the further transformation unit 112 is configured to perform a discrete Fourier transformation, then the signal power (of the input signal) is distributed uniformly at the plurality of outputs 116 of the further transformation unit 112 (i.e. same absolute values). The signal power is then amplified in parallel by the plurality of amplifier circuits 102 and concentrated at one output of the plurality of outputs 110 (the (mirrored) output of the plurality of outputs 110 that corresponds to the input of the plurality of inputs 114) by the transformation unit 106. If the component losses are neglected and if an amplification factor (gain) of K is assumed, then the output signal at the selected output 110 of the transformation unit 106 can be calculated to:

$$c = OT^{-1}(K \cdot OT(a)) = OT^{-1}(K \cdot b) = NK \cdot a \tag{6}$$

[0058] In other words, the further transformation unit 112 can be configured to transform the transmit signal present at one input (e.g. a selected input) of the plurality of inputs 114 into the plurality of phase shifted transmit signals and to provide the plurality of phase shifted transmit signals at the plurality of outputs 116. The plurality of amplifier circuits 102 can be configured to amplify the plurality of phase shifted transmit signals in order to obtain the plurality of amplified transmit signals. The transformation unit 106 can be configured to transform the plurality of amplified transmit signals present at the plurality of inputs 108 into the combined power transmit signal and to provide the combined power transmit signal at the one output (e.g. the selected output corresponding (or equivalent) to the selected input) of the plurality of outputs 110 defined by the amplitudes and/or phases of the plurality of amplified transmit signals. In some embodiments, the transmit signal can be one of the input signals $a_0(t)$ to $a_{N-1}(t)$ of the further transformation unit 112, wherein the plurality of phase shifted transmit signals can be the output signals of the further transformation unit 112. Moreover, the plurality of amplified transmit signals can be the inputs signals of the transformation unit 106, wherein the combined power transmit signal can be one of the output signals $c_0(t)$ to $c_{N-1}(t)$ of the transformation unit 106.

[0059] In some embodiments, the first transformation unit 112 may not be implemented as a dedicated device (or component). It is also possible to generate the transformation, which is performed in the above embodiments by the further transformation unit 112, in an arbitrary way and to drive the individual inputs of the plurality of amplifier circuits 102 with the so-generated signals. In that case, the output vector is the transform of the input vector, amplified by the factor *NK*. In some hardware implementations, signals having the same absolute values may be applied to the inputs of the plurality of amplifier circuits 102.

[0060] Fig. 8 shows a block diagram of a transmitter 100 according to an embodiment of the present invention. The

transmitter 100 comprises the plurality of amplifier circuits 102 and the transformation unit 106. The plurality of amplifier circuits 102 can be configured to amplify a transmit signal with controllable gains and/or controllable phase shifts in order to obtain the plurality of amplified transmit signals. The transmitter 100 can be configured to control the gains and/or phase shifts such that the plurality of amplifier circuits 102 provide the plurality of amplified transmit signals with predefined amplitudes and/or phases. The transformation unit 106 can be configured to provide the combined power transmit signal at the one output of the plurality of outputs 110 defined by the amplitudes and/or phases of the plurality of amplified transmit signals.

[0061] In some embodiments, the term "predefined" may refer to a given, calculated, controlled, adapted, set and/or defined value, e.g. phase or amplitude, that can be calculated, controlled, adapted, configured, set and/or defined at runtime or prior to runtime of the transmitter 100.

[0062] In other words, an input signal *a(t)* can be applied (simultaneously) to the *N* inputs of amplifiers 102. The amplifiers 102 can be configured to alter individually the phase relationship and/or phase shift φ_i and the amplification factor (gain) $\hat{a}_i$ of the input signals *a(t).* When using the discrete Fourier transformation, these pairs of values (φ_i, $\hat{a}_i$) can be adjusted (or determined) such that the individual output signals *cj* are arbitrary amplitude shifted and/or phase shifted versions of the input signal *a(t).* Furthermore, these pairs of values (φ_i, $\hat{a}_i$) can be referred to as complex input coefficients d_i. When using a properly built high frequency lens or Butler matrix these pairs of values (φ_i, $\hat{a}_i$) can be calculated directly by means of the discrete Fourier transformation for arbitrary distributions of the output signals.

[0063] Let $c=(c_0,c_1, \ldots , c_{N-1})$ be the desired distribution of the signals at the plurality of outputs 110. The complex input coefficients can be calculated to:

$$d_i = \sum_{l=0}^{N-1} e^{-2\pi j \frac{li}{N}} \cdot c_l \tag{7}$$

[0064] Especially the coefficients that lead to a concentration of the signal energy at one specific output c_j are of interest for the desired change-over switch functionality:

$$c_k = 0 \forall k \neq j \quad \text{with} \quad j \in \{0,1,\ldots,N-1\} \tag{8}$$

[0065] If the discrete Fourier transformation is used and if the above requirements are taken into account, then all amplification factors (gains) may be equal:

$$\hat{a}_i = K \tag{9}$$

[0066] In other words, it may be enough to set at the individual amplifiers the relative phase relationships of the signals. Therewith it follows:

$$c_j = N \cdot K \cdot a(t) \tag{10}$$

[0067] This means that the parallel amplified input signal a(t) is present at one output *cj* of the plurality of outputs 110.

[0068] Hence, the parallel amplified signal can be switched over between the outputs 110 of the transformation unit 106 by proper adjusting the phase relationships (or phase shifts) at the amplifiers 102 (or the phase relationship between the input signals and the amplifiers 102).

[0069] As already mentioned, in some embodiments, the transformation unit 106 can be a high frequency lens. In the following, the construction of such a high frequency lens is mathematically derived by way of example.

[0070] The input signals (present at the plurality of inputs 114) of the inverse transformation unit 106 can be defined as:

$$S_n(t) = A_n f(t - t_n) \tag{11}$$

[0071] Thereby, *f*(*t*) is a common (or mutual) time domain function, Moreover, it is assumed that *f(t)* is a stationary complex function comprising the form $f(t) = be^{j\omega t}$, wherein *b* denotes the (complex) amplitude of the signal, and wherein $\omega = 2\pi f_0$ denotes the frequency of the signal.

[0072] The amplitude shifted, and phase or time shifted input signal $s_n(t)$ thus can be calculated to:

$$s_n(t) = A_n f(t - t_n) = A_n b e^{j\omega(t-t_n)} = A_n b e^{j\omega t_n} e^{j\omega t} = f(t) e^{j\omega t_n} \tag{12}$$

[0073] The path length (or line length) between an input and an output are denoted with $r_{n,m}$. Thereby, the output signal is delayed by $t_{n,m} = r_{n,m}/c_1$ with respect to the input signal due to the corresponding propagation delay (when a change in amplitude is neglected), wherein $c_1 = c_0 \Big/ \sqrt{\varepsilon_r \mu_r}$ is the propagation velocity within the high frequency lens. Thus, the output signal present at one output m of the plurality of outputs 110 can be calculated to:

$$s_m(t) = \sum_n S_n(t - t_{n,m}) = \sum_n A_n f(t - t_{n,m} - t_n) = \sum S_n(t) e^{j\omega t_{n,m}} \tag{13}$$

[0074] Moreover, the inverse discrete Fourier transformation can be calculated to:

$$h(n) = \frac{1}{M} \sum_{m=0}^{M-1} H(m) e^{\frac{2\pi j}{M} nm} \tag{14}$$

[0075] A comparison shows that the transformation function of a high frequency lens can be constructed such that the mapping (or transformation) corresponds to a discrete Fourier transformation of a time discrete signal when the above described requirements are taken into account. If the amplitude is neglected, then it follows:

$$e^{\frac{2\pi j}{M} nm} = \left(e^{j\omega t_{n,m}} = e^{2\pi j f_0 \frac{r_{n,m}}{c_1}} \right) = e^{2\pi j \frac{r_{n,m}}{\lambda_1}} \tag{15}$$

[0076] Thereby, λ_1 is the wavelength within the high frequency lens. Thus, the path length (or line length) within the high frequency lens can be calculated to:

$$r_{n,m} = \frac{\lambda_1}{M} nm + 2\pi k \tag{16}$$

[0077] Thereby, k is a natural number. Since the absolute phase relationship may be irrelevant for the targeted application, in some embodiments, an additional and for all path lengths (or line lengths) equal length ro can be allowed:

$$r_{n,m} = \frac{\lambda_1}{M} nm + 2\pi k + r_0 \qquad (17)$$

[0078] The above restriction of the input signal of the high frequency lens to signals having the form $f(t) = be^{j\omega t}$ can be extended to signals having the form $f'(t) = \Sigma_k b_k e^{jw_k t}$ without restricting the further derivation. Nevertheless, in that case, the consistency (or conformity) between the mapping function of the high frequency lens and the discrete Fourier transformation can be restricted since the phase shifts caused by the signal runtimes within the lens are frequency dependent (variable c in the above derivation).

[0079] In that case, the shape of the high frequency lens can be chosen such that an error of the mapping function is reduced for a given frequency range. In addition, the high frequency lens can be filled with a dispersive medium that compensates phase differences and/or runtime differences between different frequencies such that the error of the mapping function can be reduced (or even minimized) for a larger frequency range.

[0080] The above mathematical derivation describes the requirements that the high frequency lens may fulfill in order to perform the inverse discrete Fourier transformation. However, embodiments of the present invention also require the inverse of the inverse transformation, i.e. the actual transformation. If the discrete Fourier transformation is used, then the actual transformation can be provided by exchanging the inputs and outputs. This relationship can be easily described by means of the matrix of the discrete Fourier transformation which describes the sum as a matrix and the data to be transformed as a vector. The result of a multiplication of the matrix with the data vector yields exactly to the discrete Fourier transformation.

[0081] The exchanging rules are very simple. The first row remains unchanged. The remaining rows of the matrix of the discrete Fourier transformation (*1, 2,* ..., *N*) have to be reversed in sequence (*N*, ..., *2, 1*). Alternatively, it is also possible to rename the inputs and outputs, respectively.

[0082] In the following, different embodiments of the transmitter 100 and the corresponding signal processing are described. Moreover, in the following embodiments, the formation of a single beam by bundling the signal energy at a single output of the plurality of outputs 110 of the transformation unit 106 is considered by way of example. Nevertheless, further distributions of the signal energy at the plurality of outputs 110 can be achieved, for example, by varying the gains and/or phase shifts of the plurality of amplifier circuits 102. Fig. 9 shows a transmitter 100 according to an embodiment of the present invention. The transmitter 100 can comprise the plurality of amplifier circuits 102, the plurality of antennas 104 adapted to have different main transmit directions, the transformation unit 106 and the further transformation unit 112 as already described in detail above. In addition, the transmitter can comprises a local oscillator 128 configured to provide a local oscillator signal, a switching element 118 comprising an input and a plurality of outputs, and a mixer 136. The mixer 136 can be configured to mix a baseband or intermediate frequency transmit signal with the local oscillator signal in order to provide the transmit signal. The switching element 118 (e.g. a switch or a change-over switch) can be configured to provide the transmit signal present at its input at a selected output of its plurality of outputs, wherein the plurality of outputs of the switching element 118 can be connected to the plurality of inputs 114 of the further transformation unit 112.

[0083] As shown in Fig. 9, the transformation unit 106 and the further transformation unit 112 can be Rotman lenses (RL), e.g. operated at a frequency of 60 GHz (or at frequency in the range between 30 GHz to 100 GHz, 10 GHz to 500 GHz, or 1 GHz to 1000 GHz). The phase shifts can be generated by the further transformation unit 112 (RL), wherein the power can be combined by the transformation unit 106 (RL). Thereby, the functionality of the transmitter 100 corresponds to the above description and/or mathematical derivation.

[0084] The output of the plurality of outputs 110 at which the combined power transmit signal is provided and thus the main transmit direction (or desired beam or main lobe) in which the combined power transmit signal is radiated can be controlled (or selected) by means of the switching element 118, e.g. a mechanic or electronic switch operated at a frequency of 60 GHz (or at frequency in the range between 30 GHz to 100 GHz, 10 GHz to 500 GHz, or 1 GHz to 1000 GHz) on the input side. In contrast to state of the art solutions, the insertion losses of the switching element 118 are not caused within the power path downstream the amplifiers 102. Thus, the insertion losses of the switching element 118 are small compared to those state of the art solutions.

[0085] Note that different line lengths between the outputs 116 of the further transformation unit 112 (first Rotman lens) and the inputs of the transformation unit 106 (second Rotman lens) may result in an relative alternation of the phases of the signals present at the inputs 108 of the transformation unit 106. This could disturb the beam forming performed by the transformation unit 106 (second Rotman lens) and is denoted in the drawings with "critical line length". Thus, in some embodiments, the line lengths are equal.

[0086] Fig. 10 shows a transmitter 100 according to an embodiment of the present invention. The transmitter 100 can comprise the plurality of amplifier circuits 102, the plurality of antennas 104 adapted to have different main transmit

directions, the transformation unit 106 and the further transformation unit 112 as already described in detail above. In addition, the transmitter 100 can comprise a local oscillator 128 configured to provide a local oscillator signal, a switching element 118 comprising an input and a plurality of outputs, and a plurality of mixers 136. The plurality of mixers 136 can be connected in series between the plurality of outputs of the switching element 118 and the plurality of inputs 114 of the further transformation unit 112. The switching element 118 can be configured to provide a baseband or intermediate frequency transmit signal present at its input at a selected output of its plurality of outputs. Each mixer of the plurality of mixers 136 can be configured to mix the baseband or intermediate transmit signal present at the selected output of the plurality of outputs of the switching element 118 with the local oscillator signal in order to provide the transmit signal.

[0087] The embodiment of the transmitter 100 shown in Fig. 10 differs from the embodiment shown in Fig. 9 by the fact that the switching over is performed in the baseband or at the intermediate frequency. The subsequent up mixing to the high frequency carrier frequency is performed for each input of the further transformation unit 112 (first Rotman lens) with a separate mixer. In general, the switching over of the signals is easier to realize in the baseband (or at the intermediate frequency) than at the high frequency carrier frequency.

[0088] Fig. 11 shows a transmitter 100 according to an embodiment of the present invention. The transmitter can comprise the plurality of amplifier circuits 102, the plurality of antennas 104 adapted to have different main transmit directions, and the transformation unit 106 as already described in detail above. In addition, the transmitter 100 can comprise a local oscillator 128 configured to provide a local oscillator signal and a local oscillator transformation unit 140. The local oscillator transformation unit 140 can comprise a plurality of inputs 142 and a plurality of outputs 144. The local oscillator transformation unit 140 can be configured to transform the local oscillator signal present at one of the plurality of inputs 142 into a plurality of phase shifted local oscillator signals such that the input at which the local oscillator signal is present defines the phases of the plurality of phase shifted local oscillator signals and to provide the plurality of phase shifted local oscillator signals at the plurality of outputs 144. Furthermore, the plurality of amplifier circuits 102 can comprise control inputs 146 connected to the plurality of outputs 144 of the local oscillator transformation unit 140. The plurality of amplifier circuits 102 can be configured to obtain the plurality of amplified transmit signals based on mixing a baseband or an intermediate frequency transmit signal or amplified versions thereof with the plurality of phase shifted local oscillator signals present at the control inputs 146, thereby applying the phases of the plurality of phase shifted local oscillator signals to the plurality of amplified transmit signals.

[0089] In some embodiments, the local oscillator transformation unit 140 can be configured to transform the local oscillator signal into the plurality of phase shifted local oscillator signals by means of an orthogonal transformation or a discrete Fourier transformation. The local oscillator transformation unit 140 can be a high frequency lens, a Butler matrix, or as shown in Fig. 11 a Rotman lens.

[0090] In other words, another possibility to control the beam (or main lobe) is to generate the necessary phase shifts at the frequency of the local oscillator. The so-generated local oscillator signals can be transformed by the local oscillator transformation unit 140 (or first Rotman lens) and afterwards mixed and amplified in parallel with the baseband transmit signal. The plurality of amplified transmit signals are then transformed by the transformation unit 106 (second Rotman lens) into the combined power transmit signal.

[0091] Fig. 12 shows a block diagram of a transmitter 100 according to an embodiment of the present invention. The transmitter 100 can comprise the plurality of amplifier circuits 102, the plurality of antennas 104 adapted to have different main transmit directions, and the transformation unit 106 as already described in detail above. In addition, the transmitter 100 can comprise a local oscillator 128 configured to provide a local oscillator signal and a plurality of controllable phase shifters 150. The plurality of controllable phase shifters can be connected to the local oscillator 128 and configured to provide a plurality of phase shifted local oscillator signals having predefined phases. Thereby, the plurality of amplifier circuits 102 can comprise control inputs 146 connected to the plurality of controllable phase shifters 150. The plurality of amplifier circuits 102 can be configured to obtain the plurality of amplified transmit signals based on mixing a baseband or intermediate frequency transmit signal or amplified versions thereof with the plurality of phase shifted local oscillator signals present at the control inputs 146, thereby applying the phases of the plurality of phase shifted local oscillator signals to the plurality of amplified transmit signals.

[0092] In other words, another possibility is to generate the required phase shifts of the local oscillator signals by means of individually programmable phase shifters 150. Thus, different or varying line lengths can be compensated or calibrated out such that the layout of the transmitter 100 can be simplified.

[0093] Fig. 13 shows a block diagram of a receive path 200 of a transceiver according to an embodiment of the present invention. In some embodiments, the transceiver can comprise the transmitter 100 as described above and the receive path 200 shown in Fig. 13. The receive path 200 can comprise an output 202 and a plurality of receive path amplifiers 204 connected in series between the output 202 and the plurality of antennas 104. The plurality of antennas 104 can be adapted to have different main receive directions in order to receive a plurality of receive signals from the different main receive directions.

[0094] Note that in Fig. 13, four antennas 104 and four receive path amplifiers 204 are shown by way of example. In general, the receive path 200 can comprise *N* receive path amplifiers 204 connected to *N* antennas 104. In some

embodiments, the number *N* of antennas and the number *N* of receive path amplifiers 204 can be equal to the number *N* of outputs of the transformation unit 106 of the transmitter 100.

[0095] In some embodiments, the plurality of receive path amplifiers 204 can be connected in series between the plurality of antennas 104 and the output 202 of the receive path 200 by means of a switching element 206 comprising an output and a plurality of inputs such that the plurality of inputs are connected to the plurality of receive path amplifiers 204 and the output to the output 202 of the receive path 200.

[0096] In other words, Fig. 13 shows the receive path (or receiver) 200 corresponding to the transmitter 100. The plurality of antennas 104 are connected to separate receive path amplifiers 204. The selection of one of the plurality of antennas 104 and thus of a receive direction can be performed by means of the switching element 206 (e.g. a switch or a change-over switch).

[0097] Fig. 14 shows a block diagram of a receive path 200 according to an embodiment of the present invention. The receive path 200 can comprise an output 202 and a plurality of receive path amplifiers 204 connected in series between the output 202 and the plurality of antennas 104. The plurality of antennas 104 can be adapted to have different main receive directions in order to receive a plurality of receive signals from the different main receive directions.

[0098] In other words, the receive path 200 shown in Fig. 14 can be used for selecting the receive signal or the antenna receiving the receive signal. Each antenna of the plurality of antennas 104 can be connected to an amplifier 204, e.g. a low noise high frequency amplifier (LNA) 204, and to an optional mixer that can be configured to down mix the receive signal to an intermediate frequency or a baseband. The downstream signal processing of the receive path (e.g. analog-to-digital conversion, reconstruction of data) is thus performed only once for the combined signals present at the output 202 of the receive path 200. In contrast to this, MIMO receivers require a parallel processing of all receive signals. As indicated in Fig. 14, the signal of the desired antenna (and hence remote station) can be received by activating (or selecting, or switching on) the corresponding amplifier.

[0099] Moreover, although beamforming receivers and beamforming transmitters may require only a single signal processing unit when using a planar antenna array, there is the problem that when using a non-planar antenna array, averted antennas only increase the noise ratio.

[0100] Fig. 15 shows a block diagram of a receive path 200 according to an embodiment of the present invention. The plurality of receive path amplifiers 204 can be switchable between a switch on state and a switch off state in order to select one of the plurality of antennas for receiving the receive signal. The plurality of receive path amplifiers 204 can be configured to provide an output impedance that is in the switch on state adapted to a specific impedance of the receive path 200, and in the switch off state at least by a factor of 10 (or 20, 30, 40, 50, 100, 200, 300 or 1000) higher than the specific impedance of the receive path 200.

[0101] In some embodiments, the plurality of receive path amplifiers 204 can comprise inputs 208, e.g. control inputs or supply voltage inputs, and be adapted to switch over between the switch on state and the switch off state based on a signal, e.g. a control signal or supply voltage, present at the inputs 208.

[0102] Note that in Fig. 15, a first receive path amplifier 204_1 (comprising a (control) input 208_1) connected in series between a first antenna 104_1 and the output 202, and a second receive path amplifier 204_2 (comprising a (control) input 208_2) connected in series between a second antenna 104_2 and the output 202 are shown for illustration purposes.

[0103] Thereby, Fig. 15 shows the typical properties of the first and second receive path amplifiers 204_1 and 204_2. The first and second receive path amplifiers (e.g. low noise amplifiers) 204_1 and 204_2 can be switched on (or activated) or switched off (or deactivated) by means of a supply voltage or by any other means. Therefore, the receive path amplifiers 204_1 and 204_2 can comprise control inputs 208_1 and 208_2 (e.g. enable inputs). In Fig. 15, the first amplifier 204_1 is shown in the switch-off state ("zero" present at the input 208_1), wherein the second receive path amplifier 204_2 is shown in the switch-on state ("one" present at the input 208_2). The outputs of the first and second receive path amplifiers 204_1 and 204_2 can be connected by means of lines, e.g. transmission lines, having a specific impedance Z_0 and length $(2N+1)\lambda/2$ to the output 202. The first and second receive path amplifiers 204_1 and 204_2 can be adapted to have in the switch off state (or deactivated state) an output impedance that is at least by a factor of 10 higher (ideally infinite) than the specific impedance Z_0. In the switch on state (or active state) the output impedance corresponds to the specific line impedance Z_0. The high output impedance (ideally infinite output impedance) of the switched off receive path amplifier 204_1 is mapped to the output 202 by means of the line connecting the first amplifier 204_1 and the output 202. Thus, the impedance of the line connecting the switched on amplifier 204_2 and the output 202 appears to be ideally matched to the specific impedance Z_0. Hence, no additional matching network may be required even if a plurality of receive path amplifiers 204 are interconnected.

[0104] The common output 202 of the (low noise) receive path amplifiers 204 can thus be connected to a further signal processing unit (not shown). By switching on (or activating) a selected receive path amplifier 204 the signal present at the input of the selected (low noise) receive path amplifier can be switched to the common output 202.

[0105] Fig. 16 shows a block diagram of a receive path 200 according to an embodiment of the invention. The receive path 200 comprises the plurality of antennas 104, the plurality of receive path amplifiers 204 connected to the plurality of antennas 104, and the output 202. Furthermore, the receive path 200 can comprise a receive path local oscillator

210 configured to provide a receive path local oscillator signal, a plurality of receive path mixers 212 connected in series between the plurality of receive path amplifiers 204 and the output 202 of the receive path 200, and a receive path switching element 206. Thereby, the plurality of receive path mixers 212 can be connected in series between the plurality of receive path amplifiers 204 and the output 202 of the receive path 200 by means of the receive path switching element 206 such that a plurality of inputs of the receive path switching element 206 are connected to the plurality of receive path mixers 212 and an output of the receive path switching element 206 is connected to the output 202 of the receive path 200. The switching element 206 can be used to select one of the plurality of receive signals (or amplified and down mixed versions thereof). The local oscillator can be running at a frequency of, for example, 1 GHz, 7,5 GHz, 15 GHz, 30 GHz, 60 GHz or 100 GHz.

[0106] As shown in Fig. 16, the switching over between the receive signals can be performed at the intermediate frequency (or in the baseband). The receive signals received by the plurality of antennas 104 can be amplified by the plurality of (parallel) receive path amplifiers 204 and down mixed to the intermediate frequency (or baseband). Afterward, the desired receive signal can be selected by means of the switching element 206 (e.g. an electrical or mechanical switch) and be further processed, e.g. by a signal processing unit (not shown).

[0107] Fig. 17 shows a block diagram of a receive path according to an embodiment of the present invention. The receive path 200 comprises the plurality of antennas 104, the plurality of receive path amplifiers 204 connected to the plurality of antennas 104, and the output 202. Furthermore, the receive path 200 can comprise a receive path local oscillator 210 configured to provide a receive path local oscillator signal, a plurality of receive path mixers 212 connected in series between the plurality of receive path amplifiers 204 and the output 202 of the receive path 200, and a receive path switching element 206. Thereby, the receive path switching element 206 comprises an input connected to the receive path local oscillator 210 and a plurality of outputs connected to the plurality of receive path mixers 212.

[0108] In contrast to Fig. 16, where the switching over is performed in the signal path, the switching over between the receive signals is performed in Fig. 17 at the frequency of the local oscillator 210 (e.g. 1 GHz, 7,5 GHz, 15 GHz, 30 GHz, 60 GHz or 100 GHz). Thereby, the plurality of receive path amplifiers 204 and/or plurality of mixers 212 can be switched on or off separately in order to match the line impedances as described above.

[0109] Fig. 18 shows a block diagram of a system 400 comprising a first and a second transceiver 300_1 and 300_2 according to an embodiment of the present invention. Each of the first and a second transceivers 300_1 and 300_2 can comprise a transmitter 100 and a receive path 200 as described in the above embodiments.

[0110] As exemplarily shown in Fig. 18, each of the first and second transceivers 300_1 and 300_2 can comprise four (directional) antennas 104_1 to 104_4 adapted to have different main transmit/receive directions, wherein each antenna of the four antennas 104_1 to 104_4 can be adapted to cover an azimuthal angle of 90° (indicated in Fig. 18 by the dotted lines).

[0111] Setting up a connection between the transceivers 300_1 and 300_2 can be challenging when using directional antennas since the transceivers 300_1 and 300_2 do not necessarily know the exact position of each other. In order to set up a connection, it can be required to determine the relative position of the other transceiver and to select an optimal directional antenna and hence an optimal transmission path.

[0112] As already mentioned, the power of the plurality of amplified transmit signals is bundled by the transformation unit 106 to one output of the plurality of outputs 110 and hence to one main lobe or beam. Driving the plurality of outputs 110 in parallel is only possible if merely one amplifier of the plurality of amplifiers 102 is active. In that case, the achievable transmission power for each antenna is considerably smaller.

[0113] Nevertheless, on the receiver side is possible to receive simultaneously the signals of the plurality of antennas 104 if a matching of impedances is taken into account. However, assuming a constant signal power, the noise power at the at the output 202 of the receive path 200 is increased since the uncorrelated noise levels of the plurality of receive path amplifiers 204 are added.

[0114] According to the concept of the present invention, in order to set up the connection between the first and second transceiver 300_1 and 300_2, the increased noise power at the output 202 of the receive path 200 can be compensated by means of code spreading. The signal to noise ratio depends on the implementation of the plurality of (parallel) receive path amplifiers 204, but is in general not better than the signal to noise ratio of a single antenna and the corresponding reduced gain. Thus, the signal to noise ratio is reduced at least by $B = 10log(N)\ dB$, wherein N is the number of antennas 104. This loss of signal to noise ratio can be compensated by using a direct sequence CDMA (code division multiple access) code having a number of chips N_C of $N_C \geq N$.

[0115] Furthermore, according to the concept of the present invention, the procedure of setting up the connection (selecting the appropriate antenna and/or beam) can be accelerated if the relative position of the other transceiver is known. The direction of the other transceiver can be calculated directly by calculating the difference of the positions. Thereby, each transceiver can be configured to determine its position by means of satellite navigation (e.g. GPS) and/or position sensors (e.g. gravitational sensors or a compass). If a separate data channel is available between the transceivers, then the data channel can be used to exchange position data. This data channel can be a unidirectional radio channel having a high spreading factor and thus a high spreading gain since the amount of data to be exchanged can be small.

[0116] Fig. 19 shows a state diagram of a method for setting up a connection between the first and second transceiver 300_1 and 300_2 shown in Fig. 18. Thereby, it is assumed by way of example that the first transceiver 300_1 performs the following steps. Naturally, the following steps can also be performed by the second transceiver 300_2.

[0117] At the start the first transceiver 300_1 can be in a first state (TX ID) 500. In this state, the first transceiver 300_1 can transmit subsequently with all antennas 104 a certain spreading code sequence. After a given time span t_{TX} the first transceiver 300_1 can pass over to a second state (RX omnidir.) 502 in which the first transceiver 300_1 can use all antennas 104 to scan for signals of the second transceiver 300_2. If no second transceiver 300_2 can be detected within a given time span t_{RX}, then the first transceiver 300_1 can pass over again to the first state (TX ID) 500.

[0118] If the second transceiver 300_2 is detected, then the first transceiver 300_1 can determine the direction of the second transceiver 300_2 by switching the antennas 104 individually (e.g. to the receiver or signal processing unit) until the strongest receive signal is detected. Thereby, it may have to be taken into account that the identifier is only transmitted in limited time slots.

[0119] If the characteristics (main lobes) of adjacent antennas 104 overlap, then scanning can be accelerated. For example, to begin with, the antennas not having overlapping characteristics (main lobes) may be scanned (e.g. starting with a random antenna). Afterwards, the remaining antennas may be scanned. Moreover, as soon as a receive signal is detected, the adjacent antennas can be scanned in order to detect the receive maxima.

[0120] As soon as the first transceiver 300_1 detects a receive signal of the second transceiver 300_2, the first transceiver 300_1 can pass over to a third state (RX dir. estim.) 504 in which an improved (or even optimal) beam form can be determined, e.g. by trying. Afterwards, the first transceiver 300_1 can transmit its own identifier in the direction of the second transceiver 300_2 in a fourth state (TX EST in dir.) 506 and wait for a confirmation from the second transceiver 300_2 in a fifth state (RX in dir.) 508. This procedure can be repeated for N times and if no reply is received then the first transceiver can pass over to the second state (RX omnidir.) 502, or in other words, setting up the connection can be started over again.

[0121] If the first transceiver 300_1 receives a confirmation from the second transceiver 300_2, then the first transceiver 300_1 can pass over to a sixth state (connect) 510 in which the connection (or link) to the second transceiver 300_2 is established.

[0122] The selection of the different time slots can be matched such that it can be guaranteed that the first and second transceivers 300_1 and 300_2 (e.g. two arbitrary receivers that are operated asynchronously) are not transmitting continuously at the same time and hence may not find each other. Therefore, the timespan t_{RX} for signal scanning can be extended by random timespans respectively.

[0123] Further embodiments of the present invention provide a method for operating a transmitter, wherein the transmitter comprises a plurality of amplifier circuits, a plurality of antennas adapted to have different main transmit directions, and a transformation unit comprising a plurality of inputs connected to the plurality of amplifier circuits and a plurality of outputs connected to the plurality of antennas. In a first step, the plurality of amplified transmit signals present at the plurality of inputs of the transformation unit are transformed into a combined power transmit signal. In a second step, the combined power transmit signal is provided at one of the plurality of outputs of the transformation unit.

[0124] Embodiments of the present invention provide a transmitter configured to bundle simultaneously a transmit signal (or transmit signals) in the direction of one or more receive stations. Thereby, the transmitter can be configured to cover an azimuthal angle of 360°. Furthermore, the transmitter can be configured to adapt the main lobe(s) to the position(s) of the receive station(s), i.e. changing the azimuth angle. The transmitter can be configured to estimate the azimuth angle(s) in order to provide a dynamic alignment of the main lobe(s). In addition, the transmitter can be capable of providing sufficient transmit power for providing the just mentioned functionality.

[0125] Further embodiments of the present invention provide a receive path that is configured to form simultaneously one or more main lobes in the direction of one or more transmitters. Thereby, the receive path can be configured to cover an azimuthal angle of 360°. Furthermore, the receive path can be configured to adapt the main lobe(s) to the position(s) of the transmitter(s), i.e. changing the azimuth angle. The receive path can be configured to estimate the azimuth angle(s) in order to provide a dynamic alignment of the main lobe(s).

[0126] The herein presented concept for parallel amplification and switching over or distribution of the transmit signal to one or more outputs has specific advantages compared to prior art solutions. The transmitter 100 comprising a high frequency lens as transformation unit comprises small losses compared to traditional power combiner networks. In addition, the size of the high frequency lens increases (only) linearly with the number of inputs and outputs and not quadratically as it is the case when using cascaded structures of simple 2:1 power dividers.

[0127] The transmitter 100 according to the concept of the present invention contains no mechanically moving components. Thus, the transmitter 100 can be assembled in a compact manner and be robust against external influences. In addition, the transmitter 100 according to the concept of the present invention does not contain any consumables such that the transmitter 100 does not require (additional) maintenance and is in principle not limited in life time. Furthermore, the transmitter 100 is able to switch over between the outputs without delay since no mechanical components have to be moved.

[0128] In contrast to some state of the art solutions, the transmitter 100 does not require an electronic switch due to the transformation unit 106. Thus, the presented solution has lower losses. In addition, the transmitter 100 is capable of generating any distribution of the signals at the outputs. When using electronic switches this can be realized only with very complex circuits. However, when generating arbitrary signal distributions at the plurality of outputs 110 parallelization in amplification is reduced since the plurality of amplifier circuits 102 are not driven with signals having the same absolute values.

[0129] When using circular beamforming arrays not all antenna elements (or radiating elements) can contribute to the generation of the signal since each antenna element is driven by an individual amplifier and since the different antenna elements may shield each other. In contrast to this, in embodiments all amplifiers 102 contribute to the generation of the combined power output signal.

[0130] Moreover, in order to calculate the beamforming coefficients, knowledge about the exact positioning of the antenna layout is required. Furthermore, the calculation of the beamforming coefficients has to be adapted to the antenna layout. In contrast to this, the transformation function according to the concept of the present invention can be equivalent to the (fast) Fourier transformation that is efficient to implement and independent of the position of the plurality of antennas.

[0131] Although some aspects have been described in the context of an apparatus, it is clear that these aspects also represent a description of the corresponding method, where a block or device corresponds to a method step or a feature of a method step. Analogously, aspects described in the context of a method step also represent a description of a corresponding block or item or feature of a corresponding apparatus. Some or all of the method steps may be executed by (or using) a hardware apparatus, like for example, a microprocessor, a programmable computer or an electronic circuit. In some embodiments, some one or more of the most important method steps may be executed by such an apparatus.

[0132] Depending on certain implementation requirements, embodiments of the invention can be implemented in hardware or in software. The implementation can be performed using a digital storage medium, for example a floppy disk, a DVD, a Blu-Ray, a CD, a ROM, a PROM, an EPROM, an EEPROM or a FLASH memory, having electronically readable control signals stored thereon, which cooperate (or are capable of cooperating) with a programmable computer system such that the respective method is performed. Therefore, the digital storage medium may be computer readable.

[0133] Some embodiments according to the invention comprise a data carrier having electronically readable control signals, which are capable of cooperating with a programmable computer system, such that one of the methods described herein is performed.

[0134] Generally, embodiments of the present invention can be implemented as a computer program product with a program code, the program code being operative for performing one of the methods when the computer program product runs on a computer. The program code may for example be stored on a machine readable carrier.

[0135] Other embodiments comprise the computer program for performing one of the methods described herein, stored on a machine readable carrier.

[0136] In other words, an embodiment of the inventive method is, therefore, a computer program having a program code for performing one of the methods described herein, when the computer program runs on a computer.

[0137] A further embodiment of the inventive methods is, therefore, a data carrier (or a digital storage medium, or a computer-readable medium) comprising, recorded thereon, the computer program for performing one of the methods described herein. The data carrier, the digital storage medium or the recorded medium are typically tangible and/or non-transitionary.

[0138] A further embodiment of the inventive method is, therefore, a data stream or a sequence of signals representing the computer program for performing one of the methods described herein. The data stream or the sequence of signals may for example be configured to be transferred via a data communication connection, for example via the Internet.

[0139] A further embodiment comprises a processing means, for example a computer, or a programmable logic device, configured to or adapted to perform one of the methods described herein.

[0140] A further embodiment comprises a computer having installed thereon the computer program for performing one of the methods described herein.

[0141] A further embodiment according to the invention comprises an apparatus or a system configured to transfer (for example, electronically or optically) a computer program for performing one of the methods described herein to a receiver. The receiver may, for example, be a computer, a mobile device, a memory device or the like. The apparatus or system may, for example, comprise a file server for transferring the computer program to the receiver.

[0142] In some embodiments, a programmable logic device (for example a field programmable gate array) may be used to perform some or all of the functionalities of the methods described herein. In some embodiments, a field programmable gate array may cooperate with a microprocessor in order to perform one of the methods described herein. Generally, the methods are preferably performed by any hardware apparatus.

[0143] The above described embodiments are merely illustrative for the principles of the present invention. It is understood that modifications and variations of the arrangements and the details described herein will be apparent to others skilled in the art. It is the intent, therefore, to be limited only by the scope of the impending patent claims and not

by the specific details presented by way of description and explanation of the embodiments herein.

Claims

1. Transmitter (100), comprising:

   a plurality of amplifier circuits (102);
   a plurality of antennas (104) adapted to have different main transmit directions; and
   a transformation unit (106) comprising a plurality of inputs (108) connected to the plurality of amplifier circuits (102) and a plurality of outputs (110) connected to the plurality of antennas (104), wherein the transformation unit (106) is configured to transform a plurality of amplified transmit signals present at the plurality of inputs (108) into a combined power transmit signal and to provide the combined power transmit signal at one of the plurality of outputs (110);
   wherein the transformation unit (106) is configured to transform the plurality of amplified transmit signals into the combined power transmit signal such that the one output at which the combined power transmit signal is provided is defined by amplitudes and/or phases of the plurality of amplified transmit signals; and
   wherein the plurality of amplifier circuits (102) are configured to amplify a transmit signal with controllable gains and/or controllable phase shifts in order to obtain the plurality of amplified transmit signals, wherein the transmitter (100) is configured to control the gains and/or phase shifts such that the plurality of amplifier circuits (102) provide the plurality of amplified transmit signals with predefined amplitudes and/or phases, wherein the transformation unit (106) is configured to provide the combined power transmit signal at the one output defined by the amplitudes and/or phases of the plurality of amplified transmit signals.

2. Transmitter (100) according to claim 1, wherein the transformation unit (106) is configured to transform the plurality of amplified transmit signals into the combined power transmit signal by means of an orthogonal transformation or a discrete Fourier transformation.

3. Transmitter (100) according to claim 1 or 2, wherein the transformation unit (106) is a high frequency lens, a Rotman lens or a Butler matrix.

4. Transmitter (100) according to claim 1 to 3, wherein the transmitter (100) further comprises:

   a local oscillator (128) configured to provide a local oscillator signal; and
   a local oscillator transformation unit (140) comprising a plurality of inputs (142) and a plurality of outputs (144), wherein the local oscillator transformation unit (140) is configured to transform the local oscillator signal present at one of the plurality of inputs (142) into a plurality of phase shifted local oscillator signals such that the input at which the local oscillator signal is present defines the phases of the plurality of phase shifted local oscillator signals and to provide the plurality of phase shifted local oscillator signals at the plurality of outputs (144);
   wherein the plurality of amplifier circuits (102) comprise control inputs (146) connected to the plurality of outputs (144) of the local oscillator transformation unit (140), wherein the plurality of amplifier circuits (102) are configured to obtain the plurality of amplified transmit signals based on mixing a baseband or intermediate frequency transmit signal or amplified versions thereof with the plurality of phase shifted local oscillator signals present at the control inputs (146), thereby applying the phases of the plurality of phases shifted local oscillator signals to the plurality of amplified transmit signals.

5. Transmitter (100) according to claim 1 to 3, wherein the transmitter (100) further comprises:

   a local oscillator (128) configured to provide a local oscillator signal; and
   a plurality of controllable phase shifters (150) connected to the local oscillator (128) and configured to provide a plurality of phase shifted local oscillator signals having predefined phases;
   wherein the plurality of amplifier circuits (102) comprise control inputs (146) connected to the plurality of controllable phase shifters, wherein the plurality of amplifier circuits (102) are configured to obtain the plurality of amplified transmit signals based on mixing a baseband or intermediate frequency transmit signal or amplified versions thereof with the plurality of phase shifted local oscillator signals present at the control inputs (146), thereby applying the phases of the plurality of phases shifted local oscillator signals to the plurality of amplified transmit signals.

6. Transceiver (300), comprising:

a transmitter (100) according to one of the claims 1 to 5; and
a receive path (200), wherein the receive path (200) comprises:

an output (202); and
a plurality of receive path amplifiers (204) connected in series between the output (202) and the plurality of antennas (104), wherein the plurality of antennas (104) are adapted to have different main receive directions in order to receive a plurality of receive signals from the different main receive directions.

7. Transceiver (300) according to claim 6, wherein the plurality of receive path amplifiers (204) are switchable between a switch on state and a switch off state, wherein each receive path amplifier of the plurality of receive path amplifiers (204) is configured to provide at its output an impedance that is in the switch on state adapted to a specific impedance of the receive path (200) and that is in the switch-off state at least by a factor of 10 higher than the characteristic impedance of the receive path (200).

8. Transceiver (300) according to claim 6 or 7, wherein the receive path (200) further comprises:

a receive path local oscillator (210) configured to provide a receive path local oscillator signal;
a plurality of receive path mixers (212) connected in series between the plurality of receive path amplifiers (204) and the output (202) of the receive path (200); and
a switching element (206);
wherein the receive path switching element (206) comprises an input connected to the receive path local oscillator and a plurality of outputs connected to the plurality of receive path mixers (212); or
wherein the plurality of receive path mixers (212) are connected in series between the plurality of receive path amplifiers (204) and the output (202) of the receive path (200) by means of the receive path switching element (206) such that a plurality of inputs of the receive path switching element (206) are connected to the plurality of receive path mixers and an output of the receive path switching element is connected to the output (202) of the receive path (200).

9. System (400), comprising:

a first and a second transceiver (300) according to one of the claims 6 to 8;
wherein the first transceiver is configured to transmit a transmit signal comprising a spreading code subsequently with each antenna of the plurality of its antennas in order to establish a connection between the first and second transceiver; and
wherein the second transceiver is configured to receive simultaneously a plurality of receive signals with the plurality of its antennas, to derive a direction from which the transmit signal is received based on the plurality of receive signals, and to select the antenna of the plurality of antennas having the main receive directions that corresponds to the direction from which the transmit signal is received, in order to establish the connection between the first and second transceiver.

10. Method for operating a transmitter, wherein the transmitter comprises a plurality of amplifier circuits, a plurality of antennas adapted to have different main transmit directions, and a transformation unit comprising a plurality of inputs connected to the plurality of amplifier circuits and a plurality of outputs connected to the plurality of antennas, wherein the method comprises:

amplifying a transmit signal with controllable gains and/or controllable phase shifts in order to obtain the plurality of amplified transmit signals;
controlling the gains and/or phase shifts such that the plurality of amplifier circuits provide the plurality of amplified transmit signals with predefined amplitudes and/or phases;
transforming the plurality of amplified transmit signals present at the plurality of inputs of the transformation unit into a combined power transmit signal; and providing the combined power transmit signal at one of the plurality of outputs of the transformation unit;
wherein transforming the plurality of transmit signals comprises transforming the plurality of amplified transmit signals into the combined power transmit signal such that the one output at which the combined power transmit signal is provided is defined by amplitudes and/or phases of the plurality of amplified transmit signals; and
wherein providing the combined power transmit signal comprises providing the combined power transmit signal

at the one output defined by the amplitudes and/or phases of the plurality of amplified transmit signals.

11. Computer program having a program code for performing, when running on a computer or microprocessor, a method according to claim 10.

Patentansprüche

1. Sender (100), der folgende Merkmale aufweist:

eine Mehrzahl von Verstärkerschaltungen (102);
eine Mehrzahl von Antennen (104), die angepasst ist, um unterschiedliche Hauptsenderichtungen aufzuweisen; und
eine Transformationseinheit (106), die eine Mehrzahl von Eingängen (108) aufweist, die mit der Mehrzahl von Verstärkerschaltungen (102) verbunden ist, und eine Mehrzahl von Ausgängen (110), die mit der Mehrzahl von Antennen (104) verbunden ist, wobei die Transformationseinheit (106) konfiguriert ist, um eine Mehrzahl von verstärkten Sendesignalen, die an der Mehrzahl von Eingängen (108) vorliegt, in ein kombiniertes Leistungssendesignal zu transformieren, und um das kombinierte Leistungssendesignal an einem der Mehrzahl von Ausgängen (110) bereitzustellen;
wobei die Transformationseinheit (106) konfiguriert ist, um die Mehrzahl von verstärkten Sendesignalen in das kombinierte Leistungssendesignal zu transformieren, so dass der eine Ausgang, an dem das kombinierte Leistungssendesignal bereitgestellt wird, durch Amplituden und/oder Phasen der Mehrzahl von verstärkten Sendesignalen definiert ist; und
wobei die Mehrzahl von Verstärkerschaltungen (102) konfiguriert ist, um ein Sendesignal mit steuerbaren Gewinnen und/oder steuerbaren Phasenverschiebungen zu verstärken, um die Mehrzahl von verstärkten Sendesignalen zu erhalten, wobei der Sender (100) konfiguriert ist, um die Gewinne und/oder Phasenverschiebungen zu steuern, so dass die Mehrzahl von Verstärkerschaltungen (102) die Mehrzahl von verstärkten Sendesignalen mit vordefinierten Amplituden und/oder Phasen bereitstellt, wobei die Transformationseinheit (106) konfiguriert ist, um das kombinierte Leistungssendesignal an dem einen Ausgang bereitzustellen, der durch die Amplituden und/oder Phasen der Mehrzahl von verstärkten Sendesignalen definiert ist.

2. Sender (100) gemäß Anspruch 1, bei dem die Transformationseinheit (106) konfiguriert ist, um die Mehrzahl von verstärkten Sendesignalen durch eine orthogonale Transformation oder eine diskrete Fourier-Transformation in das kombinierte Leistungssendesignal zu transformieren.

3. Sender (100) gemäß Anspruch 1 oder 2, bei dem die Transformationseinheit (106) eine Hochfrequenzlinse, eine Rotman-Linse oder eine Butler-Matrix ist.

4. Sender (100) gemäß Anspruch 1 oder 3, wobei der Sender (100) ferner folgende Merkmale aufweist:

einen Lokaloszillator (128), der konfiguriert ist, um ein Lokaloszillatorsignal bereitzustellen; und
eine Lokaloszillatortransformationseinheit (140), die eine Mehrzahl von Eingängen (142) und eine Mehrzahl von Ausgängen (144) aufweist, wobei die Lokaloszillatortransformationseinheit (140) konfiguriert ist, um das Lokaloszillatorsignal, das an einem der Mehrzahl von Eingängen (142) vorliegt, in eine Mehrzahl von phasenverschobenen Lokaloszillatorsignalen zu transformieren, so dass der Eingang, an dem das Lokaloszillatorsignal vorliegt, die Phasen der Mehrzahl von phasenverschobenen Lokaloszillatorsignalen definiert, und um die Mehrzahl von phasenverschobenen Lokaloszillatorsignalen an der Mehrzahl von Ausgängen (144) bereitzustellen;
wobei die Mehrzahl von Verstärkerschaltungen (102) Steuereingänge (146) aufweist, die mit der Mehrzahl von Ausgängen (144) der Lokaloszillatortransformationseinheit (140) verbunden sind, wobei die Mehrzahl von Verstärkerschaltungen (102) konfiguriert ist, um die Mehrzahl von verstärkten Sendesignalen zu erhalten basierend auf dem Mischen eines Basisband- oder Zwischenfrequenzsendesignals oder verstärkter Versionen desselben mit der Mehrzahl von phasenverschobenen Lokaloszillatorsignalen, die an den Steuereingängen (146) vorliegt, wodurch die Phasen der Mehrzahl von phasenverschobenen Lokaloszillatorsignalen an die Mehrzahl von verstärkten Sendesignalen angelegt werden.

5. Sender (100) gemäß einem der Ansprüche 1 bis 3, wobei der Sender (100) ferner folgende Merkmale aufweist:

einen Lokaloszillator (128), der konfiguriert ist, um ein Lokaloszillatorsignal bereitzustellen; und

eine Mehrzahl von steuerbaren Phasenschiebern (150), die mit dem Lokaloszillator (128) verbunden ist und konfiguriert ist, um eine Mehrzahl von phasenverschobenen Lokaloszillatorsignalen mit vordefinierten Phasen bereitzustellen;
wobei die Mehrzahl von Verstärkerschaltungen (102) Steuereingänge (146) aufweist, die mit der Mehrzahl von steuerbaren Phasenschiebern verbunden ist, wobei die Mehrzahl von Verstärkerschaltungen (102) konfiguriert ist, um die Mehrzahl von verstärkten Sendesignalen zu erhalten basierend auf dem Mischen eines Basisband- oder Zwischenfrequenzsendesignals oder verstärkter Versionen desselben mit der Mehrzahl von phasenverschobenen Lokaloszillatorsignalen, die an den Steuereingängen (146) vorliegen, wodurch die Phasen der Mehrzahl von phasenverschobenen Lokaloszillatorsignalen an die Mehrzahl von verstärkten Sendesignalen angelegt werden.

6. Sende/Empfangsgerät (300), das folgende Merkmale aufweist:

einen Sender (100) gemäß einem der Ansprüche 1 bis 5; und
einen Empfangsweg (200), wobei der Empfangsweg (200) folgende Merkmale aufweist:

einen Ausgang (202); und
eine Mehrzahl von Empfangswegverstärkern (204), die in Reihe geschaltet ist zwischen den Ausgang (202) und die Mehrzahl von Antennen (104), wobei die Mehrzahl von Antennen (104) angepasst ist, um unterschiedliche Hauptempfangsrichtungen aufzuweisen, um eine Mehrzahl von Empfangssignalen von den unterschiedlichen Hauptempfangsrichtungen zu empfangen.

7. Sende/Empfangsgerät (300) gemäß Anspruch 6, bei dem die Mehrzahl von Empfangswegverstärkern (204) zwischen einem Einschaltzustand und einem Ausschaltzustand schaltbar ist, wobei jeder Empfangswegverstärker der Mehrzahl von Empfangswegverstärkern (204) konfiguriert ist, um an seinem Ausgang eine Impedanz bereitzustellen, die in dem Einschaltzustand ist, angepasst an eine spezifische Impedanz des Empfangswegs (200), und die in dem Ausschaltzustand zumindest um einen Faktor von 10 höher ist als die charakteristische Impedanz des Empfangswegs (200).

8. Sende/Empfangsgerät (300) gemäß Anspruch 6 oder 7, bei dem der Empfangsweg (200) ferner folgende Merkmale aufweist:

einen Empfangsweglokaloszillator (210), der konfiguriert ist, um ein Empfangsweglokaloszillatorsignal bereitzustellen;
eine Mehrzahl von Empfangswegmischern (212), die in Reihe geschaltet sind zwischen die Mehrzahl von Empfangswegverstärkern (204) und den Ausgang (202) des Empfangswegs (200); und
ein Schaltelement (206);
wobei das Empfangswegschaltelement (206) einen Eingang, der mit dem Empfangsweglokaloszillator verbunden ist, und eine Mehrzahl von Ausgängen aufweist, die mit der Mehrzahl von Empfangswegmischern (212) verbunden ist; oder
wobei die Mehrzahl von Empfangswegmischern (212) in Reihe geschaltet ist zwischen die Mehrzahl von Empfangswegverstärkern (204) und den Ausgang (202) des Empfangswegs (200) durch das Empfangswegschaltelement (206), so dass eine Mehrzahl von Eingängen des Empfangswegschaltelements (206) mit der Mehrzahl von Empfangswegmischern verbunden ist, und ein Ausgang des Empfangswegschaltelements mit dem Ausgang (202) des Empfangswegs (200) verbunden ist.

9. System (400), das folgende Merkmale aufweist:

ein erstes und ein zweites Sende/Empfangsgerät (300) gemäß einem der Ansprüche 6 bis 8;
wobei das erste Sende/Empfangsgerät konfiguriert ist, um ein Sendesignal, das einen Spreizcode aufweist, nachfolgend mit jeder Antenne der Mehrzahl seiner Antennen zu senden, um eine Verbindung zwischen dem ersten und dem zweiten Sende/Empfangsgerät herzustellen; und
wobei das zweite Sende/Empfangsgerät konfiguriert ist, um gleichzeitig eine Mehrzahl von Empfangssignalen mit der Mehrzahl von seinen Antennen zu empfangen, um eine Richtung abzuleiten, von der das Sendesignal empfangen wird, basierend auf der Mehrzahl von Empfangssignalen, und um die Antenne der Mehrzahl von Antennen auszuwählen, die die Hauptempfangsrichtung aufweist, die der Richtung entspricht, von der das Sendesignal empfangen wird, um die Verbindung zwischen dem ersten und dem zweiten Sende/Empfangsgerät herzustellen.

10. Verfahren zum Betreiben eines Senders, wobei der Sender eine Mehrzahl von Verstärkerschaltungen, eine Mehrzahl von Antennen, die angepasst ist, um unterschiedliche Hauptsenderichtungen aufzuweisen, und eine Transformationseinheit aufweist, die eine Mehrzahl von Eingängen aufweist, die mit der Mehrzahl von Verstärkerschaltungen verbunden ist, und eine Mehrzahl von Ausgängen, die mit der Mehrzahl von Antennen verbunden ist, wobei das Verfahren folgende Schritte aufweist:

Verstärken eines Sendesignals mit steuerbaren Gewinnen und/oder steuerbaren Phasenverschiebungen, um die Mehrzahl von verstärkten Sendesignalen zu erhalten;
Steuern der Gewinne und/oder Phasenverschiebungen, so dass die Mehrzahl von Verstärkerschaltungen die Mehrzahl von verstärkten Sendesignalen mit vordefinierten Amplituden und/oder Phasen bereitstellt;
Transformieren der Mehrzahl von verstärkten Sendesignalen, die an der Mehrzahl von Eingängen der Transformationseinheit vorliegt, in ein kombiniertes Leistungssendesignal; und
Bereitstellen des kombinierten Leistungssendesignals an einem der Mehrzahl von Ausgängen der Transformationseinheit;
wobei das Transformieren der Mehrzahl von Sendesignalen das Transformieren der Mehrzahl von verstärkten Sendesignalen in das kombinierte Leistungssendesignal aufweist, so dass der eine Ausgang, an dem das kombinierte Leistungssendesignal vorgesehen ist, durch Amplituden und/oder Phasen der Mehrzahl von verstärkten Sendesignalen definiert ist; und
wobei das Bereitstellen des kombinierten Leistungssendesignals das Bereitstellen des kombinierten Leistungssendesignals an dem einen Ausgang aufweist, der durch die Amplituden und/oder Phasen der Mehrzahl von verstärkten Sendesignalen definiert ist.

11. Computerprogramm mit einem Programmcode zum Durchführen eines Verfahrens gemäß Anspruch 10, wenn dasselbe auf einem Computer oder Mikroprozessor läuft.

Revendications

1. Emetteur (100), comprenant:

une pluralité de circuits amplificateurs (102);
une pluralité d'antennes (104) adaptées pour présenter différentes directions d'émission principales; et
une unité de transformation (106) comprenant une pluralité d'entrées (108) connectées à la pluralité de circuits amplificateurs (102) et une pluralité de sorties (110) connectées à la pluralité d'antennes (104), où l'unité de transformation (106) est configurée pour transformer une pluralité de signaux d'émission amplifiés présents à la pluralité d'entrées (108) en un signal d'émission de puissance combiné et pour fournir le signal d'émission de puissance combiné à l'une de la pluralité de sorties (110);
dans lequel l'unité de transformation (106) est configurée pour transformer la pluralité de signaux d'émission amplifiés en signal d'émission de puissance combiné de sorte que l'une sortie à laquelle est fourni le signal d'émission puissance combiné soit définie par les amplitudes et/ou les phases de la pluralité de signaux d'émission amplifiés; et
dans lequel la pluralité de circuits amplificateurs (102) sont configurés pour amplifier un signal d'émission à gains contrôlables et/ou à déphasages contrôlables, pour obtenir la pluralité de signaux d'émission amplifiés, dans lequel l'émetteur (100) est configuré pour contrôler les gains et/ou des déphasages de sorte que la pluralité de circuits amplificateurs (102) fournissent la pluralité de signaux d'émission amplifiés à amplitudes et/ou phases prédéfinies, dans lequel l'unité de transformation (106) est configurée pour fournir le signal d'émission de puissance combiné à l'une sortie définie par les amplitudes et/ou les phases de la pluralité de signaux d'émission amplifiés.

2. Emetteur (100) selon la revendication 1, dans lequel l'unité de transformation (106) est configurée pour transformer la pluralité de signaux d'émission amplifiés en signal d'émission de puissance combiné à l'aide d'une transformation orthogonale ou d'une transformation de Fourier discrète.

3. Emetteur (100) selon la revendication 1 ou 2, dans lequel l'unité de transformation (106) est une lentille haute fréquence, une lentille de Rotman ou une matrice de Butler.

4. Emetteur (100) selon la revendication 1 à 3, dans lequel l'émetteur (100) comprend par ailleurs:

un oscillateur local (128) configuré pour fournir un signal d'oscillateur local; et
une unité de transformation d'oscillateur local (140) comprenant une pluralité d'entrées (142) et une pluralité de sorties (144), où l'unité de transformation d'oscillateur local (140) est configurée pour transformer le signal d'oscillateur local présent à l'une de la pluralité d'entrées (142) en une pluralité de signaux d'oscillateur local déphasés, de sorte que l'entrée à laquelle est présent le signal d'oscillateur local définisse les phases de la pluralité de signaux d'oscillateur local déphasés et pour fournir la pluralité de signaux d'oscillateur local déphasés à la pluralité de sorties (144);
dans lequel la pluralité de circuits amplificateurs (102) comprennent des entrées de commande (146) connectées à la pluralité de sorties (144) de l'unité de transformation d'oscillateur local (140), dans lequel la pluralité de circuits amplificateurs (102) sont configurés pour obtenir la pluralité de signaux d'émission amplifiés sur base du mélange d'une bande de base ou d'un signal d'émission de fréquence intermédiaire ou de versions amplifiées de ce dernier avec la pluralité de signaux d'oscillateur local déphasés présents aux entrées de commande (146), appliquant ainsi les phases de la pluralité signaux d'oscillateur local déphasés à la pluralité de signaux d'émission amplifiés.

5. Emetteur (100) selon la revendication 1 à 3, dans lequel l'émetteur (100) comprend par ailleurs:

un oscillateur local (128) configuré pour fournir un signal d'oscillateur local; et
une pluralité de déphaseurs contrôlables (150) connectés à l'oscillateur local (128) et configurés pour fournir une pluralité de signaux d'oscillateur local déphasés présentant des phases prédéfinies;
dans lequel la pluralité de circuits amplificateurs (102) comprennent des entrées de commande (146) connectées à la pluralité de déphaseurs contrôlables, dans lequel la pluralité de circuits amplificateurs (102) sont configurés pour obtenir la pluralité de signaux d'émission amplifiés sur base du mélange d'une bande de base ou d'un signal d'émission de fréquence intermédiaire ou de versions amplifiées de ce dernier avec la pluralité de signaux d'oscillateur local déphasés présents aux entrées de commande (146), appliquant ainsi les phases de la pluralité de signaux d'oscillateur local déphasés à la pluralité de signaux d'émission amplifiés.

6. Emetteur-récepteur (300), comprenant:

un émetteur (100) selon l'une des revendications 1 à 5; et
un trajet de réception (200), où le trajet (200) de réception comprend:

une sortie (202); et
une pluralité d'amplificateurs de trajet de réception (204) connectés en série entre la sortie (202) et la pluralité d'antennes (104), où la pluralité d'antennes (104) sont adaptées pour présenter des directions de réception principales différentes, pour recevoir une pluralité de signaux de réception des différents directions de réception principales.

7. Emetteur-récepteur (300) selon la revendication 6, dans lequel la pluralité d'amplificateurs de trajet de réception (204) sont commutables entre un état d'enclenchement et un état de déclenchement, dans lequel chaque amplificateur de trajet de réception de la pluralité d'amplificateurs de trajet de réception (204) est configuré pour fournir, à sa sortie, une impédance qui est, à l'état d'enclenchement, adaptée à une impédance spécifique du trajet de réception (200) et qui est, à l'état de déclenchement, supérieure d'au moins un facteur de dix à l'impédance caractéristique du trajet de réception (200).

8. Emetteur-récepteur (300) selon la revendication 6 ou 7, dans lequel le trajet de réception (200) comprend par ailleurs:

un oscillateur local de trajet de réception (210) configuré pour fournir un signal d'oscillateur local de trajet de réception;
une pluralité de mélangeurs de trajet de réception (212) connectés en série entre la pluralité d'amplificateurs de trajet de réception (204) et la sortie (202) du trajet de réception (200); et
un élément de commutation (206);
dans lequel l'élément de commutation de trajet de réception (206) comprend une entrée connectée à l'oscillateur local de trajet de réception et une pluralité de sorties connectées à la pluralité de mélangeurs de trajet de réception (212); ou
dans lequel la pluralité de mélangeurs de trajet de réception (212) sont connectés en série entre la pluralité d'amplificateurs de trajet de réception (204) et la sortie (202) du trajet de réception (200) à l'aide de l'élément de commutation de trajet de réception (206), de sorte qu'une pluralité d'entrées de l'élément de commutation

de trajet de réception (206) soient connectées à la pluralité de mélangeurs de trajet de réception et qu'une sortie de l'élément de commutation de trajet de réception soit connectée à la sortie (202) du trajet de réception (200).

9. Système (400), comprenant:

un premier et un deuxième émetteur-récepteur (300) selon l'une des revendications 6 à 8;
dans lequel le premier émetteur-récepteur est configuré pour émettre un signal d'émission comprenant un code d'étalement à la suite de chaque antenne de la pluralité de ses antennes, pour établir une connexion entre le premier et le deuxième émetteur-récepteur; et
dans lequel le deuxième émetteur-récepteur est configuré pour recevoir simultanément une pluralité de signaux de réception par la pluralité de ses antennes, pour dériver une direction à partir de laquelle est reçu le signal d'émission sur base de la pluralité de signaux de réception, et pour sélectionner l'antenne parmi la pluralité d'antennes présentant les directions de réception principales correspondant à la direction à partir de laquelle est reçu le signal d'émission, pour établir la connexion entre le premier et le deuxième émetteur-récepteur.

10. Procédé pour faire fonctionner un émetteur, dans lequel l'émetteur comprend une pluralité de circuits amplificateurs, une pluralité d'antennes adaptées de manière à présenter des directions d'émission principales différentes, et une unité de transformation comprenant une pluralité d'entrées connectées à la pluralité de circuits amplificateurs et une pluralité de sorties connectées à la pluralité d'antennes, dans lequel le procédé comprend le fait de:

amplifier un signal d'émission avec des gains contrôlables et/ou des déphasages contrôlables, pour obtenir la pluralité de signaux d'émission amplifiés;
contrôler les gains et/ou les déphasages de sorte que la pluralité de circuits amplificateurs fournissent la pluralité de signaux d'émission amplifiés avec des amplitudes et/ou phases prédéfinies;
transformer la pluralité de signaux d'émission amplifiés présents à la pluralité d'entrées de l'unité de transformation en un signal d'émission de puissance combiné; et
fournir le signal d'émission de puissance combiné à l'une de la pluralité de sorties de l'unité de transformation;
dans lequel la transformation de la pluralité de signaux d'émission comprend le fait de transformer la pluralité de signaux d'émission amplifiés en signal d'émission de puissance combiné de sorte que l'une sortie à laquelle est fourni le signal d'émission de puissance combiné soit définie par les amplitudes et/ou les phases de la pluralité de signaux d'émission amplifiés; et
dans lequel la fourniture du signal d'émission de puissance combiné comprend le fait de fournir le signal d'émission de puissance combiné à l'une sortie définie par les amplitudes et/ou les phases de la pluralité de signaux d'émission amplifiés.

11. Programme d'ordinateur ayant un code de programme pour réaliser, lorsqu'il est exécuté sur un ordinateur ou un microprocesseur, un procédé selon la revendication 10.

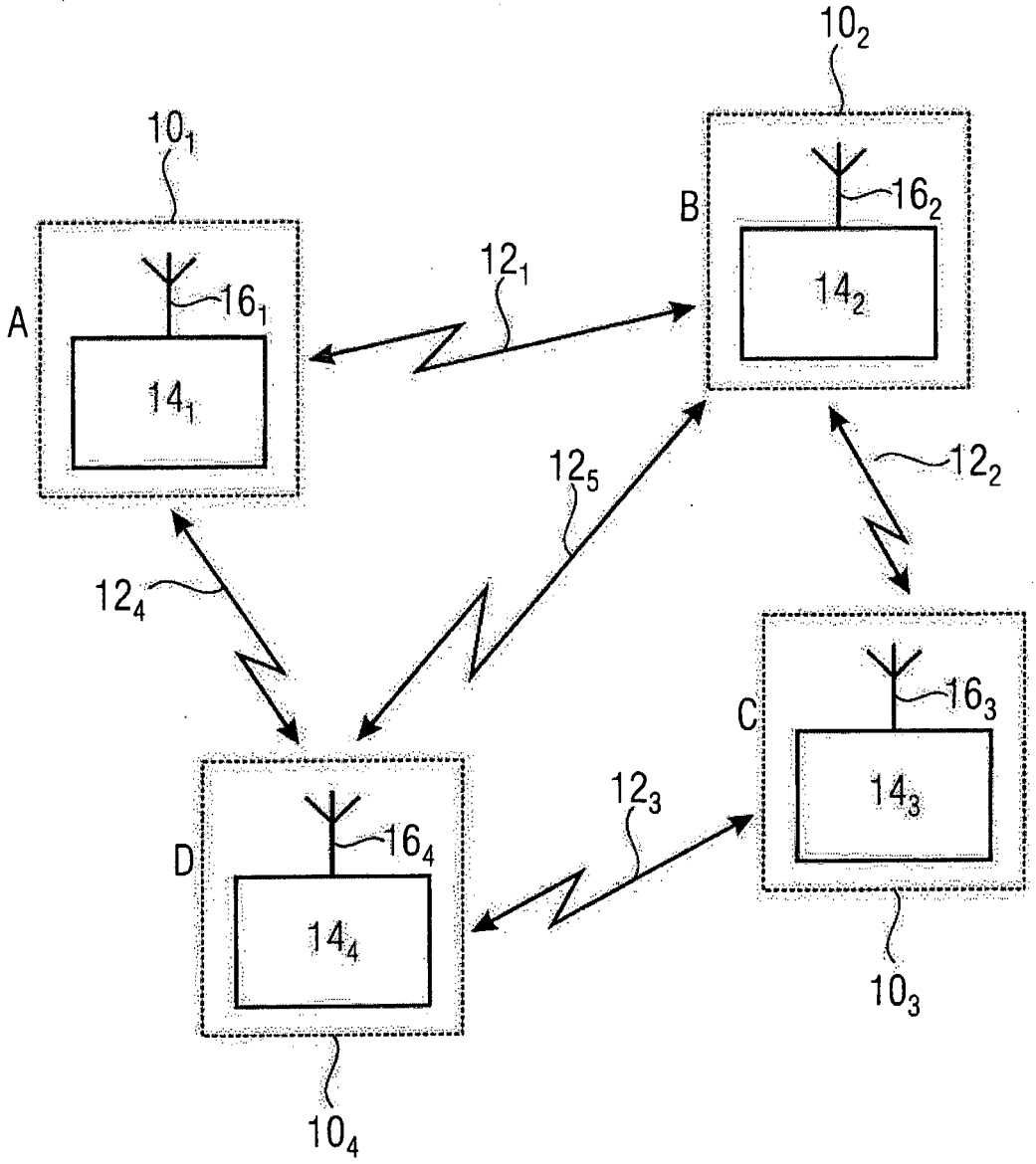
10_2
10_1
B
16_2
A
12_1
16_1
14_2
14_1
12_5
12_2
12_4
C
16_3
14_3
D
12_3
16_4
14_4
10_3
10_4

FIG 1

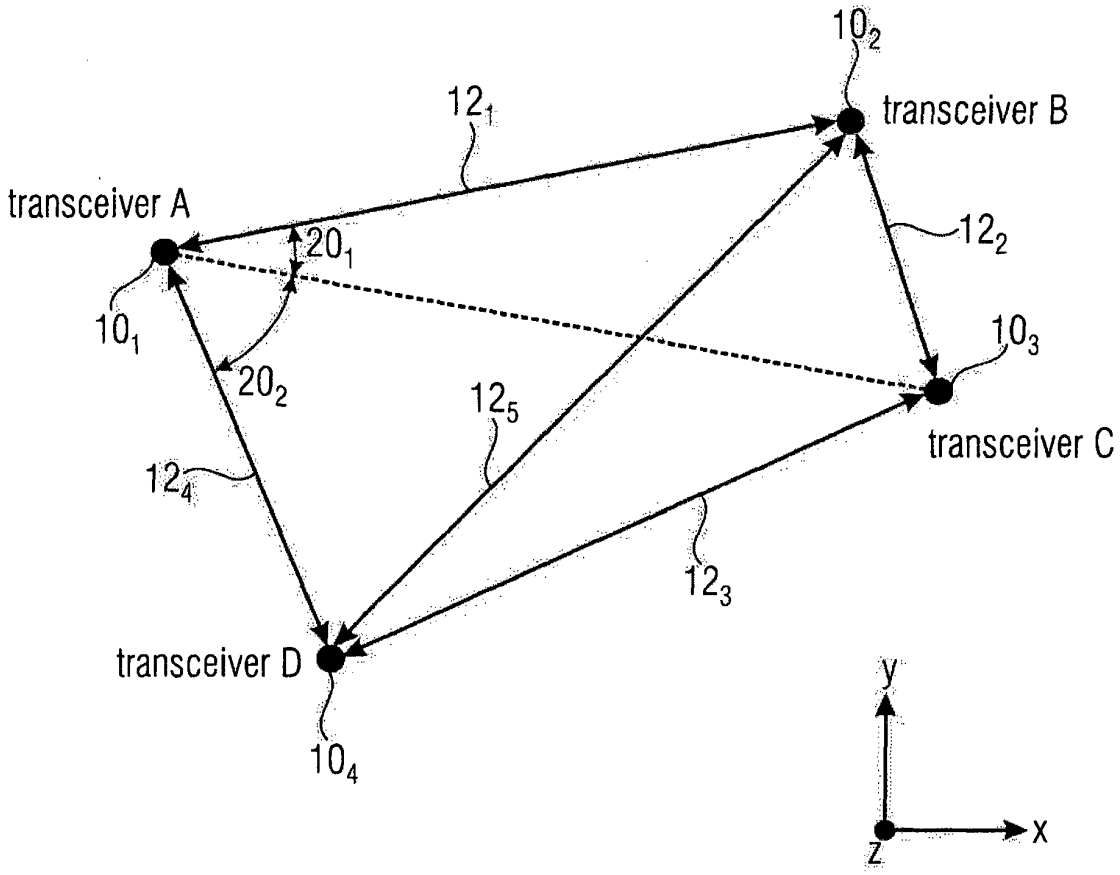
10_2
12_1
transceiver B
transceiver A
12_2
20_1
10_1
10_3
20_2
12_5
transceiver C
12_4
12_3
transceiver D
10_4
y
x
z

FIG 2

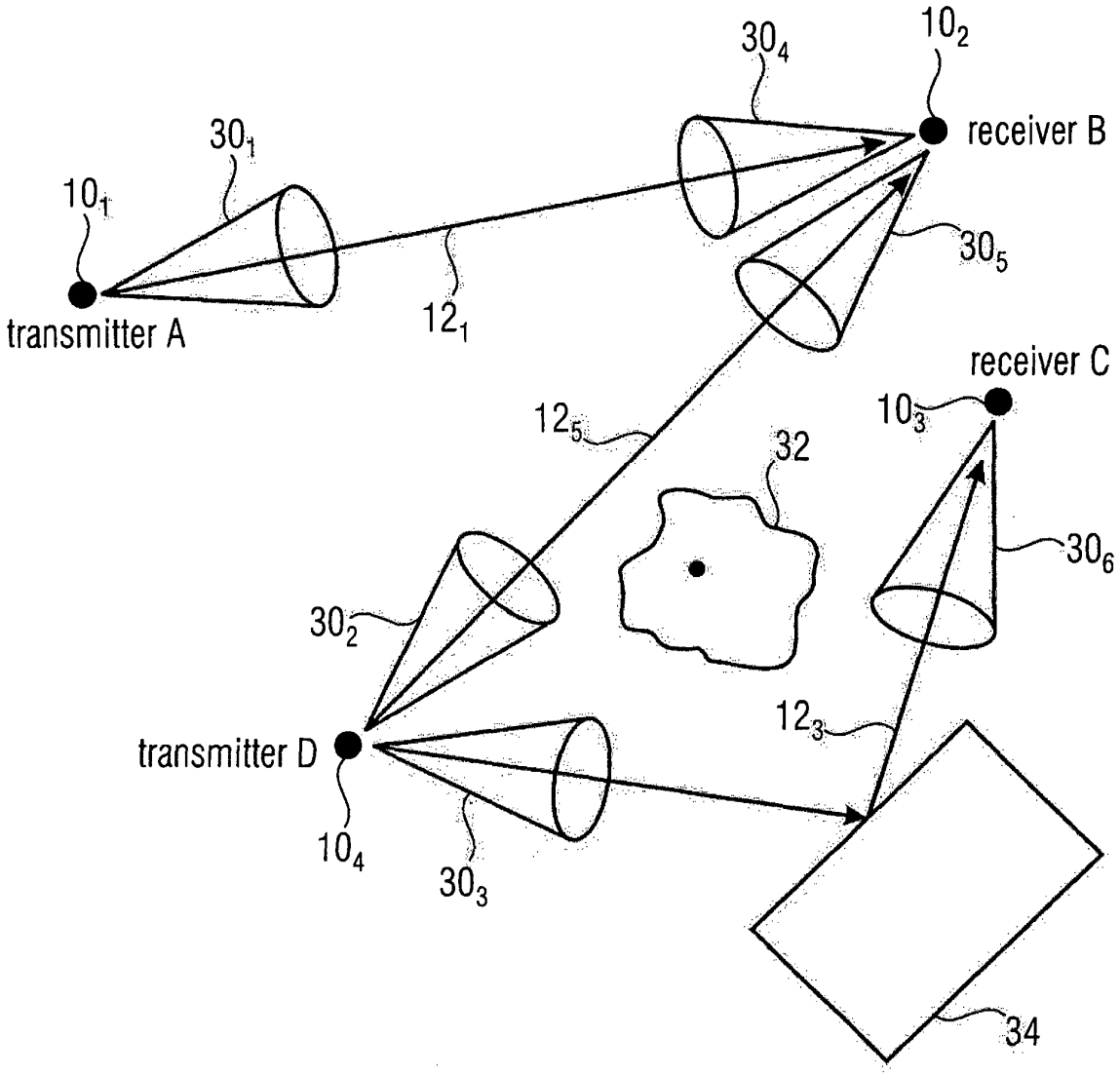
30_4
10_2
receiver B
30_1
10_1
30_5
transmitter A
12_1
receiver C
12_5
10_3
32
30_6
30_2
12_3
transmitter D
10_4
30_3
34

FIG 3

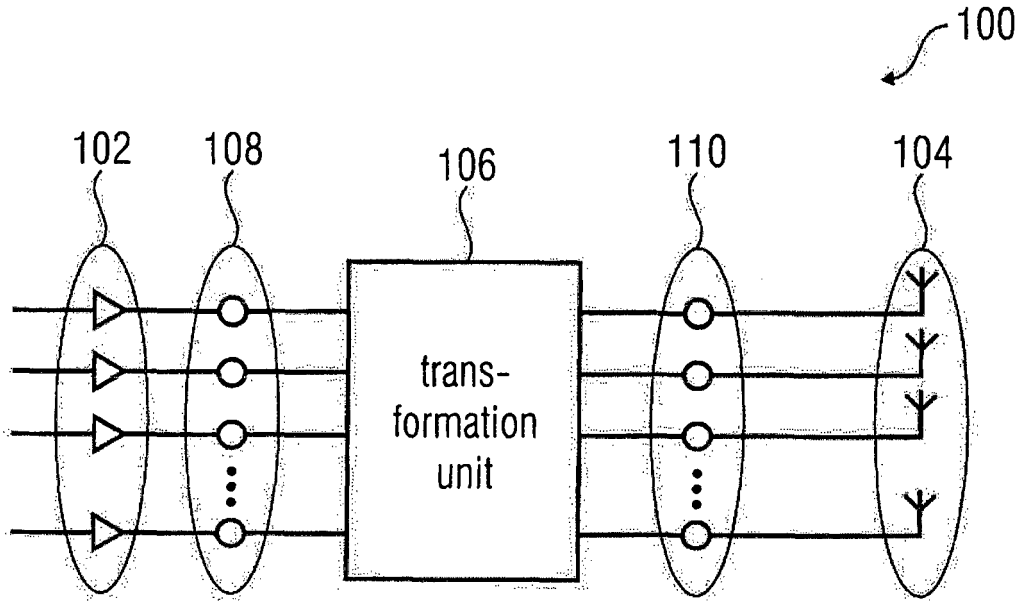

FIG 4

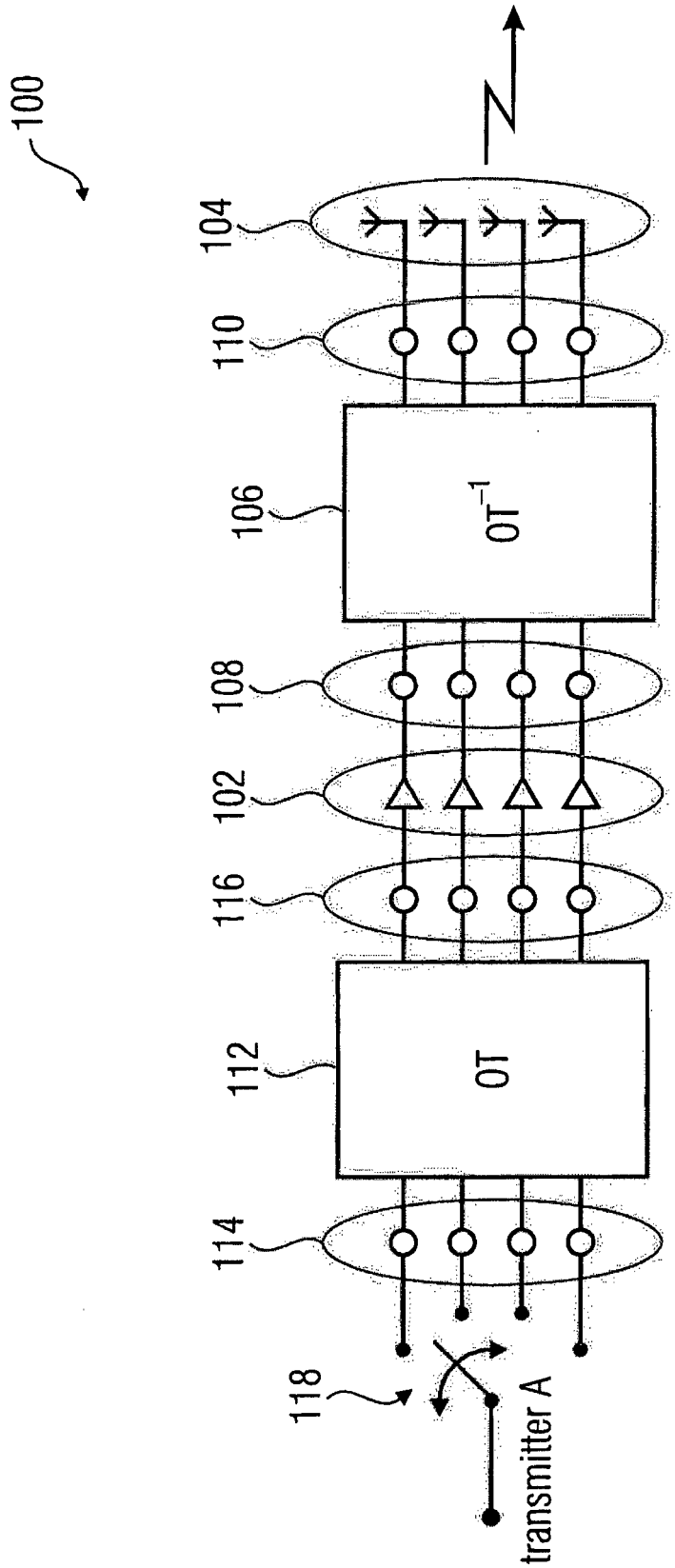

FIG 5

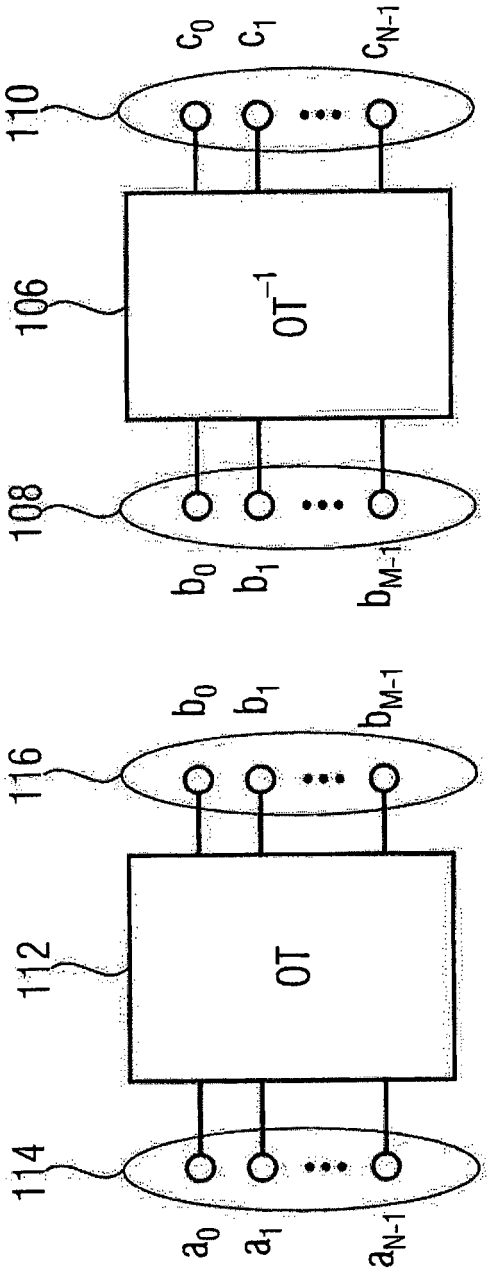
110
c_0
c_1
c_{N-1}
106
OT^{-1}
108
b_0
b_1
b_{M-1}
116
b_0
b_1
b_{M-1}
112
OT
114
a_0
a_1
a_{N-1}

FIG 6

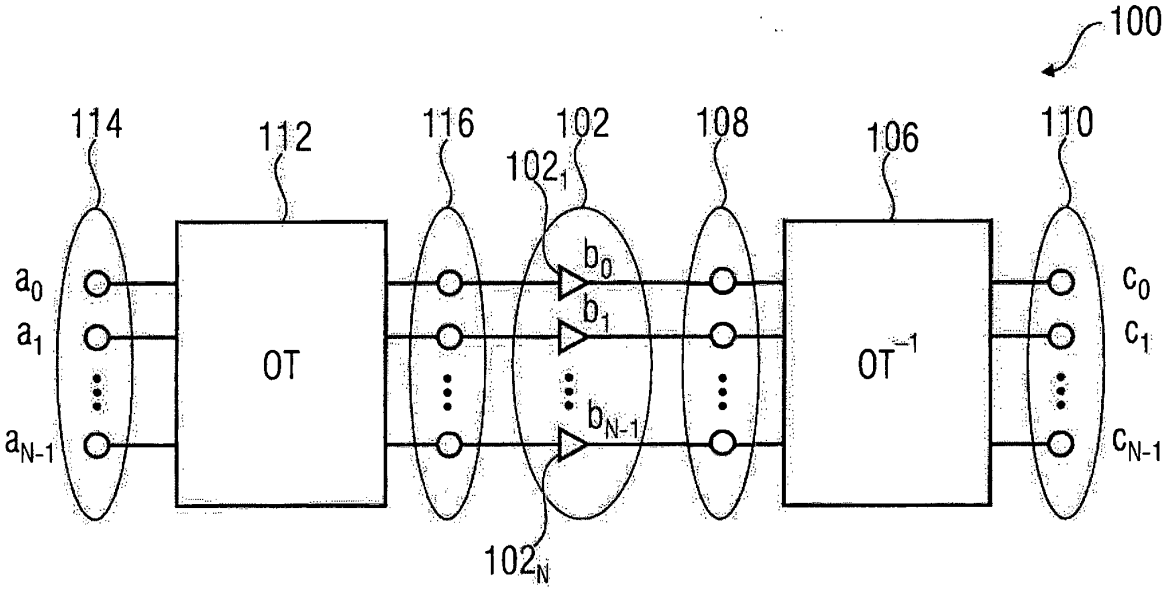
100
114
112
116
102
108
106
110
102_1
a_0
a_1
a_{N-1}
OT
b_0
b_1
b_{N-1}
OT^{-1}
c_0
c_1
c_{N-1}
102_N

FIG 7

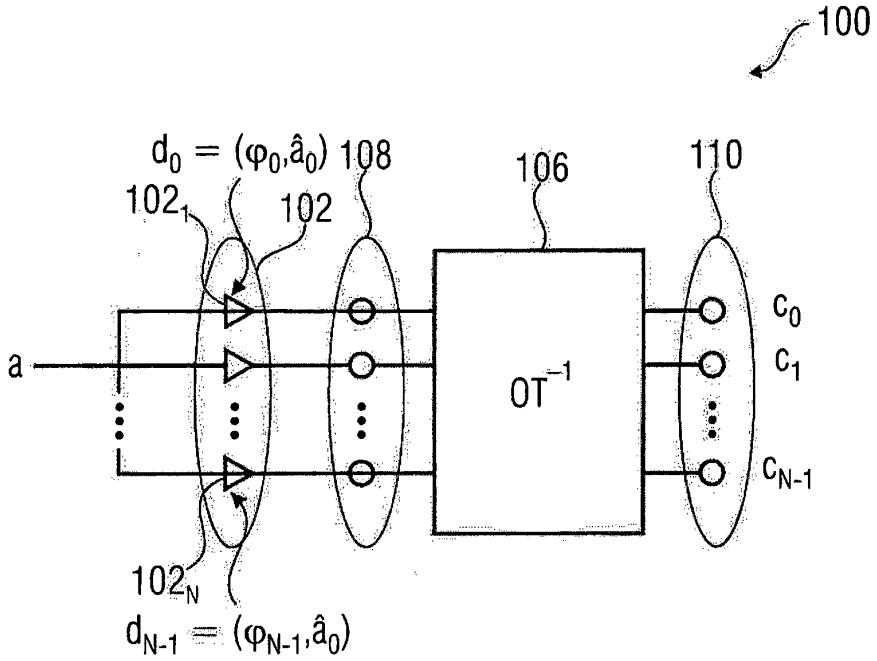
100
$d_0 = (\varphi_0, \hat{a}_0)$
108
106
110
102_1
102
a
OT^{-1}
c_0
c_1
c_{N-1}
102_N
$d_{N-1} = (\varphi_{N-1}, \hat{a}_0)$

FIG 8

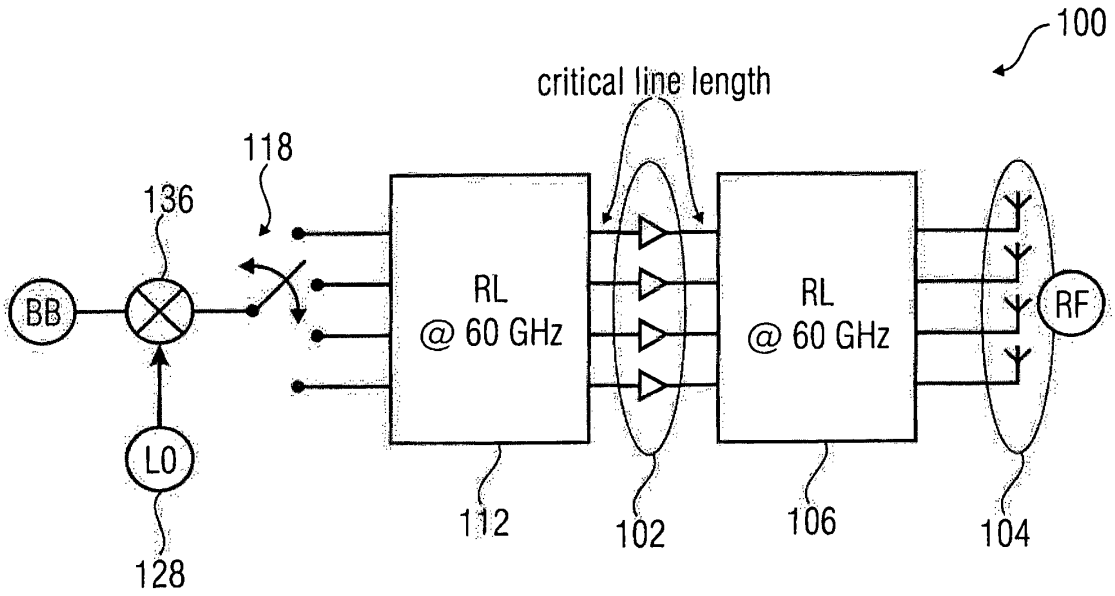
100
critical line length
118
136
BB
LO
128
RL
@ 60 GHz
RL
@ 60 GHz
RF
112
102
106
104

FIG 9

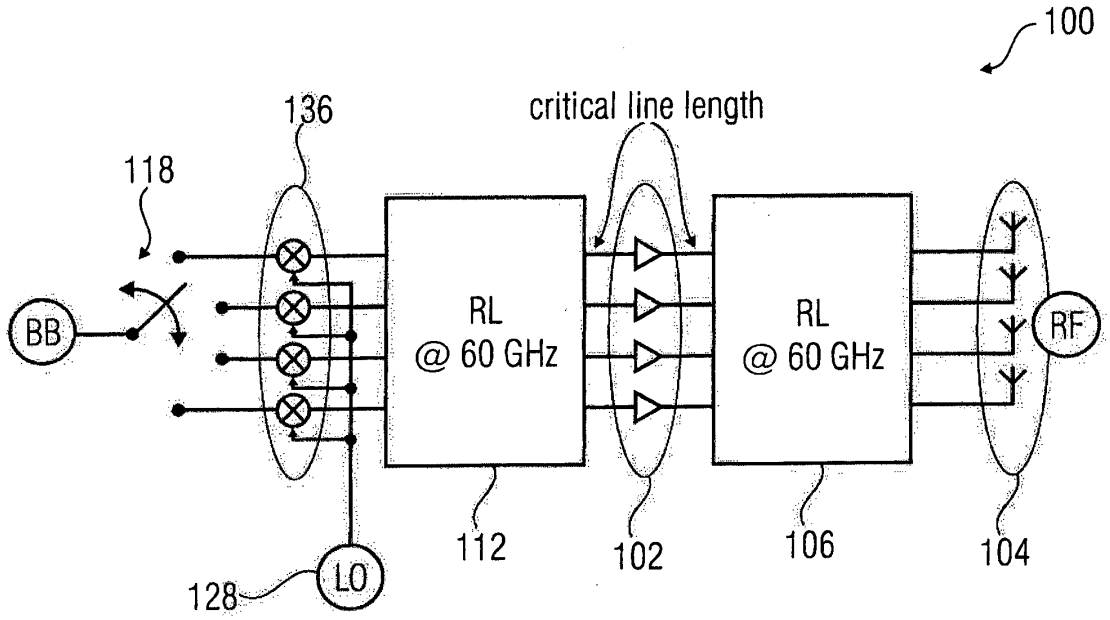
100
136
critical line length
118
BB
LO
128
RL
@ 60 GHz
RL
@ 60 GHz
RF
112
102
106
104

FIG 10

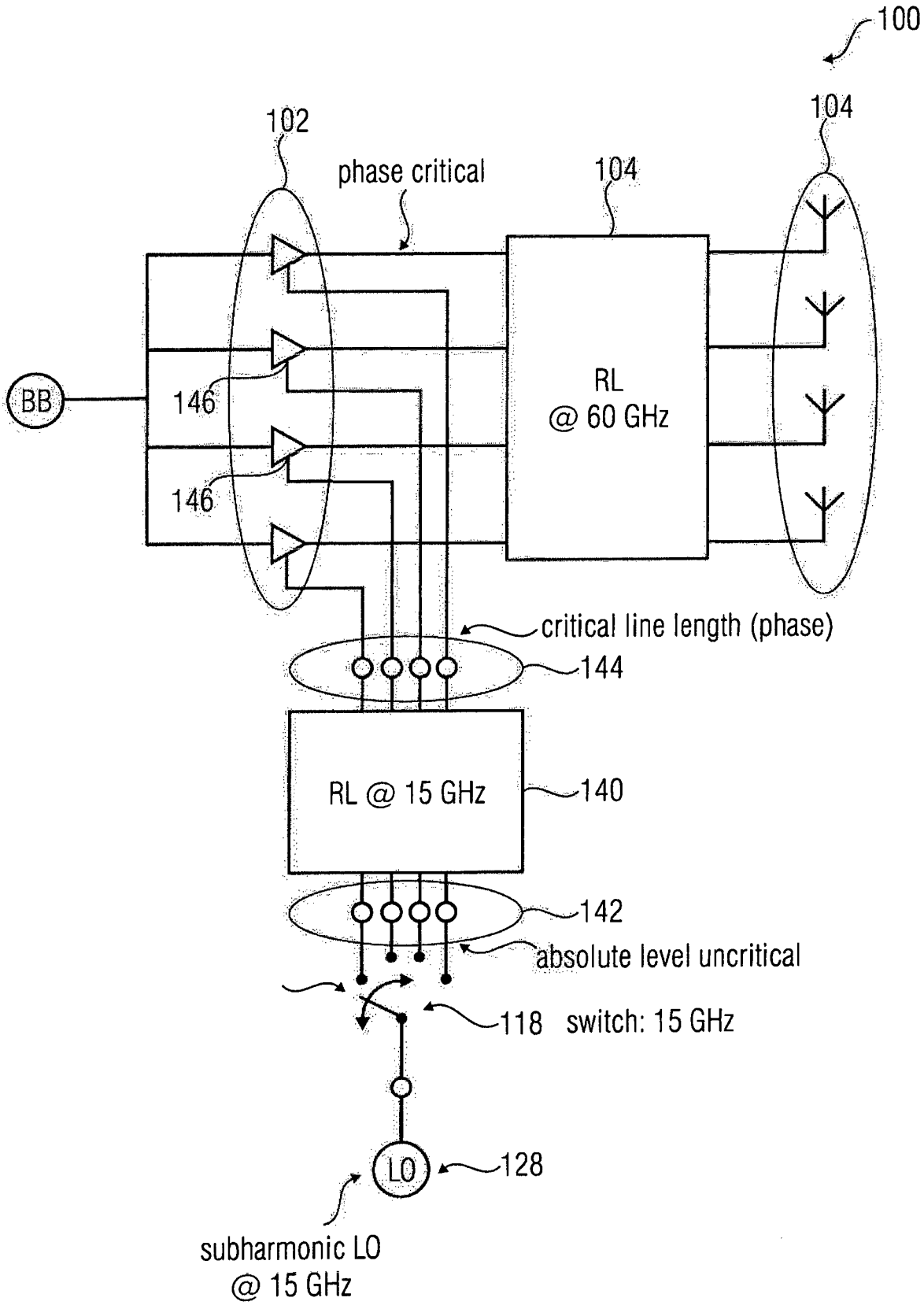
100
102
phase critical
104
104
BB
146
146
RL
@ 60 GHz
critical line length (phase)
144
RL @ 15 GHz
140
142
absolute level uncritical
118 switch: 15 GHz
LO
128
subharmonic LO
@ 15 GHz

FIG 11

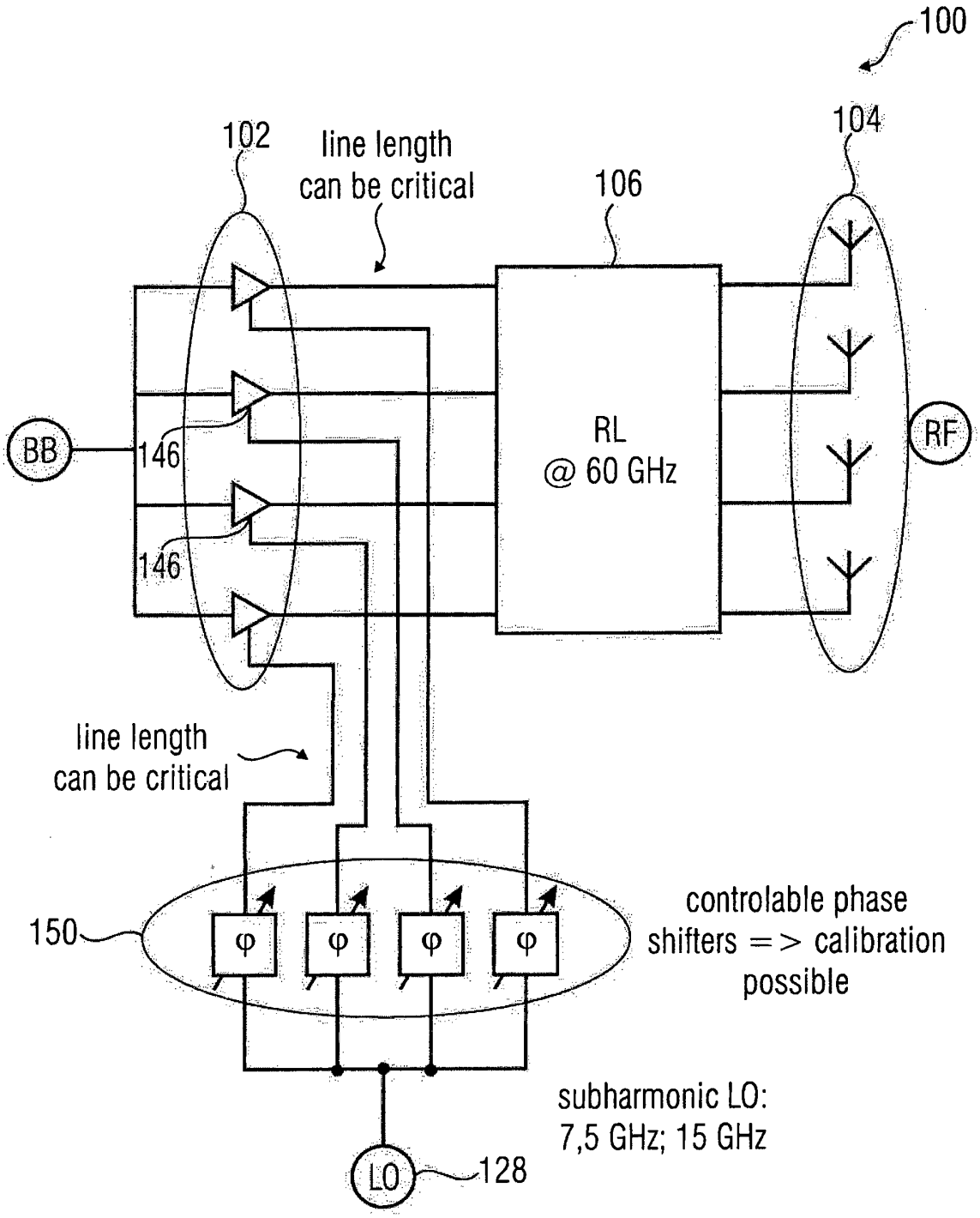
100
102
line length
can be critical
104
106
BB
146
146
RL
@ 60 GHz
RF
line length
can be critical
150
φ
φ
φ
φ
controlable phase
shifters => calibration
possible
subharmonic LO:
7,5 GHz; 15 GHz
LO
128

FIG 12

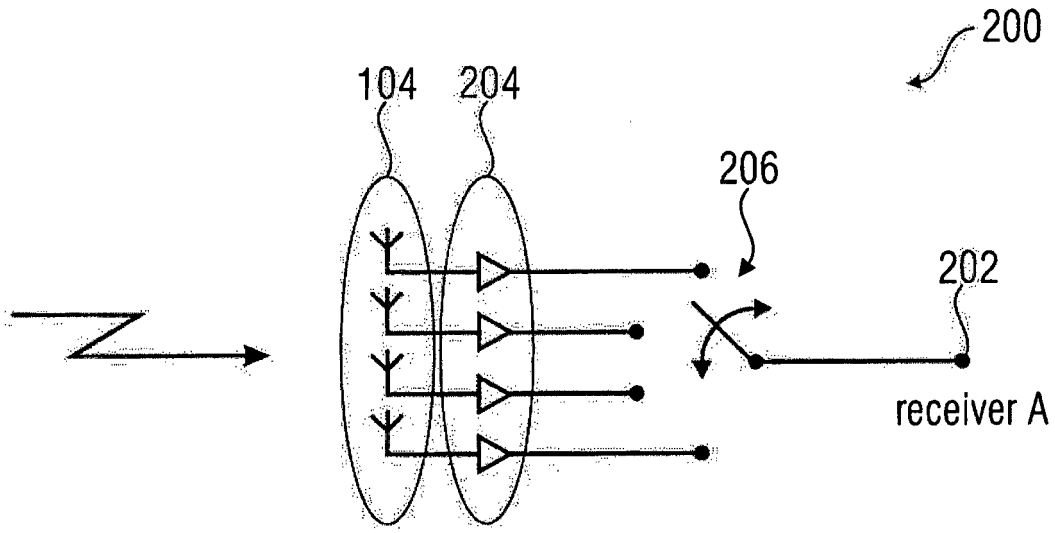

FIG 13

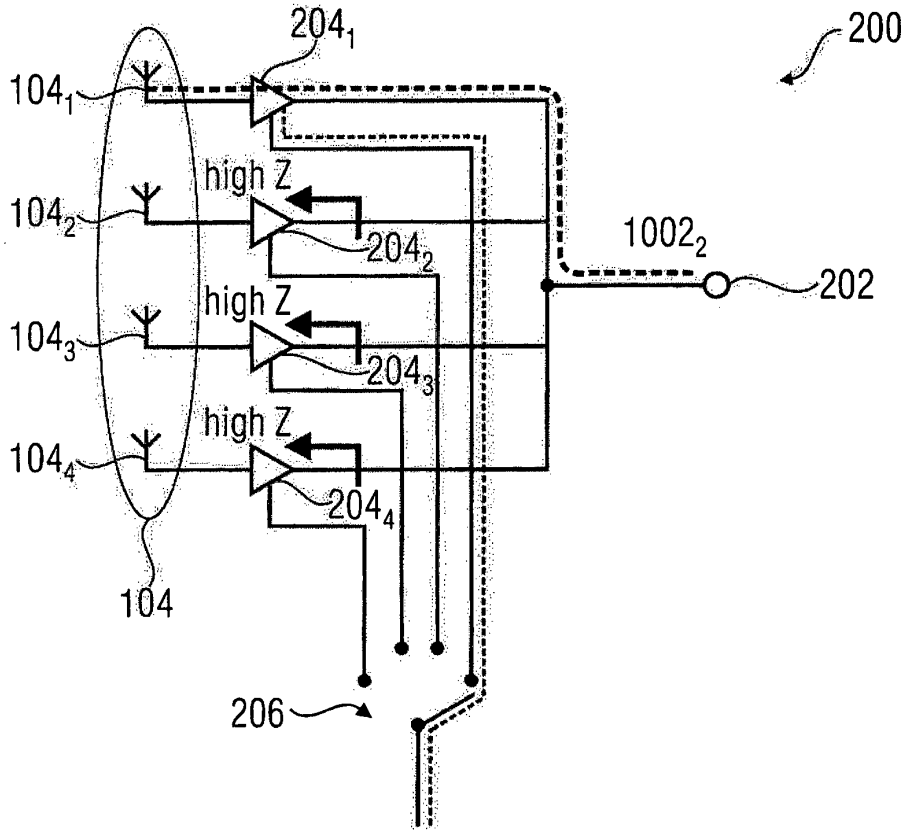
204_1
200
104_1
high Z
104_2
204_2
1002_2
202
high Z
104_3
204_3
high Z
104_4
204_4
104
206

FIG 14

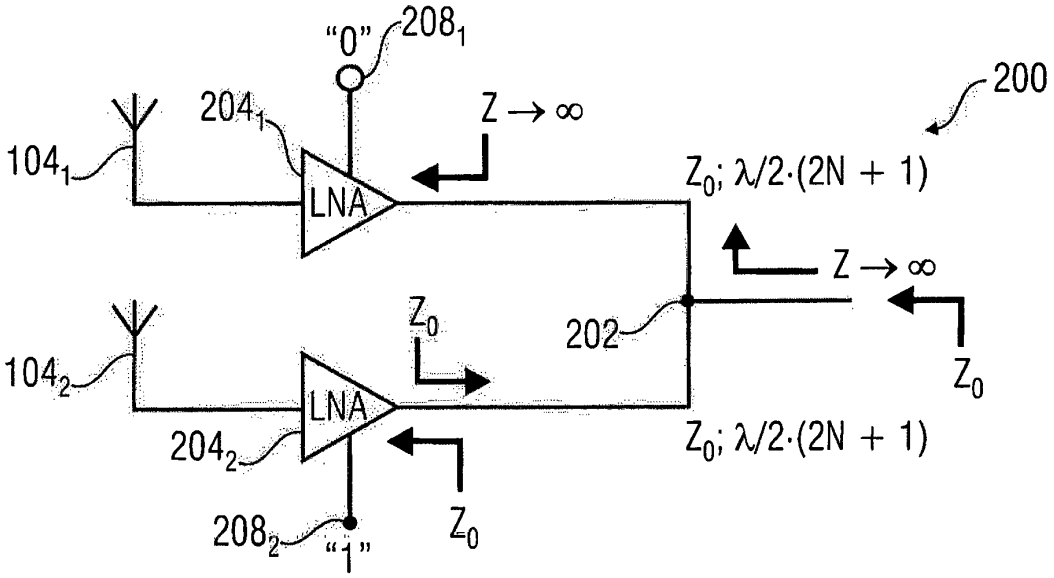
"0"
208_1
200
204_1
$Z \rightarrow \infty$
104_1
LNA
Z_0; $\lambda/2 \cdot (2N + 1)$
$Z \rightarrow \infty$
Z_0
202
104_2
LNA
Z_0
204_2
Z_0; $\lambda/2 \cdot (2N + 1)$
208_2
"1"
Z_0

FIG 15

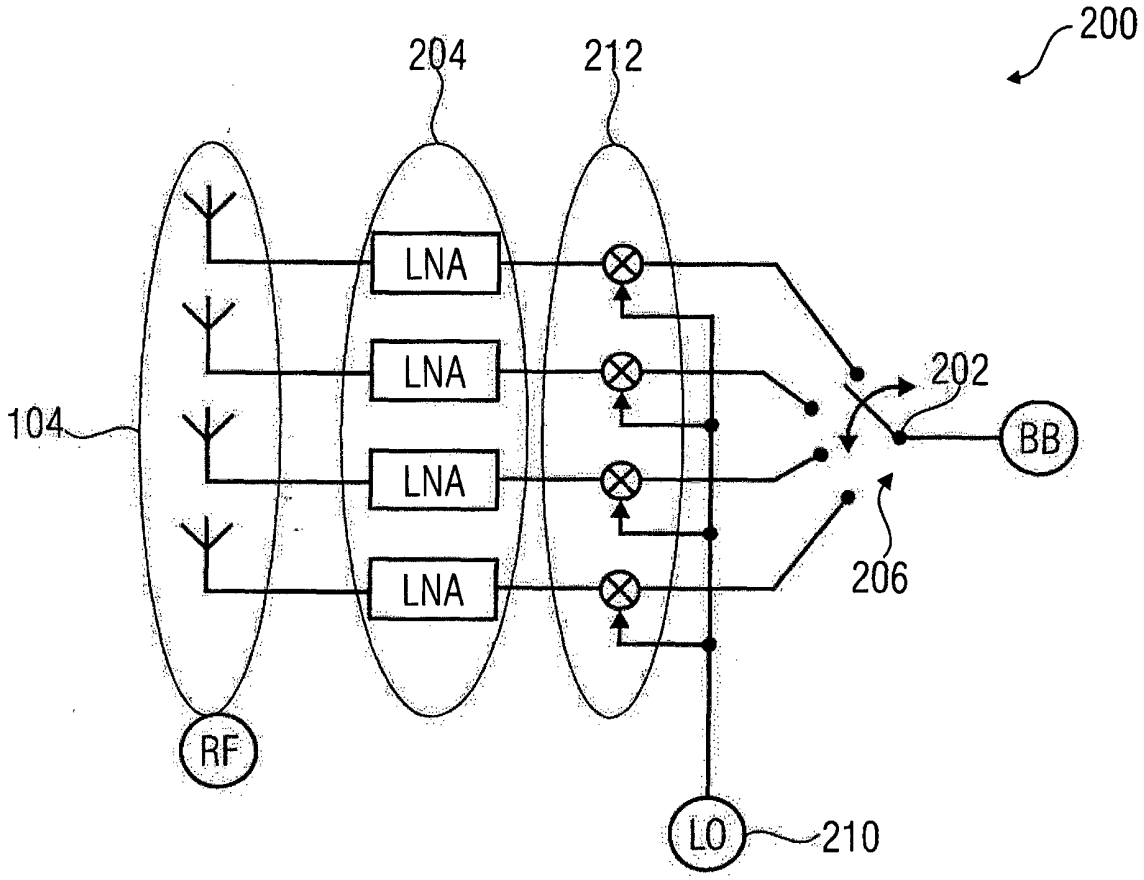

FIG 16

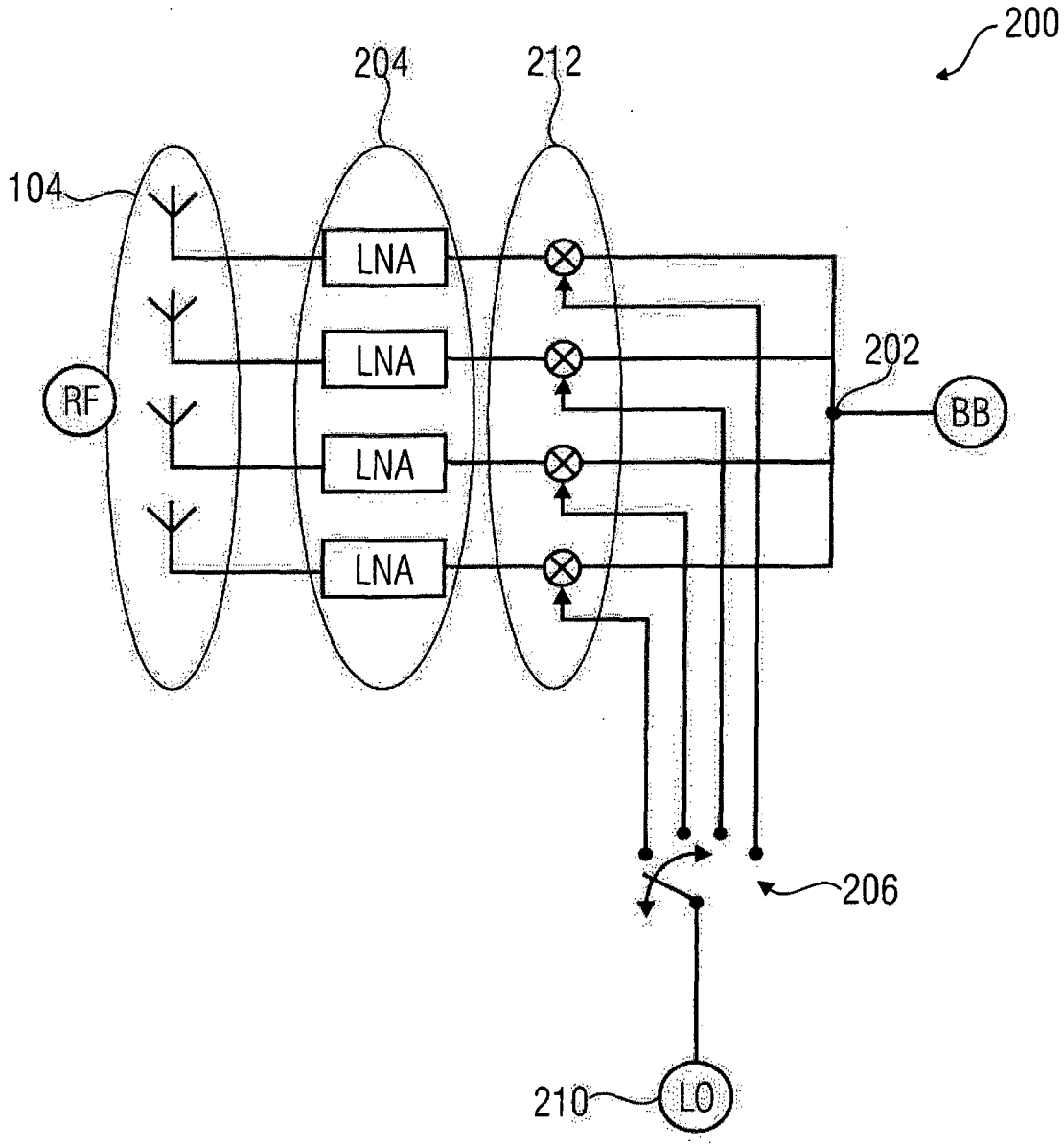

FIG 17

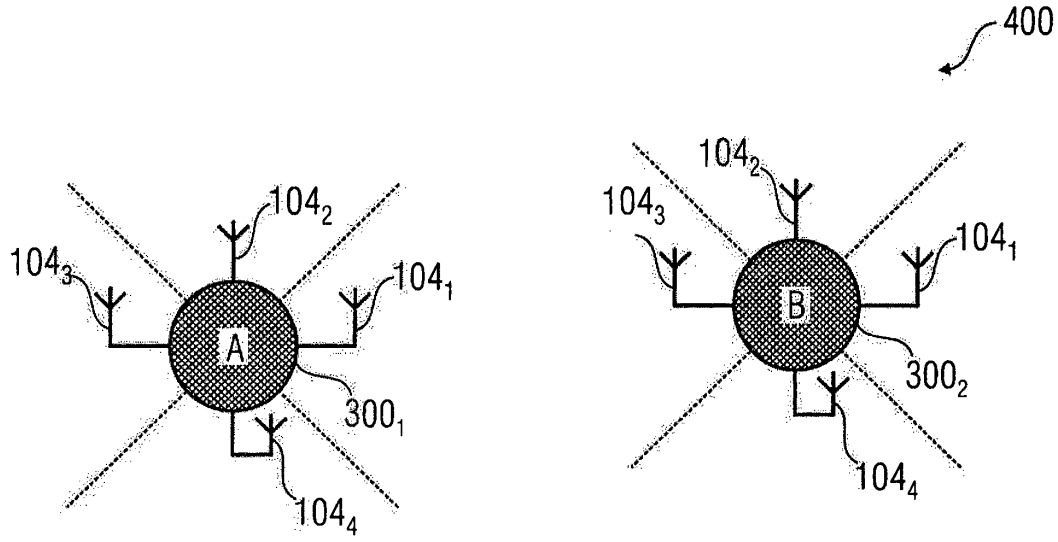
400
104_2
104_3
104_1
A
300_1
104_4
104_2
104_3
104_1
B
300_2
104_4

FIG 18

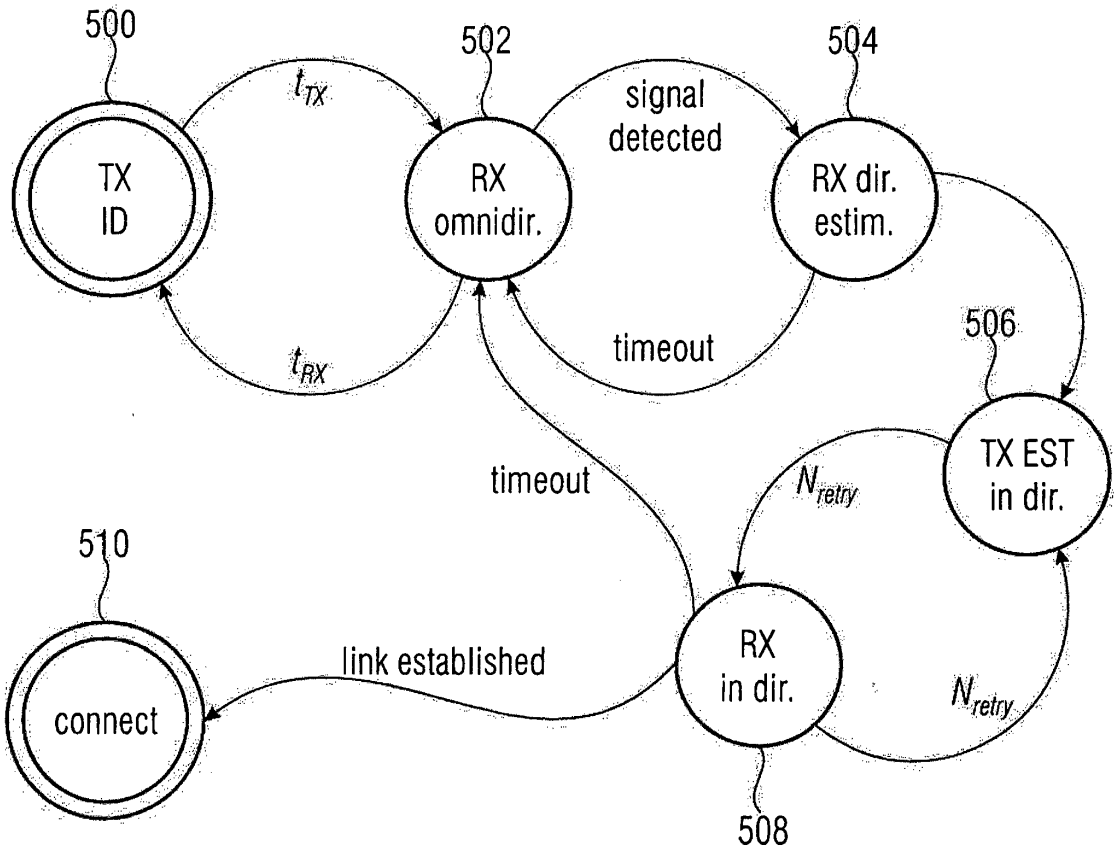
500
502
504
t_{TX}
signal detected
TX ID
RX omnidir.
RX dir. estim.
t_{RX}
timeout
506
timeout
N_{retry}
TX EST in dir.
510
link established
RX in dir.
N_{retry}
connect
508

FIG 19

6 Conclusions

In this thesis I presented channel measurement campaigns that were conducted to investigate the properties of urban outdoor millimeter-wave access channels. An overlay concept was presented that will allow network operators to gradually update their access networks using previously unused frequency bands in order to cater the ever growing user demands for mobile broadband data connectivity.

I showed that using the spectrum in the millimeter-wave bands can be beneficial compared to the legacy bands from a capacity and energy perspective. The common assumption that the free space path loss increases with frequency needs to be put into perspective with the effective antenna gain, which also increases with the frequency when its absolute aperture size is kept constant. This leads to a shift of the design paradigm from omnidirectional to directional signal transmission and reception, implying new requirements for the wireless communication hardware and protocols. The channel models therefore also need to be adapted to include the necessary information for the simulation and design of new systems.

Path loss exponents obtained for typical street canyon and open square scenarios with free line-of-sight at 10 GHz and 60 GHz carrier frequency were close to 2, which is well in line with other reported findings. Two characteristic properties of millimeter-wave access links stood out during the measurements and might play a crucial role in the design of future communication systems.

One is the existence of strong ground reflections that can lead to severe flat fading. Depending on the link distance and height of the communicating stations above ground, even signals with wide bandwidths of multiple gigahertz can be prune to significant fading losses, imposing an extra penalty on the link budget and therefore achievable capacity.

The other important finding is the strong and volatile impact of environment induced shadowing on line-of-sight links. Human bodies and other mobile or static objects, such as cars and buses, can cause significant temporary attenuation of multipath components. This makes new physical (PHY) and medium access control (MAC) layers necessary to guarantee uninterrupted

communication links. The necessary higher gain and directionality of the antennas is a new design challenge compared to legacy systems in the sub 6 GHz bands, where omnidirectional transmission and reception has been the design principle for a long time. Chanel models are widely used in the process of the development and standardization of such new communication systems and need to implement these important peculiarities.

The quasi-determinstic channel model was derived based on measurement results presented in this work. The ground reflection is explicitly modeled based on the geometry of the environment and the base station and mobile user position. The shadowing effects can be included by applying the observed shadowing statistics on the individual path components in the model. The effect of steerable directional antennas can be applied to the channel model in a post processing step, as full angular information is available for all components. The model is therefore a good candidate for the investigation of the performance of new PHY and MAC layer implementations.

Future steps are planned to proceed beyond the scope of this work. The frequency dependence of the observed propagation phenomena was only touched with the simultaneous channel sounding campaign in an urban street canyon at 10 GHz and 60 GHz. A hardware update of the channel sounding equipment is currently being developed to allow parallel sounding of up to 4 channels. This update will also increase the resolvable signal bandwidth to 2 GHz per channel, allowing a better temporal resolution of multipath components and the ground reflection.

The measurements and models in this thesis are an important building block towards millimeter-wave access links in future mobile radio networks.

Bibliography

[AK40] Andrew Alford and A. G. Kandoian. Ultrahigh-frequency loop antennas. *Electrical Engineering*, 59(12):843–848, Dec 1940.

[ALS+14] M. R. Akdeniz, Y. Liu, M. K. Samimi, S. Sun, S. Rangan, T. S. Rappaport, and E. Erkip. Millimeter wave channel modeling and cellular capacity evaluation. *IEEE Journal on Selected Areas in Communications*, 32(6):1164–1179, June 2014.

[AMS+12] A.P.G. Ariza, R. Muller, R. Stephan, F. Wollenschlager, A. Schulz, M. Elkhouly, C. Scheytt, U. Trautwein, J. Muller, R.S. Thoma, and M.A. Hein. 60 GHz polarimetric MIMO sensing: Architectures and technology. In *Antennas and Propagation (EUCAP), 2012 6th European Conference on*, pages 2578–2582, March 2012.

[ASC08] A. V. Alejos, M. G. Sanchez, and I. Cuinas. Measurement and analysis of propagation mechanisms at 40 GHz: Viability of site shielding forced by obstacles. *IEEE Transactions on Vehicular Technology*, 57(6):3369–3380, Nov 2008.

[Bel69] P. Bello. Measurement of random time-variant linear channels. *IEEE Transactions on Information Theory*, 15(4):469–475, Jul 1969.

[BHL+14] F. Boccardi, Jr. Heath, R.W., A. Lozano, T.L. Marzetta, and P. Popovski. Five disruptive technology directions for 5G. *Communications Magazine, IEEE*, 52(2):74–80, February 2014.

[CBH+14] Youngbin Chang, Sangkyu Baek, Sooyoung Hur, Youngjoong Mok, and Youngju Lee. A novel dual-slope mm-wave channel model based on 3D ray-tracing in urban environments. In *Personal, Indoor, and Mobile Radio Communication (PIMRC), 2014 IEEE 25th Annual International Symposium on*, pages 222–226, Sept 2014.

[Chu72] D. Chu. Polyphase codes with good periodic correlation properties (corresp.). *Information Theory, IEEE Transactions on*, 18(4):531–532, Jul 1972.

[CHW+08] Yu. J. Cheng, Wei Hong, Ke Wu, Z. Q. Kuai, Chen Yu, J. X. Chen, J. Y. Zhou, and H. J. Tang. Substrate integrated waveguide (siw) Rotman lens and its Ka-band multibeam array antenna applications. *Antennas and Propagation, IEEE Transactions on*, 56(8):2504–2513, 2008.

[CR96] Luis M Correia and Judite R Reis. Wideband characterisation of the propagation channel for outdoors at 60 GHz. In *Personal, Indoor and Mobile Radio Communications, 1996. PIMRC'96., Seventh IEEE International Symposium on*, volume 2, pages 752–755. IEEE, 1996.

[CZZ04] S. Collonge, G. Zaharia, and G. E. Zein. Influence of the human activity on wide-band characteristics of the 60 GHz indoor radio channel. *IEEE Transactions on Wireless Communications*, 3(6):2396–2406, Nov 2004.

[ECM10] Standard ECMA-387 – high rate 60 GHz PHY, MAC and PALs, 2010.

[Fri46] Harald T Friis. A note on a simple transmission formula. *proc. IRE*, 34(5):254–256, 1946.

[FZH62] Raphael Frank, S Zadoff, and R Heimiller. Phase shift pulse codes with good periodic correlation properties (corresp.). *IRE Transactions on Information Theory*, 6(8):381–382, 1962.

[Gol05] Andrea Goldsmith. *Wireless Communications*. Cambridge University Press, 2005.

[GPWK15] Baris Göktepe, Michael Peter, Richard J. Weiler, and Wilhelm Keusgen. The influence of street furniture and tree trunks in urban scenarios on ray tracing simulations in the millimeter wave band. In *Microwave Conference (EuMC), 2015 45th European*, 2015.

[HBK+15] Sooyoung Hur, Sangkyu Baek, ByungChul Kim, JeongHo Park, A.F. Molisch, K. Haneda, and M. Peter. 28 GHz channel modeling

using 3D ray-tracing in urban environments. In *Antennas and Propagation (EuCAP), 2015 9th European Conference on*, pages 1–5, April 2015.

[HCL+14a] Sooyoung Hur, Yeon-Jae Cho, Kyoungtae Lee, Jung-Hoon Ko, and Jeongho Park. Millimeter-wave channel modeling based on measurements in in-building and campus environments at 28 GHz. In *COST IC1004 TD(14)10053*, 2014.

[HCL+14b] Sooyoung Hur, Yeon-Jea Cho, JungAun Lee, Noh-Gyoung Kang, JeongHo Park, and H. Benn. Synchronous channel sounder using horn antenna and indoor measurements on 28 GHz. In *Communications and Networking (BlackSeaCom), 2014 IEEE International Black Sea Conference on*, pages 83–87, May 2014.

[IEE09] IEEE standard for information technology– local and metropolitan area networks– specific requirements– part 15.3: Amendment 2: Millimeter-wave-based alternative physical layer extension. *IEEE Std 802.15.3c-2009 (Amendment to IEEE Std 802.15.3-2003)*, Oct 2009.

[IEE12] IEEE standard for information technology–telecommunications and information exchange between systems–local and metropolitan area networks–specific requirements-part 11: Wireless LAN medium access control (MAC) and physical layer (PHY) specifications amendment 3: Enhancements for very high throughput in the 60 GHz band. *IEEE Std 802.11ad-2012 (Amendment to IEEE Std 802.11-2012, as amended by IEEE Std 802.11ae-2012 and IEEE Std 802.11aa-2012)*, Dec 2012.

[JP99] Dieter Jungnickel and Alexander Pott. Perfect and almost perfect sequences. *Discrete Applied Mathematics*, 95(1):331–359, 1999.

[Kai62] T. Kailath. Measurements on time-variant communication channels. *IRE Transactions on Information Theory*, 8(5):229–236, September 1962.

[Kak11] Michio Kaku. *Physics of the Future: How Science Will Shape Human Destiny and Our Daily Lives by the Year 2100*. Doubleday, 2011.

[KKK+11] W. Keusgen, A Kortke, L. Koschel, M. Peter, R. Weiler, H. Zirath, Marcus Gavell, and Zhongxia He. An NLOS-capable 60 GHz MIMO demonstrator: System concept amp; performance. In *New Circuits and Systems Conference (NEWCAS), 2011 IEEE 9th International*, pages 265–268, June 2011.

[KKPW13] W. Keusgen, A Kortke, M. Peter, and R. Weiler. A highly flexible digital radio testbed and 60 GHz application examples. In *Microwave Conference (EuMC), 2013 European*, pages 740–743, Oct 2013.

[KMH+07] P Kyösti, J Meinilä, L Hentilä, X Zhao, T Jämsä, C Schneider, M Narandzić, M Milojević, A Hong, J Ylitalo, et al. WINNER II channel models D1.1.2 V1.1, european commission, deliverable IST-WINNER D. Technical report, IST-4-027756 WINNER II, 2007.

[Koz97] W. Kozek. On the transfer function calculus for underspread ltv channels. *IEEE Transactions on Signal Processing*, 45(1):219–223, Jan 1997.

[KP05] W. Kozek and G. E. Pfander. Identification of operators with bandlimited symbols. *SIAM Journal on Mathematical Analysis*, 37(3):867–888, 2005.

[KWP+14] Wilhelm Keusgen, Richard J. Weiler, Michael Peter, Mike Wisotzki, and Baris Göktepe. Propagation measurements and simulations for millimeter-wave mobile access in a busy urban environment. In *39th International Conference on Infrared, Millimeter, and Terahertz Waves*, 2014.

[Lie89] Hans J Liebe. MPM—an atmospheric millimeter-wave propagation model. *International Journal of Infrared and Millimeter Waves*, 10(6):631–650, 1989.

[Lük88] Hans Dieter Lüke. Sequences and arrays with perfect periodic correlation. *IEEE Transactions on Aerospace and Electronic Systems*, 24(3):287, 1988.

[MDS+14] R. Müller, D.A. Dupleich, C. Schneider, R. Herrmann, and R.S. Thomä. Ultrawideband 3D mmWave channel sounding for 5G.

In *General Assembly and Scientific Symposium (URSI GASS), 2014 XXXIth URSI*, pages 1–4, Aug 2014.

[MHD+14] R. Müller, R. Herrmann, D.A. Dupleich, C. Schneider, and R.S. Thomä. Ultrawideband multichannel sounding for mm-wave. In *Antennas and Propagation (EuCAP), 2014 8th European Conference on*, pages 817–821, April 2014.

[MMH+02] G. Matz, A. F. Molisch, F. Hlawatsch, M. Steinbauer, and I. Gaspard. On the systematic measurement errors of correlative mobile radio channel sounders. *IEEE Transactions on Communications*, 50(5):808–821, May 2002.

[MMS+99] G. Matz, A. F. Molisch, M. Steinbauer, F. Hlawatsch, I. Gaspard, and H. Artes. Bounds on the systematic measurement errors of channel sounders for time-varying mobile radio channels. In *Vehicular Technology Conference, 1999. VTC 1999 - Fall. IEEE VTS 50th*, volume 3, pages 1465–1470 vol.3, 1999.

[MMS+09] A. Maltsev, R. Maslennikov, A. Sevastyanov, A. Khoryaev, and A. Lomayev. Experimental investigations of 60 GHz WLAN systems in office environment. *Selected Areas in Communications, IEEE Journal on*, 27(8):1488–1499, October 2009.

[MMS+10] A. Maltsev, R. Maslennikov, A. Sevastyanov, A. Lomayev, and A. Khoryaev. Statistical channel model for 60 GHz WLAN systems in conference room environment. In *Antennas and Propagation (EuCAP), 2010 Proceedings of the Fourth European Conference on*, pages 1–5, April 2010.

[MPB+14] Alexander Maltsev, Andrey Pudeyev, Ilya Bolotin, Gregory Morozov, Ingolf Karls, Michael Faerber, Isabelle Siaud, Anne-Marie Ulmer-Moll, Jean-Marc Conrat, Richard Weiler Michael Peter, and Wilhelm Keusgen. *Deliverable D5.1: Channel Modeling and Characterization, WP5: Propagation, Antennas and Multi-Antenna Techniques*. MiWEBA (FP7-ICT-608637), 2014.

[MPK+14] Alexander Maltsev, Andrey Pudeyev, Ingolf Karls, Ilya Bolotin, Gregory Morozov, Richard J. Weiler, Michael Peter, and Wilhelm Keusgen. Quasi-deterministic approach to mmwave channel modeling in a non-stationary environment. In *GLOBECOM 2014*

Workshop on Emerging Technologies for 5G Wireless Cellular Networks, Dec. 2014.

[MSR15] G.R. Maccartney, M.K. Samimi, and T.S. Rappaport. Exploiting directionality for millimeter-wave wireless system improvement. In *Communications (ICC), 2015 IEEE International Conference on*, pages 2416–2422, June 2015.

[MZNR13] George R. MacCartney, Junhong Zhang, Shuai Nie, and Theodore S. Rappaport. Path loss models for 5G millimeter wave propagation channels in urban microcells. In *Global Communications Conference (GLOBECOM), 2013 IEEE*, pages 3948–3953, Dec 2013.

[OBB+14] A. Osseiran, F. Boccardi, V. Braun, K. Kusume, P. Marsch, M. Maternia, O. Queseth, M. Schellmann, H. Schotten, H. Taoka, H. Tullberg, M.A. Uusitalo, B. Timus, and M. Fallgren. Scenarios for 5G mobile and wireless communications: the vision of the METIS project. *Communications Magazine, IEEE*, 52(5):26–35, May 2014.

[Par00] J.D. Parsons. *The Mobile Radio Propagation Channel*. Wiley, 2000.

[Pas14] Panagiotis Paschalidis. *The development of a wideband multiple-input multiple-output (MIMO) channel sounder and the measurement of the vehicular channel*. PhD thesis, TU Braunschweig, 2014.

[PDT91] J.D. Parsons, D.A. Demery, and A.M.D. Turkmani. Sounding techniques for wideband mobile radio channels: a review. *Communications, Speech and Vision, IEE Proceedings I*, 138(5):437–446, Oct 1991.

[PK11] Z. Pi and F. Khan. An introduction to millimeter-wave mobile broadband systems. *IEEE Communications Magazine*, 49(6):101–107, June 2011.

[PKW15] Michael Peter, Wilhelm Keusgen, and Richard J. Weiler. On path loss measurement and modeling for millimeter-wave 5G. In *Antennas and Propagation (EUCAP), 2015 9th European Conference on*, April 2015.

[Por97] B. Porat. *A course in digital signal processing.* John Wiley, 1997.

[PW06] G. E. Pfander and D. F. Walnut. Measurement of time-variant linear channels. *IEEE Transactions on Information Theory*, 52(11):4808–4820, Nov 2006.

[PWK+16] Michael Peter, Richard J. Weiler, Wilhelm Keusgen, Taro Eichler, Meik Kottkamp, and Alexander Nähring. Characterization of mm-wave channel sounders up to W-Band and validation of measurement results. In *The 10th European Conference on Antennas and Propagation (EuCAP 2016)*, pages 2866–2870, Davos, Switzerland, April 2016.

[PWRM+12] Michael Peter, Mike Wisotzki, Miruna Raceala-Motoc, Wilhelm Keusgen, Robert Felbecker, Martin Jacob, Sebastian Priebe, and T Kurner. Analyzing human body shadowing at 60 GHz: Systematic wideband MIMO measurements and modeling approaches. In *Antennas and Propagation (EUCAP), 2012 6th European Conference on*, pages 468–472. IEEE, 2012.

[QL06] Z. Qingling and J. Li. Rain attenuation in millimeter wave ranges. In *2006 7th International Symposium on Antennas, Propagation EM Theory*, pages 1–4, Oct 2006.

[RASM12] Sridhar Rajagopal, Shadi Abu-Surra, and Mehrzad Malmirchegini. Channel feasibility for outdoor non-line-of-sight mmwave mobile communication. In *Vehicular Technology Conference (VTC Fall), 2012 IEEE*, pages 1–6. IEEE, 2012.

[RBDMQ12] Theodore S Rappaport, Eshar Ben-Dor, James N Murdock, and Yijun Qiao. 38 GHz and 60 GHz angle-dependent propagation for cellular & peer-to-peer wireless communications. In *Communications (ICC), 2012 IEEE International Conference on*, pages 4568–4573. IEEE, 2012.

[RGBD+13] T.S. Rappaport, F. Gutierrez, E. Ben-Dor, J.N. Murdock, Yijun Qiao, and J.I. Tamir. Broadband millimeter-wave propagation measurements and models using adaptive-beam antennas for outdoor urban cellular communications. *Antennas and Propagation, IEEE Transactions on*, 61(4):1850–1859, April 2013.

[RKH+09] S. Ranvier, M. Kyro, K. Haneda, T. Mustonen, C. Icheln, and P. Vainikainen. VNA-based wideband 60 GHz MIMO channel sounder with 3-D arrays. In *Radio and Wireless Symposium, 2009. RWS '09. IEEE*, pages 308–311, Jan 2009.

[RMSS15] T.S. Rappaport, G.R. Maccartney, M.K. Samimi, and Shu Sun. Wideband millimeter-wave propagation measurements and channel models for future wireless communication system design. *Communications, IEEE Transactions on*, 63(9):3029–3056, Sept 2015.

[RP92] E. O. Rausch and A. F. Peterson. Theory and measurements of a compact high dielectric microstrip Rotman lens. In *Microwave Conference, 1992. 22nd European*, volume 2, pages 876 –881, sept. 1992.

[RPW97] E. O. Rausch, A. F. Peterson, and W. Wiebach. Electronically scanned millimeter wave antenna using a Rotman lens. In *Proc. Radar 97 (Conf. Publ. No. 449)*, pages 374–378, 1997.

[RQT+12] Theodore S Rappaport, Yijun Qiao, Jonathan I Tamir, James N Murdock, and Eshar Ben-Dor. Cellular broadband millimeter wave propagation and angle of arrival for adaptive beam steering systems. In *Radio and Wireless Symposium (RWS), 2012 IEEE*, pages 151–154. IEEE, 2012.

[RSM+13a] T. S. Rappaport, S. Sun, R. Mayzus, H. Zhao, Y. Azar, K. Wang, G. N. Wong, J. K. Schulz, M. Samimi, and F. Gutierrez. Millimeter wave mobile communications for 5g cellular: It will work! *IEEE Access*, 1:335–349, 2013.

[RSM+13b] Theodore S Rappaport, Shu Sun, Rimma Mayzus, Hang Zhao, Yaniv Azar, Kevin Wang, George N Wong, Jocelyn K Schulz, Mathew Samimi, and Felix Gutierrez. Millimeter wave mobile communications for 5G cellular: It will work! *IEEE Access*, pages 335–349, 2013.

[RT63] W. Rotman and R. Turner. Wide-angle microwave lens for line source applications. *Antennas and Propagation, IEEE Transactions on*, 11(6):623–632, 1963.

[SC97] PFM Smulders and LM Correia. Characterisation of propagation in 60 GHz radio channels. *Electronics & communication engineering journal*, 9(2):73–80, 1997.

[SR15] M.K. Samimi and T.S. Rappaport. 3-D statistical channel model for millimeter-wave outdoor mobile broadband communications. In *Communications (ICC), 2015 IEEE International Conference on*, pages 2430–2436, June 2015.

[THR+01] Reiner S Thomä, Dirk Hampicke, Andreas Richter, Gerd Sommerkorn, and Uwe Trautwein. MIMO vector channel sounder measurement for smart antenna system evaluation. *European Transactions on Telecommunications*, 12(5):427–438, 2001.

[Wis07] Mike Wisotzki. Entwicklung und Test eines Synchronisationsgerätes für Funkkanalmessungen. Studienarbeit, TU Berlin, 2007.

[WK15] Richard Weiler and Wilhelm Keusgen. Combined power transmission. European Patent 2 624 475, 2015. filed January 31, 2012, and issued January 28, 2015.

[WKFC14] Richard J. Weiler, Wilhelm Keusgen, Ilario Filippini, and Antonio Capone. Split control plane functionality in millimeter-wave overlay access. In *1st International Conference on 5G for Ubiquitous Connectivity*, Levi, Finland, 2014.

[WKM+16] Richard J. Weiler, Wilhelm Keusgen, Alexander Maltsev, Thomas Kühne, Andrey Pudeyev, Liang Xian, Joongheon Kim, and Michael Peter. Millimeter-Wave outdoor access shadowing mitigation using beamforming arrays. In *Antennas and Propagation (EuCAP), 2016 10th European Conference on*, pages 1900–1904, Davos, Switzerland, April 2016.

[WKNP14] Richard J. Weiler, Wilhelm Keusgen, Hung-Anh Nguyen, and Michael Peter. On the choice of carrier frequency and bandwidth for 5G small cell deployments. In *Personal Indoor and Mobile Radio Communications (PIMRC), 2014 IEEE 25rd International Symposium on*, Washington D.C., USA, 2014.

[WPK+14a] Richard J. Weiler, Michael Peter, Wilhelm Keusgen, Emilio Calvanese-Strinati, Antonio De Domenico, Ilario Filippini, Antonio Capone, Isabelle Siaud, Anne-Marie Ulmer-Moll, Alexander Maltsev, and Thomas Haustein and Kei Sakaguchi. Enabling 5G backhaul and access with millimeter-waves. In *Conference on Networks and Communications (EuCNC), 2014 European*, Bologna, Italy, 2014.

[WPK+14b] Richard J. Weiler, Michael Peter, Wilhelm Keusgen, Hidekazu Shimodaira, Khanh Tran Gia, and Kei Sakaguchi. Outdoor millimeter-wave access for heterogeneous networks - path loss and system performance. In *Personal, Indoor and Mobile Radio Communications (PIMRC Workshops), 2014 IEEE 25th International Symposium on*, Washington D.C., USA, 2014.

[WPK+15a] Richard J. Weiler, Michael Peter, Wilhelm Keusgen, Andreas Kortke, and Mike Wisotzki. Millimeter-wave channel sounding of outdoor ground reflections. In *Radio and Wireless Symposium (RWS), 2015 IEEE*, San Diego, USA, Jan 2015.

[WPK+15b] Richard J. Weiler, Michael Peter, Thomas Kühne, Mike Wisotzki, and Wilhelm Keusgen. Simultaneous millimeter-wave multi-band channel sounding in an urban access scenario. In *Antennas and Propagation (EUCAP), 2015 9th European Conference on*, Lisbon, Portugal, April 2015.

[WPK+16a] R. J. Weiler, M. Peter, W. Keusgen, K. Sakaguchi, and F. Undi. Environment induced shadowing of urban millimeter-wave access links. *IEEE Wireless Communications Letters*, 5(4):440–443, Aug 2016.

[WPK+16b] Richard J. Weiler, Michael Peter, Wilhelm Keusgen, Alexander Maltsev, Ingolf Karls, Andrey Pudeyev, Ilya Bolotin, Isabelle Siaud, and Anne-Marie Ulmer-Moll. Quasi-deterministic millimeter-wave channel models in MiWEBA. *EURASIP Journal on Wireless Communications and Networking*, 2016(1):1–16, 2016.

[WPKW14] Richard J. Weiler, Michael Peter, Wilhelm Keusgen, and Mike Wisotzki. Measuring the busy urban 60 GHz outdoor access radio

channel. In *Ultra-Wideband (ICUWB), 2014 IEEE International Conference on*, Paris, France, 2014.

[WRC15] Ting Wu, T.S. Rappaport, and C.M. Collins. The human body and millimeter-wave wireless communication systems: Interactions and implications. In *Communications (ICC), 2015 IEEE International Conference on*, pages 2423–2429, June 2015.